· UNIVERSITY OF OXFORD ·

· DEPARTMENT OF ENGINEERING SCIENCE ·

Liquid Crystal Devices for Optical Beam Control

Zimo Zhao

Somerville College

A thesis submitted for the degree of

Doctor of Philosophy

Supervised by Prof. Stephen M. Morris, Prof. Steve J. Elston and Prof. Chao He

Michaelmas Term 2024

Declaration

I declare that this thesis is entirely my own work, and except where otherwise stated, describes my own research.

Zimo Zhao

Somerville College

This thesis is dedicated to

My mother,

Whose endless care cradled me through every moment.

My father,

Whose unwavering faith in me never faltered.

My younger self,

Who took the first bold steps on this unforgettable journey.

And to all those who choose this adventure,

May you find courage, wisdom, and strength.

Abstract

This thesis investigates the development of liquid crystal (LC) devices for deployment in advanced optical beam control, with a focus on their potential to enhance precision, efficiency, and versatility in various optical applications. The key innovations of this work include the development of diffractive optical elements, new intensity adaptive optics (I-AO) systems and a generator of optical quasiparticles using LC devices. For the development of direct laser written (DLW) diffractive optical elements, such as Dammann gratings and computer-generated holograms (CGHs), they are fabricated using two-photon polymerisation (TPP) DLW, achieving diffraction efficiencies above 60% and response times of 20 ms for thin (5 μm) devices and 120 ms for thick (20 μm) devices.

The thesis also presents significant advances in intensity-based adaptive optics (I-AO) systems, proposing the I-AO aberration corrector with corresponding calibration methods and utilising dual-loop feedback correction mechanisms along with sensor-based and sensorless methods to correct the intensity aberrations. This system improves intensity distribution uniformity under aberrations and enables control of the total energy level at the pupil plane, distinguishing it from conventional phase-only adaptive optics (AO) and expanding the existing AO toolboxes. Furthermore, the thesis explores the generation of optical quasiparticles, including optical skyrmions and optical merons, through cascaded LC spatial light modulators (SLMs). The proposed structure allows for the dynamic manipulation of the beam polarisations, providing flexibility in optical quasiparticle generation. The generated optical quasiparticles demonstrate topological protection against combinations of various perturbations (e.g. attenuators, retarders and depolarisers) with experimental robustness exceeding 90%.

Future work will focus on refining LC mixtures for faster response times, developing advanced I-AO correction algorithms, and exploring the potential of optical quasiparticles for optical computing and high-bandwidth communications.

Acknowledgements

Acknowledgements Time always flies. In the blink of an eye, my doctoral journey is nearing its end. As I reflect on this enriching experience, the memories remain fresh and the cherished moments etched in my heart. Life, as someone aptly put it, is like a train in constant motion: some passengers share beautiful parts of the journey, while others quietly disembark, leaving lasting impressions behind. Thankfully, the ever-changing scenery along the way has offered companionship and strength, making the journey all the more worthwhile.

Looking back on the twenty years of academic pursuit, I recognise that none of this would have been possible without the unwavering support of my family, friends, supervisors, and colleagues. Each shared moment has been invaluable and I would like to take this rare opportunity to express my heartfelt gratitude and deepest thanks to you all, in the order in which you got on board my train.

Firstly, I would like to express my deepest gratitude to my parents, Mr. Zhengquan Zhao and Mrs. Yuying Li. Your unwavering care has shaped who I am today, and your constant support has empowered me to face challenges with confidence and pursue my dreams on this unique journey of life. I love you both dearly.

1998

2004

Next, I want to thank my dear friends from school: Miss Fei Gu, Miss Jiayu Wang, Mr. Junxian Han, Mr. Kehan Zhao, Miss Qihang Wang, Miss Wenyi Wang, Miss Yue Zhou, and Mr. Yun Wang. The friendships formed in school days are truly precious and I am fortunate to have kept in touch with all of you till now. Your emotional support during my doctoral journey, especially while I writing this thesis, has been a guiding light.

2010

2016

I extend my sincere thanks to my supervisor, Prof. Stephen Morris. I still vividly remember that sweltering summer day when your interview invitation quietly slipped into my mailbox, setting the wheels of my fate in motion. It was your trust and belief in me that gave me the invaluable opportunity to join Oxford, the institution I had long aspired to. Without your dedicated guidance and mentorship during my time in the Soft Matter Photonics group, I would not have been able to achieve what I have today. Your support and kindness will always remain in my heart and never to be forgotten.

2020

To my other supervisor, Prof. Steve Elston, thank you for your generous guidance and thoughtful discussions that have enriched my research. You have always been generous with your time, patiently and meticulously discussing every aspect of my research. Each conversation with you has not only provided invaluable insight but also led to constructive suggestions. Your guidance has been instrumental to my continuous progress in research. Your mentorship and support are truly a cherished part of my life in Oxford.

I would also like to express my sincere gratitude to my third supervisor, Dr. Chao He. Your unwavering trust in my abilities has been invaluable. Not only did you welcome me into your group, but you also provided steadfast support and guidance across various projects, enabling me to achieve what I have today. Beyond the lab, you have been like a brother to me, always offering care and thoughtful attention to my daily life. It has been both an honour and a privilege to be part of the Vectorial Optics and Photonics group and to work alongside you in pursuing our scientific dreams. I will cherish your kindness and support forever.

I would like to thank the senior members who have supported me throughout my DPhil journey. My deepest gratitude goes to my examiner, Prof. Ekaterina Shamonina, for your guidance in improving my presentation skills, and to my college advisor, Prof. Noa Zilberman,

2021

for your support in college affairs. Thank you also to Prof. Martin Booth for your advice on my research.

A special thanks to Dr. Patrick Salter, whose expertise in laser fabrication provided immense support when my project faced challenges. Discussing problems with you has always been a pleasure, and each conversation has broadened my perspective and enriched my understanding. Your generosity in sharing your experience and unique insights has been invaluable.

Then I would also like to express my sincere gratitude to my close colleague, Mr. Yifei Ma. Working alongside you has been an absolute joy. In the lab, you have been my most reliable partner, always ready to engage in discussions, testing, and troubleshooting, no matter how long or complex the experiments are. Beyond the experiments in labs, you are also a thoughtful and considerate friend in life, always looking out for everyone around you. It has been a true honour to work with you.

My gratitude extends to Dr. Jacopo Antonello and Mr. Zipei Song. Although I met Dr. Jacopo Antonello only once, the materials you provided have benefited me greatly. Mr. Zipei Song, your foundational work on the theoretical aspects has been instrumental in helping me achieve my goals. I am also sincerely thankful to Professor Andong Wang, Dr. Jingyu Wang, Dr. Jiahe Cui, and Dr. Mohan Wang. Whenever I encountered difficulties in my research, you generously took time out of your busy schedules to engage in deep discussions with me, always offering invaluable insights. Your guidance has been truly enlightening, helping me overcome obstacles and broadening my understanding. It is through your kind and selfless assistance that I have been able to make steady progress in my research.

2022

Next, I would like to extend my sincerest gratitude to Mr. An Aloysius Wang. You are truly a genius, having developed numerous groundbreaking theories that have laid a solid foundation for many of our research topics. Your humility and approachability are admirable, and it has been a great privilege to work alongside you. Your guidance has not only enriched my academic journey but also inspired me to view problems from entirely new perspectives. This friendship will remain etched in my memory, and I shall always be grateful.

2023

I am deeply grateful to all members of the SMP group and VOP group for their friendship, inspiration, and encouragement over the years. Specifically, I want to thank the members I was closely involved with: Miss Ji Qin, Mr. Runchen Zhang, Mr. Tádé Marozsak, Mr. Xiaoyi Shang, Mr. Xuke Qiu, Mr. Yunqi Zhang, Mr. Yuxi Cai and Mr. Zhi Kai Pong for all the precious time we had.

Finally, I extend my heartfelt thanks to everyone who has offered help and support throughout my research journey. Due to the constraints of space, I am unable to mention each of you by name, but please know that your kindness and encouragement have left a lasting impression on me. It is because of your companionship and support that I have been able to move forward in pursuit of my academic dreams. I am truly grateful for your understanding and assistance, and I hope our friendships will endure.

Zimo Zhao

in Oxford

2024

Publications and Presentations

• Chapter-related Publications

Chapter 3: Polychromatic Multi-Element Liquid Crystal Dammann Gratings

Zhao, **Z.**, Chen, B., Salter, P. S., Booth, M. J., O'Brien, D., Elston, S. J. and Morris, S. M. Multielement polychromatic 2D liquid crystal dammann gratings. *Adv. Mater. Technol.* **8,** 2200861 (2022)

Chapter 4: Laser Written Liquid Crystal Computer Generated Holograms

Sandford O'Neill, J., Salter, P., **Zhao**, **Z.**, Chen, B., Daginawalla, H., Booth, M. J., Elston, S. J. and Morris, S. M. 3D switchable diffractive optical elements fabricated with two-photon polymerization. *Adv. Opt. Mater.* **10,** 2102446 (2022)

Chapter 5: Liquid Crystal Devices for Intensity Aberration Correction

Zhao, **Z.**, Ma, Y., Antonello, J., Song, Z., Cui, J., Chen, B., Wang, J., Sun, B., He, H., Luo, L., Fells, J. A. J., Elston, S. J., Booth, M. J., Morris, S. M. and He, C. Intensity adaptive optics. *Light: Sci. Appl.* **14,** 128 (2024)

Chapter 6: Optical Quasiparticles Generation using Liquid Crystals

Wang, A. A., **Zhao**, **Z.**, Ma, Y., Cai, Y., Zhang, R., Shang, X., Zhang, Y., Qin, J., Pong, Z.-K., Marozsák, T., Chen, B., He, H., Luo, L., Booth, M. J., Elston, S. J., Morris, S. M. and He, C. Topological protection of optical skyrmions through complex media. *Light: Sci. Appl.* **13,** 314 (2024)

• Other Publications

Articles

He, C., Chen, B., Song, Z., **Zhao**, **Z.**, Ma, Y., He, H., Luo, L., Marozsak, T., Wang, A. A., Xu, R., Huang, P., Qiu, X., Zhang, Y., Sun, B., Cui, J., Cai, Y., Zhang, Y., Wang, A., Wang, M., Salter, P., Fells, J. A. J., Dai, B., Liu, S., Guo, L., Ma, H., Elston, S. J., Zhan, Q., Qiu, C., Morris, S. M., Booth, M. J. and Forbes, A. A reconfigurable arbitrary retarder array as complex structured matter. *Nat. Commun.* Accepted (2024)

Ma, Y., **Zhao**, **Z.**, Chen, B., Wang, A. A., Cai, Y., Qin, J., Zhang, R., Zhang, Y., Cui, J., Sun, B., He, H., Luo, L., Elston, S. J., Morris, S. M., Booth, M. J. and He, C. Using optical skyrmions to assess vectorial adaptive optics capabilities in the presence of complex aberrations. *Sci. Adv.* In revision (2024)

Wang, A. A., Ma, Y., Zhang, Y., **Zhao**, **Z.**, Cai, Y., Qiu, X., Dong, B. and He, C. Unlocking new dimensions in photonic computing using optical Skyrmions. *arXiv* (2024)

Ma, Y., **Zhao**, **Z.**, Cui, J., Wang, J. and He, C. Vectorial adaptive optics for advanced imaging systems. *J. Opt.* **26,** 065402 (2024)

Chen, B., Xie, P., **Zhao**, **Z.**, Salter, P. S., Li, M., Xue, L., Qiu, X., Booth, M. J., Elston, S. J. and Morris, S. M. Ultrafast Laser Writing of Liquid Crystal Waveguides. *Ultrafast Science* **4,** 0065 (2024)

Shi, Y., Wright, M., Sharpe, M. K., McAleese, C. D., Polzin, J.-I., Niu, X., **Zhao**, **Z.**, Morris, S. M. and Bonilla, R. S. Characterization of solar cell passivating contacts using time-of-flight elastic recoil detection analysis. *Appl. Phys. Lett.* **123,** 261106 (2023)

Chen, B., **Zhao**, **Z.**, Nourshargh, C., He, C., Salter, P. S., Booth, M. J., Elston, S. J. and Morris, S. M. Laser written stretchable diffractive optic elements in liquid crystal gels. *Crystals* **12,** 1340 (2022)

Jin, Y., Elston, S. J., Fells, J. A. J., Chen, B., Li, M., Kamal, W., **Zhao**, **Z.** and Morris, S. M. Backflow-assisted time-resolved phase modulation in nematic liquid crystal Pi-Cells. *Opt. Laser Technol.* **156,** 108596 (2022)

News & Views

Chen, B., **Zhao**, **Z.** and Morris, S. M. Chiral switches bring new twist to photonics. *Nat. Photonics* **16,** 174 (2022)

Ma, Y., **Zhao**, **Z.**, Morris, S. M. and He, C. Twisted microdomains in liquid crystals for polarization-insensitive phase modulation. *Light: Sci. Appl.* **13,** 8 (2024)

Conference Proceedings

Zhao, **Z.**, Ma, Y., Elston, S. J., Booth, M. J., Morris, S. M. and He, C. *Intensity adaptive optics* in *The Oxford International Conference on Advanced Optics and Photonics (OIC)* (2024)

Zhao, **Z.**, Ma, Y., Elston, S. J., Booth, M. J., Morris, S. M. and He, C. *Feedback-controlled adaptive optics for intensity error correction* in *Adaptive Optics and Wavefront Control for Biological Systems X* (SPIE, 2024)

Zhao, **Z.**, Ma, Y., Elston, S. J., Booth, M. J., Morris, S. M. and He, C. *Topological meronic beams* in *Complex Light and Optical Forces XVIII* (SPIE, 2024)

Ma, Y., **Zhao**, **Z.**, Elston, S. J., Morris, S. M., Booth, M. and He, C. *Polarization adaptive optics for diattenuation aberration* in *Adaptive Optics and Wavefront Control for Biological Systems X* (SPIE, 2024)

Ma, Y., **Zhao**, **Z.**, Elston, S. J., Morris, S. M., Booth, M. and He, C. *Polarization adaptive optics for enhanced Stokes vector measurements* in *Polarized Light and Optical Angular Momentum for Biomedical Diagnostics 2024* (SPIE, 2024)

Chen, B., **Zhao**, **Z.**, Nourshargh, C., He, C., Salter, P., Booth, M. J., Elston, S. J. and Morris, S. M. *Laser written stretchable diffractive optic elements in polymerizable liquid crystal gels* in *Liquid Crystals XXVII* (SPIE, 2023)

Zhao, **Z.**, Chen, B., Salter, P. S., Booth, M. J., O'Brien, D., Elston, S. J. and Morris, S. M. *3D laser sculpted tunable diffractive optics elements in liquid crystal devices* in *The 10th Optical Manipulation and Structured Materials Conference (OMC2023)* (2023)

Contents

CHAPTER 6: Optical Quasiparticle Generation using Liquid Crystals

CHAPTER 7: Conclusions and Future Work

List of Figures

List of Abbreviations

1D	One Dimensional
2D	Two Dimensional
3D	Three Dimensional
AF	Auto Focusing
AO	Adaptive Optics
CAD	Computer-aided Design
CCD	Charge-coupled Device
CGH	Computer-generated Holograms
CMOS	Complementary Metal-oxide-semiconductor
CW	Continuous Wave
DLW	Direct Laser Writing
DM	Deformable Mirrors
DOE	Diffractive Optical Element
DPSS	Diode-pumped Solid State
FFT	Fast Fourier Transform
FID	Focus Intensity Distribution
FWHM	Full Width at Half Maximum
GS	Gerchberg-Saxton
I-AO	Intensity Adaptive Optics
IFFT	Inverse Fast Fourier Transform
ITO	Indium Tin Oxide
LC	Liquid Crystal
LCoS	Liquid Crystal on Silicon
LED	Light-emitting Diode
LUT	Look-up Table
MEMS	Micro-electromechanical Systems
ML	Machine Learning
NA	Numerical Aperture
ND	Neutral Density
NLC	Nematic Liquid Crystal
OD	Optical Density
OPA	One-photon Absorption
P-AO	Polarisation Adaptive Optics
PI	Polyimide
PID	Proportional-Integral-Derivative
POM	Polarising Optical Microscope
SEM	Scanning Electron Microscope
SLM	Spatial Light Modulator
SNR	Signal-to-noise Ratio
SoP	State of Polarisation
TPA	Two-photon Absorption
TPP	Two-photon Polymerisation
UV	Ultraviolet
V-AO	Vectorial Adaptive Optics

Doctor: the word for "healer" and "wise man",

throughout the universe.

— River Song

CHAPTER 1

Overview

1.1 Introduction

This thesis investigates the development and application of liquid crystal (LC) devices in sophisticated optical systems, particularly focusing on their capability for complex beam control. This introductory chapter establishes the research motivation and provides a structured overview of the whole thesis, setting the stage for in-depth discussions in subsequent chapters. These chapters explore various aspects of LC technology, from fundamental principles to advanced applications, aiming to offer a comprehensive view of their potentials to enhance and unlock new optical systems.

1.2 Research Motivation

LCs have been pivotal in optical engineering, known for their ability to modulate light properties such as amplitude, phase, and polarisation[1,2]. Initially applied in flat-panel displays[3,4], their remarkable electro-optical properties have led to widespread adoption in fields ranging from telecommunications[5] and adaptive optics[6] to biomedical imaging[7]. As LC technology progressed, spatial light modulators (SLMs)[8] and diffractive optical elements (DOEs)[9] emerged, enabling precise control of light for applications like beam shaping[10,11], aberration correction[12], and structured light generation[13].

The evolution of LC technology has seen significant advances in material science[14] and fabrication techniques[15]. Nematic LCs (NLCs), with their anisotropic molecular alignment, are particularly suited for real-time optical modulation due to their ability to rapidly reorient under external electric fields[16]. While early uses focused on switching between transparent and opaque states, the potential for more complex light modulation became clear when researchers began using nematic LCs for phase control, leading to the development of SLMs for high-resolution imaging and complex light field generation[17,18]. However, challenges such as response speed, resolution, diffraction efficiency, and form factor remain.

Today, LC-based SLMs are integral to adaptive optics systems, providing real-time wavefront correction in fields like astronomy[19], where atmospheric turbulence degrades image quality, and biomedical imaging[20], where tissue-induced aberrations must be corrected. Compared to traditional deformable mirrors, LCs offer a more compact and cost-effective solution, with precise phase and polarisation modulation capabilities[21]. Innovations such as two-photon polymerisation direct laser writing (TPP-DLW) have further expanded LC applications, enabling the creation of intricate 3D optical structures and compact, high-performance devices[15]. LCs have also played a crucial role in structured light generation, producing optical vortices with orbital angular momentum, which are essential for applications in high-speed communication and beyond[22–24].

Despite these advancements, challenges persist. LC response speed requires improvement for ultra-fast, real-time corrections, such as in high-resolution telescopes and high-speed data transmission[17,18]. Diffraction efficiency is also hindered by pixelation in SLMs, which reduces system resolution[8]. To address these issues, further research into different LC mixtures, improved device architectures, and advanced fabrication techniques are needed[4]. Expanding LC functionality beyond the visible spectrum, particularly in the infrared and ultraviolet ranges, is

crucial for emerging fields like optical computing and optical communication[23,25].

Also, miniaturising LC-based devices to reduce their form factor without compromising performance presents a significant opportunity. While techniques like TPP-DLW have enabled more compact designs[26,27], optimisation is still needed to make these devices cost-effective and scalable. Developing multi-functional LC devices capable of simultaneously modulating phase and intensity could lead to more efficient and versatile systems for real-time optical control[14,28].

This thesis aims to advance LC-based devices through innovative approaches in design, fabrication, and integration into advanced optical systems. The research starts from focuses on enhancing the performance of nematic LCs in complex laser written diffractive optical elements, including Dammann gratings and computer-generated holograms (CGHs), with demonstrations of good response times and diffraction efficiencies, as well as reduced device complexity. By employing advanced fabrication techniques such as TPP-DLW, the work seeks to develop smaller, more efficient LC devices capable of real-time optical beam modulation.

Additionally, this thesis demonstrates new LC-based systems capable of correcting complex intensity distortions and generating structured light in real time. Leveraging dual-loop feedback mechanisms and optimised control algorithms, novel approaches to adaptive optics are explored, proposing new correction methods for intensity aberrations. The research also investigates the generation of optical quasiparticles using cascaded LC devices. These robust quasiparticles hold the advantage of topological protection, which is also explored and investigated. The outcomes of this thesis underscore the versatility and enhanced functionality of LC devices in optical beam control.

1.3 Thesis Outline

This thesis details the development of LC devices and accompanying optical systems for complex beam control. This introductory chapter provides the motivation of the research and an overview of the thesis structure, setting the stage for subsequent detailed discussions on the innovations and applications of LC technology in optical systems.

Chapter 2 provides important background on LCs and their expansive roles in optical technologies. The chapter initiates with a foundational introduction to LC phases, demonstrates their distinct physical and electro-optical properties that are crucial for a wide range of optical system applications. This section explains how the anisotropic properties of LCs enable their utility in modulating light based on the orientation of their molecules, which is influenced by electrical fields among other stimuli. Progressing further, the chapter reviews the innovative technique of two-photon polymerisation direct laser writing in LCs. This segment elucidates the underlying theory of two-photon absorption – a non-linear optical process – that allows for the precise fabrication of complex 3D polymer structures at the micro-scale. This process is particularly significant for creating diffractive optical elements with extremely high precision, which is the subject of Chapters 3 and 4, and are critical for advanced optical systems in fields such as telecommunications and medical imaging.

In addition to these technologies, the chapter also introduces the integration of LC devices within adaptive optics systems. A comprehensive overview of adaptive optics is provided, explaining how these systems are used to correct distortions in optical beams in real-time. Detailed applications of LCs in adaptive optics are then discussed, illustrating how they improve system adaptability and performance through dynamic control of beam intensity and phase correction.

Chapter 2 concludes by reinforcing the versatility and significance of LCs, not only in advancing existing optical technologies but also in pioneering new applications in diffractive optical elements and adaptive optics. This summary underscores the importance of continuous innovation in LC technologies for achieving superior beam control in cutting-edge optical systems.

Chapter 3 presents an in-depth exploration of the development of polychromatic multi-element LC Dammann gratings. The chapter opens with an in-depth theoretical background on Dammann gratings, providing insights into their design principles and the specific techniques used for their generation. This foundational knowledge is critical for understanding the unique capabilities of these gratings in distributing light evenly across a defined area, making them ideal for applications requiring uniform light distribution across multiple wavelengths. Utilising a SLM imaging system, simulations are conducted to predict the performance of these gratings, providing a predictive framework for their practical deployment. The chapter then transitions to a detailed description of the two-photon polymerisation direct laser writing system employed for fabricating these gratings. It discusses the structural nuances of the system and various optimisations that have been developed to enhance the stability and accuracy of the fabrication process.

Detailed fabrication procedures are provided for both single and multi-element Dammann gratings, with particular emphasis on the single-element switchable 2D Dammann grating. This section presents a thorough analysis of experimental results, including assessments of fabrication quality, diffraction efficiency, response time, temperature stability, and multiwavelength compatibility. Furthermore, the chapter examines the performance of multi-element interchangeable 2D Dammann gratings, emphasizing their fabrication quality and functional metrics.

Chapter 3 concludes by summarising the key contributions of this research to advancing

Dammann grating design and application. It highlights the successful integration of theoretical models, simulation methods, and experimental validation, demonstrating the creation of 2D LC-based Dammann gratings that can be switched using voltage. These gratings are designed to operate across multiple wavelengths and temperatures, with quantified response times and diffraction efficiencies. The results in this chapter have been published in the paper 'Multielement Polychromatic 2D Liquid Crystal Dammann Gratings' *Advanced Materials Technologies* **8**, 2200861 (2023).

Chapter 4 focuses on the advanced topic of laser-written LC Computer Generated Holograms (CGH), which represent a more sophisticated class of diffractive optical elements compared to Dammann gratings in Chapter 3. The chapter starts with a detailed overview of CGHs, outlining the critical hologram generation algorithms and the methods used to evaluate their effectiveness through numerical simulations and experimental results using a SLM.

The narrative then shifts to a detailed examination of single-element, switchable laser-written CGHs. Experimental findings related to their diffraction efficiency and response times are presented, along with in-depth discussions of these results. This section not only highlights the technical successes but also discusses the challenges and limitations encountered during the experiments. Additionally, the chapter explores the characteristics and performance of multi-element interchangeable CGHs. Data on their efficiency and response characteristics are provided, followed by comprehensive analyses of these results. This part of the chapter provides insights into the practical applications and potential of these laser written CGHs in enhancing optical systems without the need for SLM technology.

Chapter 4 concludes with a summary that underscores the advancements in the laser-written CGH technology, particularly emphasising the adaptability and efficiency of the laser-written LC method in generating dynamically switchable holographic patterns to form different images

in the replay field. Some of the results presented in this chapter have formed the basis of the published paper '3D Switchable Diffractive Optical Elements Fabricated with Two-Photon Polymerisation' *Advanced Optical Materials* **10**, 2102446 (2022).

Chapter 5 examines the use of LC devices for correcting intensity aberrations in adaptive optical systems, addressing principles of adaptive optics, system development, calibration of the adaptive optical elements, correction methods, and experimental outcomes. It begins with an introduction to the fundamental principles of intensity aberration correction in both sensor-based and sensorless formats, with a spotlight on Zernike polynomials and their intensity-specific modifications. These concepts establish the basis for various correction modes tailored to diverse optical applications such as high-resolution microscopy and biomedical issue observations. The chapter then details the development and calibration of a dual-loop feedback correction system, crucial for dynamically adjusting and correcting aberrations in real-time and ensuring that all optical components, such as SLMs and sensors, function optimally.

The discussion of correction methods focuses on two main approaches: sensor-based and sensorless methods. The sensor-based method includes calibration and the use of a look-up-table (LUT) derived from system characterisation to correct aberrations detected by a pupil sensor. In contrast, the sensorless method iteratively applies specially designed patterns to the SLM to compensate for intensity aberrations, inspired by traditional wavefront sensorless algorithms but adapted for intensity corrections. Experimental results provide a comparative analysis of corrective performance for each method, discussing their practical strengths and limitations.

Chapter 5 concludes with a summary that emphasises the innovative use of LC devices and dual-loop feedback mechanisms, enhancing the adaptability and performance of optical systems for intensity aberration correction. This approach promises significant advancements in fields such as astronomy and medical imaging, paving the way for more precise imaging solutions,

particularly in applications where precise intensity control is crucial for accurate diagnostics, like high-resolution microscopy or disease diagnosis. The results in this chapter are accepted for publication in paper 'Intensity Adaptive Optics' *Light: Science & Applications*.

Chapter 6 investigates the use of LC devices for generating structured light, focusing on the creation of optical skyrmions and merons. It explores the construction of cascaded LC systems using SLMs to manipulate light fields and presents experimental results on the generation and stability of skyrmionic and meronic beams. These beams are essential for understanding the behaviour and stability of light fields under optical perturbations.

The construction of cascaded LC devices using multiple SLMs is discussed, explaining how they can be used to manipulate light to form optical skyrmions and merons. While the theory behind cascaded SLMs is established, this work demonstrates for the first time the successful generation of skyrmionic and meronic beams using this configuration. This setup enables dynamic control of light fields, allowing the formation of complex topological textures with high robustness. The results confirm the high efficiency and structural fidelity of the generated beams, closely matching theoretical predictions. The chapter also evaluates the topological protection of these beams, demonstrating their resilience against optical perturbations and highlighting their potential for robust structured light applications.

Chapter 6 concludes with a summary of the advancements in the field of optical skyrmions and optical merons generated using LCs. It highlights the novel approaches developed in this research for manipulating light with LCs to create robust topological structures. These developments not only have the potential to enhance understanding of topological photonics but also pave the way for innovative applications in optical communications, microscopy, and on-chip optical computing technologies.

Chapter 7 summarises the advancements achieved in this research, focusing on the devel-

opment of LC-based DOEs, adaptive optics, and structured light systems. It highlights the contributions made in replacing SLMs with laser-written LC devices, correcting intensity aberrations, and generating topologically protected light fields. In the latter case, these concluding remarks highlight the significant findings related to the development and application of LC devices in generating complex light patterns, adaptive optics, and optical skyrmions and optical merons. The chapter concludes with potential directions for future research, including the exploration of more complex topological structures and the extension of LC technologies in optical communication, optical computing and beyond.

Study the present, in the light of the past, for the purpose of future.

— John Maynard Keynes

CHAPTER 2

Background

2.1 Liquid Crystals

2.1.1 Introduction to Liquid Crystals

The term *Liquid Crystal* (LC) refers to an intermediate state of matter between the crystalline solid and the isotropic liquid phases[1,2,29,30]. The molecules in crystalline solids are highly organised, which means they are both positionally and orientationally ordered. They are constrained to occupy specified locations in a lattice and to point their molecular axes in specific directions. Molecules in liquids, on the other hand, diffuse randomly throughout the volume with their molecular axes rotating freely and have no regularity in terms of the molecular orientation. Therefore, as its name suggests, the LC phase is a state of matter lying between the crystalline solid and the isotropic liquid phase and is classified as a mesophase. The molecules in all LC phases have no rigid positional order like the molecules in a solid and diffuse much like the molecules in a liquid[2]. However, they also maintain some degrees of orientational and positional ordering which an isotropic fluid does not have.

In general, LCs can be first divided into two categories depending upon the manner in which the LC phase is formed: thermotropic and lyotropic[29]. For thermotropic LCs, the changes in the mesophase depend on the temperature. For lyotropic LCs, the phase transition

depends on the concentration of the LC molecules in a solvent[4]. Thus, in the following context of this thesis, if it is not specifically mentioned, the use of the term 'LC' refers to thermotropic LC by default. The anisotropic structure as well as the chemical structure of a typical thermotropic LC molecule is illustrated in **Figure 2.1**. In the chemical structure of a LC molecule, it typically consists of two or more ring structures which are separated by a rigid linking group with hydrocarbon chains at one end and a nitrile group at the other.

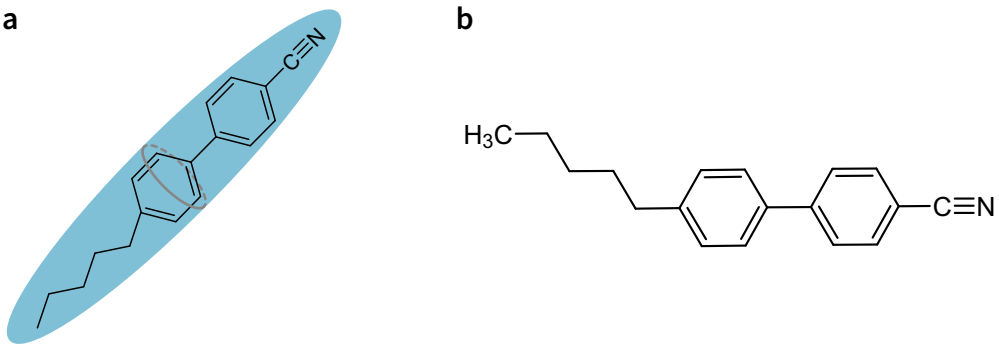

Figure 2.1: Illustration of a liquid crystal molecule. (a) The typical rod-like structure of a thermotropic LC molecule. (b) The chemical structure of a commonly used thermotropic LC (5CB).

The vast majority of thermotropic LCs are composed of rod-like molecules, with one axis that is longer than the others. Following the nomenclature originally proposed by Friedel[31], LCs of rod-like molecules can exhibit a range of different mesophases such as the nematic, cholesteric and smectic phases. A schematic of the molecular arrangement of the different LC mesophases is illustrated in **Figure 2.2**. Nematic LC is the most commonly used in commercial technologies and is the only LC phase considered in this thesis. Thus, the following discussions will mainly focus on nematic LCs.

In the nematic LC phase, these rod-like molecules have no long-range translational order but have a high degree of long-range orientational order, as the molecules are self-aligned with their long axes being roughly parallel to each other[32]. Though the LC molecules are pointing in different directions in a microscopic view, in general the nematic phase can be described

macroscopically by the director $\hat{\mathbf{n}}$. The director $\hat{\mathbf{n}}$ is a vector which lies in parallel with the average orientation of the molecules. An illustration of the director $\hat{\mathbf{n}}$ is also displayed in Figure 2.2.

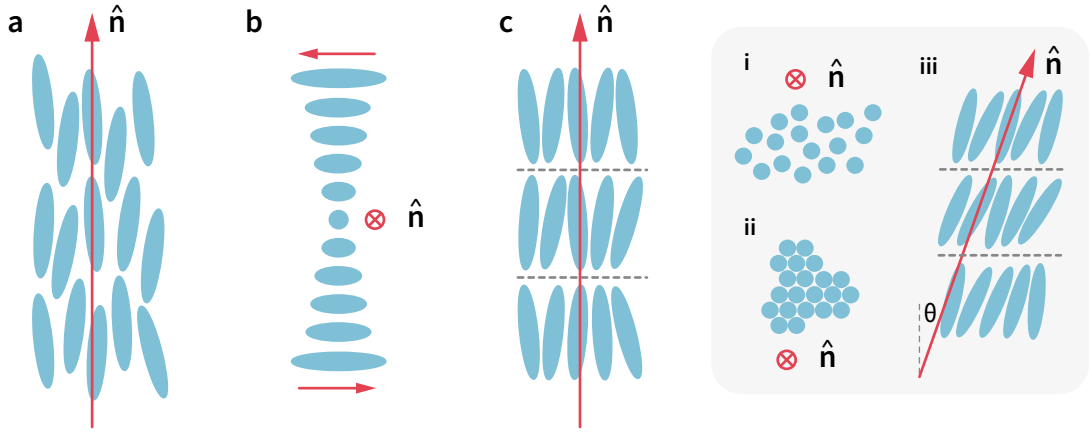

Figure 2.2: Schematics of different LC mesophases. (a) Nematic phase, where the rod-like molecules have no long-range translational order but have a high degree of long-range orientational order. (b) Cholesteric (chiral nematic) phase, where the molecules form a spontaneous twist about the axis normal to the preferred helix direction. (c) Smectic phase, where the molecules form a stratified structure. A variety of arrangements are possible within each stratification and are classified into type A (i), B (ii), C (iii) and so on.

To describe the ordering of molecules in a nematic LC phase quantitatively, the order parameter S is defined to describe the orientational order of the LC phase, where $S = 1$ for a perfectly aligned LC with all the molecules pointing in the same direction and $S = 0$ for the isotropic liquid where the molecules are pointing in random directions. For the nematic LC phase, an average of the second Legendre polynomial is utilised to express the order parameter S mathematically:

$$S = \langle P_2(\cos\theta) \rangle = \frac{1}{2} \langle 3\cos^2\theta - 1 \rangle \tag{2.1}$$

where θ is the angle between the orientation of a LC molecule and the director $\hat{\mathbf{n}}$. The average symbol $\langle \cdot \rangle$ is used to calculate the order parameter over a large volume of molecules. Typically, the value of S for general nematic LC is around 0.6.

As the temperature of a thermotropic nematic LC is increased, the microscopic order of the LC molecules will transition gradually from highly ordered structure through the LC phase and into the isotropic liquid phase[3,33]. When the temperature is below the melting point of the material, it will show a crystalline solid structure with periodic positional and orientational order. However, when the temperature increases, it melts into the nematic LC phase where the LC molecules are roughly in parallel with each other with a high degree of orientational order and no positional order. When the temperature increases above the clearing temperature, the LC will transition into the isotropic liquid phase where all the molecules are pointing in a random direction. **Figure 2.3** illustrates the variation in order with the change of temperature, with typical melting and clearing points of the commonly used LC material E7.

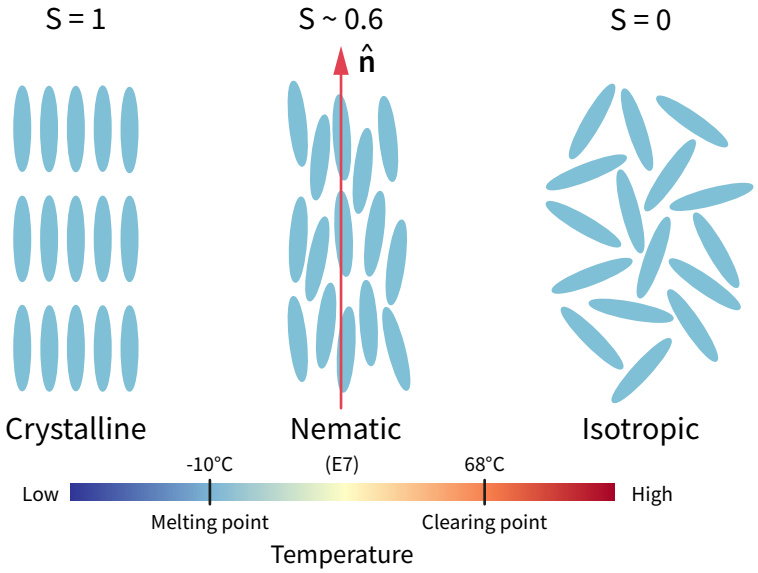

Figure 2.3: LC order variation with temperature. At low temperatures, a crystalline state forms with both orientational and positional order. When the temperature is increased over the melting point, a nematic phase is formed. An isotropic arrangement of the molecules will be observed after the temperature reaches the clearing point.

2.1.2 Properties of Nematic Liquid Crystals

(i) Physical Properties

The physicist Sir Charles Frank developed a continuum theory to explain the behaviour of LCs in the 1950s, based on the work of Oseen and Zocher in 1933[32,34,35]. Frank constructed a model

to describe the elastic free energy density of a LC by considering numerous ways of deforming a nematic LC. The elastic energy of a nematic LC material is minimised if the molecules are in thermodynamic equilibrium, which indicates that the director does not vary in space. In other words, when the nematic LC molecules reach a ground state, the LC director will not vary throughout space. Thus, Frank reduced all possible deformations to three fundamental distortions: splay, twist, and bend. Each of these is illustrated in **Figure 2.4**.

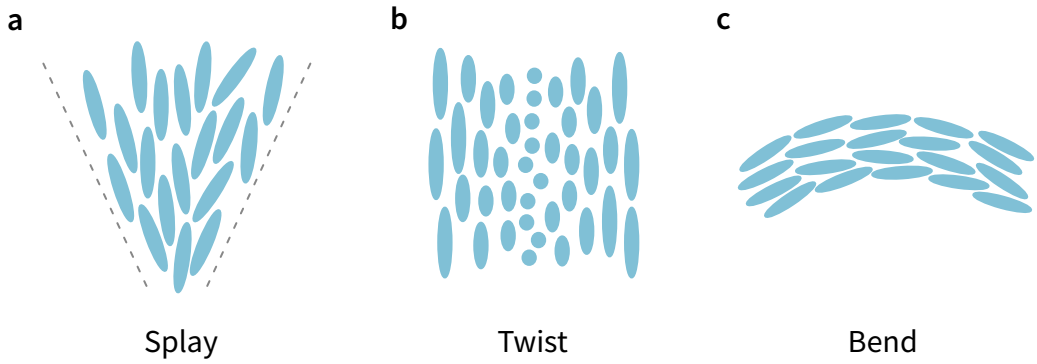

Figure 2.4: Three fundamental distortions of the nematic LC phase. The deformations of a nematic LC phase are classified as (a) splay, (b) twist, and (c) bend.

The splayed elastic distortion is represented as the divergence of the director ($\nabla \cdot \hat{\mathbf{n}}$); the twisted elastic distortion is characterised as the dot product of the curl of the director and the director ($\hat{\mathbf{n}} \cdot \nabla \times \hat{\mathbf{n}}$); and the bend elastic distortion is described as the cross product of the curl of the director and the director ($\hat{\mathbf{n}} \times \nabla \times \hat{\mathbf{n}}$). The amount each distortion contributes to the total distortion is different, thus three relative elastic coefficients K_{11}, K_{22} and K_{33} are used to determine the ratios. The total amount of energy gained by each distortion can be described by the Frank-Oseen free energy density as[32,34]:

$$\begin{aligned} f_{\text{elastic}}(\hat{\mathbf{n}}) &= f_{\text{splay}}(\hat{\mathbf{n}}) + f_{\text{twist}}(\hat{\mathbf{n}}) + f_{\text{bend}}(\hat{\mathbf{n}}) \\ &= \frac{1}{2}\left\{K_{11}\left|\nabla \cdot \hat{\mathbf{n}}\right|^2 + K_{22}\left|\hat{\mathbf{n}} \cdot \nabla \times \hat{\mathbf{n}}\right|^2 + K_{33}\left|\hat{\mathbf{n}} \times \nabla \times \hat{\mathbf{n}}\right|^2\right\} \end{aligned} \tag{2.2}$$

where $\hat{\mathbf{n}} = (n_x, n_y, n_z)$ represents the orientation of the LC director and K_{11}, K_{22} and K_{33} are the Frank splay, twist and bend elastic constants, respectively, with unit of [N]. In general, $K_{33} > K_{11} > K_{22}$, which means that bend distortions have a more significant energy than splay and twist distortions. For the commonly used LC material E7 this thesis, the elastic coefficients are: $K_{11} = 10.8$pN, $K_{22} = 6.8$pN and $K_{33} = 17.5$pN. In practice, to simplify the analytical process, a one-constant elastic free energy density expression is often utilised with the assumption $K_{33} = K_{11} = K_{22} = K$ resulting in

$$f_{\text{elastic}}(\hat{\mathbf{n}}) = \frac{1}{2}K\left\{|\nabla \cdot \hat{\mathbf{n}}|^2 + |\nabla \times \hat{\mathbf{n}}|^2\right\}. \tag{2.3}$$

(ii) Electrical and Optical Properties

A nematic LC is a type of dielectric material. When an electric field is applied to a nematic LC, dipole moments will be induced in the molecules that are opposite to the applied electric field. The effect of these dipole moments is described by the polarisation density field **P**. With the assumption that the polarisation density is linear, homogeneous, and isotropic along each direction, the equation for the polarisation density **P** under applied field **E** is given by:

$$\mathbf{P} = \varepsilon_0 \chi_e \mathbf{E}. \tag{2.4}$$

Therefore, the electric displacement field can be described as:

$$\mathbf{D} = \varepsilon_0 \mathbf{E} + \mathbf{P} = \varepsilon_0(1 + \chi_e)\mathbf{E} = \varepsilon_0 \varepsilon_r \mathbf{E} \tag{2.5}$$

where ε_0 is the vacuum permittivity, χ_e is the electric susceptibility and ε_r is the material relative permittivity related to the electric susceptibility by $\varepsilon_r = 1 + \chi_e$. For LC materials, which are

usually anisotropic, ε_r needs to be written in the tensor form:

$$\varepsilon_r = \begin{pmatrix} \varepsilon_\perp & 0 & 0 \\ 0 & \varepsilon_\perp & 0 \\ 0 & 0 & \varepsilon_\parallel \end{pmatrix} \tag{2.6}$$

where $\varepsilon_\perp$ and $\varepsilon_\parallel$ represent the electric permittivity being perpendicular and parallel to the director, respectively (which is along the z axis in the current expression). By defining the dielectric anisotropy as $\Delta\varepsilon = \varepsilon_\parallel - \varepsilon_\perp$[36], the electric displacement field $\mathbf{D}$ can be simplified to

$$\mathbf{D} = \varepsilon_0\varepsilon_\perp\mathbf{E} + \Delta\varepsilon\varepsilon_0 \left|\hat{\mathbf{n}} \cdot \mathbf{E}\right| \hat{\mathbf{n}}. \tag{2.7}$$

By substituting Equation 2.7 into the free dielectric energy expression $f_{\text{dielectric}}(\hat{n}) = -\frac{1}{2}\mathbf{D} \cdot \mathbf{E}$, and omitting the orientation independent term $-\frac{1}{2}\varepsilon_0\varepsilon_\perp E^2$, the free dielectric energy density can be simplified as[37]:

$$f_{\text{dielectric}}(\hat{n}) = -\frac{1}{2}\Delta\varepsilon\varepsilon_0 \left|\hat{\mathbf{n}} \cdot \mathbf{E}\right|^2. \tag{2.8}$$

In order to describe the LC behaviour in a more complete way, the free energy introduced by distortion should be taken into consideration as well. Thus, the overall Frank energy density with the one constant approximation can be expressed as:

$$F = f_{\text{elastic}} + f_{\text{dielectric}} = \frac{1}{2}K\left\{\left|\nabla \cdot \hat{\mathbf{n}}\right|^2 + \left|\nabla \times \hat{\mathbf{n}}\right|^2\right\} - \frac{1}{2}\Delta\varepsilon\varepsilon_0 \left|\hat{\mathbf{n}} \cdot \mathbf{E}\right|^2 \tag{2.9}$$

It can be seen from this equation that the LC director will reorient when an external electric field is applied. However, due to the existence of elastic distortion, by using the Euler-Lagrange differential method to analyse the equation, it can be shown that there exists a critical field below which a reorientation will not occur. This is known as the Fréedericksz threshold and is

expressed as:

$$\mathrm{V_{TH}} = \mathrm{E_{TH}} d = \pi \sqrt{\frac{K}{\Delta \varepsilon \varepsilon_0}} \tag{2.10}$$

where d is the thickness of the LC layer along the direction of electric field, E_{TH} is the strength of the uniform electric field and V_{TH} is the voltage applied across the LC layer. It is useful to note that the Fréedericksz threshold voltage for a given material is independent of the thickness of the LC layer and is related only to the electric permittivity and Frank elastic constants of the LC phase.

In optics, the refractive index is a dimensionless number that describes the propagation of light through a material. It is defined as the ratio between the speed of light in vacuum to that in the medium. For a typical isotropic material with relative permittivity ε_r in optical spectrum, the refractive index can also be expressed as the square root of the relative permittivity. Thus

$$n = \frac{c}{v} = \sqrt{\varepsilon_r}. \tag{2.11}$$

For an LC material, as it is an anisotropic material, the effective refractive index is different for incident light with different polarisations. Thus, two refractive indices are defined for LC, one is the extraordinary refractive index, n_e, which refers to the situation where the polarisation of the light is parallel to the optical axis, and an ordinary refractive index, n_o, which refers to the situation where the polarisation of the light is perpendicular to the optical axis.

For a uniformly aligned nematic LC, the optical axis is aligned along the director $\hat{\mathbf{n}}$. This phenomenon is referred to as birefringence and is defined as $\Delta n = n_e - n_o$. **Figure 2.5** illustrates the anisotropic refractive indices of the optical indicatrix. As expressed in Equation 2.9, the LC director will reorient when an external electric field is applied, which will cause the refractive index difference between the optical indicatrix changing along with the field applied.

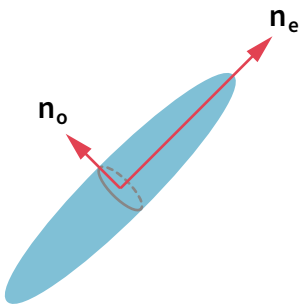

Figure 2.5: Birefringence of a uniformly aligned nematic LC. The anisotropic refractive indices along the optical indicatrix are labelled. The refractive index that is parallel to the optical axis is referred to as n_e. The refractive index perpendicular to the optical axis is referred to as n_o.

Due to the anisotropy in the refractive index mentioned above, light travelling through an LC with different polarisation components will have different velocities for components that are either aligned parallel or perpendicular to the optical axis of the LC. Thus, a phaselag will be developed between polarisation components, which results in a change of the overall polarisation of the light. This phenomenon is called optical retardation and is the principle used in electrically switchable waveplates. The optical retardation can be expressed as

$$\Delta\varphi = \frac{2\pi}{\lambda}\Delta n d \tag{2.12}$$

where Δn is the birefringence and d is the distance over which the light travels.

A common way of retrieving the optical retardation is to measure the transmission-voltage curve. If a pair of crossed identical polarisers (named "polariser" and "analyser" based on their positions) is placed before and after a LC sample and with a fixed angle χ between the polariser and the LC director, by changing the birefringence Δn of the LC via different applied voltages, the light intensity through the analyser can be changed accordingly. For the experiments in this thesis, the voltage applied across the LC layer is typically an AC voltage at 1 kHz, chosen to avoid DC damage to LCs and to balance the LC's reorientation speed for a fast switching.

Figure 2.6 illustrates the configuration of whole measurement system with polariser, analyser, and LC layer for a typical transmission-voltage curve measurement system.

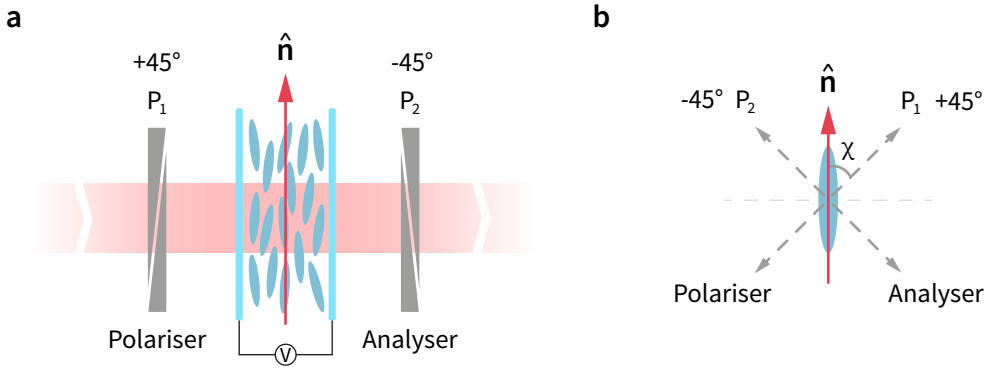

Figure 2.6: Fréedericksz transmission curve measurement system. (a) A schematic of the system with a pair of crossed polarisers sandwiching a voltage-controlled LC layer in between. (b) The angular relationship between the polarisers and the rubbing direction of the nematic LC.

By measuring the intensity of the light after the analyser and by comparing that with the incident light intensity, the transmission-voltage dependence can be derived as

$$T = \frac{I}{I_0} = \sin^2(2\chi)\sin^2\left(\frac{\pi \Delta n d}{\lambda}\right) \tag{2.13}$$

where I is the transmitted light intensity measured after the analyser, I_0 is the incident light intensity measured before the light entering the LC layer, χ is the fixed angle between the polariser and the LC director, Δn is the birefringence, d is the thickness of the LC layer and λ is the wavelength of incident light.

Since χ is a fixed angle for a certain measurement, which acts as a constant scaling factor in the results, the measurement transmission result T can then be normalised to $[0, 1]$ as T' to eliminate the consideration of χ. Thus the optical retardation $\Delta\varphi$ can be derived as

$$\Delta\varphi = 2\arcsin\left(\sqrt{\frac{T}{\sin^2(2\chi)}}\right) = 2\arcsin\left(\sqrt{T'}\right). \tag{2.14}$$

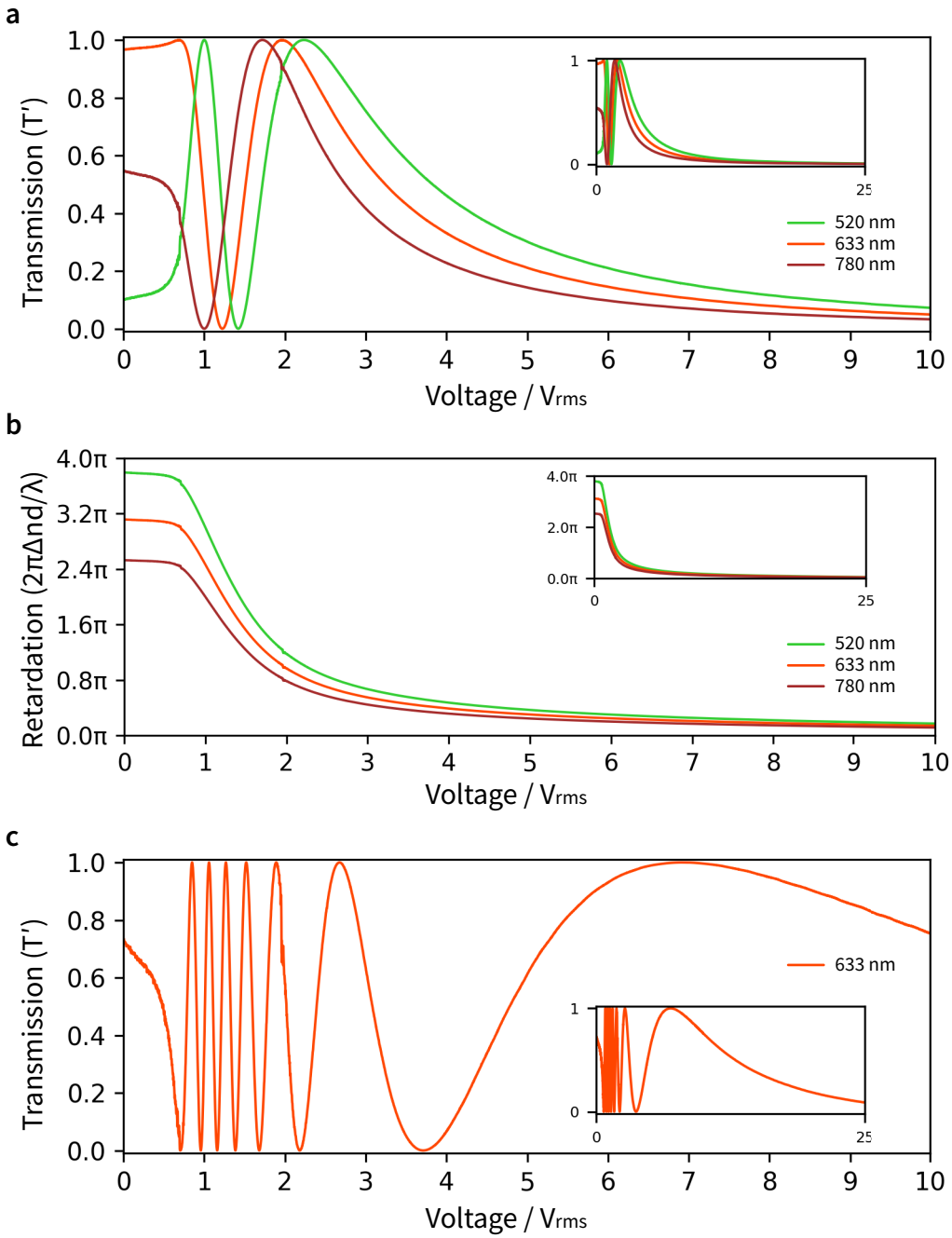

Figure 2.7: Typical transmission-voltage dependence results. (a) The normalised transmission-voltage dependence results for nematic LC at various wavelengths and different voltages from 0 V_{rms} to 10 V_{rms}, with the inset figure demonstrating the overall performance up to 25 V_{rms}. The thickness of the LC layer is 5 μm. (b) The optical retardation retrieved from the measurement at various wavelengths and different voltages from 0 V_{rms} to 10 V_{rms}, with an inset figure demonstrating the overall performance within a higher range up to 25 V_{rms}.The thickness of the LC layer is 5 μm. (c) The normalised transmission-voltage dependence results for nematic LC with 20 μm layer thickness.

Since T' is constrained to the range $[0, 1]$, the direct result from this equation is mathematically limited to $\Delta\varphi \in [0, \pi]$. However, in practice, phase retardation varies continuously with

the voltage, requiring phase be flipped at its extremes to resolve total phase values larger than π. A typical transmission-voltage curve measurement result with normalised values and the optical retardation retrieved from measurements for various wavelengths (520 nm, 633 nm, 780 nm) and layer thicknesses (5 μm and 20 μm) are illustrated in **Figure 2.7**.

2.2 Two-Photon Polymerisation Direct Laser Writing in Liquid Crystals

2.2.1 Two-Photon Absorption

3D microstructures have widespread applications in many different fields including micro-optics[26], microelectronics[38], communications[23], biomedical tools[39], Micro-Electro-Mechanical systems (MEMS)[40] and more. Furthermore, there are increasing demands to develop new methods with which to fabricate miniaturised and integrated 3D microstructures[41]. Thus, this leads to the development of various microfabrication technologies including deep ultraviolet (UV) lithography[42], electron/ion beam lithography[43,44], nanoimprint lithography[45], micro-stereolithography[46], inkjet printing[47] and self-assembly[48]. However, these techniques are sometimes limited by one or more of the following properties: ability to fabricate delicate 3D microstructures, resolution of the fabrication process, and high cost. In comparison, two-photon polymerisation (TPP) enables the fabrication of complex and delicate 3D microstructures in various materials with sub-diffraction-limit resolution. As a result, TPP fabrication process has attracted great interest all over the world.

In addition, direct laser writing (DLW), which belongs to the category of laser-based 3D printing techniques[49], has the ability to fabricate delicate microstructures in various media using computer aided designs[50], similar to classic stereolithography[51–53] and selective laser sintering techniques[54,55]. In comparison with the latter two techniques, the advantage of DLW is that it offers superior feature resolution and does not require the need for recoating; however,

a downside is that DLW can be much slower than other methods and requires expensive fabrication equipment.

Initial work on DLW was carried out in the early 90s utilising a single-photon absorption method[56,57]. After that, Maruo et al.[26] demonstrated the first successful DLW fabrication with multi-photon polymerisation in 1997. The potential for fabricating full 3D microstructures was immediately embraced by the photonics community and many applications were exploited[58]. More recently this technique has been applied in more diverse fields such as micro-optics[59,60], microfluidics[61], biomedical implants[62,63], and tissue engineering[39,64,65].

By using multiphoton absorption in DLW, TPP-DLW has emerged as a powerful laser-processing technique that can be used to fabricate complex and delicate polymer structures at the scale of micrometres[38,40,66]. TPP-DLW is sometimes referred as 3D two-photon printing, nanoprinting, and advanced additive manufacturing etc.[67], which indicates its ability to fabricate delicate structures in a volume of material. Usually, a high intensity femtosecond laser with ultrafast pulses is focused into a target polymerisable resin, and a photochemical process called two photon absorption occurs which triggers a free-radical polymerisation process and crosslinks the monomers in the resin. Compared with a conventional focused UV laser/LED polymerising system, where the whole illumination area is polymerised, TPP-DLW ensures that absorption only occurs in a much smaller volume due to the non-linear nature of two-photon absorption. By translating the sample with respect to the focus spot of the laser, tiny, complex, and delicate structures can be fabricated in three dimensions. In some cases, the fabrication of features below the optical diffraction limit have been reported[68,69].

2.2.2 Two-Photon Polymerisation in Liquid Crystals

The kernel process of TPP is from the physics of two-photon absorption (TPA), which is a non-linear optical process that only occurs when the material is exposed to the light source of a very

high intensity. TPA was first theoretically proposed in 1931 by Maria Göppert Mayer[70] and was experimentally confirmed in 1961 by Werner Kaiser[71], made possible 30 years later by the invention of the laser. It was a historical moment when a microstructure had a feature size of 120 nm beyond the diffraction limit of the fabrication wavelength in 2001[40], after which various TPP applications sprang up. It includes photonic crystals[72–74], microfluidic devices[61,62,75], biomedical science[76–78], micro-optics[60,79–81], dielectrics[82], metamaterials[83] and so on. The TPP process is initiated by focusing a high intensity femtosecond laser beam tightly through a high-numerical-aperture (high-NA) objective lens into a volume of photosensitive resin. The formation of the polymer networks can be represented in Equation 2.15, Equation 2.16 and Equation 2.17[84]. It corresponds to three processes: the initiation process (Equation 2.15), the propagation process (Equation 2.16) and the termination process (Equation 2.17).

$$\mathrm{PI} \xrightarrow{\mathrm{hv+hv}} \mathrm{PI}^{*} \longrightarrow \mathrm{R}\cdot + \mathrm{R}\cdot \tag{2.15}$$

$$\mathrm{R}\cdot + \mathrm{M} \longrightarrow \mathrm{RM}\cdot \xrightarrow{\mathrm{M}} \mathrm{RMM}\cdot \cdots \longrightarrow \mathrm{RM}_{n}\cdot \tag{2.16}$$

$$\mathrm{RM}_{n}\cdot + \mathrm{RM}_{m}\cdot \longrightarrow \mathrm{RM}_{n+m}\mathrm{R} \tag{2.17}$$

During the initial process, by absorbing two photons, the photoinitiators (PIs) reach an excited state (PI*) and decompose into radicals (R·). Then, during the propagation process, monomer radicals (RM_n·) are formed by combining radicals together with monomers (M). After that, in the termination process, two monomer radical chains are combined together to form a long chain and the polymerisation process is terminated. This TPA process is the fundamental process of TPP. Different from one-photon absorption (OPA) process, where a single photon can make the initiator increase from a low energy level to a high energy level, in the TPA process, photoinitiators (PIs) absorb two photons simultaneously to make the initiator transit from a low energy level to a high energy level. A comparison between OPA and TPA in polymerisable

resin and their corresponding absorption region is illustrated in **Figure 2.8** and **Figure 2.9**.

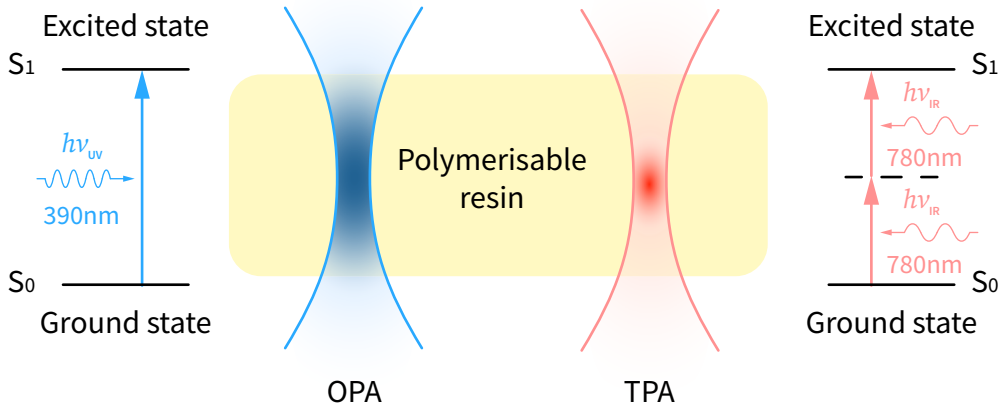

Figure 2.8: Comparison between OPA and TPA processes in a polymerisable resin. The figure illustrates the fundamental differences in absorption mechanisms, with OPA involving the absorption of a single photon at a shorter wavelength to transition from the ground state to an excited state, and TPA involving the simultaneous absorption of two photons at a longer wavelength to reach the same excited state. The diagram highlights the different sizes of polymerised region in each process.

It can be observed from Figure 2.9 that for the normalised laser intensity, the full width at half maximum (FWHM) of the laser source of TPA is narrower than that of OPA. Due to the non-linear nature of TPA, the absorption rate depends on the square of the light intensity, which confines polymerisation to the focal point where the intensity exceeds the threshold. This enables highly localised fabrication with high spatial resolution. This means that, given the same polymerisation threshold energy for a certain material, the TPA process will polymerise a narrower region in the resin compared to the OPA process.

In general, at least two components should be included in the resin for use with TPP-DLW fabrication. One is a monomer, or a mixture of monomers, which will provide the final polymer network. The other component needed is a photoinitiator, which will absorb the laser light through a multi-photon absorption process and generated active radicals which will cause the monomers to be polymerised[50]. Several monomer and photoinitator combinations have been used for this purpose. In recent years, the use of LC materials as polymerisable

resins for TPP-DLW has been investigated. In general, there are two ways of using TPP-DLW to fabricate microstructures in mixtures with LCs. One method is to fabricate micropolymer surface structures that are then filled with an LC mixture afterwards. Another method is laser writing into a polymerisable mixture containing LCs to form a crosslinked polymer network to lock the LC director inside the network. In this thesis, the polymerisable mixture prepared is 1%wt IR819 + 29%wt RM257 + 70%wt E7, where IR819 is the photoinitator necessary for TPA, RM257 is the monomer for network forming and E7 is the host liquid crystal. All of them are supplied from Merck.

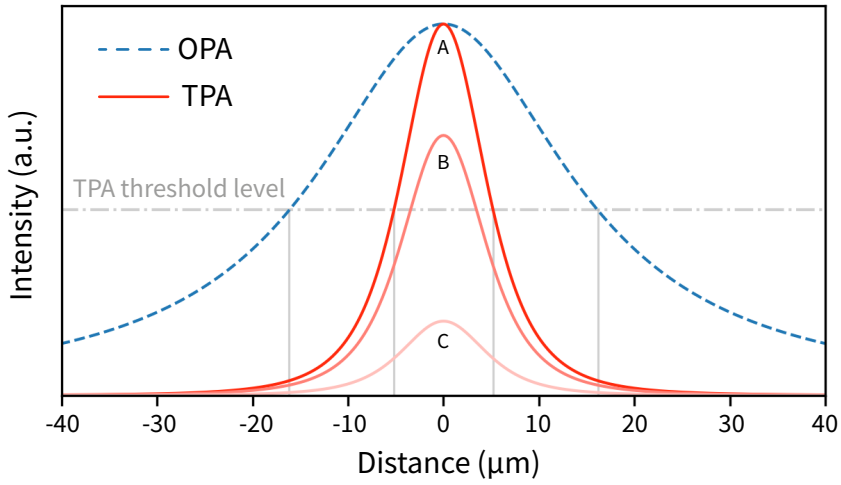

Figure 2.9: normalised laser intensity profiles for OPA and TPA in polymerisable resin. The FWHM is narrower for TPA than for OPA, indicating that TPA polymerises a much narrower region in the resin at the same polymerisation threshold energy.

2.2.3 3D Nano- and Micro-Fabrication in Liquid Crystals

A common way of aligning LCs is to make them contact with micro grooves, scratches or gratings on a polymer surface[85,86], as it is a well known method to align LCs in mass device production. The fabrication of LC alignment structures with TPP-DLW in a positive photoresist was first reported by Xie[87], which was utilised to align nematic LCs. A positive photoresist becomes soluble in the exposed regions upon UV exposure, allowing selective removal and patterning. Later on, a similar fabrication structure and results were reported by Lee in commercial

negative photoresist[88]. In contrast, a negative photoresist becomes insoluble in the exposed areas, leaving behind the patterned structure after development. Following these two successful demonstrations, several studies reported the fabrication of complex 2D polymer microstructures based on single gratings[89]. Serra et al.[90] successfully demonstrated a simple cubic microlattice polymer structure which was then treated with homeotropic (vertical) alignment agent and filled with LC. This approach extended the idea of surface polymer structures from 2D layers into 3D structures.

A number of interesting and novel phenomena have been demonstrated with LC-filled polymer surface structures. For example, Ho et al.[91] showed that by changing the temperature, the diffraction of light through a microlattice structure could be tuned. Separately, He et al.[92] created a fast, polarisation-independent LC phase modulator using TPP-DLW by fabricating polymer shelf structures in LC devices. However, a drawback of fabricating surface alignment structures is that it is impossible to control the exact direction for every point in the bulk of the LC. The LC director alignment in the bulk is determined by the elastic energy between the surface network and LC after the fabrication and it cannot be directly controlled during the fabrication. **Figure 2.10** illustrates the concept of etching out surface polymer structures with TPP-DLW.

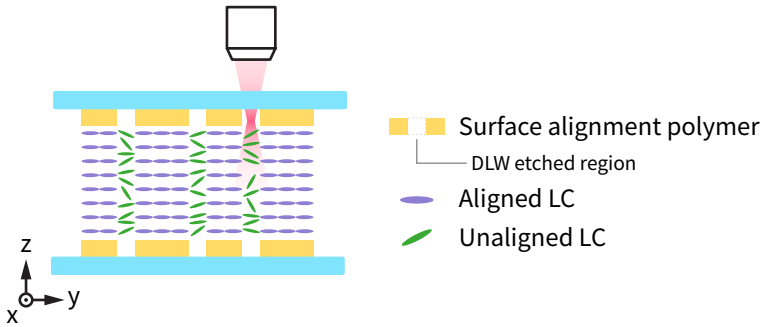

Figure 2.10: Demonstration of TPP-DLW fabrication of LC alignment structures in polymers. This technique aligns LCs through contact with structured polymer surfaces, enabling the creation of devices with varied functionality.

Compared to the results above, TPP-DLW fabrication in polymerisable LCs follows a different methodology. The polymerisable resin is prepared with monomer, photoinitiator and host LC and it is then injected into a glass cell. Then TPP-DLW is utilised to fabricate the 3D microstructures directly in the cell. Here, the polymerisable resin is liquid crystalline as well, which is also anisotropic. It means that the property of polymer structures depends on the director alignment during fabrication. Thus by forming a network with the crosslinked polymer, the orientation of the LC director inside the network will be locked in the same direction. **Figure 2.11** illustrates the concept in details. This provides significant new opportunities for fabricating novel LC devices as the orientation of the LC director in the polymer mixture can be precisely controlled using external fields during TPP-DLW fabrication. The first successful fabrication of polymer microstructure using TPP-DLW was first reported by Yoshida et al. where a chiral nematic monomer mixture was polymerised[25,93]. Subsequently, a fabrication of microcylinders using TPP-DLW and a polymerisable nematic LC mixture was reported by Ito et al[94]. And Tartan et al. demonstrated the advantages of polymerising LCs with voltage-controlled alignment of the director in selected regions inside an LC device using TPP-DLW[15,95].

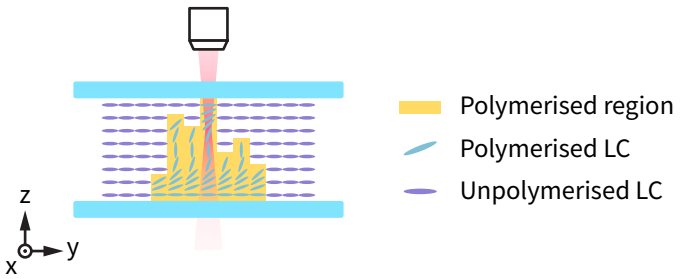

Figure 2.11: Demonstration of TPP-DLW fabrication in polymerisable LCs. The polymerisable resin, comprising monomer, photoinitiator, and host LC, is injected into an LC glass cell where 3D microstructures are fabricated using TPP-DLW. The resin locks the director orientation within the crosslinked polymer network, allowing precise control with external fields. This technique enables the creation of advanced LC devices with tailored electro-optic properties.

In summary, TPP-DLW is a powerful and versatile technique for fabricating microstruc-

tures in LC-polymer composite materials. Furthermore, by fabricating directly inside the polymerisable LC-polymer mixture, it shows great potential for controlling the alignment precisely with external electric fields applied during fabrication, which allows highly-localised polymer stabilisation of voltage-dependent director profiles. This is a largely unexplored area for advanced microfabrication of functional structures in LCs. This thesis demonstrates new optical devices fabricated using TPP-DLW in the form of Dammann gratings and computer generated holograms.

2.3 Liquid Crystal Devices for Adaptive Optics

2.3.1 Introduction

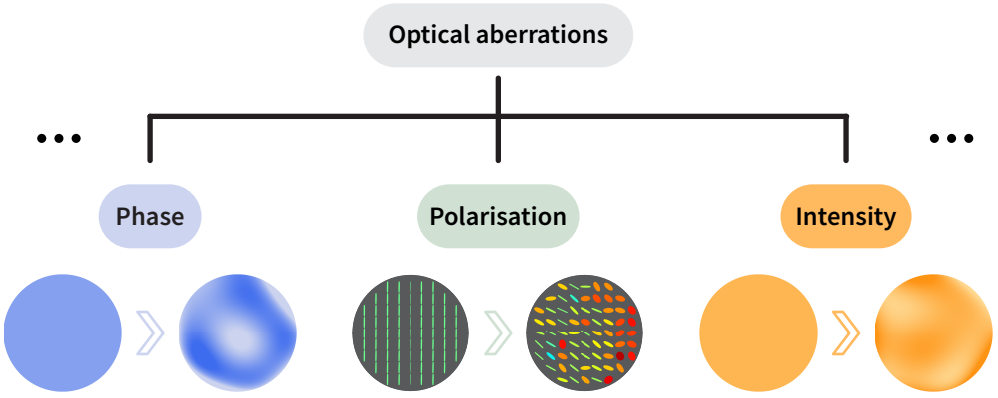

Figure 2.12: Illustrations of common optical aberrations, including phase aberration, polarisation aberration, and intensity aberration. The effects of these aberrations and how they distort the optical wavefront are demonstrated.

Adaptive optics (AO) is a sophisticated technology engineered to optimise the performance of optical systems by actively correcting aberrations[20,96–101]. These aberrations, manifesting as distortions of the light, degrade image quality and affect the system performance[102]. Primary causes of optical aberrations include atmospheric turbulence[103], optical component imperfections such as irregular lens shapes or compositions[104], and misalignment of optical paths[105]. Common aberrations include phase aberrations, where variations in the wavefront phase cause blurring and

distortion[106]; polarisation aberrations, which alter the states of polarisation of light, affecting image contrast and resolution[107]; and intensity aberrations, leading to uneven light distribution and brightness inconsistencies[108]. The effects of these aberrations on the optical wavefronts are demonstrated in **Figure 2.12**.

The concept of AO was first proposed by Horace W. Babcock in 1953[109]. Babcock envisioned a system in a telescope to dynamically compensate for wavefront distortions caused by atmospheric turbulence, which is particularly problematic for ground-based astronomical observations. His foundational work led to the development of AO systems incorporating deformable mirrors (DM), capable of real-time wavefront adjustments to correct incoming aberrations in telescopes by the fine movement of each mirror segment in the DM. This dynamic adjustment significantly enhanced image resolution and clarity[100]. Since the conceptual inception of the correction system, AO has been extensively refined and now has broader applications, including mitigating the phase aberrations in astronomical telescopes[104], optical communications[110,111], super-resolution microscopy/nanoscopy[112] and high-precision laser fabrication[113]. The typical schematics of AO systems for these applications have been demonstrated in **Figure 2.13**.

In astronomical telescopes, AO compensates for atmospheric turbulence that blurs celestial images[19,114]. Light from stars and other celestial objects scatters and distorts as it passes through the atmosphere, reducing image resolution[115]. AO systems address this by dynamically adjusting optical elements, such as DMs, in real time to detected aberrations, restoring the wavefront and enabling telescopes to reach near-diffraction-limited resolution[96,116]. This advancement has led to breakthroughs in exoplanet studies, star formation, and black hole dynamics[102,117,118].

In optical communications, AO stabilises signals affected by atmospheric turbulence or optical fibre imperfections, ensuring signal coherence and reducing data transmission errors[119–121]. Real-time phase correction improves throughput and reliability, enhancing performance in free-

space and terrestrial communication networks, including satellite-based systems[122–124].

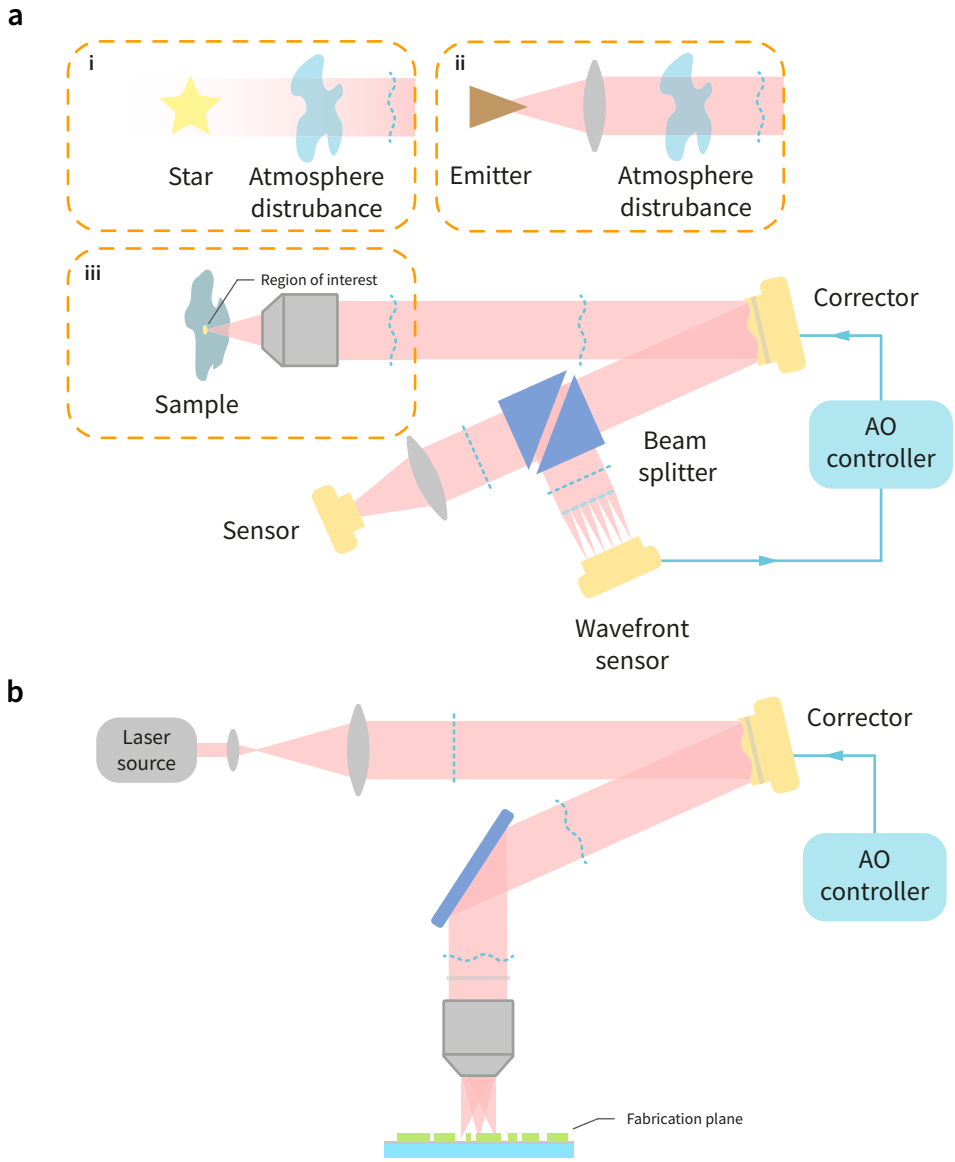

Figure 2.13: AO applications in astronomy, optical communication, laser fabrication, and microscopy. AO dynamically corrects wavefront distortions in (a) astronomy, optical communication, and laser fabrication, and (b) microscopy, enhancing resolution, signal integrity, and imaging accuracy.

In microscopy, AO corrects aberrations caused by the heterogeneous refractive index of biological tissues, enhancing image resolution and contrast[97,101]. This is particularly valuable for deep-tissue imaging in neuroscience, where AO improves the visualisation of neuronal structures and activity in vivo[125,126].

AO also plays a critical role in high-precision laser fabrication by optimising laser beam

focus and intensity. This ensures high spatial resolution in micro/nanofabrication processes, essential for manufacturing MEMS, semiconductor wafers, and medical devices[127–130]. In direct laser writing (DLW), AO enables fine structural control, improving feature accuracy and resolution[131].

Beyond traditional phase AO, advancements including vectorial AO (V-AO), intensity AO (I-AO), and polarisation AO (P-AO) broaden its potential application. For example, in V-AO, it corrects both phase and polarisation aberrations, crucial for deep-tissue microscopy and astronomical imaging, using advanced wavefront sensors and DMs to ensure precise control of the vectorial state of light[132,133]. P-AO, on the other hand, targets purely polarisation aberrations, vital for applications involving structured light, optical computing, and polarisation-sensitive biomedical imaging, using specialised sensors and adaptive elements to maintain the desired polarisation state[13,134]. As for I-AO, Chapter 5 in this thesis elaborates on this system and corresponding correction methods in detail.

2.3.2 Sensor-Based and Sensorless Adaptive Optics

AO operates on the principle of wavefront correction, addressing deviations from the ideal phase of the light that cause image blurring and distortion[6,135–137]. Aberrations such as spherical, astigmatism, coma, trefoil, and higher-order types uniquely impact optical system performance[138]. AO implementation involves applying an equal and opposite phase aberration to an adaptive device based on the measured aberrations[117]. The method can be classified into two categories: sensor-based (direct) methods, where the wavefront is directly measured to retrieve the aberration and sensorless (indirect) methods, where the aberration is estimated from indirect measurement[12,139–142].

In sensor-based AO systems, wavefront sensors are employed to directly measure the wave-

front distortions caused by aberrations[99,115,135]. The most commonly used wavefront sensor is the Shack-Hartmann sensor, which consists of an array of lenses that focus light onto a detector array, creating a pattern of spots[102]. **Figure 2.14**(a) demonstrates the basic concept of Shack-Hartmann sensor. The displacement of these spots from their ideal positions is used to calculate the wavefront distortions[143,144], which is shown in Figure 2.14(b). Other types of wavefront sensors include the pyramid sensor and the curvature sensor[145,146].

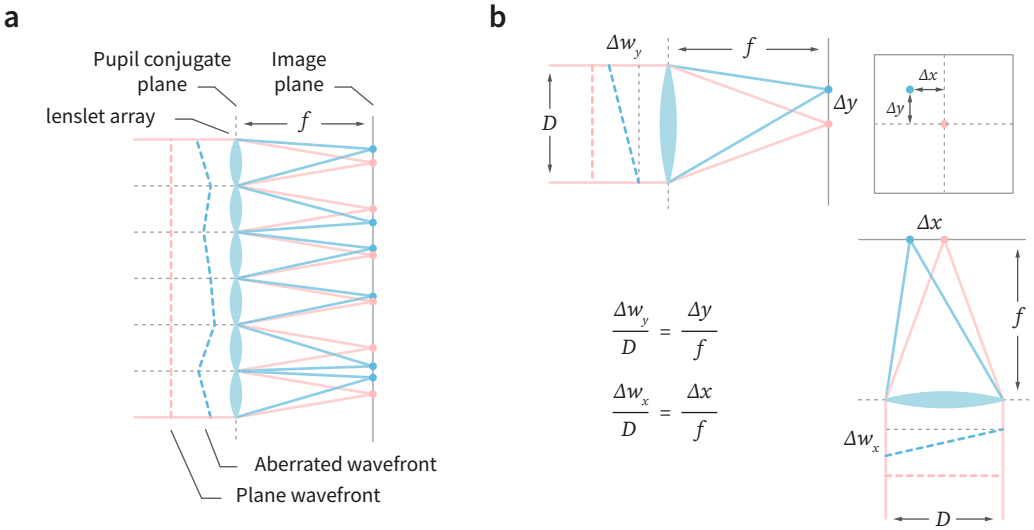

Figure 2.14: Schematic representation of the Shack-Hartmann wavefront sensor. (a) The basic concept of the Shack-Hartmann sensor, illustrating how an array of lenses focuses light onto a detector array, creating a pattern of spots. (b) For a single lenslet, the displacement of these spots from their ideal positions is used to calculate wavefront distortions, demonstrating the ability of the sensor to detect and measure aberrations in the optical wavefront.

Once the wavefront distortions are measured, this information is used to control a DM or other adaptive optical element that adjusts its shape to correct the aberrations[147,148]. An illustration of a sensor-based method is presented in **Figure 2.15**. Recent advancements in adaptive elements, sensor technology, computational algorithms, and materials science have significantly improved sensor-based AO[149]. Modern DMs, with increased actuator density and response times, allow for a finer aberration correction even in rapidly changing environments, accommodating thousands of actuators for higher spatial resolution[150].

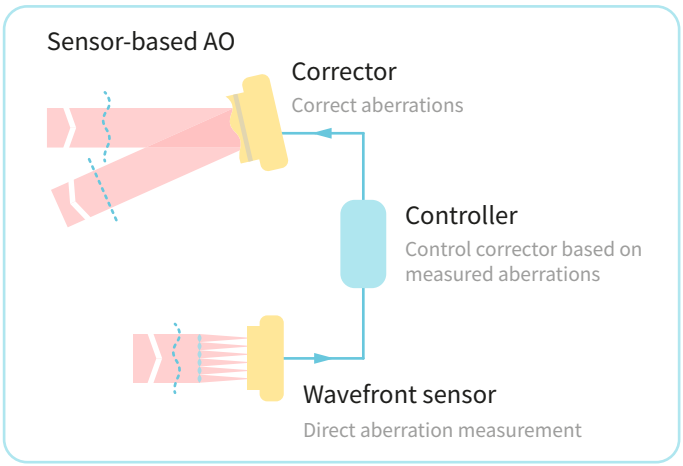

Figure 2.15: Illustration of sensor-based AO concept. The sensor-based method includes a wavefront sensor that directly measures aberrations. These measurements are sent to a controller, which processes the data and instructs the corrector to adjust and correct for the aberrations, ensuring improved image quality or beam focus. The flow of correction is cyclic, maintaining optimal system performance by real-time continuous adjustments.

Sensor-based AO systems are widely used in astronomical telescopes to correct for atmospheric turbulence. By continuously measuring the distortions in the incoming light from celestial objects and adjusting the DMs in real-time, these systems enable ground-based telescopes to achieve near-diffraction-limited imaging, significantly enhancing the resolution and clarity of astronomical observations[102]. In ophthalmology, sensor-based AO systems improve retinal imaging by compensating for optical aberrations in the eye. This enhancement allows for high-resolution imaging of the retina, aiding in the diagnosis and monitoring of eye diseases[151].

Sensorless AO, on the other hand, does not rely on direct wavefront measurements[139]. Instead, it uses image quality metrics and computational algorithms to infer and correct aberrations[152]. The correction process in sensorless AO involves iteratively optimising an image quality criterion, such as sharpness or contrast[153]. This approach is advantageous in scenarios where integrating a wavefront sensor is impractical due to space, cost, or other constraints[141].

In sensorless AO, aberrations are often represented as a series of modes, typically using

mathematical functions such as Zernike polynomials[154]. These modes describe different types of aberrations, including defocus, astigmatism, and coma[155,156]. The AO system applies a series of predefined aberration modes to the adaptive elements and evaluates the resulting changes in the image quality metric[12,157]. Optimisation algorithms, such as genetic algorithms or gradient descent, are used to determine the optimal combination of modes that maximise the image quality metric[117]. An illustration of the configuration for the sensorless method is presented in **Figure 2.16**.

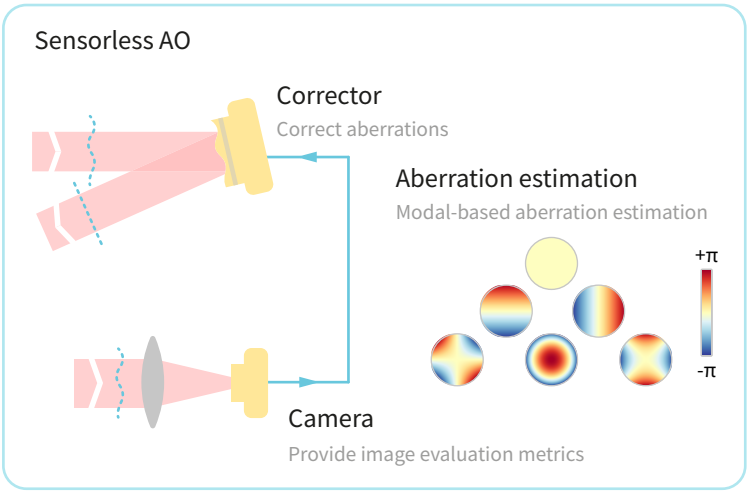

Figure 2.16: Illustration of sensorless AO concept. For the sensorless method, aberrations are corrected without direct measurement. Instead, a camera provides image for quality metrics evaluation, which are used for modal-based aberration estimation. The commonly used modals are Zernike polynomials. These estimations inform the corrector to adjust the adaptive elements and correct aberrations, thereby enhancing image quality. The process involves a feedback loop where the corrected images are continuously evaluated to maintain optimal performance.

Sensorless AO has found applications in biological microscopy, where it is used to correct aberrations induced by heterogeneous tissue structures. This capability enables high-resolution imaging deep within biological samples, facilitating detailed studies of cellular and subcellular structures[112]. Recent advancements in sensorless AO systems include the integration of machine learning (ML) techniques. These systems continuously learn from previous observations, dynamically improving their performance in real-time[158–160].

2.3.3 Liquid Crystals for Adaptive Optics

One critical requirement for adaptive elements in AO systems is the ability to provide real-time modulation across the pupil with high resolution for each individual region[97,101,102,126,161]. This capability is essential for correcting aberrations and ensuring high-quality imaging or signal transmission[21]. When an electric field is applied to a nematic LC, the director orientation will be changed, altering the refractive index and birefringence through the LCs[14,162,163]. This characteristic allows for precise control over the phase of light passing through the LC layer, making it ideal for AO systems to compensate the aberrations by modulating the light[28]. Consequently, spatial light modulators (SLMs) have been designed as key components in modern AO systems due to their versatility and precision in phase modulation.

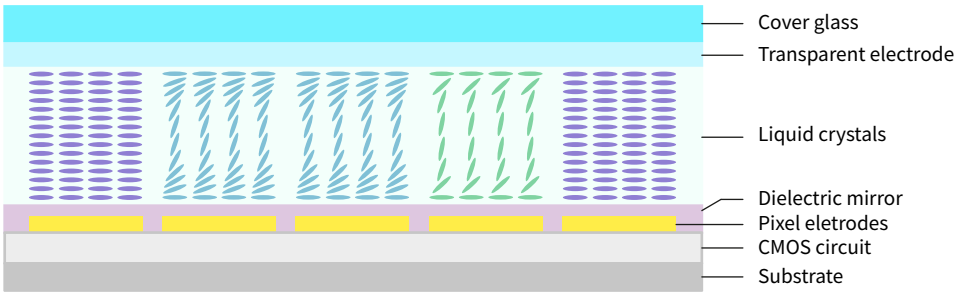

Figure 2.17: Illustration of LCoS structure. The schematic shows the layered configuration of a typical LCoS device used for adaptive optics.

SLMs are capable of modulating the amplitude, phase, or polarisation of light on a pixel-by-pixel basis, crucial for aberration corrections in AO systems. Most SLMs use LC on Silicon (LCoS) technology to fabricate the internal core adaptive element[164–166]. LCoS comprise a nematic LC layer between a transparent ITO (Indium-Tin-Oxide) electrode and a reflective silicon backplane. The structure includes, from top to bottom, a high-transparency cover glass, a transparent electrode layer, a LC layer, and a silicon backplane with a dielectric mirror, pixel electrodes, and a CMOS (Complementary Metal-Oxide-Semiconductor) circuit. Alignment

layers are coated on the inner surfaces of the transparent electrode and dielectric mirror. A schematic of a typical LCoS device is presented in **Figure 2.17**.

SLMs modulate the phase of reflected light by applying a voltage across the LC layer, changing the orientation of the director. The refractive index at each pixel will be altered to affect the light with different phase delay. This high-resolution capability is crucial for applications such as correcting atmospheric turbulence in telescopes and compensating for refractive index variations in biological tissues in microscopy. The typical retardation modulation range of a single pixel against the greyscale level on the SLM is demonstrated in **Figure 2.18**(a). Normally, nematic phase SLMs operate at switching rates of the order of tens of Hertz and are slower for longer optical wavelengths due to increased device thickness. However, overdrive techniques can increase modulation rates to approximately 1 kHz with the so-called greyscale modulation[17]. Faster modulation speed higher than 1 kHz can be achieved with ferroelectric LC SLMs, but are typically limited to binary modulation[18]. The concept of using LCoS to modulate the phase of light for aberration correction is illustrated in **Figure 2.18**(b).

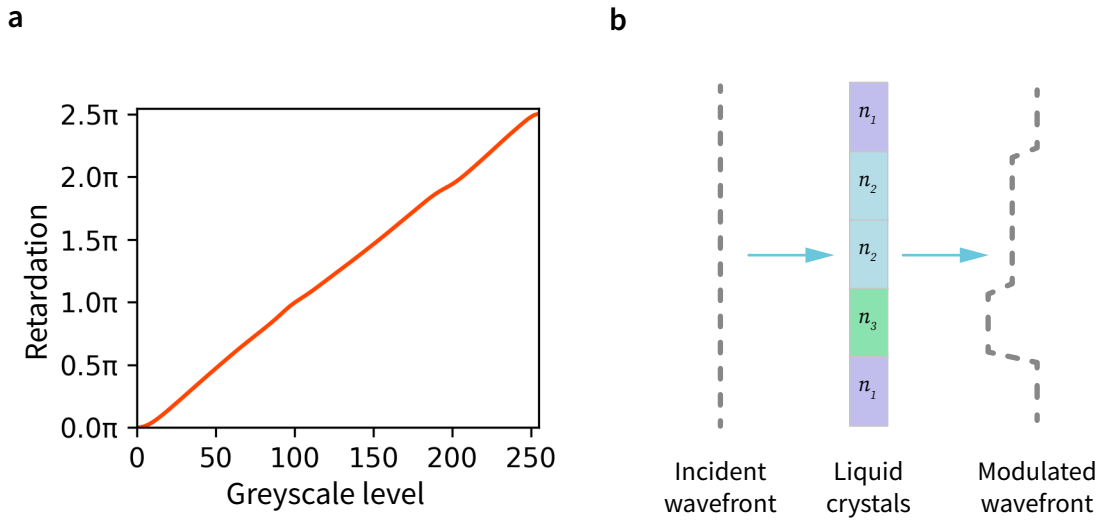

Figure 2.18: Concept illustration of using LCoS to modulate the light. (a) The relationship between greyscale levels and phase retardation shows the modulation range of a single pixel. (b) Light phase modulation is achieved by varying the voltage across the LC layer, altering the refractive indices n_1, n_2, n_3 at each pixel.

In this thesis, the primary SLM model used is the Hamamatsu LCOS-SLM (X15213-01) operated in reflective mode for real-time adaptive optics control. This device features a high-density array of 1024 × 768 pixels, each with a 20 μm × 20 μm pitch, resulting in a fill factor exceeding 95%. The effective area size is 20.5 mm × 15.4 mm. It runs at a 60 Hz refresh rate and accepts 8-bit (0-255) grey-level input, thereby providing continuously adjustable phase modulation. Typically, a linear polariser is placed before the SLM so that the incident beam has a well-defined polarisation aligned with the LC directors, ensuring pure phase-only wavefront shaping. However, amplitude modulation or complex vectorial control can be achieved by incorporating additional polarisers and waveplates at the input or output, as demonstrated in Chapter 5 for amplitude modulation and in Chapter 6 for polarisation generation.

In summary, SLMs, particularly those based on LCoS technology with nematic LCs, are indispensable in modern AO systems. Their precision and resolution in light modulation make them ideal for applications in astronomy, biological microscopy, optical communication, and high-precision laser fabrication. This thesis demonstrates a new I-AO system that improves intensity distribution uniformity under aberrations and controls total energy level at the pupil plane, along with companion sensor-based and sensorless methods, which expanding the existing AO toolboxes.

2.4 Summary

This chapter provides an overview of LCs and their applications in advanced optical technologies. It begins with an introduction to LC phases, highlighting their unique state of matter that combines properties of both liquids and solids. LCs exhibit distinct physicochemical characteristics, including anisotropic behaviour, which is fundamental to their functionality in various optical applications. The chapter delves into the physical properties, emphasising their molec-

ular alignment and phase transitions, and their electric and optical properties, focusing on the dielectric anisotropy and birefringence.

The discussion progresses to the theory and applications of TPP direct laser writing in LCs. The theory of two photon absorption is explained, describing how simultaneous absorption of two photons can induce polymerisation in photoreactive materials. This process is then contextualized within LC mixtures, elucidating how it enables precise 3D nano- and micro-fabrication. These advanced fabrication techniques facilitate the creation of intricate polymer structures within LCs, which are crucial for developing new photonic devices with a high degree of functionality.

AO, a pivotal technology in modern optics, is also explored with a focus on LC devices. The chapter introduces the general principles of AO, which involve real-time correction of optical aberrations to enhance image quality. It contrasts sensor-based and sensorless AO, explaining the methodologies and advantages of each approach. The application of LCs in AO is detailed, demonstrating how their real-time tunable refractive indices allow for dynamic wavefront correction, thereby improving the performance of optical systems in various fields ranging from astronomy to microscopy.

In summary, this chapter establishes a comprehensive background on LCs and their multi-faceted roles in cutting-edge optical technologies. It lays the foundation for understanding how these unique materials are harnessed in TPP and AO, setting the stage for further exploration and innovation in the field of photonics.

When you have eliminated the impossible, whatever remains, however improbable, must be the truth.

— Sherlock Holmes

CHAPTER 3

Polychromatic Multi-Element Liquid Crystal Dammann Gratings

3.1 Design and Generation of Dammann Gratings

3.1.1 Introduction

A Dammann grating is a beamlet array generator which efficiently converts a monochromatic incident beam into a finite array of spots with a uniform intensity distribution[8,167–172]. The original design of the grating was put forward by Dammann in 1977, when a binary-phase $(0, \pi)$ grating structure was proposed that could generate an array of multiple beams in the Fourier plane (the focal plane)[167,168]. Compared with conventional gratings, which consist of narrow grooves separated by a fixed period, Dammann gratings consist of features of specific lengths that can generate beamlets of different configurations in the far field.

Dammann's method of generating beams with uniformly distributed intensity is attractive for three reasons. First, it is based on modifying the phase information of the incident light without changing the intensity distribution, which allows for a high throughput of light. Second, these gratings are binary, which means that they can be fabricated with techniques such as photolithography, ion etching or laser writing. Third, since a Dammann grating can split the incident beam into a uniform array, it can be combined with other more advanced patterns to

modify multiple beams simultaneously into desired beam shapes and profiles.

Since the first demonstration, and with the rapid development of contemporary microfabrication technologies[5,173–175], Dammann gratings have been successfully fabricated in a range of different materials and for various technological applications[8,10,176–178]. The initial pattern design method proposed by Dammann was for a symmetric grating that was targeted for the generation of an odd number of spots along one direction. The nonsymmetric pattern design was first proposed by Mait[171] in 1988 to generate a pattern consisting of an even number of spots. Later, Morrison reduced further the computational complexity of the process that is required to generate the pattern parameters by utilising a symmetric phase shift profile, which led to the generation of an even number of spots in the far field[179]. Alternatively, a grating with a non-orthogonal 2D pattern was proposed by Vasara[180] in order to develop arrays with more irregular configurations[177]. A group of numerical solutions for Dammann gratings from 2 to 64 was computed and presented by Zhou[181] and was later employed for a number of different Dammann grating designs including circular Dammann gratings[182], 3D Dammann gratings[183], and a beam shaping device[10]. In terms of technological applications, Dammann gratings have been widely applied to the fields of optical communications[184], optical computing[9,185], and laser beam shaping[10,170,186].

A common method for fabricating Dammann gratings is to use UV lithography with high-resolution binary phase masks to form the required pattern on a fused silica substrate. This method, in general, can produce high quality Dammann gratings with fabrication errors less than 2%[177,187]. There have also been a number of attempts to fabricate Dammann gratings in various liquid crystal (LC) materials and devices[11,188–191]. To create different phase profiles within LC materials, the spatial orientation of the director should be precisely controlled. Towards this end, photoalignment materials have been used to functionalise the surface of a

substrate so as to align the LC director along a desired direction[181,182], and this has been a popular approach for the fabrication of Dammann gratings in LC devices[188,190–193]. In this case, the sulphonic azo-benzene dye, which is a photoalignment material, is the surface alignment material of choice that has been employed in the literature[188,190–193].

There are, however, significant limitations when using photoalignment layers of this type, such as the perishable nature of the alignment layer after a relatively short period of time. Moreover, because the orientation of the LC director is determined by the static alignment pattern on the surface, it is difficult to generate complex 3D structures using this method. Meanwhile, to fabricate Dammann gratings with photoalignment layers, predesigned photomasks are often required, which restricts the flexibility of the pattern design. Even though electrical tunability of an LC Dammann grating has been reported by Wang et al.[190], the Dammann grating pattern presented was still based on surface photoalignment layers that were patterned with photomasks. In this case, the application of an external electric field resulted in overcoming the surface alignment effects so as to reorient the LC director and switch the Dammann pattern on and off. Here the whole structure was limited to a surface-induced alignment rather than a bulk 3D configuration. Additionally, these Dammann gratings are often designed for operation at a single specific wavelength rather than a range of wavelengths.

In this chapter, bi-element switchable Dammann gratings are reported that can operate at multiple wavelengths by tuning the applied voltage. These switchable gratings have been fabricated in polymerisable LC resins using two-photon polymerisation direct laser writing (TPP-DLW), which negates the need for perishable photoalignment layers or static configurations; it also enables more than one grating to be encoded into the LC layer at any one time. As discussed in Section 2.2, TPP-DLW allows for the fabrication of sophisticated 3D microstructures in the polymerisable LC resin by locking-in the orientation of the LC director inside the

network at the moment of exposure to the laser writer[15,95,194,195]. Results are presented of the fabrication and characterisation of both a single element switchable 2D Dammann grating and multi-element interchangeable 2D Dammann gratings written into a region of LC covering a size of 1024 μm by 1024 μm. Simulations are conducted before fabrication to determine the optimum fabrication parameters that result in voxels with dimensions of ~1 μm radius and ~8 μm in length. The fabricated gratings produce a uniform intensity distribution across the far-field array, with fast response times and high diffraction efficiency. They demonstrate stable operation across a range of wavelengths by adjusting the applied voltage, highlighting their potential for dynamic beam shaping and optical communication.

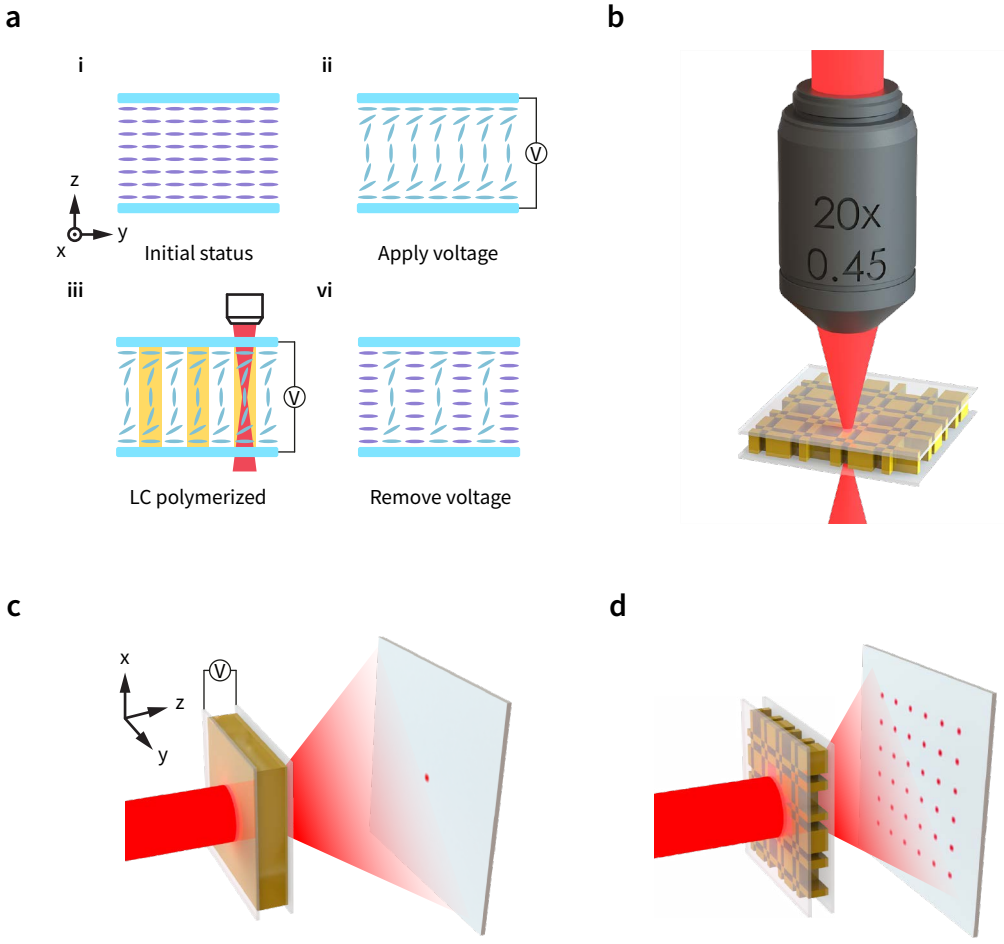

Figure 3.1: Concept of an electrically-switchable LC Dammann grating fabricated using TPP-DLW. (a) Laser writing into an LC device under an electric field. (b) Laser-written Dammann grating with polymerised regions. (c) Replay field under fabrication voltage. (d) Replay field with no voltage.

Figure 3.1 illustrates the novel concept of fabricating a single layer Dammann grating in a LC device with TPP-DLW along with the corresponding diffraction patterns observed in the replay (far) field when the grating is activated or deactivated. This is the first demonstration of using DLW to fabricate a switchable Dammann grating in LC device, which enables dynamic pattern switching through the application of an external electric field. Figure 3.1(a) demonstrates the process of laser writing into an LC device. The alignment of the LC director is first controlled by an external electric field, and then locked by a polymer network using direct laser writing. The writing process of locked and tunable regions of a Dammann grating using two-photon laser writing is illustrated in Figure 3.1(b). After the fabrication of a Dammann grating, an external electric field is applied again to activate and deactivate the pattern in the replay (far) field and the expected results are shown in Figure 3.1(c) and Figure 3.1(d), respectively.

3.1.2 Design of LC Dammann Gratings

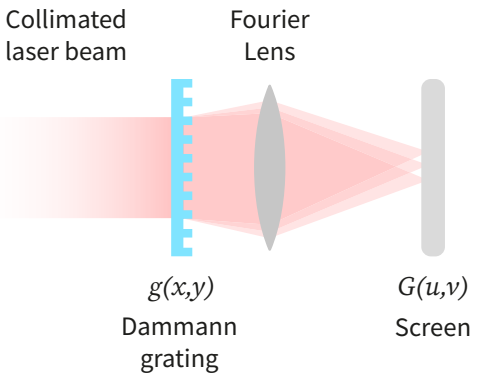

Figure 3.2: Concept illustration of a Dammann grating. It is assumed that the grating is illuminated by a collimated laser beam with a planar wavefront and the output pattern is captured in the far field. The designed Dammann grating is represented as its transparency function $g(x, y)$ and its diffraction pattern after a Fourier lens is represented by the Fourier transform of transparency function as $G(u, v)$.

The design of the LC Dammann gratings used is based on scalar diffraction theory[167,168,170]. It is assumed that the grating is illuminated by a collimated laser beam with a planar wavefront and the output pattern is captured in the far field. The designed 2D Dammann grating can be represented as a transparency function $g(x, y)$ and the diffraction pattern is represented

mathematically by the Fourier transform of the 2D Dammann grating as $G(u, v)$. The concept of a Dammann grating is demonstrated in **Figure 3.2**.

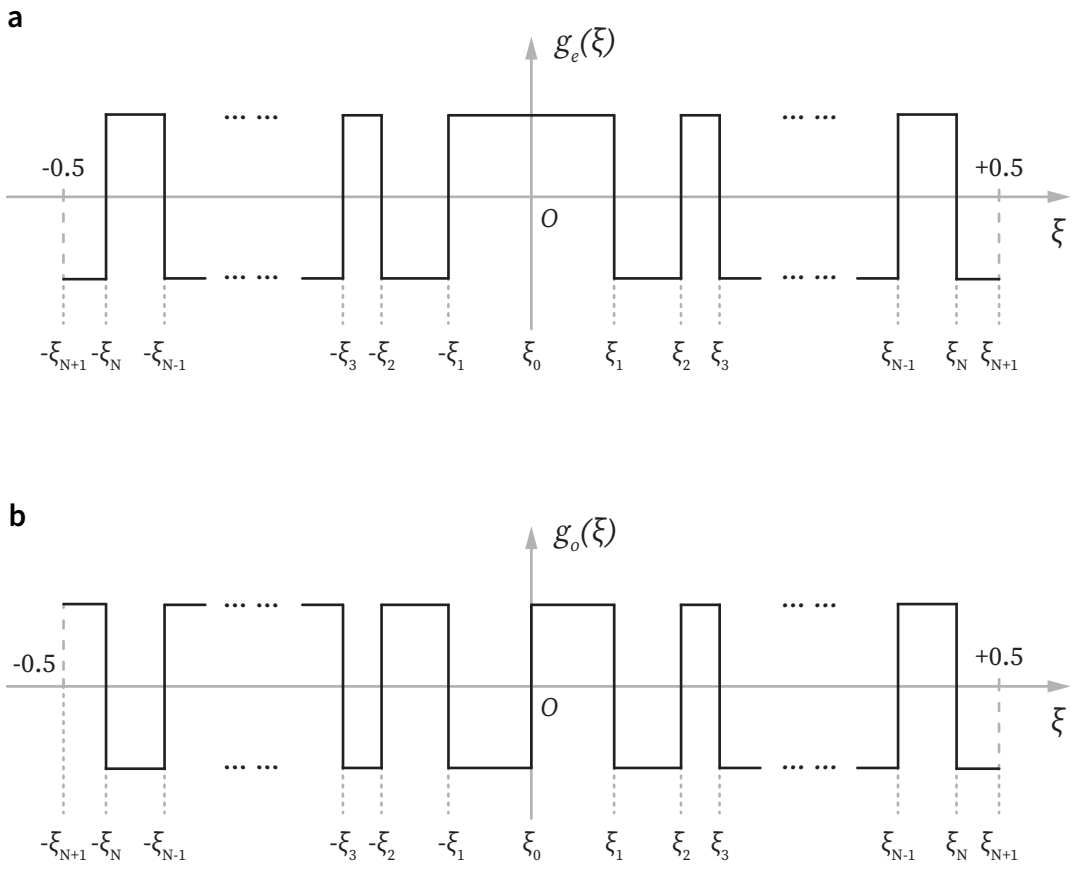

Figure 3.3: Illustration of typical Dammann gratings. The typical 1D structure of a Dammann grating over one period $-0.5 \leqslant \xi \leqslant 0.5$ with **(a)** symmetric structure and **(b)** nonsymmetric structure. The designed transition points are shown as ξ_1, ξ_2, ξ_3, ..., ξ_N within one period.

The transparency function $g(x, y)$ can be represented by the product of two individual 1D grating functions in the x and y directions: $g(x, y) = g_1(x)g_2(y)$. For this situation, the Fourier transform of $g(x, y)$ is separable into two directions: $G(u, v) = G_1(u)G_2(v)$, where $G_1(u)$ and $G_2(v)$ are the 1D Fourier transform of $g_1(x)$ and $g_2(y)$, respectively. The grating structures in the x direction ($g_1(x)$) and y direction ($g_2(y)$) do not necessarily need to be the same, as the number of spots in the diffraction pattern in either direction can be different. However, for simplicity, let's assume $g_1(x) = g_2(y) = g(\xi)$ and $G_1(u) = G_2(v) = G(u)$.

Then the main computational problem becomes finding the transparency function $g(\xi)$ with phase-only form: $g(\xi) = e^{-i\phi(\xi)}$ and its Fourier transform will then generate $G(u)$.

In order to reduce the computational complexity and increase grating usability, the phase difference $\phi(\xi)$ introduced by the grating was restricted to be 0 and π only. So, for the grating, the value of $g(\xi)$ was restricted to be $g(\xi) = 1$ and $g(\xi) = -1$ only. Furthermore, in order to generate a diffraction pattern, the grating should be a periodic pattern, thus $g(\xi) = g(\xi + \Delta\xi)$. For our analysis, it is convenient to set $\Delta\xi = 1$ as a way of normalising the results. **Figure 3.3** illustrates the typical 1D structure of a Dammann grating over one period $-0.5 \leqslant \xi \leqslant 0.5$ with symmetric structure and nonsymmetric structure.

Since the grating can be either even or odd, the transition points in the negative half-period are mirrored from those in the positive half-period. Therefore, the only free parameters for either structure are the positive transition points ξ_1, ξ_2, ξ_3, …, ξ_N within the interval $0 < \xi \leqslant 0.5$.

The next goal is to compute the transition points ξ_1, ξ_2, ξ_3, …, ξ_N so that the zeroth (only for the odd grating) and $\pm 1^{\text{st}}$, …, $\pm N^{\text{th}}$ diffraction orders have equal intensities. The number of transition points N relates to the number of spots in the array. For an even symmetric grating, it will generate $2N + 1$ spots in the 1D diffraction pattern. For an odd nonsymmetric grating, it will generate $2N$ spots in the 1D diffraction pattern. In the following discussion, we use the boundary conditions $\xi_0 = 0$ and $\xi_{N+1} = 0.5$.

For the even symmetric grating[168], the transparency function $g_e(\xi)$ is written as

$$g_e(\xi) = \begin{cases} \displaystyle\sum_{n=0}^{N} (-1)^n \text{rect}\left[\frac{\xi - (\xi_{n+1} + \xi_n)/2}{\xi_{n+1} - \xi_n}\right] & 0 < \xi \leqslant 0.5 \\ \displaystyle\sum_{n=0}^{N} (-1)^n \text{rect}\left[\frac{\xi + (\xi_{n+1} + \xi_n)/2}{\xi_n - \xi_{n+1}}\right] & -0.5 \leqslant \xi < 0 \end{cases} \tag{3.1}$$

where rect[·] is the rectangular function. The Fourier transform $G(u)$ of Equation 3.1 can then be derived for both halves of the function. For the positive half $0 < \xi \leqslant 0.5$ of the transparency function $g_e(\xi)$, its corresponding $G(u)$ can be represented as

$$\begin{aligned} G(u)|_{0<\xi\leqslant 0.5} &= \mathcal{F}\{g_e(\xi)|_{0<\xi\leqslant 0.5}\} \\ &= \sum_{n=0}^{N} (-1)^n \mathcal{F}\Big\{\text{rect}\left[\frac{\xi - (\xi_{n+1}+\xi_n)/2}{\xi_{n+1}-\xi_n}\right]\Big\} \\ &= \sum_{n=0}^{N} (-1)^n \mathcal{F}\Big\{\text{rect}\left[\frac{1}{\xi_{n+1}-\xi_n}\cdot\left(\xi - \frac{\xi_{n+1}+\xi_n}{2}\right)\right]\Big\} \\ &= \sum_{n=0}^{N} (-1)^n (\xi_{n+1}-\xi_n)\cdot \text{sinc}((\xi_{n+1}-\xi_n)u)\cdot e^{-\pi u i(\xi_{n+1}+\xi_n)}. \end{aligned} \tag{3.2}$$

If $u = 0$, which represents the zeroth order of the diffraction, the transform is calculated as

$$G(u)|_{0<\xi\leqslant 0.5} = \sum_{n=0}^{N} (-1)^n (\xi_{n+1}-\xi_n). \tag{3.3}$$

If $u \neq 0$, which represents higher orders of diffraction, their transforms can be calculated as

$$\begin{aligned} G(u)|_{0<\xi\leqslant 0.5} &= \frac{1}{u\pi}\sum_{n=0}^{N} (-1)^n \sin(\pi u(\xi_{n+1}-\xi_n))\cdot e^{-\pi u i(\xi_{n+1}+\xi_n)} \\ &= \frac{1}{u\pi}\sum_{n=0}^{N} (-1)^n \frac{e^{\pi u i(\xi_{n+1}-\xi_n)} - e^{-\pi u i(\xi_{n+1}-\xi_n)}}{2i}\cdot e^{-\pi u i(\xi_{n+1}+\xi_n)} \\ &= \frac{1}{u\pi}\sum_{n=0}^{N} (-1)^n \frac{e^{-2\pi u i\xi_n} - e^{-2\pi u i\xi_{n+1}}}{2i}. \end{aligned} \tag{3.4}$$

For the negative half $-0.5 \leqslant \xi < 0$ of the transparency function $g_e(\xi)$, its corresponding $G(u)$ can be represented as

$$\begin{aligned} G(u)|_{-0.5\leqslant\xi<0} &= \mathcal{F}\{g_e(\xi)|_{-0.5\leqslant\xi<0}\} \\ &= \sum_{n=0}^{N} (-1)^n \mathcal{F}\Big\{\text{rect}\left[\frac{1}{\xi_n-\xi_{n+1}}\cdot\left(\xi + \frac{\xi_{n+1}+\xi_n}{2}\right)\right]\Big\} \\ &= \sum_{n=0}^{N} (-1)^n (\xi_{n+1}-\xi_n)\cdot \text{sinc}((\xi_n-\xi_{n+1})u)\cdot e^{\pi u i(\xi_{n+1}+\xi_n)}. \end{aligned} \tag{3.5}$$

If $u = 0$, which represents the zeroth order of the diffraction pattern, the transform is calculated as

$$G(u)|_{-0.5\leqslant\xi<0} = \sum_{n=0}^{N}(-1)^n(\xi_{n+1} - \xi_n). \tag{3.6}$$

If $u \neq 0$, which represents higher orders of diffraction, their transforms can be calculated as

$$\begin{aligned} G(u)|_{-0.5\leqslant\xi<0} &= -\frac{1}{u\pi}\sum_{n=0}^{N}(-1)^n \sin(\pi u(\xi_n - \xi_{n+1}))\cdot e^{\pi ui(\xi_{n+1}+\xi_n)} \\ &= \frac{1}{u\pi}\sum_{n=0}^{N}(-1)^n \frac{e^{-\pi ui(\xi_n-\xi_{n+1})} - e^{\pi ui(\xi_n-\xi_{n+1})}}{2i}\cdot e^{\pi ui(\xi_{n+1}+\xi_n)} \\ &= \frac{1}{u\pi}\sum_{n=0}^{N}(-1)^n \frac{e^{2\pi ui\xi_{n+1}} - e^{2\pi ui\xi_n}}{2i}. \end{aligned} \tag{3.7}$$

Thus, the odd-numbered diffraction orders of $g_e(\xi)$ in the Fourier plane $G(u)$ are then expressed as

$$G_e(u) = \mathcal{F}\{g_e(\xi)\} = \begin{cases} \dfrac{1}{u\pi}\displaystyle\sum_{n=0}^{N}(-1)^n(\sin 2\pi u\xi_{n+1} - \sin 2\pi u\xi_n) & u \neq 0 \\ 2\displaystyle\sum_{n=0}^{N}(-1)^n(\xi_{n+1} - \xi_n) & u = 0. \end{cases} \tag{3.8}$$

Alternatively, for the odd nonsymmetric grating[171], the transparency function $g_o(\xi)$ takes the form

$$g_o(\xi) = \begin{cases} \displaystyle\sum_{n=0}^{N}(-1)^n \text{rect}\left[\frac{\xi - (\xi_{n+1}+\xi_n)/2}{\xi_{n+1} - \xi_n}\right] & 0 < \xi \leqslant 0.5 \\ -\displaystyle\sum_{n=0}^{N}(-1)^n \text{rect}\left[\frac{\xi + (\xi_{n+1}+\xi_n)/2}{\xi_n - \xi_{n+1}}\right] & -0.5 \leqslant \xi < 0. \end{cases} \tag{3.9}$$

In the same way, by applying the Fourier transform to Equation 3.9, it is straightforward to derive similar results for the even-numbered diffraction orders in the Fourier plane, which take the form

$$G_o(u) = \mathcal{F}\{g_o(\xi)\} = \begin{cases} \dfrac{1}{\pi ui}\displaystyle\sum_{n=0}^{N}(-1)^n(\cos 2\pi u\xi_{n+1} - \cos 2\pi u\xi_n) & u \neq 0 \\ 0 & u = 0. \end{cases} \tag{3.10}$$

The above expressions also highlight why the symmetric grating leads to an odd number of diffraction spots while the nonsymmetric grating leads to an even number of diffraction spots in the far field. According to Parseval's theorem, the sum of the intensities of all diffraction orders is 1:

$$\sum_{u=-\infty}^{\infty} I_u = \sum_{u=-\infty}^{\infty} |G(u)|^2 = 1. \tag{3.11}$$

Thus, for the design of the gratings, a group of solutions for the transition points $\boldsymbol{\xi} = [\xi_1, \ldots, \xi_N]$ is required to create an array of diffraction spots with uniform intensity distribution, which is equivalent to $I_0(\boldsymbol{\xi}) = I_{\pm 1}(\boldsymbol{\xi}) = \cdots = I_{\pm N}(\boldsymbol{\xi})$. Numerical approaches are utilised to derive solutions for $\boldsymbol{\xi}$, and Zhou and Liu[181] have provided a detailed table of the transition points required for generating an array of any desired size. For all of the experiments reported in this chapter, the transition points used in the pattern design have been taken from their results. The transition point values for the 6-by-6 grating used for this study were: $\xi_1 = 0.11444$ and $\xi_2 = 0.20897$. An example of a 6-by-6 grating design based on these transition points ξ_1 and ξ_2 is shown in **Figure 3.4**.

Figure 3.4: Illustration of the generated Dammann grating based on the designed transition points. An example of a 6-by-6 grating design based on these transition points ξ_1 and ξ_2. Black and white regions represent the target phase of 0 and π, respectively. Grey borders in the figure are for the pattern edge illustration purpose only.

In the fabrication process, the transition points are quantised using a 1 μm square region,

which corresponds to the minimum laser voxel dimension (see Section 3.3.1) and defines each pixel on the raster image of the designed pattern. Therefore, the number of pixels in the pattern affects the quantisation error introduced at the transition points during mathematical calculations, which in turn impacts the actual phase change and the overall pattern quality. In order to gain more insight in terms of the factors that influence the actual device performance, simulations were first carried out to determine the optimum design parameters (and consequently the fabrication parameters) that would generate an array of spots with a high diffraction efficiency and a uniform intensity distribution.

3.1.3 Generation of LC Dammann Gratings

The diffraction pattern in the far field can be derived by taking the Fourier transform of the complex light distribution immediately after the grating. The propagating laser beam was modelled using a monochromatic Gaussian beam intensity profile expressed as

$$I(\rho, z) = \frac{I(0,0)}{1 + \frac{z^2}{z_R^2}} e^{\frac{-2\rho^2}{w^2}} \tag{3.12}$$

where $\rho = \sqrt{x^2 + y^2}$ is the distance away from the centre of the laser beam; z is the distance away from the waist point of the laser beam; $z_R = \frac{\pi w_0^2}{\lambda}$ is the Rayleigh length; w is the waist of the laser beam, which is a function of z; and w_0 is the beam waist at distance $z = 0$. By normalising $I(0,0)$ to 1 for calculation simplicity, Equation 3.12 at $z = 0$ can be further simplified to

$$I(x, y) = e^{\frac{-2\cdot(x^2+y^2)}{w_0^2}} \tag{3.13}$$

where (x, y) is the position in a plane perpendicular to the propagation that is relative to the central position of the beam where maximum intensity is observed.

A Dammann grating that gave rise to an array of 6-by-6 spots in the replay(far) field

was then generated by employing the transition point values provided by Zhou[181]. The total pattern size and the grating period were determined first according to the fabrication speed of our DLW system, which was 100 μm per second for a single photo-polymerised line. Each pixel of the design pattern corresponded to a 1 μm square region in the actual device fabricated with the DLW system, which had to be taken into consideration, along with the spot size of the illumination source in the experimental system used to characterise the diffraction patterns. In the design pattern, a pixel value of 1 represents a phase of π and a value of 0 represents a phase of 0, indicating a π phase difference between the two regions, which is controlled by the designed transition points. After generating a 1D grating, the 2D pattern was then generated by XOR-ing two 1D gratings with one of them being rotated by 90°. The entire process sequence as well as the simulated Gaussian beam are presented in **Figure 3.5**.

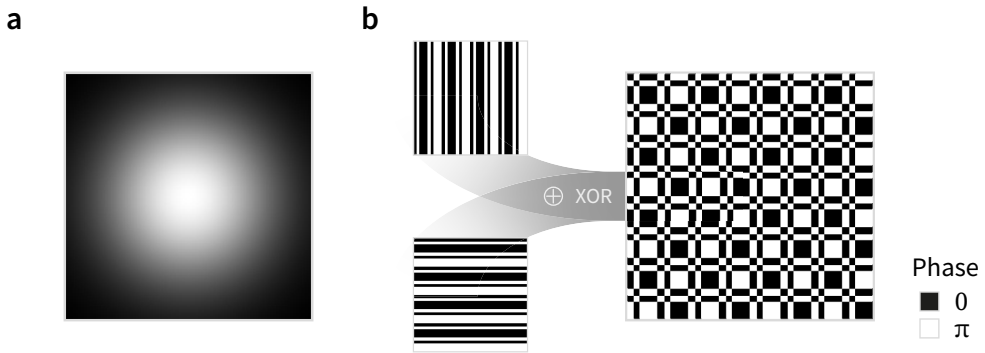

Figure 3.5: Preparations for simulating the Dammann grating. (a) The simulated Gaussian laser beam source. **(b)** Generation of a Dammann grating that gives rise to a 6-by-6 square array of spots in the replay (far) field by taking the exclusive OR result for vertical and horizontal 1D Dammann gratings.

3.2 Simulations of the Far-Field Intensity Distribution

3.2.1 Numerical Simulations

In order to determine the best fabrication coefficients, the pattern for the Dammann gratings is classified based on the parameters used to generate them. There are few parameters that can

control the quality of the far-field diffraction pattern generated by the Dammann grating.

The first tunable parameter is the number of pixels in the designed pattern that represent the width of one grating period. Each pixel in the pattern corresponds to a 1 μm square in the actual fabrication process. Simulations were performed using patterns with a total size of 8192 by 8192 pixels, varying the number of pixels per grating period from 16 to 2048 pixels. The quality of the gratings, in terms of the intensity distribution in the replay field, was assessed by calculating the maximum variation in normalised spot intensity.

The transition points were calculated based on the continuity of the axis, meaning they can be any real number within a period. However, fabricating at the exact transition points would be time-consuming. To increase fabrication speed while maintaining grating quality, the period was quantised into whole pixels. The transition points were then rounded to the nearest whole number of pixels, as fractional pixels cannot be fabricated.

When the width is small (i.e., 16 pixels), the normalised intensity difference ΔI between the maximum and minimum intensity is $\Delta I|_{T=16} = 0.76$, which indicates a pattern with a significantly non-uniform intensity distribution that mismatches with the design target of a uniform Dammann array. For a slightly larger width, i.e., 32 pixels or 64 pixels, the intensity difference becomes $\Delta I|_{T=32} = 0.26$ or $\Delta I|_{T=64} = 0.24$, respectively, which are also not in accord with the initial design. When the period is larger than or equal to 128 pixels, the difference drops to $\Delta I|_{T=128} = 0.06$, which means that the grating period with more than 128 pixels can generate a uniform intensity array with only a small degree of nonuniformity that is less than 0.06 in the Fourier plane. However, when the grating period becomes larger, the gap between each spot in the diffraction pattern will become narrower, which makes it difficult to observe the diffraction pattern on a screen in the replay field. In order to balance the need for low nonuniformity in the intensity distribution of the spots with the size of the

diffraction pattern in the replay field, a pixel width of 128 pixels for the period is selected as the fabrication parameter. The normalised intensity difference ΔI between the maximum and minimum intensity for different grating periods are listed in **Table 3.1**.

Table 3.1: Intensity difference ΔI with different grating period.

T	16	32	64	128	256	512	1024	2048
ΔI	0.76	0.26	0.24	0.06	0.05	0.03	0.01	<0.005

The distribution of the intensity and the overall quality of the diffraction pattern was affected by the phase ramp at the transition points between two adjacent pixels with different phase profiles. The ramp represents the gradual phase transition from one pixel to another pixel around the transition point. For the actual fabrication, it is impossible to make the phase change so abrupt at the transition point that there is no ramp in the phase, which reduces the accuracy of the actual fabricated pattern compared with the ideal grating, which has a perfect discontinuous phase change at the transition points. To simulate what is observed in practice, and to determine the tolerance in the fabrication, the pattern was intentionally blurred with different averaging kernels in **Figure 3.6**.

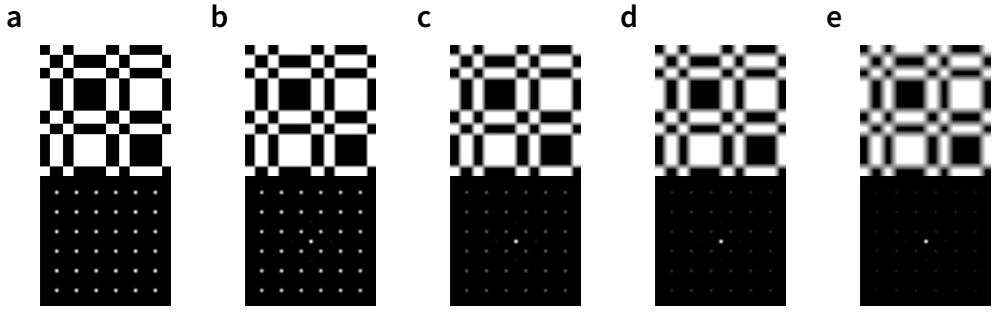

Figure 3.6: Blurred Dammann grating with an average filter and the corresponding Fourier transforms of the grating. The filter window kernels used range from 1-by-1 to 9-by-9 pixels with a step size of 2 pixels from (a) to (e).

The Fourier transform of the blurred gratings in Figure 3.6 indicate that if there is a slight blurring of the pattern edge this will not affect the quality of the diffraction spots significantly,

while the zeroth order will quickly become dominant if the quality of the fabrication of the edges is poor.

The simulations provide detailed guidance about how to choose the most appropriate parameters for the design of the grating and the fabrication of the grating in the LC device to obtain the best quality in terms of the diffraction pattern. The final parameters chosen for this study were as follows: (1) The grating image size was set to 1024 pixels by 1024 pixels, with a grating period width of 128 pixels; (2) the writing speed and power were carefully selected during the fabrication as well to minimise the blurring of the edges of the grating pattern. These fabrication parameters were further verified using a spatial light modulator (SLM), where a similar environment close to the actual laser-written LC devices is provided.

3.2.2 Testing Design using an SLM

Before writing the gratings directly into the LC glass cells, the gratings were characterised experimentally using a SLM. The SLM consists of a grid of nematic LC pixels which have a linear switching range between 0 and 2π at a wavelength of 780 nm. A Dammann grating was loaded onto the SLM, which was installed in an off-axis replay configuration. This characterisation system is illustrated in **Figure 3.7**.

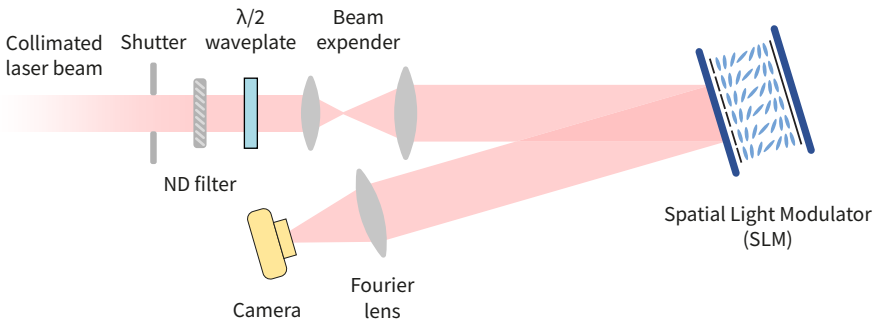

Figure 3.7: Layout of the SLM experiment setup used to inspect the Dammann gratings designed in this work. Dammann gratings were loaded onto the SLM installed in an off-axis configuration and the far-field intensity distribution are then captured by a CCD camera after the Fourier lens.

The laser had a wavelength of λ = 780 nm. The power of the laser was attenuated using a neutral density (ND) filter of optical density (OD) of OD = 0.2. A beam expanding system was also included with f_1 = 25.4 mm and f_2 = 125 mm, which resulted in an expansion of the beam to suit the size of the effective area of the SLM. The replay images were then captured by a CCD after a lens on an off-axis position. By loading the designed Dammann grating pattern on to the SLM, the far field image could then be captured by a CCD camera.

The pattern loaded onto the SLM was essentially the same as that presented in Figure 3.4 but adjusted to utilise the full tunable range and resolution of the SLM. The 24-bit RGB image, where 8 green bits are the most significant bits and 8 blue bits are the least significant bits, was loaded into the 16-bit digital video interface of the SLM. According to the datasheet of the SLM, the last 8 blue bits are ignored and only an image composed of 8 green bits and 8 red bits will result in a tunable linear output phase of the SLM across the full 16-bit range.

Figure 3.8(a) and (b) illustrate the grating pattern and simulation results of the corresponding replay image in the Fourier plane, respectively. The initial simulation results in Figure 3.8(c) indicate that the designed Dammann grating pattern creates an array of spots in the replay field as intended.

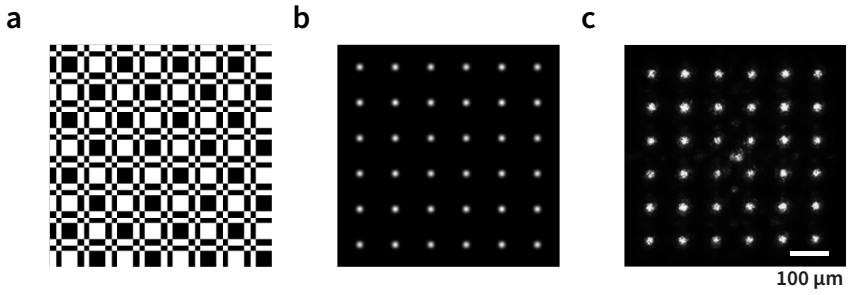

Figure 3.8: Design, simulation and experimental characterisation results of a 2D Dammann grating in an SLM imaging system. (a) Configuration of a Dammann grating that gives rise to a square array of 6-by-6 spots in the replay field. **(b)** Simulation of the corresponding replay field pattern. **(c)** Photograph of the replay field pattern observed when the Dammann grating in (a) was loaded onto the SLM.

From simulation results of the pattern formed by the SLM imaging system, it can be noticed that the outcome of the simulation is not identical to the expected pattern. This discrepancy was caused by the gap between two SLM pixels which in effect is the same as the gradient phase ramp at the pattern edge. This nonideal situation contributes to the the centre zeroth order spot and thus emphasizes the advantage of the DLW method, which can overcome this weakness.

3.3 Two-photon Polymerisation Direct Laser Writing System

3.3.1 Fabrication System

A schematic of the TPP-DLW system is illustrated in **Figure 3.9**. The laser source is a mode-locked Titanium-Sapphire femtosecond laser (Spectra-Physics Tsunami) emitting at a centre wavelength of 780 nm, which is pumped by a diode-pumped solid state (DPSS) CW laser (Spectra-Physics Millennia V) at 532 nm, emitting 100 fs pulses at a repetition rate of 80 MHz. The laser was focused into the LC layer of the cell using an Olympus 0.45 numerical aperture (NA) objective lens. The power of the fabrication laser focused into the LC layer after the objective was 40 mW. The lateral (Δx,Δy) and axial (Δz) dimensions of the voxels were estimated using the following equations[15]:

$$\Delta x, \Delta y \approx \frac{\lambda}{2NA} \tag{3.14}$$

$$\Delta z \approx \frac{3n\lambda}{2NA^2} \tag{3.15}$$

where n is the refractive index of the mixture used during the fabrication. For the formulation used in this experiment, the refractive index is estimated to be n=1.51, which results in voxel dimensions that are ~1 μm in the lateral dimension and ~8 μm along the axial dimension.

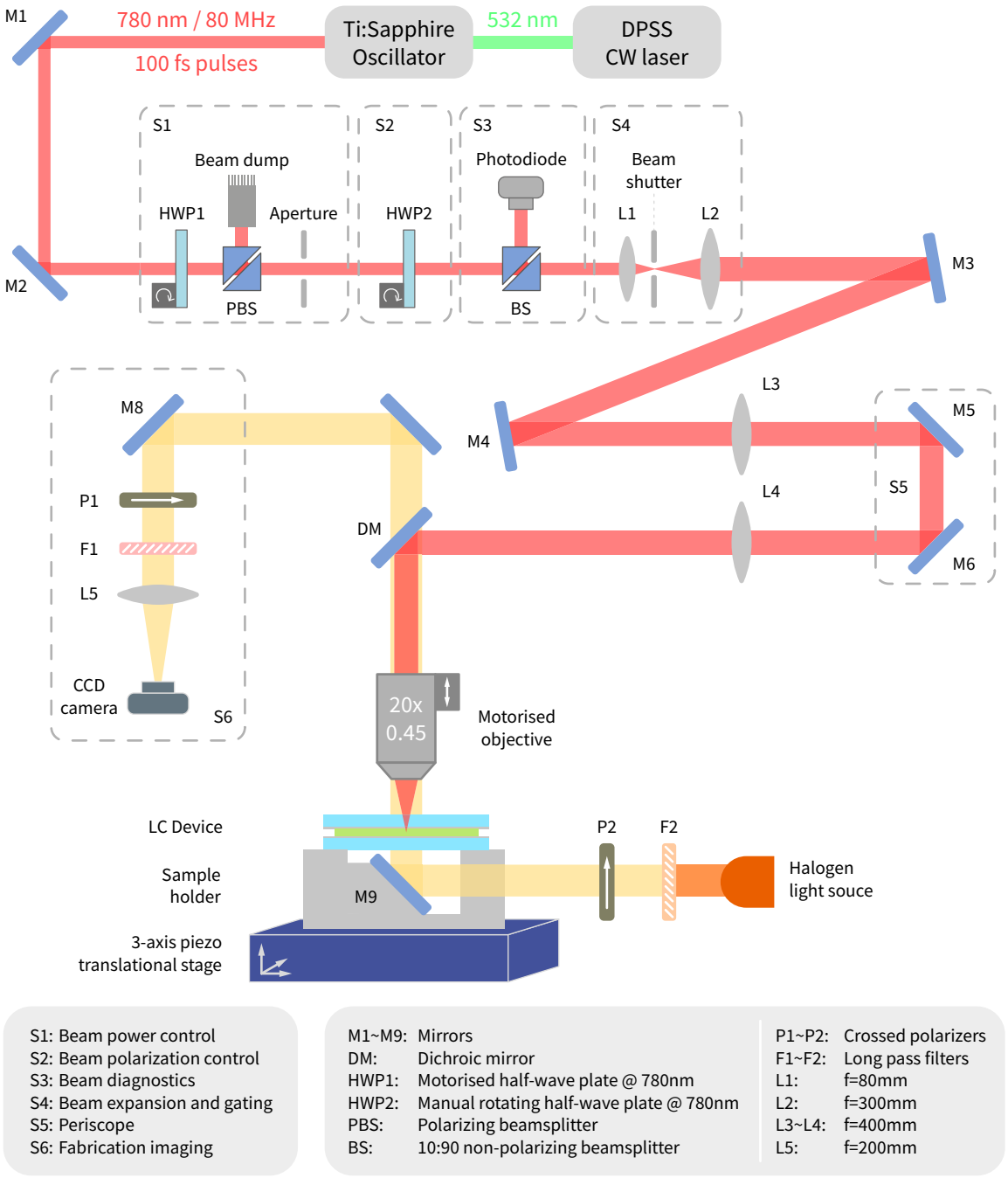

Figure 3.9: Schematic of the optical layout of the two-photon polymerisation direct laser writing system. Key optical subsystems are highlighted with the necessary components labelled. The laser source used in the TPP-DLW system is a mode-locked Titanium-Sapphire femtosecond laser (Spectra-Physics Tsunami) working at λ = 780 nm and emitting 100 fs pulses at a repetition rate of 80 MHz. The laser was focused into the fabrication plane inside the liquid crystal (LC) device using an Olympus 0.45 numerical aperture (NA) objective lens. The red lines show the path of the 780 nm femtosecond laser for two-photon fabrication, while the yellow lines show the path of the halogen source that illuminates the LC sample (filtered by a 550 nm long pass filter to prevent unwanted cross-linking).

The voltage-controlled sample was mounted onto a 3D printed adapter on a 3-axis piezo-

electric translation stage with positioning resolution of 1 nm and movement accuracy of 100 nm (Aerotech ANT95XY-050 and ANT95V-3). The halogen bulb beside the stage illuminates the sample through an orange (550 nm) filter so that the photocuring process could be monitored with an in-situ monochrome CCD camera in real time. A polarising optical microscope configuration was established by forming an image of the illuminated sample through the dichroic mirror before it was captured by a CCD camera using a lens of 200 mm focal length with a polariser and analyser installed. The LC mixture was polymerised by moving the device under the focus of the pulsed laser beam at a speed of 0.1 mm/s. The LC device was driven by a 1 kHz square wave of voltage ranging between 0 V_{rms} and 10 V_{rms}.

My contributions to the system include integrating the intensity modulation scheme (S1 in Figure 3.9) and developing an automatic control algorithm for the 3-axis stage, enabling large-scale fabrication. The intensity modulation enhances power control flexibility, accommodating a broader range of users. The embedded optimisation algorithm in the automatic control system (see Section 3.3.2) ensures consistent high-precision fabrication. These improvements have significantly enhanced overall efficiency and reliability of the DLW system.

3.3.2 System Optimisation

Based on previous experiments on the DLW system, a significant drift in the z axis was observed during the fabrication procedure, which caused an uneven distribution of the pattern in LC devices during fabrication of structures that lasted a long period of time. Some preliminary qualitative research indicated that the reason for the stage z axis drift is the thermal expansion of mechanical components in the stage during a long fabrication period. Considering that the system has been fixed and no equipment tends to be added into or removed from the system, a non-destructive method referred to as maximum contrast method was proposed for quantizing the problem with a predetermined calibration pattern. In addition, a PID control algorithm

was utilised for compensation, as it only uses the original camera in the system to obtain the contrast information of the calibration target required.

(i) Maximum Contrast Method

By utilising the same technology behind the autofocus (AF) process in a smartphone camera, we designed this method to derive the actual z axis position of the stage. The camera on a smartphone typically performs an autofocus by detecting the contrast of the image it receives and moves the position of the lens to find the best position before capturing an image. This method is classified as passive AF as the algorithm relies on image information only. Naturally, the difference between adjacent pixels of the sensor will increase with correct image focus, where the image sharpness is maximised[196]. The optical system can therefore be adjusted using the relationship between the image contrast and position derived.

The contrast is represented as the sliding average of a 3-by-3 block where the average differences in the grey scales between a pixel and its surrounding 8 pixels are calculated. Assuming that the grey scale of the original M-by-N RGB image is represented as I_{mn}, where $m \in [1, M]$, $m \in N^*$ and $n \in [1, N]$, $n \in N^*$. The average difference in each 3-by-3 block B_{ij} is represented as:

$$B_{ij} = \overline{\sum_{k=-1}^{1} \sum_{t=-1}^{1} (I_{(i+k)(j+t)} - I_{ij})} \tag{3.16}$$

where $i \in [2, M-1]$, $i \in N^*$ and $j \in [2, N-1]$, $j \in N^*$. The contrast C is defined as:

$$C = \overline{\sum_{i=2}^{M-1} \sum_{j=2}^{N-1} B_{ij}}. \tag{3.17}$$

The core principle of this method is providing a way of deriving a certain feedback signal from the calibration targets fabricated continuously across the thickness of the device and creating a closed-loop compensation system. By creating and measuring a standard reference pattern using

a camera at different depth positions, a group of values could be derived for the calibration for comparison and calibration in real-time during the fabrication process.

(ii) Algorithm Robust Test

The PID algorithm was then utilised to compensate the stage error in a dynamic way using the feedback signal provided from contrast measurements. The stage was designed to move to a random position within a relative ±5 μm deviation and then using the PID algorithm to control the stage to move back to its original height.

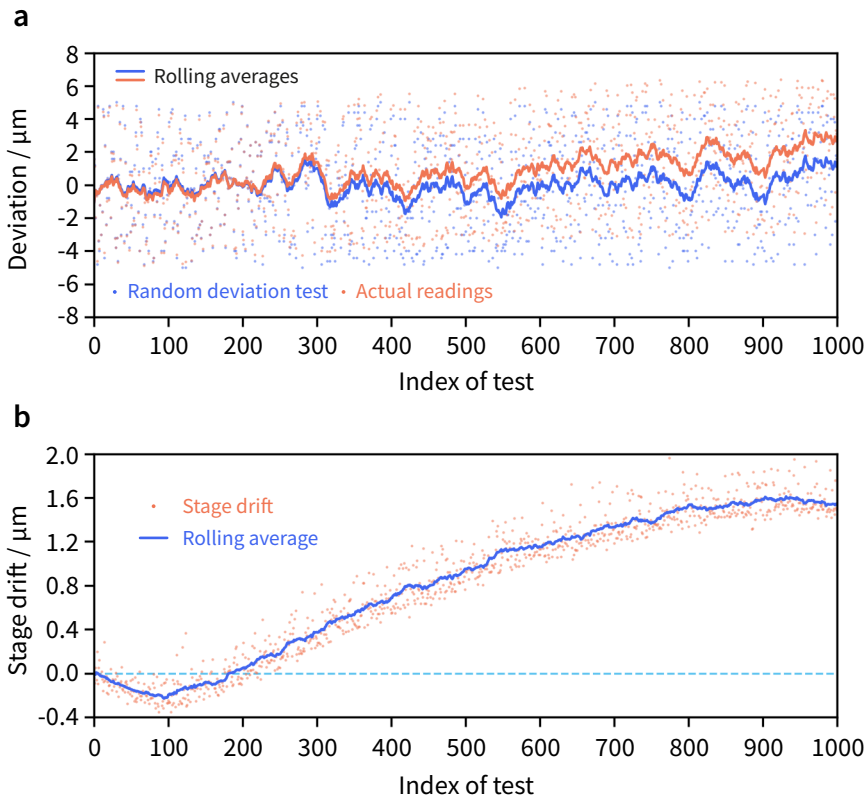

Figure 3.10: Illustration of stage position drift.(a) Results of stage position readings with random deviations using image contrast as a feedback signal with random deviations. (b) Measured position drifts of stage for error evaluations.

The whole process was then repeated for 1000 times. **Figure 3.10**(a) shows the random deviations and the stage readings as well as their trends without the compensation method. It can be noticed that there is a significant drift between the stage readings and the random

deviations, which proves that the thermal drift did exist during the whole fabrication process. To illustrate the thermal drift more clearly, Figure 3.10(b) is plotted. The drift of the stage was calculated by comparing the difference between the random deviation (target) and the z axis readings (real). The total time cost for the robust test was about 100 minutes and a significant drift over 1 μm has been noticed. Since the drift of the stage can be precisely measured, thus the real-time compensation can be achieved during a long timescale fabrication process.

Meanwhile, the stage movement error E_M could also be derived from this test as well. This calculates the error between the final reading of the z axis, Z_{final}, after returning the stage to the reference (origin) position and the sum of the accumulation of Δd_k during PID compensation $\tilde{Z}_{\text{final}}$, where $\tilde{Z}_{\text{final}} = Z_{\text{initial}} + \sum \Delta d_k$. Thus $E_M = Z_{\text{final}} - \tilde{Z}_{\text{final}}$.

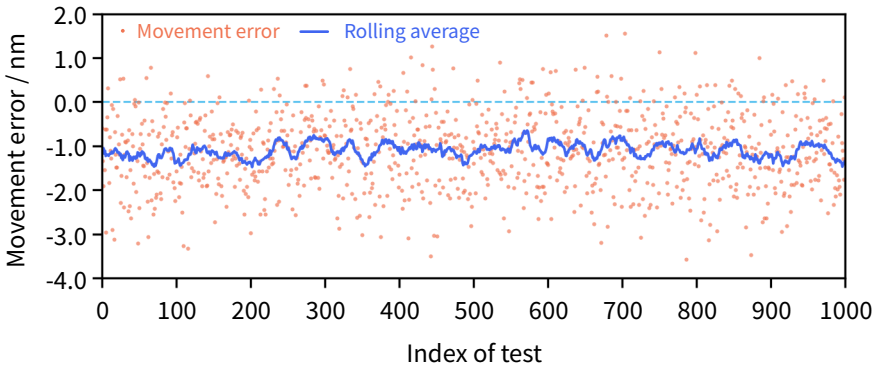

Figure 3.11: Illustration of relative movement error of the stage in the robust test. The mean value of the error is -1.11 nm and the standard deviation is 0.85 nm.

The test results after the integration of the compensation method are illustrated in **Figure 3.11**. It can be concluded that the movement error is limited within ±4nm, which is very accurate compared with the stage drift. So, the PID compensation algorithm didn't add in extra error to the stage. It also can concluded that the relative movement of the stage is accurate and reliable, while the absolute reference point (the origin) drifts significantly and is unreliable during the long-lasting fabrication process. This further supports the effectiveness of

the incremental PID algorithm in improving the accuracy and stability of the stage during long fabrication processes.

3.4 Fabrication of LC Dammann Gratings

3.4.1 Single Element Fabrication

The fabrication process for the single layer switchable 2D Dammann grating is demonstrated in **Figure 3.12**. A 5 μm thick Instec LC cell capillary filled with the prepared mixture is utilised in the fabrication. The cell was in its initial state with no external electric field applied before the fabrication. In this state, the LC director is aligned with the surface rubbing direction. Then the two-photon laser was focused into the polymerisable resin with its voxel position precisely controlled by a 3-axis piezoelectric translation stage. Because the thickness of the cell was smaller than the axial voxel dimension, the polymerised LC resin will be tethered to the substrates firmly. Different LC regions will be polymerised and the orientation of the director locked based on the designed Dammann grating pattern. After the fabrication process, the laser will be removed and different voltages will be applied to tune the free unpolymerised LC regions in the resin and create different phase profiles for various wavelengths.

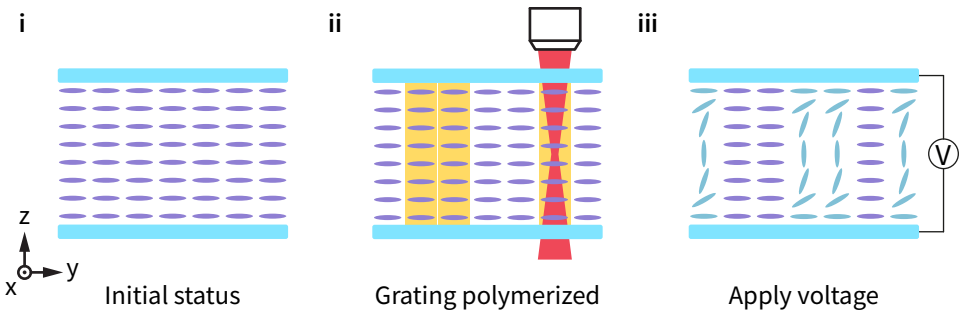

Figure 3.12: Illustration of the concept of an switchable 2D liquid crystal (LC) Dammann grating fabricated using two-photon polymerisation direct laser writing. The grating is fabricated across the LC bulk with no voltage applied and activated by applying a voltage to change the orientation of the LC director to give rise to the designed phase profile.

3.4.2 Multi-Element Fabrication

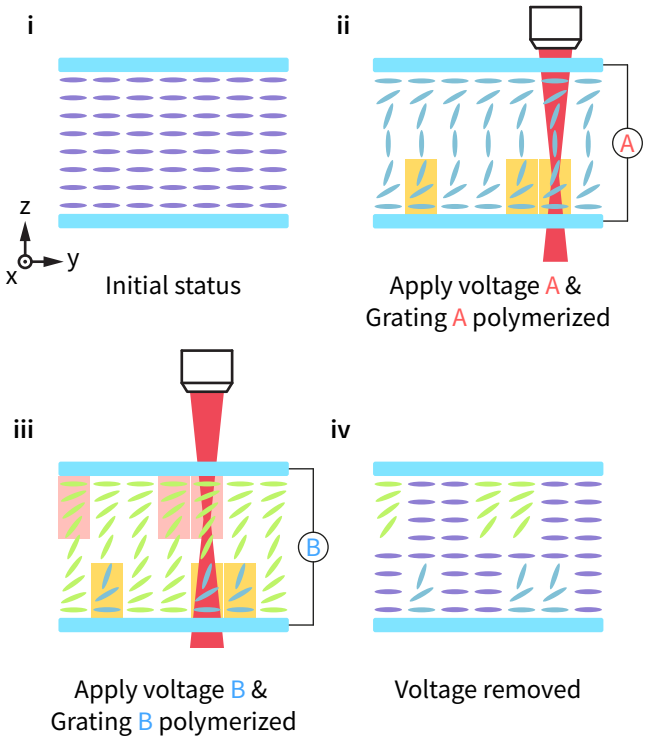

Figure 3.13: Illustration of the concept of an interchangeable 2D liquid crystal (LC) Dammann grating fabricated using two-photon polymerisation direct laser writing. One grating (Grating A) was fabricated on the substrate and activated by applying a voltage corresponding to the voltage used to write Grating B (which makes this grating inactive). The other grating (Grating B) was written next to the superstrate and activated by applying a voltage that corresponded to the voltage applied to fabricate Grating A (which renders Grating A inactive as the director profile between the polymerised and unpolymerised regions becomes continuous).

The fabrication process for the bilayer interchangeable 2D Dammann grating is demonstrated in **Figure 3.13**, which is similar to the process of the single layer switchable 2D Dammann grating in Figure 3.12. A thicker 20 μm Instec LC cell capillary filled with the prepared mixture was utilised for this demonstration. The cell was in its initial state where the LC director was aligned with the surface rubbing direction. Then, based on the design of two Dammann gratings and the requirement for the voltages at which they are activated, different voltages were applied for writing the corresponding grating structures. Due to the thicker LC layer used in the fabrication, the laser writing voxel was precisely controlled to appear at different

locations in the LC layer. A set of standard patterns was fabricated through the full thickness, and the method introduced in Section 3.3.2 was used to determine the fabrication depth. In order to separate two gratings explicitly, one of the gratings was tethered to the substrate while the other one was tethered to the superstrate during the fabrication process. Grating A that is attached to the substrate was fabricated first with voltage A applied. Only the designed regions will be locked-in by the polymer network during the fabrication. Then the same steps were repeated for Grating B that was fabricated on the superstrate with voltage B applied. After the fabrication, the writing laser was removed and different voltages were applied to tune the free unpolymerised regions in the LC layer to switch between the two different gratings.

3.5 Switchable 2D Dammann Grating

3.5.1 Experiment Results

For this study, the polymerisable nematic LC mixture (IR819-RM257-E7) was used. This was capillary filled into a glass cell with anti-parallel rubbed polyimide alignment layers, indium tin oxide electrodes, and a cell gap of 5 μm. **Figure 3.14** shows the experimental results for a Dammann grating laser written into the polymerisable nematic LC. The size of the grating was set to 512 pixels by 512 pixels where each pixel was fabricated with 2-by-2 1 μm laser-written spots and the number of pixels used to represent each period in the pattern was 128. This results in a grating size of 1024 μm by 1024 μm, which was the same configuration as that used for testing with the SLM, but with a total pattern size that was scaled by 2. The grating pattern was fabricated for the case when no voltage was applied during fabrication and the target pattern fabricated was designed to exhibit a square array of 6-by-6 spots in the replay-field. Figure 3.14(a) shows a polarising optical microscope (POM) image of the laser written pattern. As the pattern was written at $V_{\text{Fabrication}}$ = 0.0 V_{rms}, the features are barely visible because of the uniformity in the director field. This is because the laser writing has

locked-in the alignment at 0.0 V_{rms} for the regions that define the grating. When the device was inspected without an applied electric field, the director was aligned in the same direction uniformly throughout the LC layer. Some of the features of the grating can be just made out in the image, and it is believed that this is due to a slight mismatch in the refractive indices between the polymerised and unpolymerised regions. Figure 3.14(b) shows a POM image of the pattern with no analyser installed to highlight the phase-only information from the pattern (which is null here). The features are nearly invisible because the pattern was written at 0.0 V_{rms} where the phase profile is uniform as the director was aligned throughout. When no voltage was applied the grating was inactive and therefore no pattern was generated in the replay field as can be seen in Figure 3.14(c).

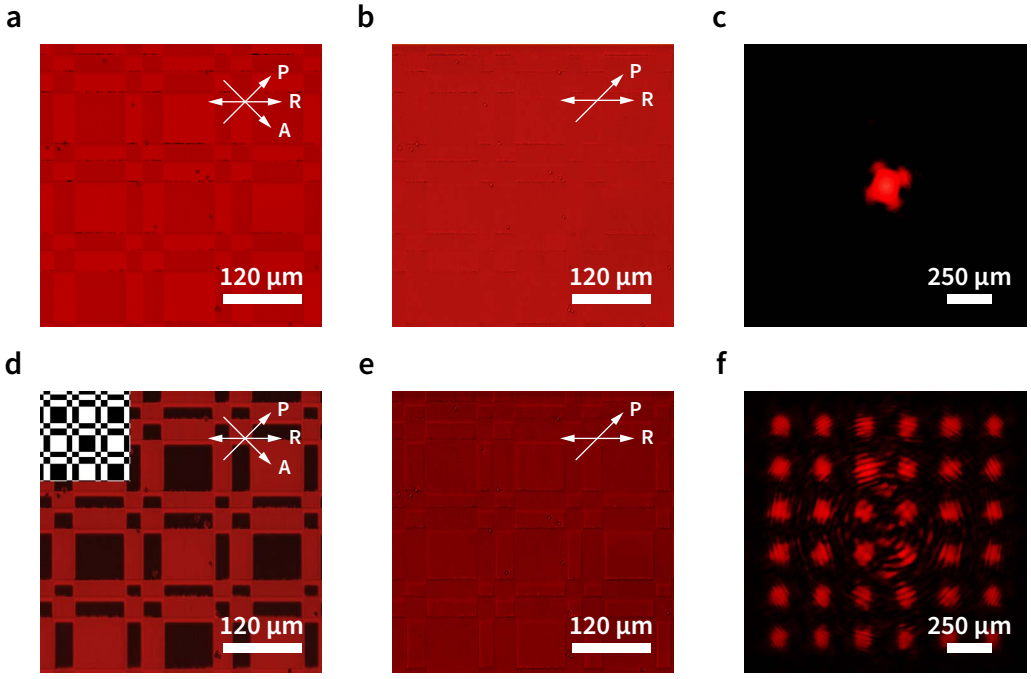

Figure 3.14: Demonstration of a switchable laser written LC Dammann grating. (a) Polarising Optical Microscope (POM) image of the Dammann grating for an illumination wavelength of 660 nm that gives rise to a 6-by-6 array of spots in the replay field when activated. The POM shows the case for the voltage off-state at $V = 0$ V_{rms}. The arrows indicate the directions of the polariser (P), analyser (A) and rubbing direction (R). **(b)** Microscope image of the 6-by-6 square grating with no analyser in the voltage off-state at $V = 0$ V_{rms}. **(c)** Corresponding replay field pattern for the voltage off-state. **(d)** Microscope image of the 6-by-6 square grating in the voltage on-state at $V = 1.3$ V_{rms} (with grating design included in the top left corner). **(e)** Phase only microscope image of the 6-by-6 square grating with no analyser in the microscope for the voltage on-state at $V = 1.3$ V_{rms}. **(f)** Corresponding replay field pattern for the voltage on-state at $V = 1.3$ V_{rms}.

To activate the grating and obtain a diffraction pattern, a replay voltage of V_{Replay} = 1.3 V_{rms}, which will generate a pattern with π phase difference at a wavelength of 630 nm laser illumination, was applied where it can be seen that a clear Dammann grating appears in the LC device (as is evident from the POM image in Figure 3.14(d)). This voltage was selected based on the transmission-voltage curve measured for the LC device in Figure 2.7. It can also be seen in Figure 3.14(d) that the fabrication has been successful by comparing the fabricated pattern in the LC cell with the designed pattern (shown as an inset). Phase information was inferred from the POM images with no analyser installed in the microscope (Figure 3.14(e)) by checking the edges of the feature where the regions with different phase profiles are clearly revealed. The director locked-in by a polymer network at 0.0 V_{rms} remains unchanged while the director in the non-laser written regions were reoriented by the replay voltage 1.3 V_{rms} to create a different phase profile. The mismatch in the refractive indices at the transition edges between the two regions results in the appearance of the grating.

Figure 3.14(f) shows the 6-by-6 array of spots generated in the replay field (far field) when the LC device was switched on with a voltage of 1.3 V_{rms}, demonstrating that the intensity is relatively uniformly distributed amongst the spots. The results show that the fabricated single layer element can readily switch between the two states with no residual appearance of the other grating when the device was set to the design voltages for activating the gratings. The results also show that the diffracted spots are distributed with a uniform intensity distribution when the grating was activated and then completely disappear when the grating was deactivated. Note that the faint concentric circles that can be seen in the image are the result of contributions from other planar optical elements in our 630 nm replay imaging system, such as a half-wave plate, polariser, beam splitter etc.

When the voltage applied to the LC was neither 0 V_{rms} nor 1.3 V_{rms}, which are the designed

replay voltages, the diffraction pattern will no longer be a uniform beamlet array or simply a non-diffracted spot. Instead, the zeroth order spot will become dominant in the replay field with the addition of a beamlet array that is much weaker in intensity. An example of the diffraction pattern recorded in the replay field when 1.0 V_{rms} was applied is illustrated in **Figure 3.15**.

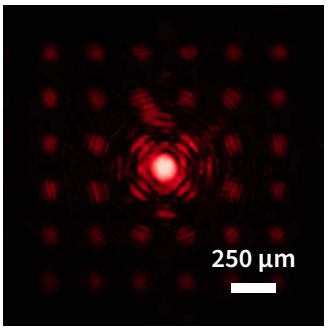

Figure 3.15: The replay field pattern for an applied voltage between the on-state and off-state. In this case, the voltage applied was 1.0 V_{rms}. The diffraction pattern is no longer a uniform beamlet array or simply a non-diffracted spot. Instead, the zeroth order spot becomes dominant in the replay field with a dim 6-by-6 beamlet array in the background.

3.5.2 Analysis and Discussion

(i) Fabrication Quality Analysis

To analyse the fabrication quality in more detail, the optical phase for the cross-sections of one grating period for the on and off states were extracted from the POM images and the results are illustrated in **Figure 3.16**. In the figure, the additional optical phase introduced by the LC birefringence when the voltage activating the pattern are binarised at the threshold, which is half the value between the maximum and minimum phase differences. The actual transition points were then derived from these binarised values. Compared with the designed transition points, which were : $\xi_1 = 0.11444$ and $\xi_2 = 0.20897$ respect to the unit period length 1, the fabricated devices exhibited a deviation $\Delta\xi$ in the transition point of less than 0.02 with respect to the unit period length or less than 2% with respect to the actual fabrication length, which is close to the fabrication quality of UV lithography[177,178]. Direct inspection of the transition

points using SEM imaging might be possible. However, due to the process of washing out the non-reacted LC mixture and coating the polymer network for SEM imaging will inevitably degrade the quality of the network, which could lead to an incorrect interpretation of the transition points.

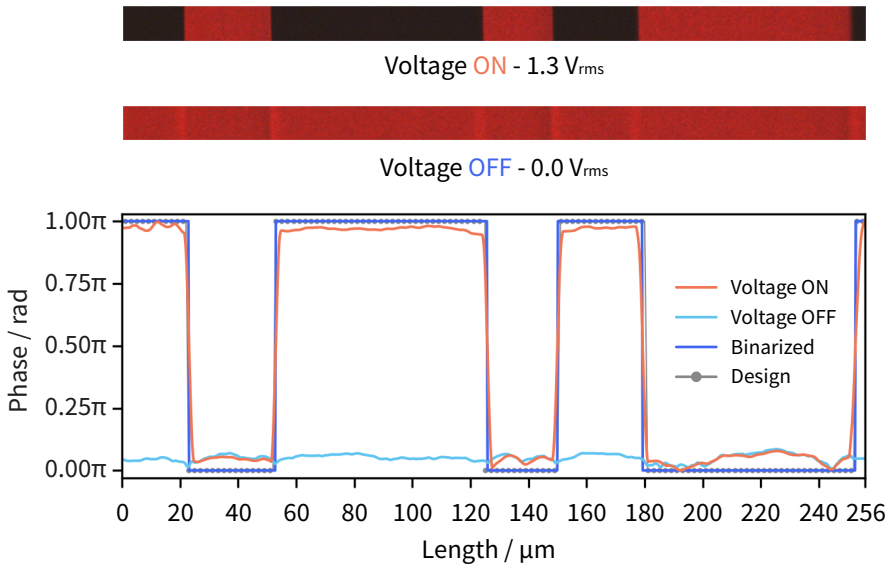

Figure 3.16: The phase extracted from a cross-section of one period of the grating along the longitudinal direction in the Dammann grating. This grating generates an array of 6-by-6 spots in the replay field. Corresponding microscope images of one period under crossed polarisers (with and without an applied voltage) for the same length scale are presented above the plot.

(ii) Diffraction Efficiency Measurements

The efficiency, which is defined as the ratio between the summation of the intensity of all desired 6-by-6 diffraction spots and the non-diffracted initial laser spot, was found to be approximately 60%. **Figure 3.17** presents the results for the diffraction efficiency as a function of voltage, which describes how much light goes into the 6-by-6 array of spots when the grating was activated. The mismatch arises because the formation of the polymer network causes a slight deviation in the voltage required to activate the pattern from the designed value. This leads to small changes in the pattern intensity under the microscope, affecting image contrast even when diffraction efficiency is maximised. These results indicate that these laser written LC devices

are promising for high-quality switchable Dammann gratings with high diffraction efficiency and relatively uniform intensity distribution across the spots in the array.

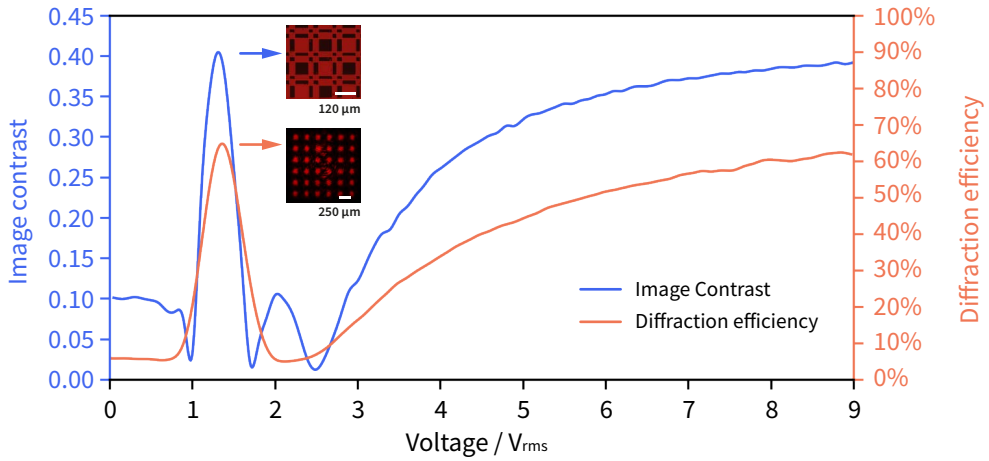

Figure 3.17: Diffraction efficiency and image contrast of a Dammann grating as a function of the applied voltage. The inset images show the diffraction pattern and polarising optical microscopy (POM) images at 1.3 V_{rms}.

(iii) Response Times

The rise (10%-90%) and fall (90%-10%) response times for the switchable grating written into this LC sample with a 5 µm cell gap were found to be of the order of 40 ms and 200 ms, respectively, which is significantly less than the response times recorded for the unpolymerised regions of the device, where response times of the order of 100 ms and 400 ms were recorded. The faster response times are due to the reduced thickness of the free LC region caused by the polymerised regions, which constrain the LC molecules and shorten the reorientation distance under an electric field. The switching time measured for the unpolymerised regions is consistent with the dynamics of the Fréedericksz transition[197] and is consistent with observations that the relaxation time is shorter for polymerised nematic LCs compared to the unpolymerised regions[198,199].

(iv) Temperature Stability

Figure 3.18 demonstrates the performance of a switchable Dammann grating when the temperature of the device was altered. In general, the grating can maintain the maximum diffraction efficiency across a range of temperatures. Figure 3.18(a) illustrates the diffraction efficiency of a Dammann grating as a function of the applied voltage at different temperatures ranging from 25 °C to 60 °C. It was noticed that the initial diffraction efficiencies at 0 V_{rms} increases due to a change in the temperature. This is caused by a change in the dielectric permittivity, the elastic coefficients and birefringence of the LC mixture at different temperatures between the polymerised and unpolymerised regions.

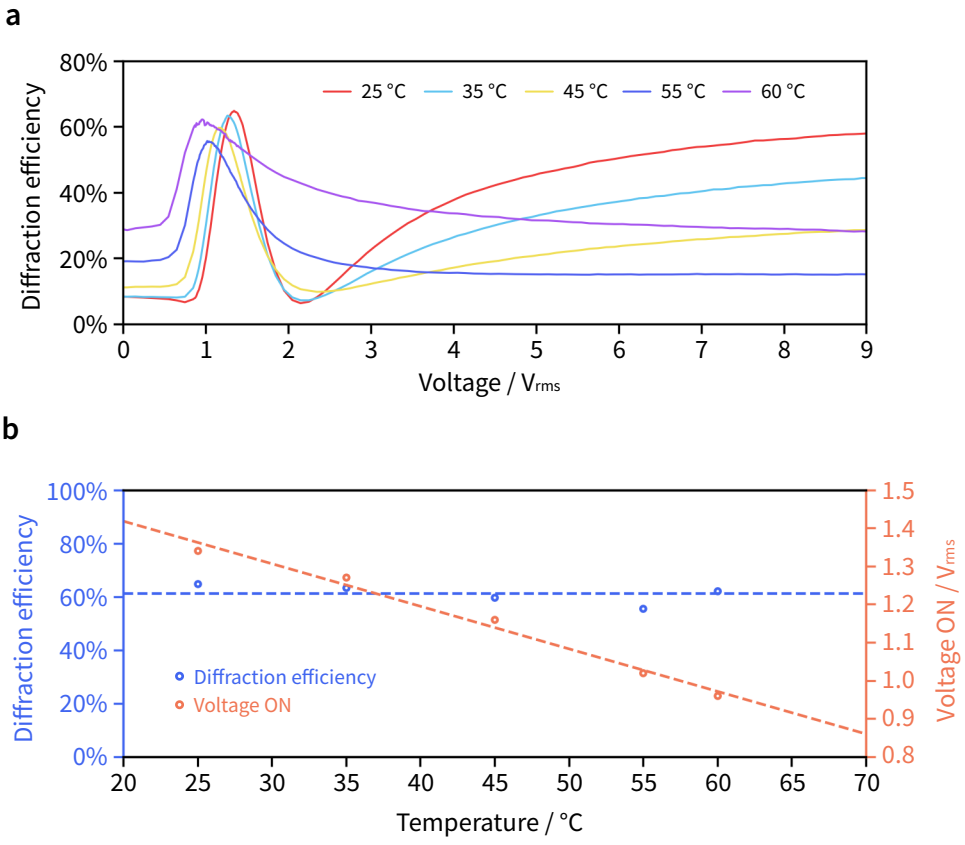

Figure 3.18: The diffraction efficiency of a switchable Dammann grating for different applied voltages and temperatures. (a) Diffraction efficiency of a Dammann grating as a function of the applied voltage at five different temperatures ranging from 25 °C to 60 °C. (b) The change in the diffraction efficiency (primary y-axis, blue symbols) and "Voltage ON" voltage (secondary y-axis, red symbols) as a function of temperature. The coloured dashed lines on the graph are intended to guide the eye.

Figure 3.18(b) reveals the change in the diffraction efficiencies and the voltage at which the grating appears on (labelled as "Voltage ON") at different temperatures. It is shown that the maximum diffraction efficiency of the switchable Dammann grating is maintained from room temperature up to the clearing temperature of the LC mixture. Meanwhile, as an increase in the temperature increases the initial optical phase difference between the polymerised regions and the unpolymerised regions, a lower voltage was then required to activate the grating and turn on the far-field diffraction pattern.

(v) Multiwavelength Compatibility

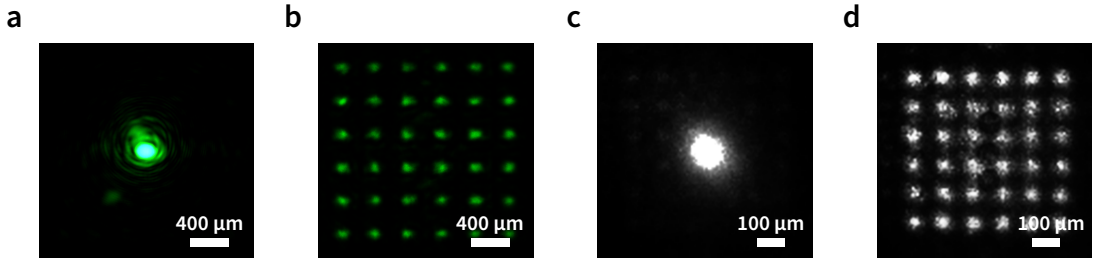

Figure 3.19: Demonstration of a switchable laser written LC Dammann grating operating at other wavelengths. The diffraction patterns are demonstrated under wavelengths of λ = 520nm and λ = 780 nm by adjusting the voltage applied to the LC device. **(a)** The replay field pattern for the voltage off-state at $V = 0$ V_{rms} for an incident wavelength of 520 nm captured with a CCD camera. **(b)** The replay field pattern for the voltage on-state at $V = 1.14$ V_{rms} at a wavelength of 520 nm. **(c)** The replay field pattern for the voltage off-state at $V = 0$ V_{rms} at a wavelength of 780 nm captured with a monochromatic CCD camera. **(d)** The replay field pattern for the voltage on-state at $V = 1.54$ V_{rms} at a wavelength of 780 nm.

Figure 3.19 demonstrates the ability of the 2D switchable Dammann grating to work at a range of different wavelengths. By adjusting the voltage applied to the LC device according to the transmission-voltage curve for the 5 µm sample in Figure 2.7(a), a phase difference of π can be achieved between the locked-in regions and the non-laser written regions. Figure 3.19(a) and Figure 3.19(b) shows the off-state and on-state of the Dammann grating when illuminated with light of a wavelength of 520 nm. The images were captured using a CCD camera. The test

voltage applied to the cell to control the director orientation of the non-laser written regions was V = 1.14 V_{rms}. Figure 3.19(c) and Figure 3.19(d), on the other hand, shows the switching of the Dammann grating when the LC device was illuminated by light of a wavelength of 780 nm. The 780 nm images were captured using a monochromatic CCD camera with the infrared filter removed. The voltage applied to turn the grating on was V = 1.54 V_{rms}. Note that the concentric circles seen in Figure 3.14(f) are not present here as the planar optical elements (e.g., waveplates) in our imaging system have been removed.

3.6 Interchangeable 2D Dammann Gratings

3.6.1 Experiment Results

Figure 3.20 shows an LC device that consists of two separate Dammann gratings that give rise to different arrays of spots in the replay field. In this case, the sizes of the two gratings are both 1024 pixels by 1024 pixels, where each pixel was fabricated using the DLW to illuminate regions of 1-by-1 1 μm spots, which results in an overall grating size of 1024 μm by 1024 μm. The two Dammann gratings that were designed give rise to an array of 6-by-6 spots in a square configuration and an array of 6-by-6 spots in a rhombus configuration. The gratings were fabricated in a glass cell with an LC layer thickness of 20 μm and were driven with a 1 kHz square wave with different voltage amplitudes during the fabrication process. The Dammann grating corresponding to the 6-by-6 rhombus pattern (pattern A) was fabricated in the presence of a voltage V_A = 3.38 V_{rms} applied to the LC cell. On the other hand, the Dammann grating corresponding to the 6-by-6 square pattern (pattern B) was fabricated when the LC cell was subjected to a voltage of V_B = 5.96 V_{rms}. The voltages applied for the fabrication is based on the transmission-voltage curve for the 20 μm LC layer in Figure 2.7(c) and a phase difference of π can be achieved between the locked-in voltages. Figure 3.13 illustrates the concept of an interchangeable Dammann grating fabricated using TPP-DLW.

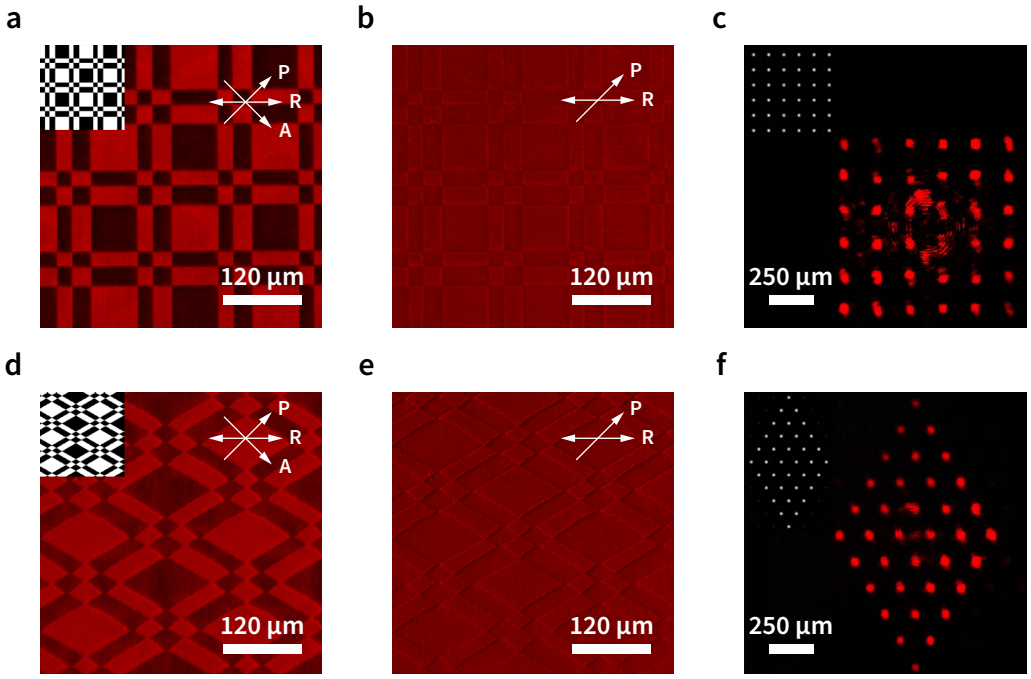

Figure 3.20: Demonstration of LC devices with interchangeable Dammann gratings. (a) Microscope image of the Dammann grating that gives rise to a 6-by-6 square array in the replay field (with the grating design shown in the top left corner) fabricated at $V_{\mathrm{A}} = 3.38\ \mathrm{V_{rms}}$. The arrows indicate the direction of the polariser (P), analyser (A) and rubbing direction of the alignment layer (R). **(b)** Phase only microscope image of the Dammann grating that gives rise to a 6-by-6 square array in the replay field fabricated at $V_{\mathrm{A}} = 3.38\ \mathrm{V_{rms}}$. **(c)** Corresponding replay field pattern for the Dammann grating that generates a 6-by-6 square array in the replay field (with simulated replay field shown in the top left corner of the image). **(d)** Microscope image of the Dammann grating that gives rise to a 6-by-6 rhombus array of spots in the replay field (with the grating design shown in the top left corner) fabricated at $V_{\mathrm{B}} = 5.96\ \mathrm{V_{rms}}$. **(e)** Phase only microscope image of the Dammann grating that gives rise to a 6-by-6 rhombus array of spots in the replay fabricated at $V_{\mathrm{B}} = 5.96\ \mathrm{V_{rms}}$. **(f)** Corresponding replay field pattern showing the 6-by-6 rhombus array of spots (the simulated replay field is shown in the top left corner).

The depths of the patterns fabricated within the LC layer were carefully chosen to ensure that they were close to the glass substrates and that they did not overlap with each other. These voltages were selected based on measurements of the transmission-voltage curve for the LC sample, which creates a π phase difference between the two laser-written gratings. It can be seen in Figure 3.20(a) and Figure 3.20(e) that the Dammann gratings compare well with the design pattern (shown in the inset of each image). The diffraction patterns were obtained by applying the voltage that was used to write the other grating, i.e., applying voltage V_{A} (voltage for rhombus pattern fabrication) to observe pattern B (square pattern) in the replay field whereas

applying V_B (voltage for square pattern fabrication) meant that pattern A (rhombus pattern) could be seen in the replay field. The phase only information from the pattern is highlighted in Figure 3.20(b) and Figure 3.20(e) which were captured from POM with no analyser installed.

The results for the 6-by-6 square diffraction pattern captured in the far field (replay field) in the replay system as well as the corresponding simulation results (shown in the insets) using the designed pattern are presented in Figure 3.20(c). The square pattern results clearly illustrate the uniformity of the diffraction intensity distribution among all the spots as well as the high diffraction efficiency of the grating. Moreover, the results for the 6-by-6 rhombus diffraction pattern captured with two diagonals aligned with the camera are presented in Figure 3.20(f). The corresponding simulation results using the designed pattern where the 2D pattern was generated by XOR-ing two 1D gratings with one of them being rotated by 30°, instead of 90°, are shown in the insets. The rhombus pattern results clearly illustrate the uniformity of the diffraction intensity distribution with irregular pattern design as well as the high diffraction efficiency of the spot generation. The results demonstrate that the fabricated bi-element grating configuration can switch readily between the two gratings by changing the voltage amplitude.

The square array of diffraction spots is distributed as designed with a uniform intensity distribution when the target voltage $V_A = 3.38\ V_{rms}$ was applied to the cell and completely changed to a rhombus pattern when a different voltage $V_B = 5.96\ V_{rms}$ was applied. The pattern designed to generate a 6-by-6 rhombus pattern in the far field consisted of more quantized errors due to discrepancies between the theoretical transition points and the real fabricated pixels, which are caused by the non-90° rotation of the grating during the pattern design process. These discrepancies, along with fabrication errors, result in as much as a 20% deviation in the intensity across the elements in the far field diffraction pattern. This non-uniformity in the intensity can be reduced through further refinements to the fabrication and design process.

When the voltage applied was neither 3.38 V_{rms} nor 5.96 V_{rms}, which are the designed replay voltages in this case, the diffraction pattern will no longer be either a uniform 6-by-6 square beamlet array or a uniform 6-by-6 rhombus beamlet array. Instead, the zeroth order spot dominates in the replay field with two lower intensity and overlapping square and rhombus beamlet arrays.

3.6.2 Analysis and Discussion

(i) Diffraction Efficiency

When the designed voltages were applied to the device, the diffraction efficiency, which is defined as the ratio between the summation of the intensity of all diffraction spots and the non-diffracted initial laser spot, can reach approximately 40%. The diffraction efficiency of the bi-element grating is lower than that of the single element grating and is believed to be due to the thicker LC layer as well as the presence of the other Dammann grating, which is not perfectly deactivated giving rise to more light scattering and loss. In order to improve the uniformity of the intensity in the diffraction pattern for interchangeable gratings, a more accurate fabrication process will be needed so as to handle the irregular pattern edges. In addition, a more sophisticated pattern would be required to compensate the quantisation errors that are introduced when interpreting the transition point values into achievable grating designs.

(ii) Response Times

As the response time is known to be proportional to the square of the device thickness[197], it is therefore reasonable that the 20 μm device exhibits a longer response time compared with that observed for the 5 μm device. Furthermore, because only two thin layers of LC close to the substrates have been polymerised by the laser writing process, there is still a large bulk of the LC that is free of a polymer network in the middle of the cell. This is unlike the situation in

the 5 μm cell, where the polymerised network extended throughout the entire thickness of the LC layer. Thus, the two types of regions (polymerised and unpolymerised) for the bi-element device have a similar response time.

(iii) Fabrication Quality Analysis

To analyse the fabrication quality in more detail, the cross-sections of one grating period of the square pattern were extracted from the microscope image and are summarized in **Table 3.2**. The normalised greyscale of the images were binarised at a threshold defined as the middle region between the maximum and minimum values. The actual transition points were then derived from these binarised values. Comparing the actual transition points derived from the cross-section with the deigned transition points, it was found that the fabrication led to a deviation in the transition points of less than 2% in accordance with that observed for the single element grating. In this case, the rise and fall response times recorded for the switchable pattern were found to be of the order of 120 ms and 900 ms, respectively, which did not vary significantly from the response times recorded from the unpolymerised regions in the same device.

Table 3.2: Comparison between designed transition points and actual fabricated transition points for the 6-by-6 patterns.

Transition points	ξ_1	ξ_2	ξ_3	ξ_4	ξ_5
Designed values	0.11444	0.20897	0.50000	0.61444	0.70897
Switchable Pattern	0.10256	0.21927	0.50398	0.59863	0.71264
Interchangeable Pattern—Square	0.09328	0.21016	0.49859	0.59520	0.71227
Interchangeable Pattern—Rhombus	0.09180	0.21093	0.49965	0.59425	0.71268

3.7 Summary

In conclusion, this chapter has demonstrated both single and bi-element LC Dammann gratings that can be switched on/off and between different gratings, respectively. For the latter case, these two different gratings give rise to different patterns in the replay field with the application of a voltage. A series of simulations have been carried out to verify the design of

the Dammann grating, predict the far-field diffraction pattern and determine the fabrication parameters required to achieve high quality gratings with good intensity uniformity across the elements in the array. These simulation results were first verified experimentally with the use of a spatial light modulator. A single element switchable grating was then fabricated and characterised to prove that the parameters derived from the simulations were suitable for fabrication. It is also demonstrated that the single element switchable grating can function across a range of wavelengths by simply varying the voltage to always ensure a phase difference of π between the laser written and non-laser written regions of the grating. Following this, a more sophisticated bi-element grating structure was designed and fabricated in an LC layer whereby the far-field pattern switches between a square array and a rhombus array with the application of a voltage. Compared to SLMs, these laser-written LC gratings offer several advantages, including faster switching speeds and higher optical efficiency due to reduced pixelation losses. They also provide a simpler and more compact structure, which can lower fabrication complexity and cost when integrating into other systems. However, SLMs retain greater flexibility for dynamic pattern generation and finer phase control due to their pixelated nature. The demonstrated high fabrication quality and reliable switching performance of LC Dammann gratings underscore their potential for applications in optical communications, optical computing, and laser beam shaping.

When God said, 'Let there be light,' he surely must have meant perfectly coherent light.

— Charles Hard Townes

CHAPTER 4

Laser Written Liquid Crystal Computer Generated Holograms

4.1 Design and Generation of Computer Generated Holograms

4.1.1 Introduction

Interference patterns with simple periodical structures like Dammann gratings fabricated using direct laser writing have been thoroughly demonstrated in Chapter 3. Now this concept is extended to the complex computer-generated holograms (CGHs) laser-written in liquid crystals (LCs). Holography is an advanced technique for creating 3D images by reconstructing wavefronts. This process involves superimposing an object wave and a reference wave to generate an interference pattern, which is then recorded on a photosensitive medium to produce a hologram[200]. CGHs extend this concept by calculating the interference pattern using computational methods and recording it in a film[201]. This computational approach enables the creation of 3D images of virtual objects stored digitally, facilitating more complex and dynamic visual representations[202]. When displayed on spatial light modulators (SLMs), CGHs can produce dynamic 3D images, adding a new dimension to visual displays. This technology has significant implications for enhancing visual experiences in fields such as entertainment, medical imaging, and scientific visualisation[203].

CGHs are designed using sophisticated algorithms that generate specific phase profiles to diffract light into desired patterns. This computational approach allows for precise control over light, enabling the production of high-resolution images and complex light field distributions[201]. The creation of a CGH involves calculating the interference pattern produced by a virtual object and encoding this pattern onto a substrate using techniques such as lithography or direct-write methods[204]. These processes involve intricate steps where the phase and amplitude of the light waves are meticulously controlled to achieve the desired holographic effect[205]. These holograms are versatile and capable of generating 3D images and dynamic light modulation, making them highly valuable for various applications, including virtual reality, augmented reality, and advanced microscopy[206].

The computational aspect of CGHs allows for the precise modulation of both amplitude and phase distributions of the object wave into the intensity distribution of the interference pattern[207]. This method offers significant advantages over traditional optical holography, including the ability to directly control the shape of the wavefront and optimise phase distribution to reduce image degradation[208]. Using algorithms, such as the Gerchberg-Saxton (GS) algorithm, CGHs can iteratively adjust the phase to minimise errors in the reconstructed image[203]. The GS algorithm, in particular, is efficient in optimising phase-only holograms by iteratively transforming the hologram between the real space and frequency domain to refine the phase profile[209]. This optimisation process is crucial for achieving high-quality holographic images with minimal artefacts.

In recent years, phase-only CGHs have become prominent due to their high light efficiency and ability to produce bright, high-quality reconstructed images. These holograms modulate only the phase distribution of the reconstruction wave, which can be optimised to enhance image clarity and reduce artefacts[210]. The phase-only modulation minimises the loss of light

intensity, making these holograms particularly efficient and suitable for applications requiring high brightness and contrast[211]. This capability has expanded the use of CGHs in various fields, including optical tweezers, which use focused laser beams to manipulate microscopic particles; optical interconnections, which enable high-speed data transfer between electronic components; and optogenetic techniques, which involve controlling biological processes with light[203,212,213].

CGHs can be fabricated using various techniques. One common method involves electron-beam lithography, which allows for precise patterning at the nanoscale to create the fine structures required for CGHs[214]. In this process, a focused electron beam writes the holographic pattern onto an electron-sensitive resist, which is then developed and etched onto the substrate. This method enables the creation of complex holographic elements with high precision and fidelity[215]. Additionally, laser writing techniques can be employed to fabricate CGHs by ablating material from a surface to form the desired holographic structures[216]. These methods offer flexibility in creating both binary and greyscale holograms, which are essential for optical applications, including beam shaping and optical trapping[217].

Moreover, the use of two-photon polymerisation direct laser writing (TPP-DLW) has advanced the fabrication of 3D structures in LC materials[218]. This technique involves the two-photon absorption process, where a femtosecond laser, focused through a high numerical aperture objective lens, induces polymerisation at the centre of the focus, creating a small volume called a voxel[219]. By translating the laser focus relative to the sample, 3D polymer network structures can be constructed voxel-by-voxel, allowing for micrometer-sized features formed in LCs[27]. This high-resolution capability is crucial for developing advanced optical components.

With the appropriate use of photoresist materials and laser pulse energies, it is possible to fabricate intricate microstructures in transparent polymer photoresists[220]. A polymerisable LC resist has been demonstrated to allow structure control by applying different electric fields

to change the director orientation during fabrication[15,95]. The variable birefringence and sensitivity to external electric fields makes LCs suitable for use as switchable optical materials in SLMs and single-pixel switchable diffractive optical elements (DOEs)[194,195]. This technological advancement has broadened the scope and efficiency of applications utilising CGHs.

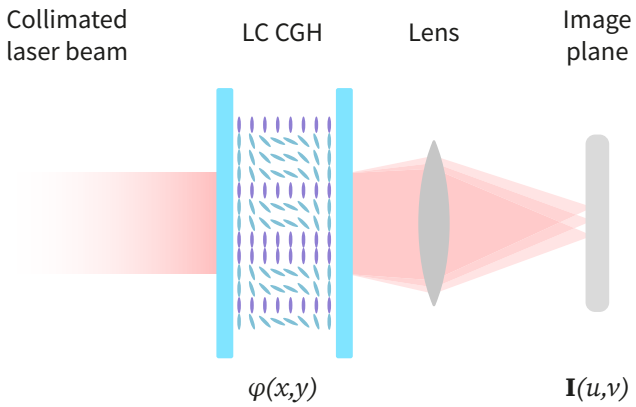

Figure 4.1: Schematic diagram of an LC device with a computer-generated holography (CGH) A collimated laser beam passes through the LC-based CGH, which modulates the phase profile $\varphi(x, y)$. The modulated light is then focused by a lens onto the image plane, where the desired intensity pattern $\mathbf{I}(u, v)$ is formed. This configuration illustrates the process of converting a collimated laser beam into a specific image through the designed CGH pattern.

In this chapter, we begin by demonstrating the method of generating CGHs and testing the generated CGH patterns on a SLM to validate their functionality. The concept of fabricating complex DOEs, such as CGHs, in LC is illustrated in **Figure 4.1**. Following this initial evaluation, a single-element switchable CGH is fabricated for the first time using TPP-DLW in a polymerisable liquid crystal resist, which can transition between visible and invisible states under different applied voltages. Building on these results, we proceed to fabricate more complex multi-layer structures of electrically switchable CGHs, which are capable of transitioning between two distinct diffraction modes under different applied voltages. These advancements pave the way for the development of highly versatile and reconfigurable optical devices in LC devices.

4.1.2 Design of Computer Generated Holograms

The method for generating CGHs can be categorized into global optimisation methods and iterative design methods[221,222]. Among these, the Gerchberg-Saxton (GS) algorithm stands out as a widely utilised iterative method for phase retrieval and optimisation in computer-generated holography. Initially developed for single-plane holographic reconstruction[223,224], the GS algorithm has evolved to find application in various fields such as optical tweezers, beam shaping, and holographic displays. The algorithm retrieves the phase profile using a Fast Fourier Transform (FFT), which ensures high computational efficiency[225]. Its primary function is to generate phase-only holograms by successively transforming between the real space and frequency domain, guided by the input and output targets as constraint conditions. In this process, the input plane constrains the CGH to be a pure-phase element, ensuring the phase-only nature of the hologram. Meanwhile, the output target ensures that the intensity of the output pattern matches the desired target, although the phase of the output is not considered in this constraint. The algorithm iterates until the diffraction pattern of the CGH are close to the output target, typically after numerous iterations that refine the accuracy and fidelity of the hologram.

The process begins by creating a complex field from the amplitude of the incident source light $\mathbf{i}_{\text{source}}$, paired with an initial guess for the phase φ_0, which can be either random or uniform. Thus, the initial incident field can be mathematically expressed as

$$h = h_0 = \mathbf{i}_{\text{source}} \cdot e^{i\varphi_0}. \tag{4.1}$$

Applying the FFT to this incident field h yields the propagation outcome H on the image plane, expressed as

$$H = \mathcal{F}(h) = \mathbf{I}_{\text{out}} \cdot e^{i\Phi} \tag{4.2}$$

where $\mathcal{F}$ represents the FFT, Φ is the output phase and $\mathbf{I}_{\text{out}}$ corresponds to the intensity profile that forms in the Fourier plane. For each point in $\mathbf{I}_{\text{out}}$, the difference from the corresponding point on the target intensity profile $\mathbf{I}_{\text{target}}$ is calculated and defined as the error ε

$$\varepsilon = \mathbf{I}_{\text{out}}(u, v) - \mathbf{I}_{\text{target}}(u, v) \tag{4.3}$$

where u and v are the indices for each points in the intensity profile.

An evaluation metric E, defined as the root-mean-square value of the error ε, is employed during the iteration process. It is expressed as

$$\begin{aligned} E &= \sqrt{\frac{\sum_{u,v} \varepsilon^2}{N}} \\ &= \sqrt{\frac{\sum_{u,v} \left[\mathbf{I}_{\text{out}}(u, v) - \mathbf{I}_{\text{target}}(u, v)\right]^2}{N}} \end{aligned} \tag{4.4}$$

where N is the total number of pixels in the Fourier plane. If E exceeds a certain threshold, indicating that the output pattern $\mathbf{I}_{\text{out}}$ does not yet sufficiently match the target, the target intensity pattern $\mathbf{I}_{\text{target}}$ replaces the output intensity pattern while retaining the phase pattern Φ. This adjustment forms a new pattern H' as

$$H' = \mathbf{I}_{\text{target}} \cdot e^{i\Phi}. \tag{4.5}$$

Then, by taking the inverse fast Fourier transform (IFFT) of the new pattern H' , the phase-only pattern φ can be derived from the outcome h' as

$$h' = \mathcal{F}^{-1}(H') = i_{in} \cdot e^{i\varphi}. \tag{4.6}$$

Since the light source remains unchanged during the experiment, the intensity profile $\mathbf{i}_{in}$ in

the outcome from IFFT will be replaced with $\mathbf{i}_{\text{source}}$. Meanwhile, to maximise the compatibility of the generated phase-only pattern with various fabrication techniques such as lithography or direct laser writing, the pattern φ is binarised into either 0 and 2π as $\mathcal{B}(\varphi)$. Thus the incident field h for the next iteration is represented as

$$h = \mathbf{i}_{\text{source}} \cdot e^{i\mathcal{B}(\varphi)}. \tag{4.7}$$

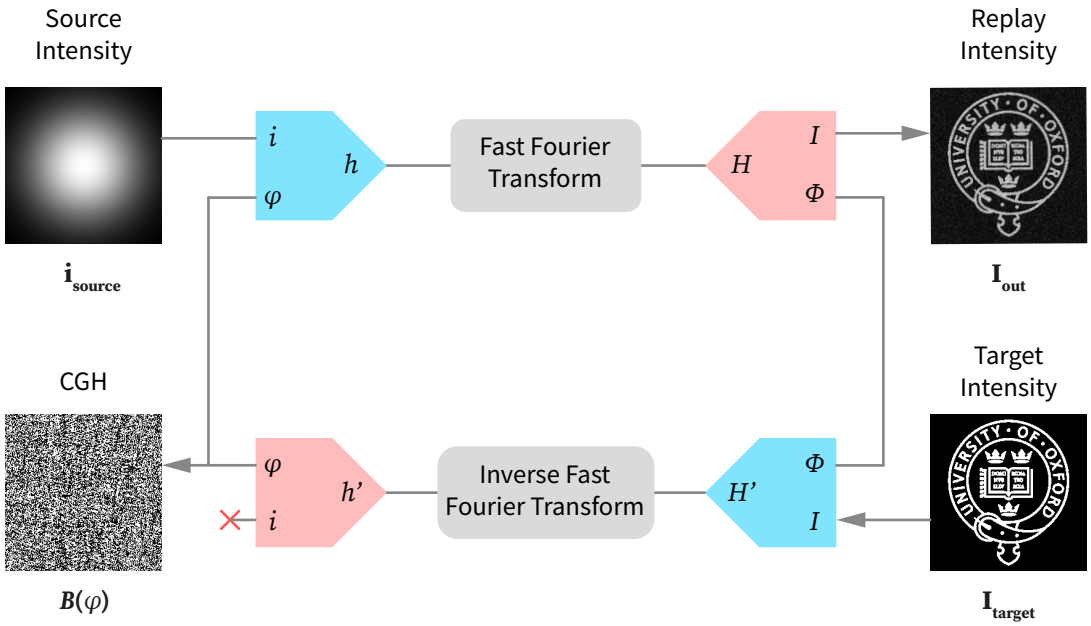

Figure 4.2: Diagram of the Gerchberg-Saxton (GS) algorithm for computer-generated holography. The process begins with an incident light source $\mathbf{i}_{\text{source}}$ and an initial phase guess φ. The complex field h is formed and subjected to a FFT to produce the field H at the image plane with intensity $\mathbf{I}_{\text{out}}$ and phase Φ. The output intensity is compared to the target intensity $\mathbf{I}_{\text{target}}$. If discrepancies exist, the target intensity replaces the output intensity while retaining the phase, forming a new field H'. This new field undergoes an IFFT to yield the updated complex field h'. The phase is binarised $\mathcal{B}(\varphi)$ to maintain phase-only modulation, and the updated complex field is used for the next iteration. The process continues iteratively until the output intensity matches the target intensity closely, minimising the error.

Following these iterative steps from Equation 4.1 to Equation 4.7, the binarised phase-only pattern $\mathcal{B}(\varphi)$ is derived when the evaluation metric E falls below the threshold value, signalling that the generated hologram sufficiently matches the desired target intensity profile. An illustration of the algorithm flow is displayed in **Figure 4.2**.

4.1.3 Generation of Phase-Only Patterns

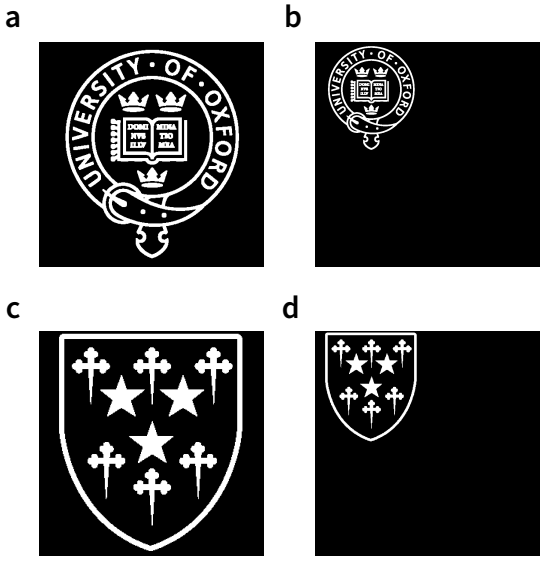

Figure 4.3: Images used for CGH pattern generation. (a) and (c) shows the target images of the University of Oxford crest and Somerville College, respectively. (b) and (d) shows the re-positioned images for CGH pattern generation. Each image was adjusted to 128 pixels by 128 pixels and positioned in the upper left corner of a 256 pixels by 256 pixels black background to avoid overlap with the 0-th order spot during the holographic reconstruction process.

The target images for the CGHs consisted of the Oxford University logo and the Somerville College crest, chosen for their distinct and recognisable designs. These images initially were both resized to 128 pixels by 128 pixels to maintain clarity and detail. Subsequently, they were positioned in the upper left corner of a black background measuring 256 pixels by 256 pixels. This specific placement was strategically selected to prevent the replay images from overlapping with the strong 0-th order spot, a common issue that can cause significant interference and reduce the quality of the holographic reconstruction. The original images as well as the image for pattern generation are demonstrated in **Figure 4.3**.

Once the images were prepared, they were processed using the GS algorithm introduced in Section 4.1.2 as $\mathbf{I}_{\text{target}}$, which generated a binarised 256 pixels by 256 pixels phase image. Then a crucial step is to convert the continuous phase values into fabrication parameters that

are suitable for the DLW system. The binarisation ensures that the resulting hologram can be accurately fabricated using the available laser technology. The resulting binary pattern for both images are presented in **Figure 4.4**.

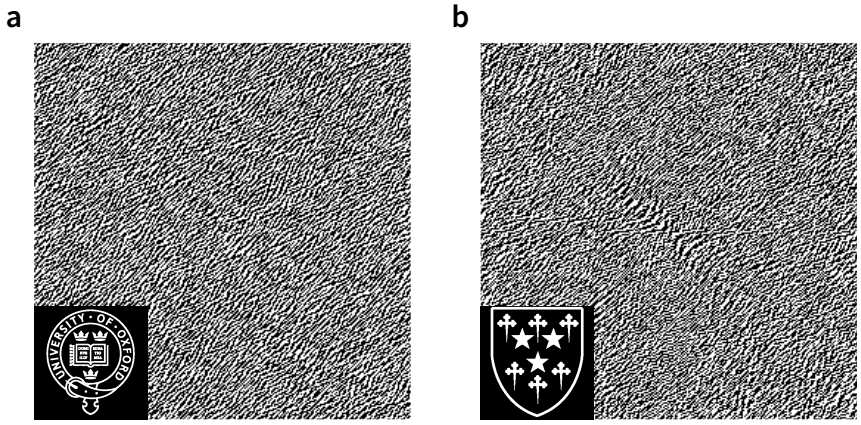

Figure 4.4: The resulting binary CGH patterns for the target images. The left image represents the binary CGH pattern for the crest of the University of Oxford, while the right image represents the binary CGH pattern for the crest of Somerville College. These patterns were generated using the GS algorithm and binarised for fabrication using the Direct Laser Writing (DLW) system. Both of them have the pattern size of 256 pixels by 256 pixels. The target intensity outcome is attached as the inset image of the pattern.

In the DLW system, careful attention was paid to the fabrication parameters. The target hologram pattern was designed to cover an area of 1024 μm by 1024 μm in the LC device, with each individual pixel of the hologram occupying an area of 4 μm by 4 μm. This area size was chosen to be multiples of the laser voxel size (approximately 1 μm by 1 μm) to simplify fabrication while maintaining high diffraction efficiency and minimising artefacts from pixelation. The hologram pattern was designed to be fabricated within an LC glass cell using the TPP-DLW technique introduced in Section 2.2. For the devices with a single CGH, the thickness of the LC layer was 5 μm. While for the device with multiple CGHs, an LC layer with a thickness of 20 μm was selected to provide sufficient space for fabrication with minimal cross-talk between the laser-written structures. These specific thicknesses were chosen to optimise the interaction between the laser-written hologram and the LC, ensuring that the phase modulation

properties of the hologram were effectively utilised.

4.1.4 Testing with an SLM Imaging System

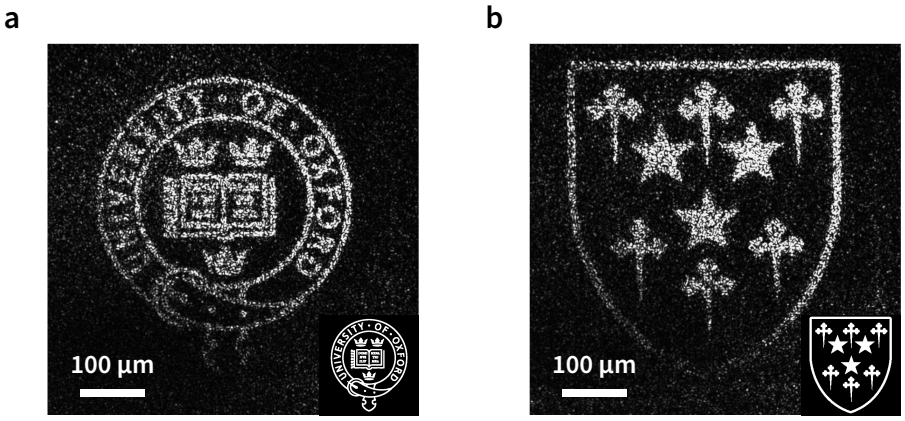

Figure 4.5: Holographic reconstruction results using an SLM imaging system. The left image shows the reconstructed image in the replay field of the University of Oxford crest, and the right image shows the reconstructed image of the Somerville College crest. These reconstructions were achieved using an SLM imaging system, demonstrating the accuracy and fidelity of the CGH patterns generated through the Gerchberg-Saxton algorithm. The insets in the lower right corners of each image display the original target crests for reference.

Before writing the CGHs directly into the LC devices, the CGHs were characterised experimentally using a SLM. The SLM imaging system used for testing the hologram was identical to the one used for the Dammann grating in Figure 3.7 in Section 3.2.2. **Figure 4.5** illustrate the CGH pattern and the test results of the corresponding replay image, respectively. The initial test results indicate that the designed CGH patterns create the desired intensity pattern in the replay field as intended.

4.2 A Laser Written Switchable Computer Generated Hologram

4.2.1 Experiment Results

In this study, we employed the same polymerisable nematic liquid crystal (LC) mixture (IR819-RM257-E7) as used in Section 3.5.1. This mixture was capillary-filled into a glass cell equipped with anti-parallel rubbed polyimide alignment layers, indium tin oxide (ITO) electrodes, and

a cell gap of 20 μm. The experimental results for a single-layer pattern inscribed into the polymerisable nematic LC with the observations under polarised optical microscope (POM) and in the replay field are illustrated in **Figure 4.6**.

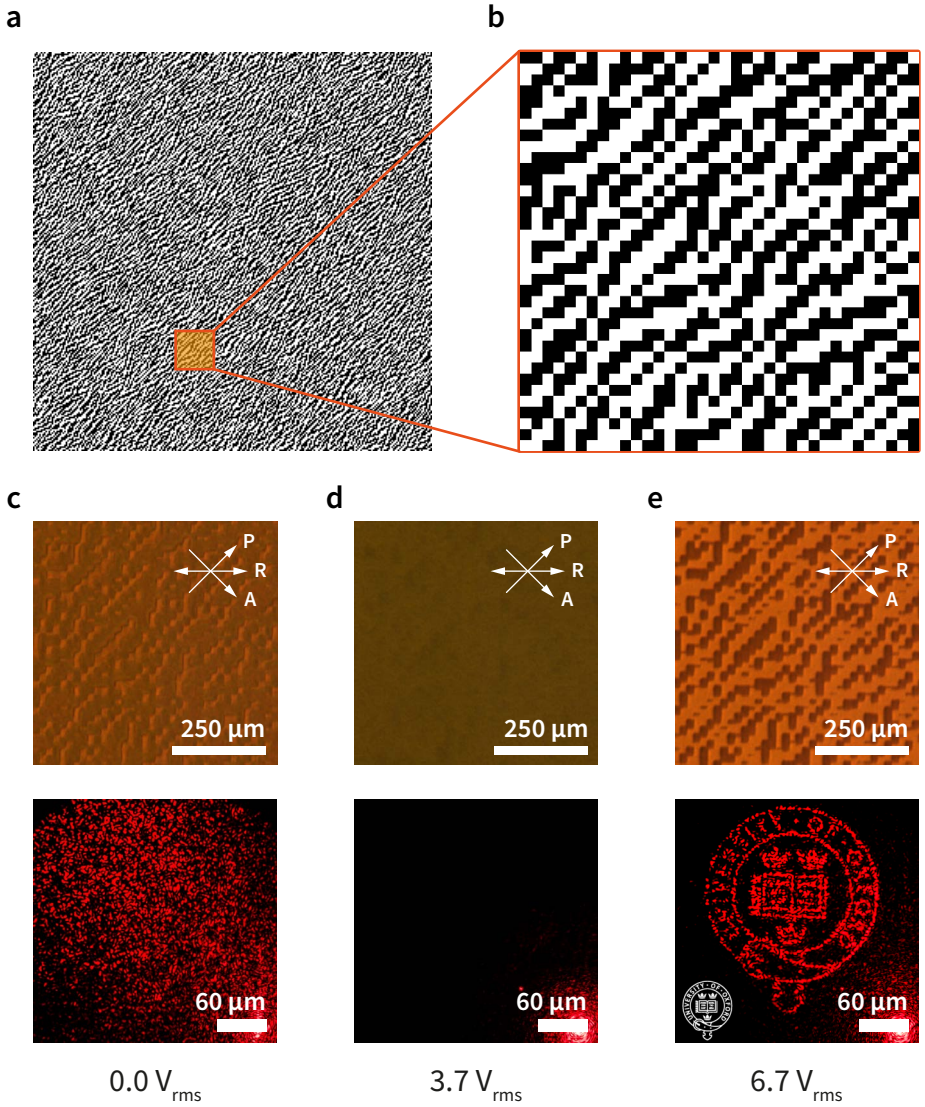

Figure 4.6: Fabrication and replay results of a switchable laser written CGH. (a) The designed hologram with an enlarged region highlighted for comparison. **(b)** Enlarged region of the hologram pattern for comparison with POM images after fabrication. **(c)** POM image of the fabricated CGH with the corresponding replay field image at a voltage $V = 0.0\,\mathrm{V_{rms}}$, where some features of the pattern can be distinguished but no meaningful images are formed in the replay field. **(d)** POM image of the fabricated CGH with the corresponding replay field image at the voltage $V = 3.7\,\mathrm{V_{rms}}$, showing uniformity in the director field with barely visible features and no significant diffraction in the replay field. **(e)** POM image of the fabricated CGH with the corresponding replay field image at a voltage $V = 6.7\,\mathrm{V_{rms}}$, where a clear POM image of the fabricated pattern and replay image of the University logo can be observed, confirming successful pattern fabrication and functionality.

The CGH dimensions were configured to 256 by 256 pixels, with each pixel consisting of 4-by-4 1 μm laser-written spots, resulting in a CGH pattern size of 1024 μm by 1024 μm. This setup is consistent with the configuration used for testing with the SLM. The CGH pattern was fabricated at a specific voltage ($V_{\text{fabrication}} = 3.7\,\text{V}_{\text{rms}}$), and the target image emerged in the replay field when an optimal voltage ($V_{\text{replay}} = 6.7\,\text{V}_{\text{rms}}$) was subsequently applied. The voltages applied for the fabrication is based on the transmission-voltage curve for the 20 μm LC layer in Figure 2.7(c) and a phase difference of π can be achieved between the locked-in voltages.

Figure 4.6(a) and (b) show the designed hologram pattern and an enlarged region, intended for comparative analysis with the fabricated results. Polarising optical microscope (POM) images of the laser-written pattern and their corresponding replay field images for three different applied voltages are displayed in Figure 4.6(c) to (e). At an applied voltage of $V = 3.7\,\text{V}_{\text{rms}}$, the features of the pattern are barely discernible, attributed to the uniformity in the director field. This occurs because the laser writing process locks the alignment at the same voltage within the regions defining the CGH pattern, as evidenced in Figure 4.6(d).

When the device is observed without an applied electric field $V = 0.0\,\text{V}_{\text{rms}}$, the LC director in the non-polymerised regions align with the substrate surface direction, while the polymerised regions retain their original orientation fixed by the laser writing process. This alignment difference results in the partial visibility of some structural features in the POM image due to the refractive index mismatch between polymerised and non-polymerised regions. The corresponding replay image at this voltage, however, does not result in a clear image of the University crest, as shown in Figure 4.6(c).

To activate the CGH and obtain an image, a replay voltage of $V_{\text{Replay}} = 6.7\,\text{V}_{\text{rms}}$ was applied, which leads to a π phase difference at a wavelength of 630 nm in selected regions of the LC device. It can be seen that a clear CGH appears in the LC device (as is evident from

the POM image in Figure 4.6(e)). This voltage was selected based on the transmission-voltage curve measured for the sample shown in Figure 2.7(b). It can also be seen in Figure 4.6(e) that the fabrication has been successful by comparing the fabricated pattern in the LC cell with the design pattern (shown in Figure 4.6(b)). The director locked-in at $V_{\text{fabrication}} = 3.7\,\text{V}_{\text{rms}}$ remains unchanged while the director in the non-laser written regions are reoriented by the replay voltage $V_{\text{Replay}} = 6.7\,\text{V}_{\text{rms}}$ to create a different phase profile. This confirms the successful fabrication and operational integrity of the CGH pattern under the specified optimal conditions, which demonstrates that the intensity is distributed as designed on the image plane.

The results show that the fabricated single layer CGH element can readily switch between the on and off states with different voltages applied. The results also show that the diffraction patterns are distributed with a relatively uniform intensity distribution when the CGH is activated and then completely disappear when the CGH is deactivated.

To demonstrate the change in replay field images with varying applied voltages, a sequence of images was captured as the voltage across the fabricated device was incrementally adjusted from $V = 0.0\,\text{V}_{\text{rms}}$ to $V = 10.0\,\text{V}_{\text{rms}}$. **Figure 4.7** illustrates the evolution of these replay field images, transitioning from a random speckled diffraction pattern to the clear University logo. Initially, at lower voltages, the replay field images exhibit significant speckle-like noise and lack clear definition of an image. As the voltage increases, this noise diminishes as the LC in both non-polymerised and polymerised regions are uniformly aligned. The speckle noise disappears completely at $V = 3.7\,\text{V}_{\text{rms}}$ by calculating the contrast and mean values of the images. At the optimal voltage of $V = 6.7\,\text{V}_{\text{rms}}$, the University logo becomes fully discernible with high contrast and minimal noise, indicating effective modulation of the LC alignment and successful creation of the desired image. However, as the voltage continues to increase, the image contrast slightly decreases, introducing some noise into the results. This sequence underscores the critical

role of precise voltage control in achieving clear and accurate holographic image reconstruction in polymerisable nematic LCs.

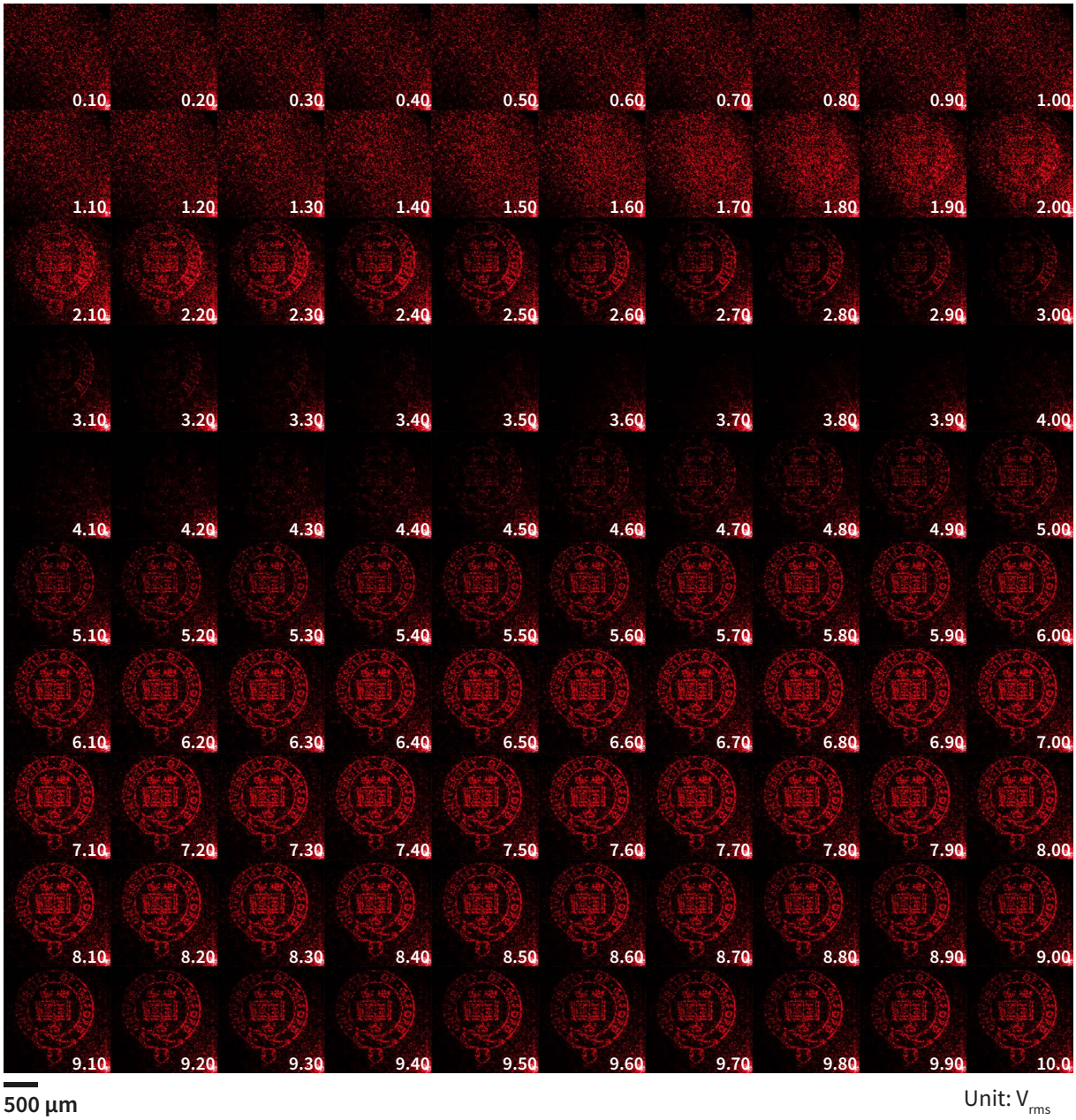

Figure 4.7: Evolution of the replay field images with varying applied voltages. The sequence of images demonstrates the transition from a random speckled pattern to the clear depiction of the University logo as the voltage increases from $V = 0.0\,\mathrm{V_{rms}}$ to $V = 10.0\,\mathrm{V_{rms}}$. Initially, no clear image is observed at lower voltages. As the voltage increases, the speckle-like noise in the images reduce before disappearing completely at $V = 3.7\,\mathrm{V_{rms}}$. The optimal voltage of $V = 6.7\,\mathrm{V_{rms}}$ results in a fully discernible University logo with high contrast and minimal noise.

4.2.2 Response Times

The switching time, or response time, is a crucial parameter for CGH fabricated in LC devices. In this experiment, LC devices with thicknesses of 5 μm and 20 μm were fabricated with the same CGH pattern using the same fabrication parameters to examine their response times. The response time of the switchable CGH is defined as the duration required for the device to transition between its on state (showing designed pattern) and off states (showing no pattern). This is specifically measured by the rise and fall times, which correspond to the intervals during which the CGH switches between two states when the applied voltage is altered. To determine the response time, the intensity of the output field pattern generated by the CGH is measured using a photo diode. This is done while the CGH is illuminated by a 633 nm laser. The measured intensities for both the on and off states are then compared against the intensity of the original illumination source to obtain the normalised intensity.

For a single-layer switchable CGH, the stable states occur when no image is displayed on the replay field ($V = 1.7\,\mathrm{V_{rms}}$ for the 5 μm device and $V = 3.7\,\mathrm{V_{rms}}$ for the 20 μm device) and when a clear image is displayed ($V = 3.3\,\mathrm{V_{rms}}$ for the 5 μm device and $V = 6.7\,\mathrm{V_{rms}}$ for the 20 μm device). The stability of these states is evaluated by their normalised total intensity. The device begins in one stable state, and a voltage drives it to the other state, resulting in a change in the total intensity, which then restabilises. The response time is defined as the total time taken for the device to reach a stable state after this change, with stability confirmed when the total intensity falls within ±5% of the target intensity.

The experimental results demonstrate distinct switching times for devices with different thicknesses, as shown in **Figure 4.8** and **Figure 4.9**. For the 5 μm device, the switching time from the off state (low voltage, no image) to the on state (high voltage, target image) is approximately 20 ms, which is defined as the rise time. Conversely, the transition from the on

state to the off state takes about 120 ms, which is defined as the fall time. In contrast, for the 20 μm device, the switching time from the off state to the on state is around 70 ms, while the transition from the on state to the off state takes about 430 ms. These measured switching times are consistent with the dynamics of the Fréedericksz transition and align with the shorter relaxation times observed in polymerised nematic LCs compared to non-polymerised regions, as reported in previous studies[197–199].

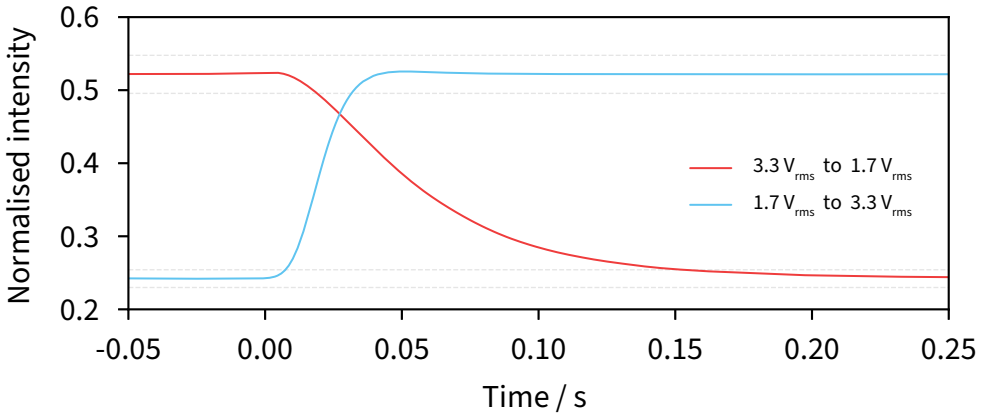

Figure 4.8: Response time measurement for a 5 μm LC CGH device. The graph shows the switching time from the off state ($V = 1.7\,\mathrm{V_{rms}}$, no image) to the on state ($V = 3.3\,\mathrm{V_{rms}}$, target image) is approximately 20 ms. The transition from the on state to the off state (red line) takes about 120 ms. These times are measured as the device transitions between the on state and the off state, with stability confirmed when the normalised total intensity falls within ±5% of the stable state intensity, which is marked as gray dashed lines for reference.

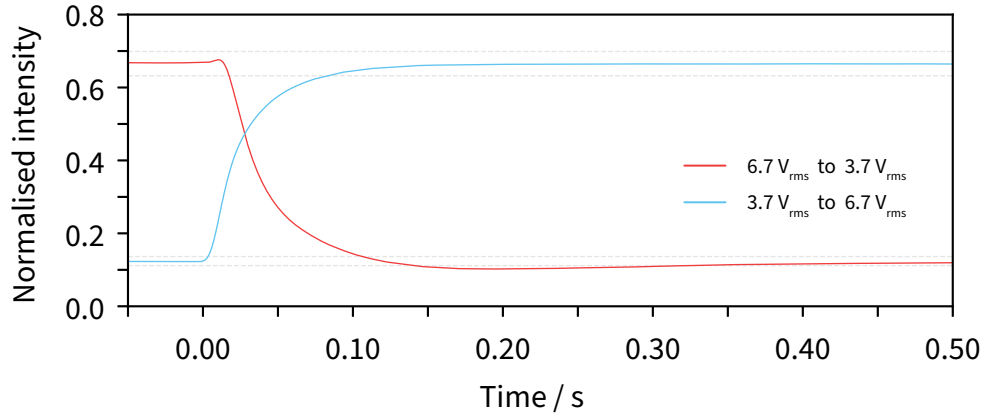

Figure 4.9: Response time measurement for a 20 μm LC CGH device. The graph shows the switching time from the off state ($V = 3.7\,\mathrm{V_{rms}}$, no image) to the on state ($V = 6.7\,\mathrm{V_{rms}}$, target image) is approximately 70 ms. The transition from the on state to the off state (red line) takes about 350 ms. These times are measured as the device transitions between the on state and the off state, with stability confirmed when the normalised total intensity falls within ±5% of the stable state intensity, which is marked as gray dashed lines for references.

The observed differences in response times can be attributed to the variation in device thickness and the change of the switching voltages, which impacts the electric field distribution and the orientations of the LC director. Thinner devices tend to have faster switching times due to the more efficient reorientation of LC director under an applied electric field. Additionally, the flow of LC molecules during reorientation influences both the response time and switching dynamics. The elastic properties and viscosity of the LC material govern the relaxation time, as the director reorientation is driven by the combined effects of the applied electric field and the internal elastic torque generated by the LC flow. These findings highlight the importance of optimising LC device parameters, such as the thickness of the LC layer, the polymerisation depth, and the LC materials, to achieve faster switching and improved optical performance for specific applications.

4.3 Interchangeable Computer Generated Holograms

The goal of this experiment is to demonstrate the feasibility of fabricating electrically switchable bilayer CGHs in an LC device and to evaluate their switching performance. The study aims to achieve rapid and high-contrast switching between distinct holographic images by selectively activating different CGH patterns through controlled voltage application. This involves fabricating two independent CGHs at different depths within the LC layer and leveraging the voltage-dependent birefringence of the LC medium to modulate the active pattern.

4.3.1 Experiment Results

The LC polymerisable mixture and fabrication technique employed in this study align with those outlined in Section 4.2. The operation parameters of the TPP-DLW system for fabricating electrically interchangeable bilayer CGHs remains consistent with the previous chapter, with the primary modification being the pattern change from Dammann gratings to CGHs. The

LC device comprises two separate CGH layers, each designed to produce distinct target images in the replay field. The CGH dimensions were configured to 256 by 256 pixels, with each pixel consisting of 4-by-4 1 μm laser-written spots, resulting in a precise CGH pattern size of 1024 μm by 1024 μm, as before. These CGHs are engineered to generate two distinct images: the crest of the University of Oxford and the crest of Somerville College.

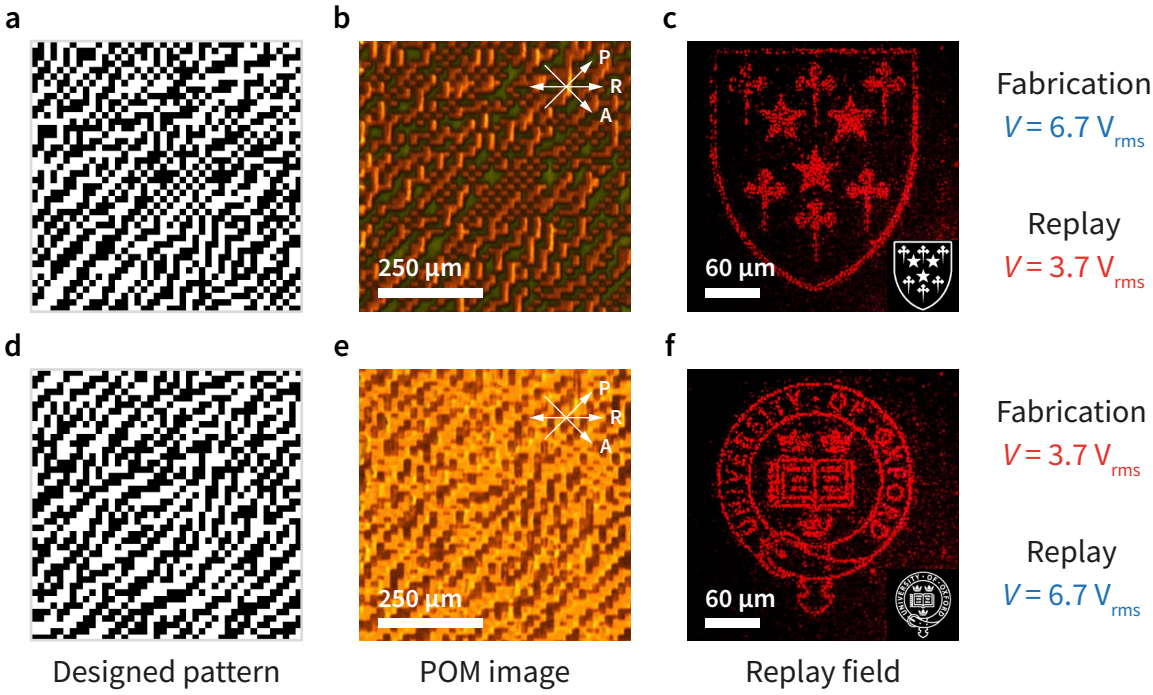

Figure 4.10: Fabrication and replay images of an interchangeable laser written CGH pattern. (a) and (d) show the cropped regions of the designed hologram patterns for the Somerville College crest and the University of Oxford crest, respectively. (b) and (e) display polarised optical microscope (POM) images of the corresponding laser-written pattern regions, indicating high fabrication quality consistent with the designs. The scale bars in the images represent the length of 60 μm. (c) and (f) illustrate the replay field images observed when the target voltages are applied, revealing clear and high-contrast images of the Somerville College crest and the University of Oxford crest, respectively.

Figure 4.10(a) and (d) illustrate the cropped regions of the designed CGHs for the two target images. These CGHs were fabricated in a 20 μm thick glass cell using DLW while driven with a 1 kHz square wave at different voltage amplitudes. According to the parameters used in Section 4.2.1, the fabrication process began by applying a voltage of $V_A = 3.7\,V_{rms}$ to the device. The CGH of the Oxford University logo was then fabricated, resulting in polymer formation on the substrate of the cell. Subsequently, the stage returns to the initial starting

point of the Oxford University hologram, and the focal point was shifted from the substrate to the superstrate. A voltage of $V_{\mathrm{B}} = 6.7\,\mathrm{V_{rms}}$ was then applied to fabricate the CGH of the Somerville College crest. All other regions of the cell remain unpolymerised and will vary with a change in the voltage. POM images of the corresponding laser-written pattern regions are displayed in Figure 4.10(b) and (e), showing the fabrication quality and similarity with the design specifications.

After fabrication, the CGH was placed in the replay field imaging system and illuminated with a collimated laser beam linearly polarised parallel to the rubbing direction of the LC mixture. This optical assembly ensures that the laser was fully modulated by the birefringence changes in the mixture as the voltage was varied. By placing a screen at a distance behind the illuminated sample, the far-field diffraction pattern generated by the hologram was captured.

During the replay of the diffraction pattern, different voltages were applied to obtain the corresponding images. When $V_{\mathrm{A}} = 3.7\,\mathrm{V_{rms}}$ was applied to the cell, there was no difference in the orientation of the LC director between the polymerised pixels of the CGH of the Oxford University logo (fabricated at V_{A}) and the non-polymerised regions, resulting in a uniform refractive index and phase profile. In contrast, the Somerville College crest on the superstrate at V_{A} exhibited polymerised pixels with the highest phase difference compared to the surrounding regions, creating a high contrast phase profile. Conversely, when $V_{\mathrm{B}} = 6.7\,\mathrm{V_{rms}}$ was applied, the CGH of the Somerville College crest on the superstrate results in a uniform refractive index and phase profile, while the Oxford University logo on the substrate exhibits the highest phase difference, thus generating an image of the Oxford University logo in the replay field.

Importantly, although the applied voltage affects the entire LC cell, the polymerised regions of each CGH retain their fixed orientation. This ensures that the applied voltage selectively activates the target CGH pattern without simultaneously influencing the other, as the polymerised

pixels maintain their refractive index and phase profile independently of the surrounding non-polymerised regions.

The results of the hologram patterns at the designed replay voltages are illustrated in Figure 4.10(c) and (f). The results unequivocally demonstrate that the fabricated bilayer structure can switch clearly and effectively between the two states. The Oxford University logo appears with high quality and clarity when the target voltage was applied to the cell, completely transforming to the Somerville College crest when a different voltage was applied. This capability highlights the potential of bilayer CGHs in dynamic optical applications, where rapid and reliable switching between distinct images is essential.

To illustrate the evolution of the replay field images with varying applied voltages, a sequence of images was captured as the voltage across the fabricated bilayer CGH device was incrementally adjusted from $V = 0.1\,\mathrm{V_{rms}}$ to $V = 10.0\,\mathrm{V_{rms}}$. **Figure 4.11** demonstrates the transition of these replay field images, starting from a random speckled diffraction pattern at zero voltage, migrating to the crest of Somerville College at lower voltages and then transitioning to the University of Oxford crest at higher voltages.

Initially, at low voltages, the replay field images display significant speckle-like noise and lack clear definition due to the entangled structure between the polymerised and unpolymerised regions from both of the designed patterns. As the voltage increases, the alignment of the LC director in both the polymerised and unpolymerised regions in the pattern fabricated at $V = 3.7\,\mathrm{V_{rms}}$ becomes more uniform, leaving the pattern fabricated at $V = 6.7\,\mathrm{V_{rms}}$ the dominate structure. At a voltage of approximately $V = 3.7\,\mathrm{V_{rms}}$, the noise diminishes completely, revealing a clear and high-contrast image of the Somerville College crest.

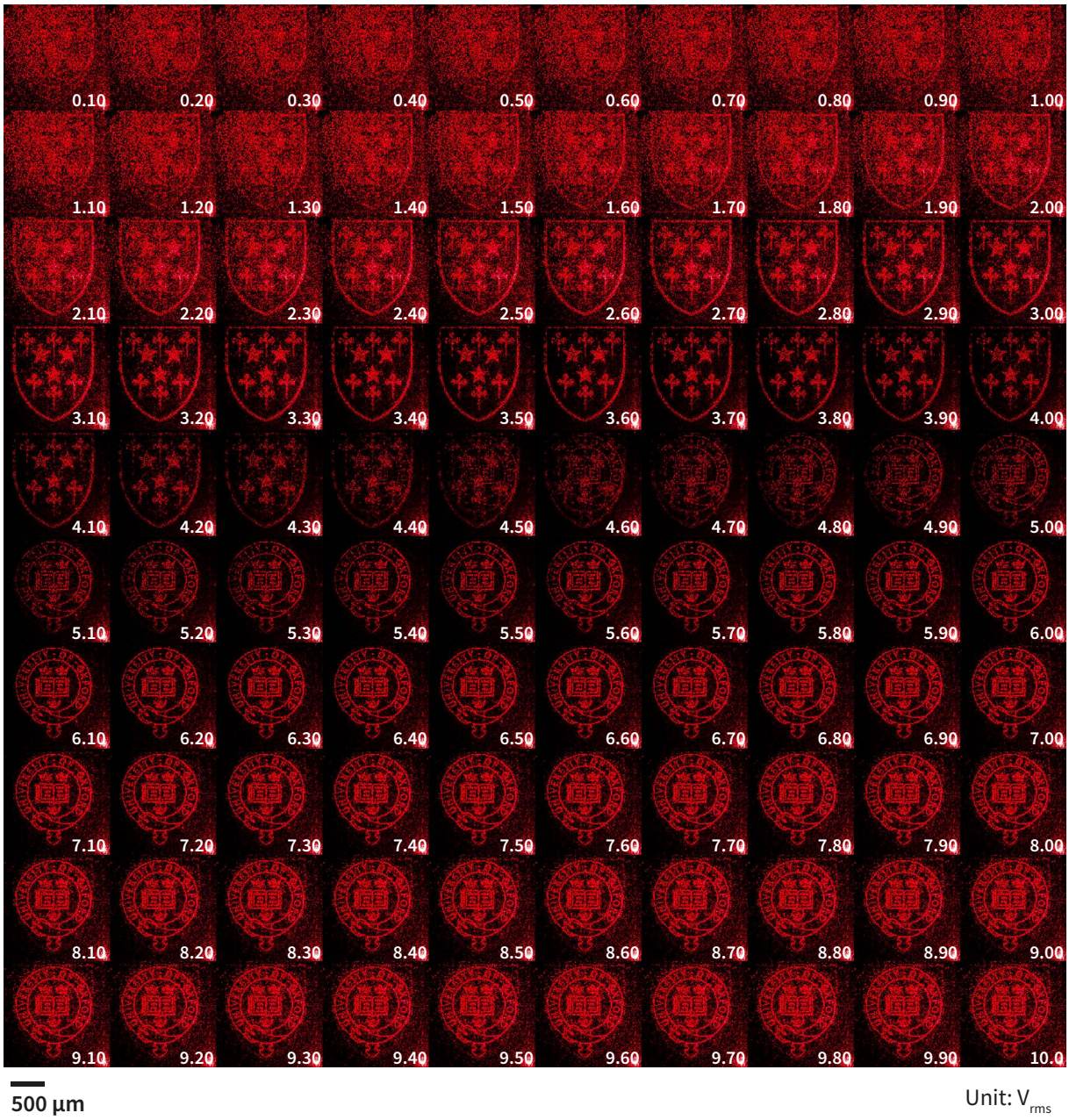

Figure 4.11: Evolution of replay field images for bilayer CGHs with varying applied voltages. The sequence of images demonstrates the transition from the Somerville College crest to the University of Oxford crest as the voltage is incrementally increased from $V = 0.1\,\mathrm{V_{rms}}$ to $V = 10.0\,\mathrm{V_{rms}}$. At low voltages, the replay field images show the Somerville College crest that is corrupted with noise. As the voltage increases, the noise diminishes, and the images become clearer. The optimal voltage for the Somerville College crest is approximately $V = 3.7\,\mathrm{V_{rms}}$, while the University of Oxford crest becomes fully discernible with high contrast at $V = 6.7\,\mathrm{V_{rms}}$. Further increases in voltage beyond the optimal levels slightly decrease image contrast and introduce some noise.

As the applied voltage is further increased, the image begins to change, and around $V = 6.7\,\mathrm{V_{rms}}$, the University of Oxford crest becomes fully discernible with high contrast and minimal noise. This voltage effectively modulates the LC alignment, successfully creating the desired

CGH. The figure captures the critical role of the precise voltage control in achieving clear and accurate holographic image reconstruction in polymerisable nematic LCs.

As the voltage continues to rise beyond the designed voltage levels for replay fields ($V = 3.7\,\mathrm{V_{rms}}$ and $V = 6.7\,\mathrm{V_{rms}}$), the image contrast slightly decreases, and some noise is reintroduced into the images. This sequence of images underscores the importance of optimising the applied voltage to balance between clarity and noise reduction in the replay field images. The ability to switch between distinct images with high fidelity highlights the potential of bilayer CGH devices in dynamic optical applications.

To demonstrate the structural changes in the fabricated bilayer CGH under POM with varying applied voltages, a sequence of images was captured as the voltage was incrementally adjusted from $V = 0.0\,\mathrm{V_{rms}}$ to $V = 10.0\,\mathrm{V_{rms}}$. **Figure 4.12** illustrates the evolution of these replay field images, transitioning from a random noisy pattern, via a clear representation of the Somerville college crest, to the University logo, showcasing how the fabricated CGH patterns appear and change under different voltages.

Initially, at low voltages, the POM images exhibit a superposition of patterns comprising the polymerised and non-polymerised regions. As the voltage increases, the LC director in the non-polymerised regions align so that the pattern formed matches that of one of the design patterns. The CGH pattern that corresponds to the Somerville College crest becomes fully revealed at $V = 3.7\,\mathrm{V_{rms}}$. As the voltage level reaches $V = 6.7\,\mathrm{V_{rms}}$, the University logo becomes fully discernible, in conjunction with the formation of the CGH that corresponds to the University logo. However, as the voltage continues to increase, the image contrast slightly decreases, introducing noise into the replay field images as the CGH formed in the LC layer deviates from the design pattern.

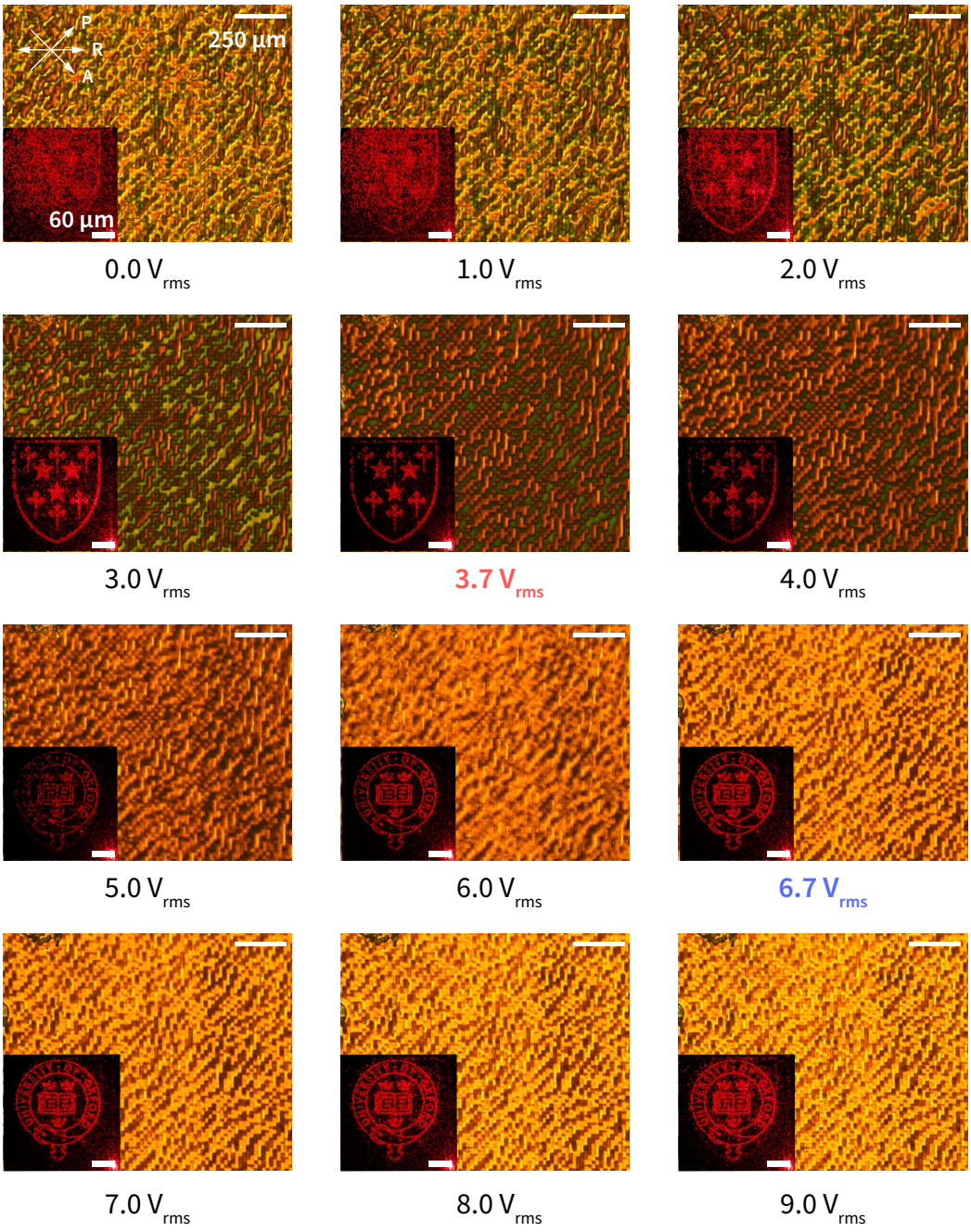

Figure 4.12: Evolution of POM images of bilayer interchangeable CGH in LC devices with varying applied voltages. The POM images were obtained at specific voltages ranging from $V = 0.0\,\mathrm{V_{rms}}$ to $V = 10.0\,\mathrm{V_{rms}}$, with the step of $V = 1.0\,\mathrm{V_{rms}}$ and two target voltages $V = 3.7\,\mathrm{V_{rms}}$ and $V = 6.7\,\mathrm{V_{rms}}$ for the designed patterns. Each sub-figure corresponds to a different voltage setting, demonstrating the impact of voltage variation on the CGH patterns produced by the bilayer when observed on a POM.

The POM images captured at various voltages clearly demonstrate the ability of the bilayer

CGH to switch between distinct images with high fidelity. At lower voltages, the Somerville College crest is prominently displayed, while at higher voltages, the University of Oxford crest emerges. The gradual transition observed in the images highlights the responsive nature of the LC alignment to the applied electric field. The uniformity and clarity of the images at specific voltages emphasise the importance of optimising voltage parameters for each targeted image.

4.3.2 Response Times

The bilayer interchangeable CGHs in LC devices with a thickness of 20 μm were fabricated to examine their response times. As outlined in Section 4.2.2, the response time is defined as the duration required for the switchable CGH to transition between its two states with clear patterns. The Somerville college crest is displayed in the replay field ($V = 3.7\,\mathrm{V_{rms}}$) and when the University of Oxford logo is displayed ($V = 6.7\,\mathrm{V_{rms}}$). Each of the patterns have a unique intensity level when the LC molecules stabilised after the corresponding voltage being applied. To monitor the change of the intensity level determine the response time, the intensity of the output field pattern generated by the CGH is measured using a photo diode. This is done while the CGH is illuminated by a 633 nm laser. The measured intensities levels are then compared against the intensity of the original illumination source to obtain the normalised intensity.

The device begins in one voltage to display one of the diffraction pattern, and another voltage is applied to drive the device to display another diffraction pattern, resulting in a change in the total intensity. The response time is defined as the total time taken for the device to display the new pattern after this change, with stability confirmed when the total intensity falls within ±5% of the intensity level of the target pattern.

The experimental results, as shown in **Figure 4.13**, demonstrate distinct switching times for the 20 μm device. The switching time from the Somerville college crest (low voltage,

$V = 3.7\,\mathrm{V_{rms}}$) to the University logo (high voltage, $V = 6.7\,\mathrm{V_{rms}}$) is approximately 50 ms. Conversely, the transition from the University logo to the Somerville college crest takes about 220 ms. Both switching times are significantly faster compared to the single-layer switchable CGH device in Section 4.2.2, Figure 4.9. This improvement arises from the increased thickness of the polymerised regions in the LC layer, which enhances the structural anchoring of the LC molecules and lowers the effective thickness of the non-polymerised region. This stronger anchoring reduces the extent of molecular reorientation required in the non-polymerised regions during switching, thereby lowering the activation energy and enabling a faster response under the same electric field when transitioning between two patterns.

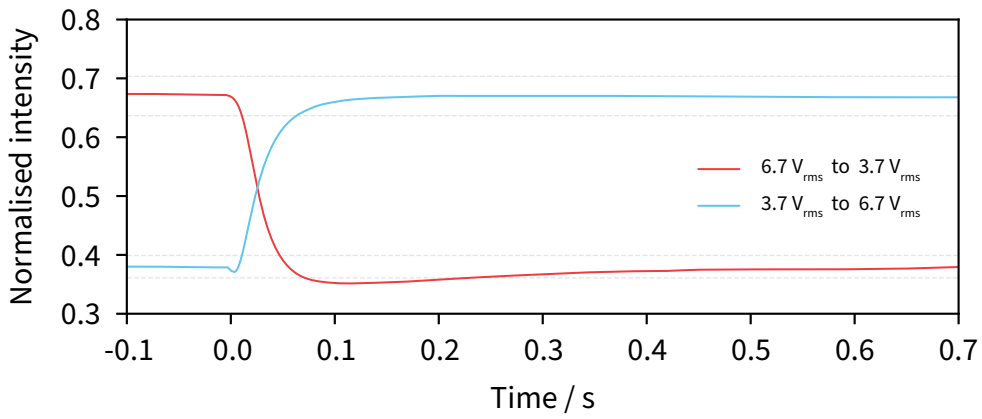

Figure 4.13: Response time measurement for an interchangeable LC CGH device. The graph illustrates the normalised total intensity changes for the transitions between showing the University logo and the Somerville college crest at applied voltages of $V = 3.7\,\mathrm{V_{rms}}$ and $V = 6.7\,\mathrm{V_{rms}}$. The red line represents the transition from the University logo to the Somerville college crest, with a response time of approximately 220 ms. The blue line depicts the transition from the Somerville College crest to the University logo, with a response time of around 50 ms.

4.4 Summary

This chapter focuses on the demonstration of laser-written LC CGHs, which represent a more sophisticated class of diffractive optical elements compared to the Dammann gratings presented in the previous chapter. This chapter has discussed the design and generation of laser-written LC CGHs. Before fabricating the LC CGHs, tests were carried out using a SLM to validate the

design. These tests ensure that the CGH pattern produces the desired intensity distribution in the replay field. The chapter details the process of generating and fabricating these phase-only patterns.

The study has explored the fabrication of single-layer and bilayer switchable CGHs using a polymerisable nematic LC mixture. The experimental results demonstrate the ability to switch between different holographic projected images by applying specific voltages. The single switchable CGHs were fabricated with a 20 μm thick LC cell, with the CGH pattern being written at one voltage and switched off at another. This capability allows for low-cost, compact dynamic holographic projection display elements. The response time was measured as the duration required for the CGH to transition between its on and off states. Experimental results indicate significantly different switching times for LC devices with thicknesses of 5 μm and 20 μm, where the 5 μm device exhibited a rise time of approximately 20 ms and a fall time of 120 ms, while the 20 μm device showed a rise time of around 70 ms and a fall time of 430 ms.

Building on the success of single-layer CGH fabrication, bilayer CGHs were developed, designed to produce distinct holographic images at different applied voltages. The fabrication process involved inscribing two separate holographic patterns into the same liquid crystal device, one on the substrate and the other on the superstrate, each with a specific target image. These bilayer CGHs were engineered to switch between the University of Oxford crest and the Somerville College crest, depending on the applied voltage. At a voltage of $V = 3.7\,\mathrm{V_{rms}}$, the Somerville College crest was prominently displayed, while increasing the voltage to $V = 6.7\,\mathrm{V_{rms}}$ altered the replay field to show the University of Oxford crest. The transitions were marked by clear, high-contrast images with minimal noise, highlighting the capability of these bilayer structures to dynamically switch between distinct holographic states. The response times for

these transitions were also measured, revealing that the switch from the Somerville College crest to the University of Oxford crest occurred in approximately 50 ms, while the reverse transition took around 220 ms. These response times are significantly faster than those observed in single-layer CGH devices, likely due to the increased polymerised region in the bilayer structure, which reduces the energy required to reorient the liquid crystal molecules.

The rapid and effective changing between active states and switching between two distinct CGH patterns within the same device, as controlled by varying the applied voltage, further emphasises the significant potential of optimised bilayer CGHs in dynamic optical applications, including adaptive optics, display technologies, and re-configurable optical systems. By tailoring the liquid crystal layer thickness and fine-tuning the voltage parameters, these devices can be precisely engineered to meet the demands of specific applications, offering enhanced performance and versatility.

A good idea is something that does not solve just one single problem, but rather can solve multiple problems at once.

— Miyamoto Shigeru

CHAPTER 5

Liquid Crystal Devices for Intensity Aberration Correction

5.1 Concept

5.1.1 Introduction

Optical aberrations, including intensity, phase, and polarisation as described in Section 2.3.1, compromise the performance of optical systems[101,117,226,227]. Adaptive optics (AO) has been a pivotal technology for decades, particularly in addressing phase aberrations, and its impact spans various fields including astronomy[19,96,100,228], optical communications[229,230], and super-resolution microscopy[20,99,231–233]. In astronomy, AO has transformed telescopic observations by compensating for atmospheric turbulence, allowing ground-based telescopes to achieve near-theoretical resolution for detailed imaging of celestial bodies like stars and galaxies[104,234]. This advancement achieved by dynamically adjusting optical elements has greatly contributed to our understanding of the universe[114,118]. In optical communications, AO is essential for maintaining signal clarity and stability, especially in systems exposed to atmospheric interference, enhancing both data transmission rates and reliability[235,236]. Moreover, AO has revolutionised microscopy by enabling high-resolution and high-contrast imaging deep within biological tissues, where optical distortions caused by tissue inhomogeneity can otherwise obscure crucial details[97,98]. By correcting these distortions in real time, AO enhances image quality, supporting advances in biological and medical research[237,238].

Recently, AO has expanded into the vectorial domain, addressing either polarisation aberrations alone (known as polarisation adaptive optics (P-AO))[7,13,134,239] or the combination of polarisation and phase aberrations (referred to as vectorial adaptive optics (V-AO))[227,240–242]. P-AO specifically targets issues where the polarisation state of light is aberrated by optical system components, which can critically affect applications requiring precise polarisation control such as structured light[24], optical computing[243], optical communication[110,111], and polarisation-sensitive imaging in biomedical applications[244,245]. By actively adjusting optical elements to compensate for these polarisation distortions, P-AO can enhance the system performance, enabling more accurate data acquisition and processing.

V-AO, on the other hand, simultaneously compensates the system for both polarisation and phase aberrations[227,242,246]. This dual capability is particularly advantageous in fields such as astronomical imaging[96] and deep-tissue microscopy[247], where light must travel through various media that can alter both its phase and polarisation state. Undesirable vector states in the illumination or detection beams compromise the performance of polarisation-sensitive microscopes[239,248,249], disrupting interference at the focus and further impacting image resolution, which is also critical for super-resolution microscopy[250–253]. V-AO systems extend the conventional phase AO by combining the compensation of both polarisation and phase aberrations using adaptive elements and multiple optimisation methods. The development and refinement of V-AO systems thus represent a significant advance in the versatility and effectiveness of AO technologies, promising substantial improvements across a range of scientific and technical fields.

However, tools for correcting intensity aberrations remain undeveloped. Note that in various modern optical systems, intensity errors adversely affect the overall system performance, manifesting as a non-uniform intensity distribution and energy loss. These errors can be at-

tributed to the light source beam propagation[254,255], diattenuation effects[227,256], or absorption of light by materials or biological tissues[127,257–260]. In microscopy, for instance, these issues disrupt the intensity uniformity across the pupil of the objective lens, compromising overall system performance. In laser applications, non-uniform intensity distribution compromises material processing efficiency, notably in the direct laser writing[127] that was introduced in Section 3.3, where precise energy delivery and focus spot shaping are essential for optimal fabrication outcomes. In fibre optic communications, light intensity fluctuations introduce transmission errors, diminishing reliability and transfer speed[261]. Similarly, in optical data storage technologies, laser intensity variations undermine data writing and reading accuracy, potentially causing data corruption[262]. Additionally, uneven intensity distribution can mask subtle celestial features or skew brightness measurements vital for astrophysical observations[263]. The concept of aberrations as well as their corresponding AO toolboxes for correction is illustrated in **Figure 5.1**.

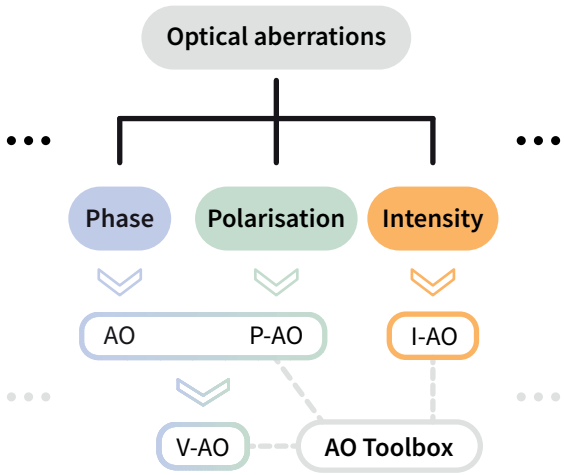

Figure 5.1: The concept of optical aberrations and relevant AO toolboxes. The performance of an optical system can be affected by different types of aberrations, such as phase, polarisation, intensity, etc. In the AO toolbox, conventional phase AO addresses phase aberrations, P-AO handles polarisation aberrations, and V-AO compensates for the combination of these aberrations. This study introduces and validates intensity adaptive optics (I-AO) method for correcting intensity aberrations, thereby enriching the AO toolbox.

Intensity aberrations in optical systems are significant distortions that adversely affect the

system imaging quality[264–266]. These aberrations typically result in a focal spot that deviates from its ideal shape[267,268]. Firstly, image resolution is degraded due to imperfect interference of the light waves at the imaging plane[161]. This is primarily because the wavefronts do not converge perfectly, causing a blurring of the image[269]. Additionally, these intensity aberrations contribute to a reduction in contrast. The scattering and loss of energy as the light waves propagate through the optical system contributes to a nonideal image formation, diminishing the overall intensity of the measurement[98]. This energy loss is particularly detrimental in low-light conditions, where maintaining high contrast is crucial for discerning fine details. The combined effect of reduced resolution and contrast directly impacts the signal-to-noise ratio (SNR) of the resultant images[270]. SNR is a critical factor in determining the quality of an image; it measures the level of desired signal relative to the background noise. Lower SNR makes it difficult to distinguish the target-of-interest from noise. **Figure 5.2** demonstrates the typical effect of these aberrations on the focal spot.

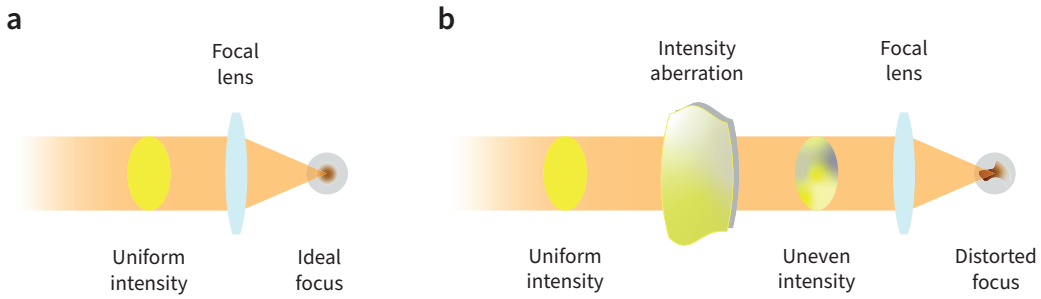

Figure 5.2: Demonstration of the typical effect of intensity aberrations. (a) An ideal optical system with a uniform intensity profile across the pupil plane, which leads to an ideal focus spot on the imaging plane. **(b)** The distorted focus caused by the uneven intensity across the pupil plane, with intensity aberration existing in the system.

In light of the features described above, the development of a correction technique that specifically targets intensity aberrations therefore becomes essential. Moreover, implementing such a technique can greatly enhance the AO toolkit. By correcting intensity aberrations,

the proposed technique would not only improve image quality but also expand the potential applications of AO in areas like astronomy, where observing faint celestial bodies requires exceptionally high-quality imaging[271], and in biomedical imaging, where enhanced contrast and resolution can lead to better diagnosis and understanding of medical conditions[272]. Such advancements would substantially benefit the AO community by providing more robust and versatile tools for high-precision imaging tasks.

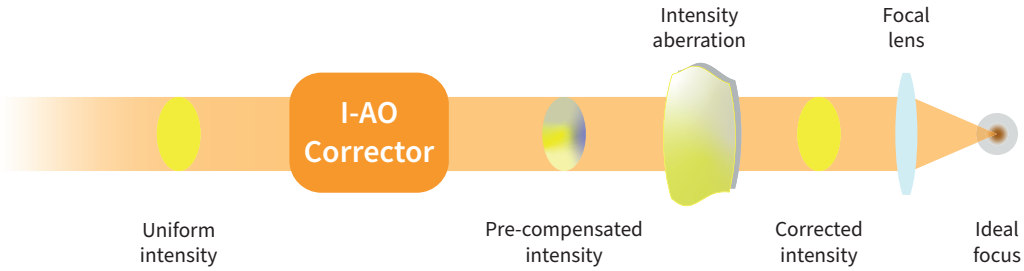

Figure 5.3: The concept of intensity aberration correction. The effect of integrating an I-AO corrector into the same system is demonstrated, where the aberrated focal spot is corrected to achieve an ideal focus.

In this work, for the first time, we put forward the concept of I-AO, which incorporates a sophisticated dual closed-loop feedback mechanism designed specifically for intensity error correction. This mechanism operates effectively in both sensor-based (e.g., direct intensity aberration measurement) and sensorless (e.g., indirect intensity inference without the use of a intensity sensor) formats, ensuring versatile applicability across different optical systems. **Figure 5.3** depicts the concept of the I-AO system after integrating the proposed I-AO correction module, showcasing the achieved focus correction. The correction module serves as the core of the I-AO, where it processes the measurement from both sensor-based and sensorless formats and subsequently adjusts the intensity profile at the pupil plane to correct intensity aberrations.

We validated the feasibility of the proposed I-AO method by demonstrating the enhance-

ment of both the focus quality and intensity values following the correction of an intensity aberrated focusing system. Note that in all I-AO experiments conducted in this work, an additional closed-loop correction routine was introduced to compensate for energy loss, beyond the standard correction loop for beam uniformity, by adjusting the attenuation filter after the laser to modify the overall intensity value. Further details are provided in subsequent sections.

Overall, this chapter demonstrates that I-AO effectively compensates for intensity aberrations, enhancing the toolkit of existing AO technology. The development of advanced AO techniques that can address these intensity-related issues across various fields would therefore not only improve the performance of various kinds of optical systems but also broaden the potential applications of AO technologies.

5.1.2 Intensity Aberration Correction Modes

In our proposed sensorless I-AO method, which will be elaborated in detail in the upcoming sections, we infer and correct intensity aberrations by measuring the focus intensity distribution (FID) profile at the focal plane as feedback for the I-AO corrector, employing a correction mechanism similar to conventional sensorless phase AO. For conventional sensorless phase AO, Zernike polynomials are used to describe an arbitrary wavefront at a defined pupil. For I-AO, we employ a similar idea and have designed a set of intensity Zernike modes for the correction of intensity aberrations appearing in the pupil plane.

The Zernike polynomials are a set of polynomials defined on a unit circle that are continuous and orthogonal. These mathematical functions were developed by Frits Zernike, a Dutch physicist, as a tool to provide a more systematic approach to understanding optical aberrations and wavefront analysis in circular systems[154]. Their uniqueness lies in their ability to best represent complex wavefront shapes in combination through a series of simpler, mathematically

defined functions. Each polynomial in the series uniquely corresponds to different common aberrations found in optical systems, such as spherical aberration, astigmatism, or coma. One of the key attributes of Zernike polynomials is their orthogonality on the unit disk, which mathematically ensures that each polynomial is independent of all others. An arbitrary wavefront in a polar coordinate (ρ, θ) denoted by $W(\rho, \theta)$ can be best represented in terms of a finite sequence of Zernike polynomials $\mathcal{Z}$ as

$$\hat{W}(\rho, \theta) = \sum_{n,m} C_n^m \mathcal{Z}_n^m(\rho, \theta) \tag{5.1}$$

where C_n^m denotes the amplitudes or coefficients of each Zernike mode and m and n denote the azimuthal frequency and radial degree, respectively[156]. Since only a finite number of Zernike modes are used, thus the derived wavefront $\hat{W}(\rho, \theta)$ is just the best approximation of the target wavefront $W(\rho, \theta)$[273].

The Zernike mode $\mathcal{Z}_n^m(\rho, \theta)$ in Equation 5.1 in the real domain can be formulated as[155]

$$\mathcal{Z}_n^m(\rho, \theta) = c_n^m R_n^{|m|}(\rho) \Theta_n^m(\theta) \tag{5.2}$$

where

$$c_n^m = \begin{cases} \sqrt{n+1} & m = 0 \\ \sqrt{2(n+1)} & m \neq 0 \end{cases} \tag{5.3}$$

$$R_n^{|m|}(\rho) = \sum_{l=0}^{(n-|m|)/2} \frac{(-1)^l (n-l)!}{l! \left[\frac{1}{2}(n+|m|-l)\right]! \left[\frac{1}{2}(n-|m|-l)\right]!} \rho^{n-2l} \tag{5.4}$$

$$\Theta_n^m(\theta) = \begin{cases} \cos(m\theta) & m \geqslant 0 \\ -\sin(m\theta) & m < 0. \end{cases} \tag{5.5}$$

The typical Zernike mode patterns are illustrated in **Figure 5.4**. The corresponding values for the radial function $R_n^{|m|}(\rho)$ and azimuthal function $\Theta_n^m(\theta)$, as well as the constant coefficients c_n^m are listed in Table 5.1.

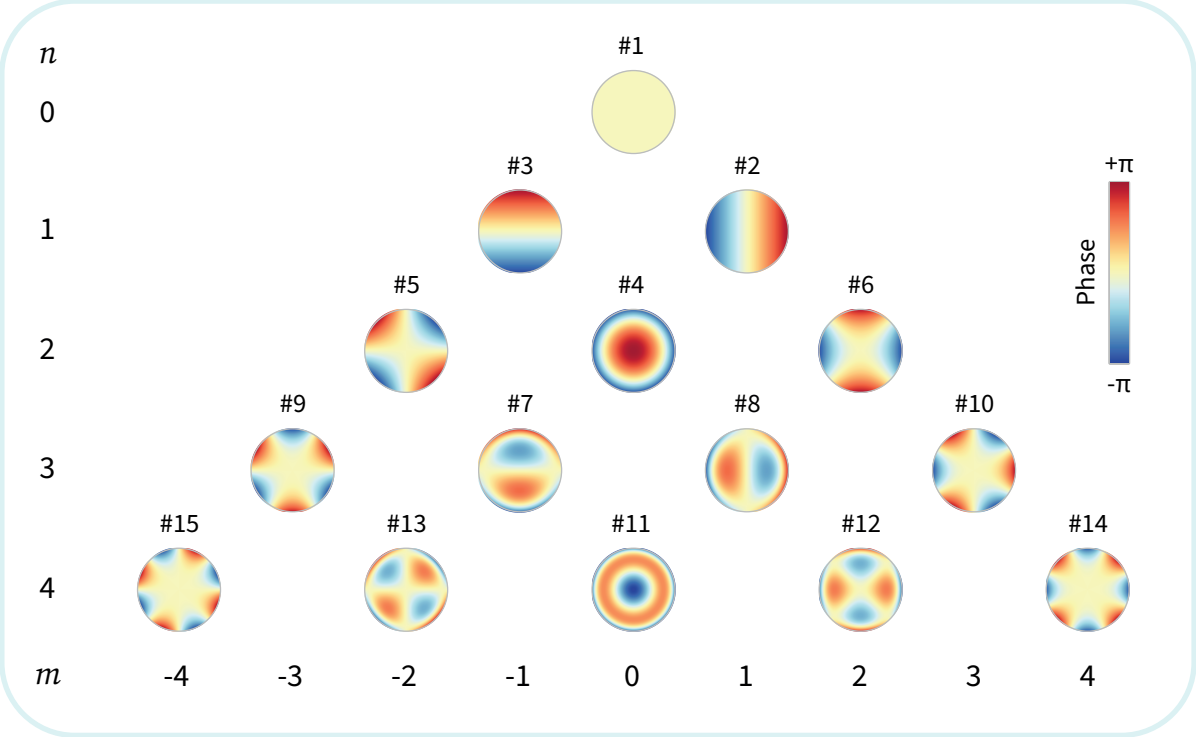

Figure 5.4: Illustration of Zernike modes. This figure displays the spatial patterns of the first 15 Zernike polynomials, which are used to represent various optical aberrations in systems with circular apertures. Each subplot corresponds to a specific mode, indexed by its radial and azimuthal orders, and visually represents the type of wavefront distortion that the polynomial corrects. The single-valued indexing of Zernike modes adheres to Noll's convention[155].

Table 5.1: Algebraic expansion of the Zernike polynomial sequence.

i	n	m	$\mathcal{Z}_n^m$	$\mathcal{C}_n^m$	$R_n^{\|m\|}(\rho)$	$\Theta_n^m(\theta)$
1	0	0	$\mathcal{Z}_0^0$	1	1	1
2	1	1	$\mathcal{Z}_1^1$	2	ρ	$\cos(\theta)$
3	1	-1	$\mathcal{Z}_1^{-1}$	2	ρ	$\sin(\theta)$
4	2	0	$\mathcal{Z}_2^0$	$\sqrt{3}$	$2\rho^2 - 1$	1

Continued on next page

Table 5.1: Algebraic expansion of the Zernike polynomial sequence. (Continued)

i	n	m	$\mathcal{Z}_n^m$	$\mathcal{C}_n^m$	$R_n^{\lvert m\rvert}(\rho)$	$\Theta_n^m(\theta)$
5	2	-2	$\mathcal{Z}_2^{-2}$	$\sqrt{6}$	ρ^2	$\sin(2\theta)$
6	2	2	$\mathcal{Z}_2^{2}$	$\sqrt{6}$	ρ^2	$\cos(2\theta)$
7	3	-1	$\mathcal{Z}_3^{-1}$	$2\sqrt{2}$	$3\rho^2 - 2\rho$	$\sin(\theta)$
8	3	1	$\mathcal{Z}_3^{1}$	$2\sqrt{2}$	$3\rho^2 - 2\rho$	$\cos(\theta)$
9	3	-3	$\mathcal{Z}_3^{-3}$	$\sqrt{3}$	ρ^3	$\sin(3\theta)$
10	3	3	$\mathcal{Z}_3^{3}$	$\sqrt{3}$	ρ^3	$\sin(3\theta)$
11	4	0	$\mathcal{Z}_4^{0}$	$\sqrt{5}$	$6\rho^4 - 6\rho^2 + 1$	1
12	4	2	$\mathcal{Z}_4^{2}$	$\sqrt{10}$	$4\rho^4 - 3\rho^2$	$\cos(2\theta)$
13	4	-2	$\mathcal{Z}_4^{-2}$	$\sqrt{10}$	$4\rho^4 - 3\rho^2$	$\sin(2\theta)$
14	4	4	$\mathcal{Z}_4^{4}$	$\sqrt{10}$	ρ^4	$\cos(4\theta)$
15	4	-4	$\mathcal{Z}_4^{-4}$	$\sqrt{10}$	ρ^4	$\sin(4\theta)$

As mentioned, instead of using conventional phase AO Zernike modes, we introduce a modified set of Zernike modes to represent intensity aberrations. Recognizing that intensity profiles are non-periodic and range between 0 and 1, these modified Zernike modes differ in both the range of possible values and application, and can be expressed as

$$\mathcal{Z}_n^m(\rho,\theta) = \frac{1}{2} c_n^m R_n^{|m|}(\rho)\Theta_n^m(\theta) + \frac{1}{2} \tag{5.6}$$

where

$$c_n^m = 1 \tag{5.7}$$

$$\Theta_n^m(\theta) = \begin{cases} \cos(m\theta) & m \geqslant 0 \\ -\sin(m\theta) & m < 0 \end{cases} \tag{5.8}$$

$$R_n^{|m|}(\rho) = \sum_{l=0}^{(n-|m|)/2} \frac{(-1)^l (n-l)!}{l!\left[\frac{1}{2}(n+|m|-l)\right]!\left[\frac{1}{2}(n-|m|-l)\right]!} \rho^{n-2l}. \tag{5.9}$$

The modified intensity Zernike modes are non-orthogonal due to the non-periodic and power-related nature of intensity variations, which restricts the use of orthogonal superposition for correction. The total number of intensity Zernike modes used in the I-AO corrector is usually determined by the characteristics of the measured sample. For the purpose of demonstrating a sensorless method for the I-AO corrector, the first 15 intensity Zernike modes were applied to a spatial light modulator (SLM) throughout the correction process. However, additional modes can be applied to deal with more complex aberrations.

Due to geometrical crosstalk between intensity and phase for the modulation of each SLM pixel[13,274], additional phase aberrations will also be introduced. The state of polarisation (SoP) and the scalar phase at the SLM in the I-AO corrector can be modelled with Jones calculus to represent the light passing through[227]. For each point on the pupil plane, the change in SoP and phase can be modelled as:

$$\mathbf{j_2} = \mathrm{J} \cdot \mathbf{j_1} \tag{5.10}$$

where $\mathbf{j_1}$ and $\mathbf{j_2}$ are the Jones vectors before and after the change in SoP and scalar phase, respectively, applied with the SLM sandwiched between crossed polarisers in the I-AO corrector. These optical elements are modelled using a 2×2 Jones matrix J. Here, we focus exclusively on retardance and phase modulation for a fully polarised beam of light. As a result, J can be expressed as

$$\mathrm{J} = e^{i\phi} \cdot U \tag{5.11}$$

where ϕ is the scalar phase applied by the SLM and U is a special unitary matrix (SU) describing the change in SoP. This latter matrix can also be parameterised[275] as

$$U = SU2(\mathbf{Q}, \phi) = \cos\left(\frac{\phi}{2}\right)\mathbf{I} + \cos\left(\frac{\phi}{2}\right) \cdot (n_1\sigma_1 + n_2\sigma_2 + n_3\sigma_3) \tag{5.12}$$

where $\mathbf{I}$ is the 2×2 identity matrix, ϕ is again the scalar phase applied by the SLM and σ_1, σ_2, σ_3 are the Pauli matrices defined as

$$\sigma_1 = \begin{bmatrix} 1 & 0 \\ 0 & 1 \end{bmatrix} \tag{5.13}$$

$$\sigma_2 = \begin{bmatrix} 0 & 1 \\ 1 & 0 \end{bmatrix} \tag{5.14}$$

$$\sigma_3 = \begin{bmatrix} 0 & i \\ -i & 0 \end{bmatrix}. \tag{5.15}$$

Note that σ_3 is defined differently from that presented in some other sources[276–280]. The coefficients n_1, n_2, n_3 belong to a vector $\mathbf{Q} = [n_1, n_2, n_3]$ with unit norm, i.e., $\|\mathbf{Q}\| = 1$. The SLM, comprised of a nematic liquid crystal (NLC), exhibits a phase delay between its two principal axes. This delay is governed by its birefringence Δn, which can be modulated by an external electric field and introduced in detail in Section 2.1.2. In the SLM, the phase delay introduced by each pixel is determined by the pixel value applied and is defined as:

$$\begin{aligned} \phi &= \frac{2\pi \cdot \Delta n \cdot d}{\lambda} \\ &= 2\arcsin\left(\sqrt{\frac{T}{\sin^2 2\chi}}\right) \end{aligned} \tag{5.16}$$

where T is the normalised transmitted intensity, χ is the angle between the polariser and the NLC director (in this case χ = 45°), Δn denotes the NLC's birefringence, d represents the distance that light travels within the NLC layer, and λ is the wavelength of the light source.

The phase delay ϕ is controlled by the voltage applied to each SLM LC pixel element and the effect can then be modelled as

$$\mathrm{J_{LC}} = \begin{bmatrix} e^{i\phi} & 0 \\ 0 & 1 \end{bmatrix}. \tag{5.17}$$

From Equation 5.17, we can then take out the common phase factor to account for the propagation through the NLC and focus on the phase difference caused by the birefringence Δn between two axes parallel and perpendicular to the LC director. The Jones matrix for the single pixel then can be represented as

$$\begin{aligned} \mathrm{J_{LC}} &= e^{i\frac{\phi}{2}} \begin{bmatrix} e^{i\frac{\phi}{2}} & 0 \\ 0 & e^{-i\frac{\phi}{2}} \end{bmatrix} \\ &= e^{i\frac{\phi}{2}} \cdot SU2(\mathbf{H}, \phi) \end{aligned} \tag{5.18}$$

where $\mathbf{H} = [1; 0; 0]$ and ϕ can be determined by the target intensity level T. In our experiment, the SLM was configured with a reflective backplane behind the pixel array. Consequently, the Jones vector after reflection from the SLM can be expressed as:

$$\mathrm{J_{SLM}} = \mathrm{J_r} \cdot e^{i\frac{\phi}{2}} SU2(\mathbf{H}, \phi) \tag{5.19}$$

where $\mathrm{J_r} = \sigma_1 = iSU2(\mathbf{H}, \pi)$ represents reflection off the backplane of the SLM[280]. The Jones matrices for linear polarisers at +45° and -45° are given by

$$\begin{aligned} \mathrm{J_{+45}} &= \frac{1}{2} \begin{bmatrix} 1 & 1 \\ 1 & 1 \end{bmatrix} \\ \mathrm{J_{-45}} &= \frac{1}{2} \begin{bmatrix} 1 & -1 \\ -1 & 1 \end{bmatrix}. \end{aligned} \tag{5.20}$$

Therefore, the Jones matrix of each pixel across the pupil through the SLM module can be

represented as:

$$\mathrm{J} = \mathrm{J}_{-45} \cdot \mathrm{J}_{\mathrm{SLM}} \cdot \mathrm{J}_{+45}. \tag{5.21}$$

Thus, this relationship leads to the input and output Jones vectors before and after the modulation by the SLM as

$$\begin{aligned} \mathbf{j_2} &= \mathrm{J}_{-45} \cdot \mathrm{J}_{\mathrm{SLM}} \cdot \mathrm{J}_{+45} \cdot \mathbf{j_1} \\ &= e^{i\frac{\phi+\pi}{2}} \mathrm{J}_{-45} \cdot SU2(\mathbf{H}, \phi) \cdot SU2(\mathbf{H}, \pi) \cdot \mathrm{J}_{+45} \cdot \mathbf{j_1}. \end{aligned} \tag{5.22}$$

Subsequently, the phase difference between $\mathbf{j_1}$ and $\mathbf{j_2}$ is computed using the Pancharatnam connection[277,281], which we define as

$$\Phi(\mathbf{j_1}, \mathbf{j_2}) = \arg(\mathbf{j_1}^{\dagger}\mathbf{j_2}). \tag{5.23}$$

This phase can be finally cancelled using the DM by setting the phase using $\varphi = -\Phi(\mathbf{j_1}, \mathbf{j_2})$. Based on the intensity Zernike pattern $T = Z_n^m(\rho, \theta)$ designed across the pupil, the corresponding phase $\varphi = \frac{\phi+\pi}{2}$ to compensate in the range from 0.5π to π can be derived across the pupil, as the modulation range of the SLM ϕ is in the range of $[0, \pi]$. Therefore, each intensity Zernike pattern applied onto the SLM will have a companion DM phase pattern to ensure that the I-AO corrector will provide a pure intensity modulation. Thus, the combined use of an SLM with polarisers and a DM forms the foundation of this I-AO sensorless algorithm. The first 15 modified intensity Zernike modes are demonstrated alongside their corresponding phase corrections in **Figure 5.5**.

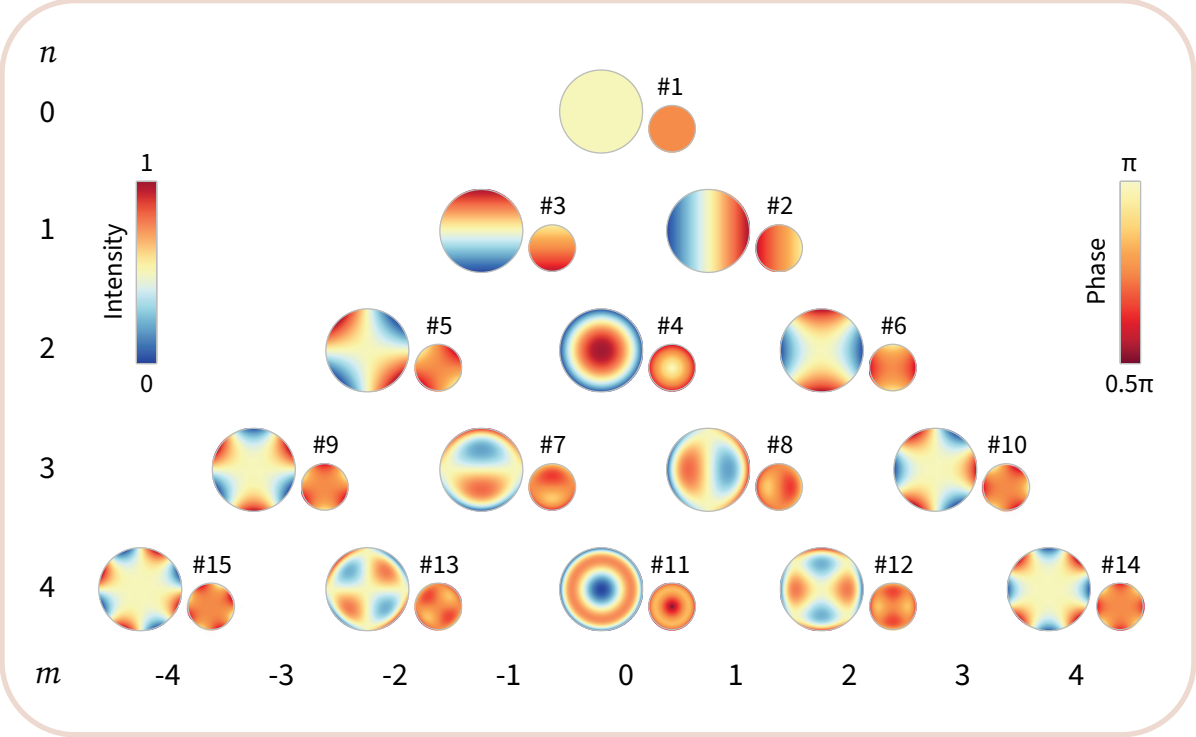

Figure 5.5: Illustration of intensity Zernike modes. The first 15 modified intensity Zernike modes (left) demonstrated alongside their corresponding phase mode (right) on the DM. Intensity Zernike modes range between [0,1], and the corresponding DM pattern for compensating additional phase aberrations introduced by the SLM (with phase ranges from 0.5π to π, as shown by the right scale bar). The indexing of intensity Zernike modes adheres to Noll's convention.

5.2 System Development and Calibration

5.2.1 Intensity Aberration Correction System

In order to correct for aberration, the I-AO corrector was deployed into our optical system. As indicated, this correction module consisted of an SLM sandwiched between two crossed polarisers for pixelated control of the intensity across the beam in the transverse plane, as shown in the simplified schematic layout in **Figure 5.6**. This configuration, previously utilised in conventional phase AO corrections[13,139], was adapted here as an I-AO corrector to deal with intensity errors. Additionally, an extra AO device, in this case a DM, was positioned next to the SLM-based module to compensate for geometrical phase effects introduced by the SLM itself during the intensity correction process[227,282], as well as residual phase errors introduced

by the optical system.

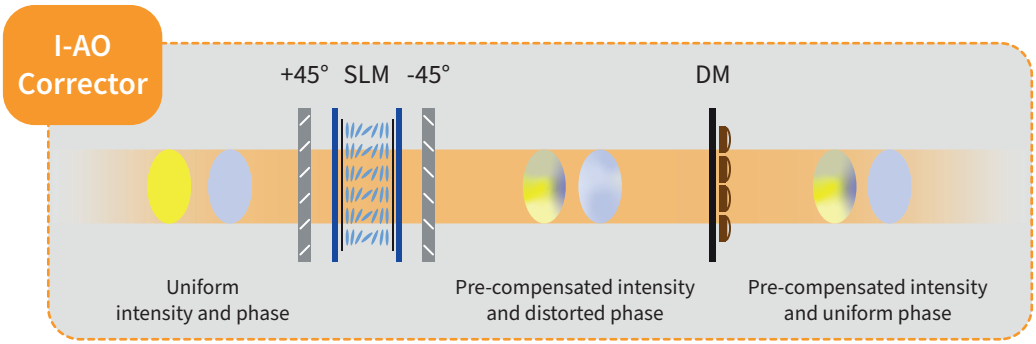

Figure 5.6: Configuration of the I-AO corrector. Detailed arrangement of the I-AO corrector, highlighting how pixelated intensity correction is facilitated by sandwiching a spatial light modulator (SLM) between a pair of crossed polarisers. Additionally, a DM is strategically incorporated to address and rectify any supplementary phase errors that arise during the intensity correction process, ensuring comprehensive aberration correction.

The configuration of the correction system employed in this work is presented in **Figure 5.7**. A He-Ne laser beam (Melles Griot, 05-LHP-171) emitting at a wavelength of 632.8 nm was expanded (by lenses L1 and L2) and directed towards the SLM (Hamamatsu, X10468-01) and a DM (Boston Micromachines Corporation, Multi-3.5). The SLM was used in combination with the DM functioning as the I-AO corrector as described above. The SLM was inserted between a pair of crossed polarisers (P1 and P2) that were installed before and after it with the polarisers configured so that the fast axis of the nematic LC in each pixel was aligned at +45 ° and -45 ° to the transmission axes of the polarisers. The pupil plane from the surface of the SLM was relayed to the surface of the DM by lenses L3 and L4, and then further relayed to the designed pupil plane by lenses L5 and L6.

Depending upon the different correction methods (i.e., sensorless or sensor-based), different elements were added for the correction process (with the aid of the flip mirror FM1). For the sensor-based method, a conjugate plane to the pupil plane was directly imaged on the CCD

and the intensity variation was directly measured on the pupil. Hence the intensity that needed to be compensated could be derived directly by comparing the difference between the current pupil profile with that of the target uniform intensity distribution. For the sensorless method, the pupil plane was focused though a lens and the distribution of the intensity at the focal point was examined by comparing the result with the ideal distribution of the focus.

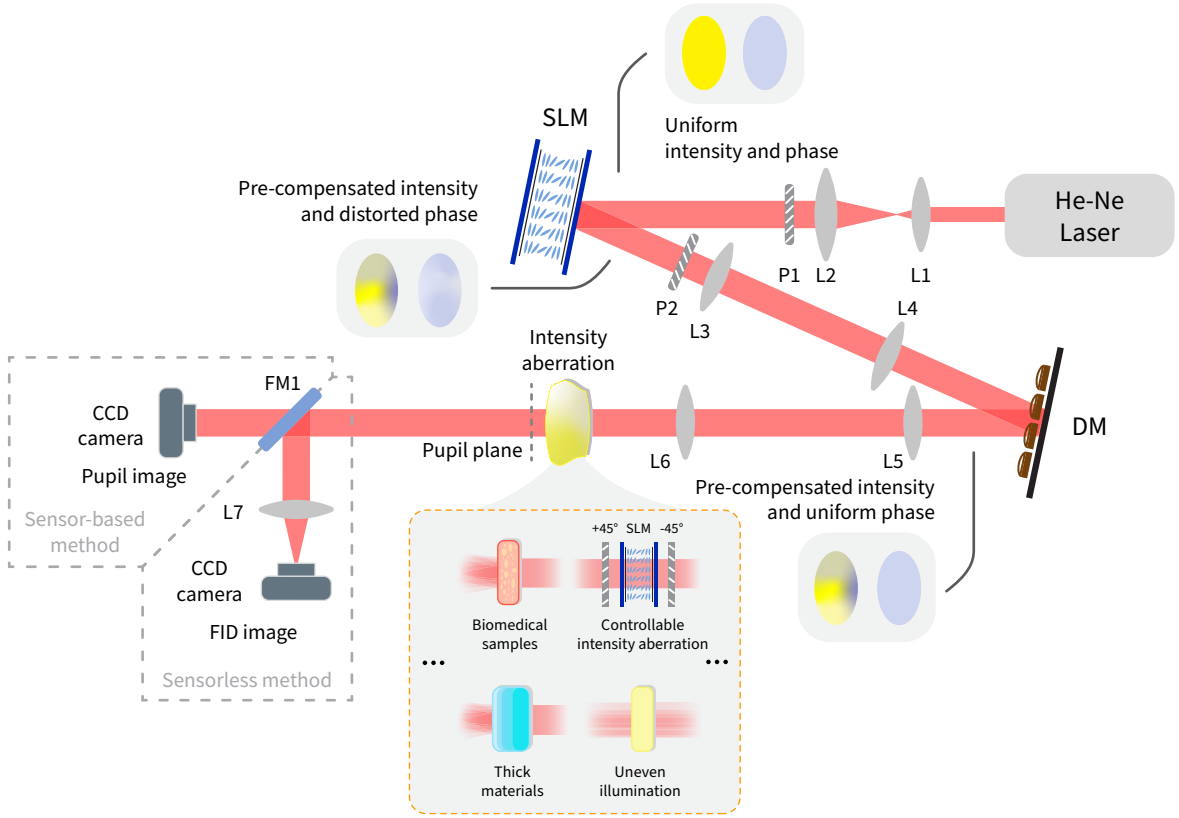

Figure 5.7: Experimental setup for intensity aberration correction. This figure presents the configuration for correcting intensity aberrations using a He-Ne laser emitting at 632.8 nm, expanded by lenses L1 and L2, and directed through a SLM paired with a DM. The SLM incorporates crossed polarisers (P1 and P2) aligned at +45° and -45° relative to the SLM. Optical paths are relayed from the SLM surface to the DM by lenses L3 and L4, and further to the final pupil plane via lenses L5 and L6. The optical arrangement accommodates both sensor-based and sensorless correction methods by changing the position of the flip mirror, FM1. Various intensity aberrations can occur in this setup, such as biomedical samples, thick materials, unevenly illuminated samples and controllable intensity aberrations. For the sensor-based method, pupil planes are imaged onto a CCD, directly measuring intensity variations for real-time correction by comparing with the target profile. The sensorless method evaluates the FID at the focal plane in relation to an ideal distribution, inferring the aberration without direct imaging.

5.2.2 Dual-loop Feedback Correction

In conventional phase AO technology, most methods necessitate and utilise a single feedback loop for correction. These methods rely on either direct wavefront measurements at the pupil plane (sensor-based method) or on inferring phase aberrations from FID profiles at the focal plane (sensorless method). In both cases, the AO corrector is iteratively adjusted to mitigate phase aberrations. The sufficiency of single loop correction stems from the periodic nature of phase in electromagnetic waves, allowing adjustments to be made without affecting the beam's total energy. However, for intensity aberration correction, a single feedback loop is insufficient because changes in intensity can alter the beam's energy distribution as well. Utilising a single feedback loop in such cases makes it difficult to maintain both the intensity distribution and total energy intact at the focal plane, with a risk of complete energy loss in severe instances.

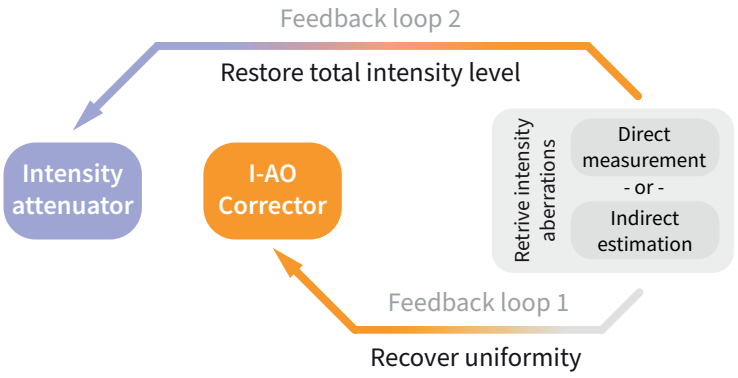

Figure 5.8: The dual-loop correction mechanism in the I-AO methods. The I-AO methods harness a dual-loop feedback correction. In the first loop, it follows the conventional phase correction principle to retrieve the intensity aberration in both sensor-based and sensorless format. In the second loop, it addresses energy deficiencies, ensuring uniform intensity and total intensity recovery without energy loss.

To preserve the intensity distribution of the beam without compromising the total energy, we introduce a dual-loop correction mechanism in the I-AO corrector. The first loop follows conventional phase AO correction principles, employing feedback from the pupil plane (sensor-based) or focal plane (sensorless) to adjust the I-AO corrector. Its objective is to restore intensity

uniformity at the pupil plane or the shape of the focus at the focal plane, which have been disrupted by external aberrations. This loop does not involve restoring the total energy of the original beam. The second loop then compensates for energy loss introduced during the first loop by making adjustments to the initial beam intensity. This dual-loop strategy effectively divides the intensity aberration correction process into two sub-tasks: intensity uniformity restoration and total intensity recovery, ensuring that no energy is sacrificed. The dual-loop correction mechanism is demonstrated in **Figure 5.8**. The response time for the sensor-based method is approximately 50 ms, which falls within the real-time correction region, making it suitable for dynamic intensity adjustments. In contrast, the sensorless method has a response time of around 1 minute due to the iterative nature of the optimisation process, which requires repeated image acquisition and analysis.

5.2.3 Calibration of Active Optical Devices

An SLM was positioned in the I-AO corrector between two polarisers aligned orthogonally. This configuration, with both polarisers aligned at a 45° relative to the NLC within the SLM, facilitates pixelated intensity modulation through the NLC's Fréedericksz transition. The formula for the transmittance (T) of light through the NLC layer as presented in Section 2.1.2, Equation 2.12 as

$$T = \frac{I}{I_0} = \sin^2(2\chi)\sin^2\left(\frac{\pi\Delta n d}{\lambda}\right) \tag{5.24}$$

where the symbols are defined the same as the ones defined in Equation 5.16.

Light intensity modulation in the I-AO corrector is achieved by controlling the voltage applied to the SLM to change the effective birefringence. This was achieved by using an 8-bit greyscale image of the same resolution as the SLM panel, which was further converted to voltages according to a manufacturer-defined greyscale-to-voltage map. However, the thickness

of the NLC layer varies due to the uneven SLM surface, which impacts the modulation quality. A pixel-specific look-up table (LUT) was therefore needed to account for these disparities. This LUT correlates pixel values with their modulated intensities, enabling precise and rapid intensity adjustments during the correction process by quickly identifying the appropriate pattern to load onto the SLM. The LUT for each SLM pixel was derived by mapping intensity modulation to greyscale levels, which required the adjustment of the laser intensity via a neutral density (ND) filter and optimisation of the monochrome camera exposure time to achieve maximal dynamic range. These parameters remained constant to ensure a consistent calibration throughout the experiment.

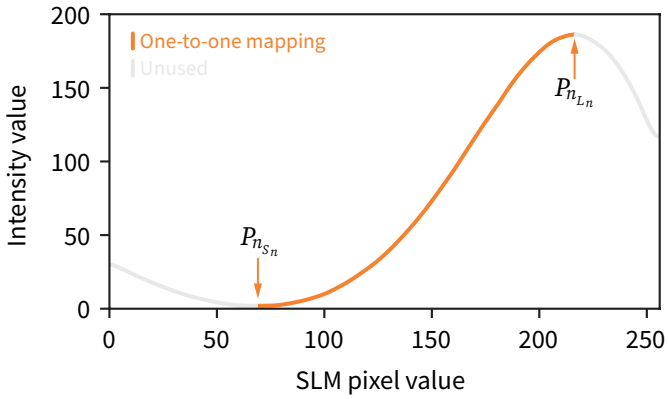

Figure 5.9: A typical calibration curve derived for each SLM pixel. Usually it will be the shape of a trigonometric function. To obtain a one-to-one value mapping between the SLM pixel value and the intensity value after modulation, the maximum and minimum intensity values $P_{n_{S_n}}$ and $P_{n_{L_n}}$ were located when the SLM pixel value was S_n and L_n. The highlighted section of the curve indicates the one-to-one mapping selected for I-AO corrector.

Next, to efficiently capture the intensity modulation response across all pixels on the SLM, uniform images with a single value (termed flat value F_i) were employed. With an 8-bit modulation depth of the SLM, flat values $F_i = i$ satisfying $i \in [0, 255]$, $i \in Z$ were systematically tested for each SLM pixel. We applied the same flat value F_i to all N pixels of the SLM by using the uniform image and then increased the flat value of the uniform image from 0 to 255. This approach allowed us to efficiently record the intensity response of each SLM pixel

by capturing the intensity response of the whole active region of the SLM from the intensity sensor for each flat value F_i applied. It should be noted that the discrepancy between SLM resolution and camera sensor size was mitigated through interpolation. This ensured an accurate one-to-one mapping between each pixel on the SLM and each pixel on the image captured by the monochromatic camera for intensity measurement, which eliminated any potential issues related to resolution mismatch. Consequently, for each image of the active region captured with the flat value F_i applied, we could determine the corresponding intensity response P_{n_i} for every pixel n across all N SLM pixels, enabling the derivation of the modulation range as $[P_{n_0}, P_{n_1}, \cdots, P_{n_{255}}]$ for each pixel n. This process recorded the modulation profile of the entire value space and enabled precise calibration of pixel-specific intensity responses which are typically represented by trigonometric functions within the modulation range. By following these steps, in total 256 intensity images were taken after which the intensity modulation range for each pixel could be derived. A typical curve measured from this calibration process is shown in **Figure 5.9**.

To ensure the mapping is unique between SLM pixel values and intensity modulation, flat values F_{S_n} and F_{L_n} corresponding to minimum intensity $P_{n_{S_n}}$ and maximum intensity $P_{n_{L_n}}$, respectively, were identified for each SLM pixel n. Intensity values within the range of $P_{n_{S_n}}$ to $P_{n_{L_n}}$ and their corresponding flat values were used for I-AO compensation, with intensity values outside this range being discarded. Thus for each SLM pixel index with *n*, when its pixel value was set between F_{S_n} and F_{L_n}, it will have a one-to-one mapping to the intensity value ranging from $P_{n_{S_n}}$ to $P_{n_{L_n}}$ on the monochromatic camera. This approach establishes the relationship between flat values of each SLM pixel and the intensity values that can be modulated for each SLM pixel through the I-AO corrector, which was then encoded into the LUT together with the valid pixel value range. This calibration methodology is illustrated in

the accompanying flowchart in **Figure 5.10**.

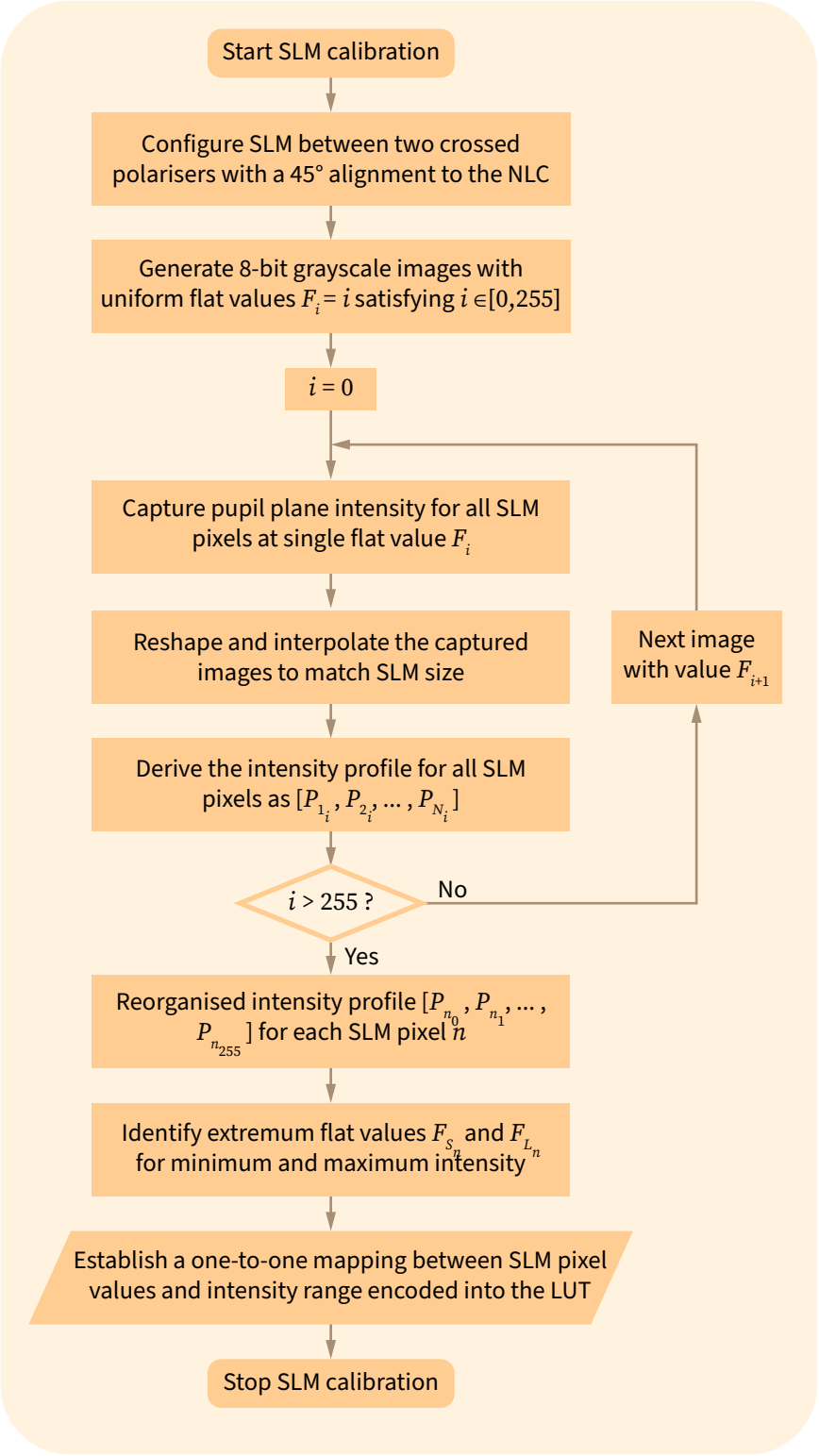

Figure 5.10: The flowchart summarises the calibration methodology employed for each pixel of the SLM. The configuration of the SLM during calibration, the measurement of the intensity modulation range for each pixel, and the generation of a pixel specific LUT for precise intensity correction is outlined.

To achieve a desired output intensity using the I-AO corrector, specific target intensities P_{n_T} were set on the monochrome camera. This was done by modulating each SLM pixel with patterns derived from a calibrated LUT. These patterns were generated by selecting a value F_i between F_{S_n} and F_{L_n} for each SLM pixel n, such that the corresponding intensities P_{n_i} closely matched the target P_{n_T}. Subsequently, conventional phase AO correction was applied using the DM to correct for phase aberrations introduced by the SLM and other system-specific optical phase aberrations. For a uniform output intensity, a single target intensity level P_{n_T} was set for the intensity reading on the monochrome camera, which furthermore determines the unique pattern on the SLM ensuring a uniform intensity at the pupil plane. The images taken at the focal plane revealed an ideal focal intensity distribution resembling a standard Airy disk shape as shown in **Figure 5.11**

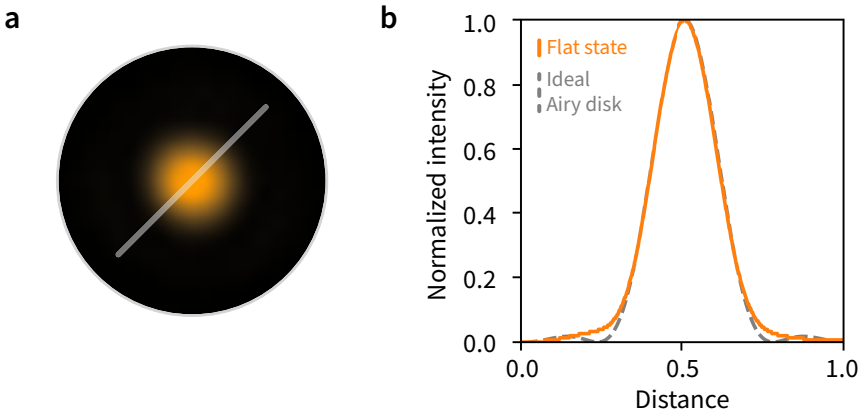

Figure 5.11: The ideal focal intensity distribution through the SLM in its flat state. (a) The ideal focal intensity distribution captured when the SLM was set to its 'flat state' and a standard Airy disk shape was obtained. **(b)** The cross section of the focal intensity distribution and the comparison to the standard Airy disk shape.

5.3 Correction Methods and Procedures

5.3.1 Sensor-Based Method

Sensor-based I-AO directly measures aberrations at the pupil plane with a sensor. Initially, the SLM was set to a flat state (as stated in Section 5.2.3), and reference images were captured from

both the pupil and focal planes. A schematic of the measurement logic is demonstrated in **Figure 5.12**. Afterwards, the external intensity aberration was introduced into the system, and the distorted intensity profile on the pupil plane was captured by the intensity sensor, initiating a dual-feedback loop for sensor-based correction. Loop 1 recovers the intensity profile and calculates the intensity loss ΔP_n for each pixel n by comparing the captured intensity values P_{n_C} with the target level P_{n_T}, where $\Delta P_n = P_{n_T} - P_{n_C}$. A new target level $\tilde{P}_n = P_{n_T} + \Delta P_n$ is then set for the pupil plane pixel intensity measured by the monochromatic camera to compensate for the intensity aberration, leading to the creation of a new pattern image onto the SLM based on the LUT. The corrected pupil intensity was further assessed to confirm optimal beam uniformity restoration. Finally, conventional phase AO correction was applied to address phase aberrations introduced by the SLM during the intensity correction process. The FID at the focal plane resembles that of an ideal Airy disk, also validating that the intensity profile at the pupil plane would be uniform.

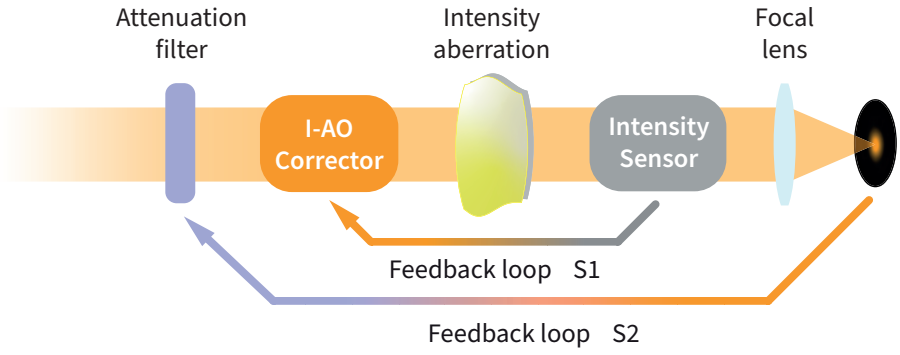

Figure 5.12: Schematic of the sensor-based I-AO method. Conceptual schematic illustrating the sensor-based I-AO method with dual closed-loop feedback correction. The intensity sensor was utilised to measure the intensity variation directly from the pupil plane to provide information for the first feedback loop, which recovers the uniformity of the pupil intensity. The intensity from the FID then provides the second feedback loop to recover the total intensity level.

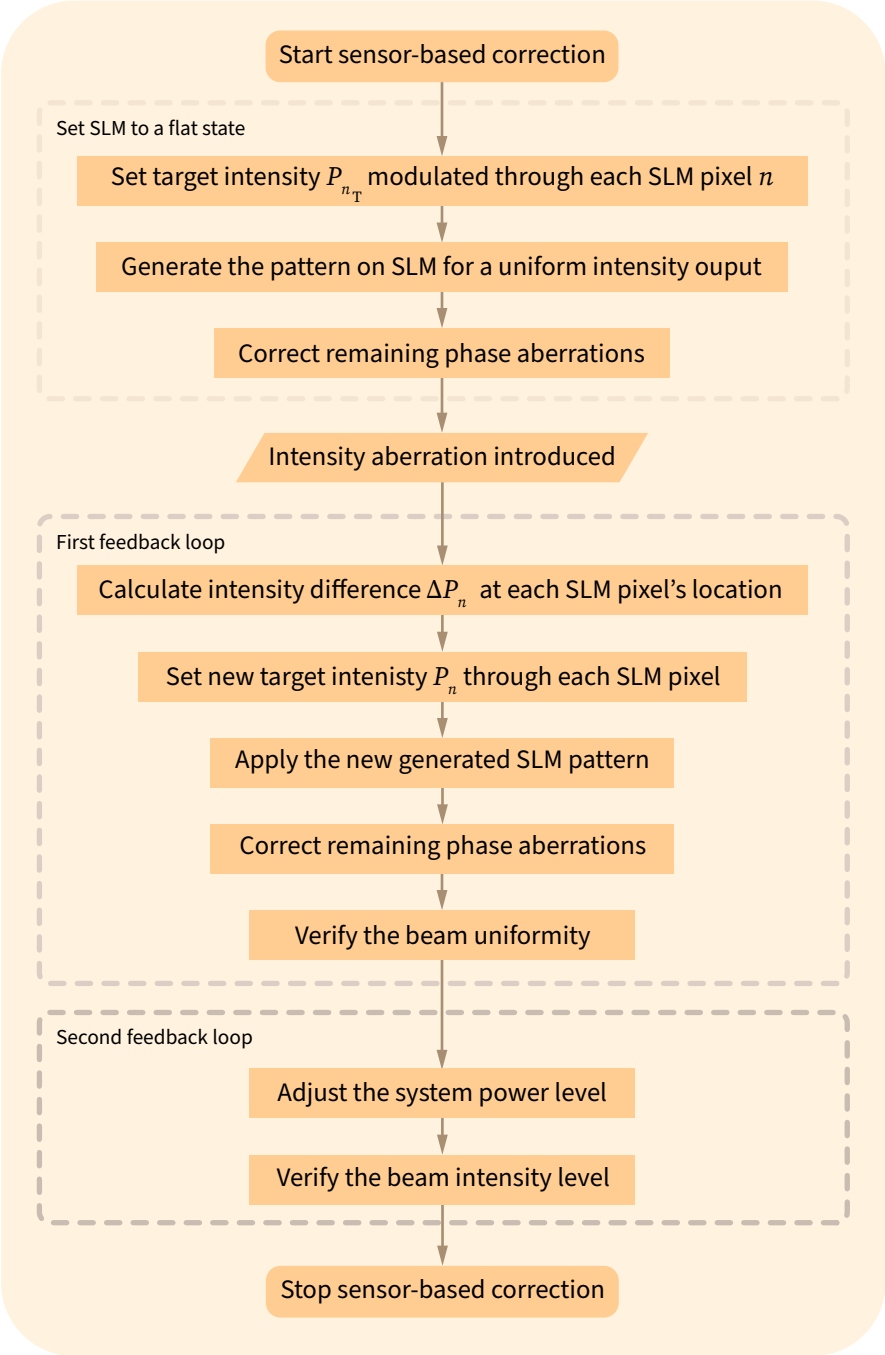

Figure 5.13: Flowchart outlining the sensor-based correction methodology. Critical steps such as the SLM flat state initialisation, beam uniformity restoration (loop 1), and total intensity recovery (loop 2) are illustrated, as detailed in Section 5.2.2. The dual feedback loop is highlighted for simultaneous beam uniformity restoration and total intensity recovery.

After rectifying the uniformity of the intensity profile at the pupil plane and the FID profile at the focal plane in the first loop, the second loop focuses on recovering the total intensity

of the initial beam by adjusting the attenuation filter at the illumination source with feedback from the intensity level measured by the camera. A flowchart presented in **Figure 5.13** outlines this sensor-based correction methodology.

5.3.2 Sensorless Method

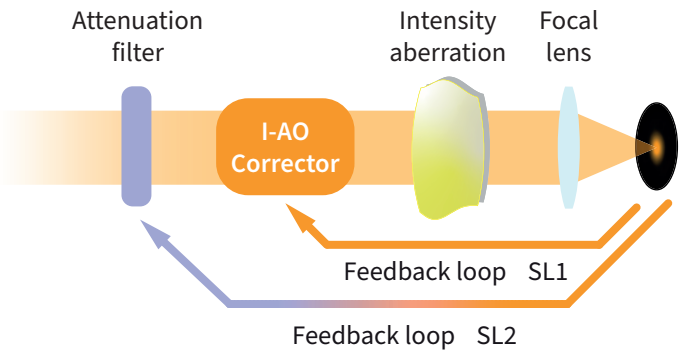

Figure 5.14: Schematic of the sensorless I-AO method. A conceptual schematic of sensorless I-AO for intensity aberration correction with dual closed-loop feedback correction. In contrast to the sensor-based approach, No intensity sensor is utilised to measure the intensity variation directly from the pupil plane. Instead, the aberration is inferred by measuring the FID from the focus plane, which is used as the first feedback loop to recover the uniformity of the pupil intensity. The same information is also used to recover the total intensity back to its original level.

Our sensorless I-AO technique iteratively applies predefined patterns to the I-AO corrector to correct for intensity aberrations detected at the focal plane. This method was inspired by established wavefront sensorless algorithms for phase aberration correction AO in microscopy. The key distinction between the sensorless and sensor-based approach is that the former relies on evaluating the FID profile at the focal plane to infer the aberration indirectly, as it cannot directly measure the intensity profile from the pupil plane. In addition, instead of using traditional phase AO Zernike modes, the modified set of intensity Zernike modes as elaborated in Section 5.1.2 were employed for intensity aberration correction. A schematic of the measurement logic is outlined in **Figure 5.14**.

Initially, the SLM was configured to maintain a uniform intensity level using a calibrated LUT, which was precisely measured following the detailed procedure outlined in the SLM calibration process described in Section 5.2.3. Subsequently, an arbitrary intensity aberration was deliberately introduced, resulting in a distortion of the FID profile at the focal plane. In the initial correction loop, a total of 15 intensity Zernike modes were evaluated to identify the mode with the optimal coefficient that would restore the uniformity of the light distribution. It is important to note that, unlike traditional Zernike modes used in phase correction, the intensity Zernike modes mentioned in Section 5.1.2 do not support super-positioning. Therefore, our method involves a systematic and sequential coarse scanning of the coefficient range from 0 to 1 for each mode, with an incremental step of 0.2. For each step, an FID profile was captured to assess the effect of the applied coefficient.

Contrary to conventional phase AO sensorless algorithms, which retain the optimal coefficients of previously scanned modes on the AO device during subsequent scans, our approach discards the previous correction mode before applying the next one. After assessment of each mode, the I-AO corrector was reset to a flat state before examining the subsequent mode. This strategy effectively prevents intensity saturation on the pupil plane by clearing coefficients after each scan, thereby ensuring accurate feedback and optimal corrective adjustments. This meticulous process of capturing focal plane images for all coefficients is critical, yet no modes are retained in the corrector after the coarse scanning phase. The correction of intensity aberrations is thus postponed until the most effective mode and corresponding coefficient have been precisely identified and selected. This methodical approach enhances the precision and efficacy of the correction process, leading to significantly improved imaging quality and consistency.

To select the optimal mode with corresponding coefficient for correcting aberrations, the FID profile images were assessed from coefficient scans, applying criteria to gauge focal spot

quality. The primary objective of this analysis was to identify the intensity Zernike mode with coefficients that restore the distorted FID profile to a configuration most closely approximating the ideal Airy disk shape. The first criterion for selecting the optimal mode and corresponding coefficient involved evaluating the low spatial frequency characteristics of the FID profile images, a measure that provides critical insight into the uniformity and smoothness of the light distribution across the focal plane[283]. The second criterion focuses on the circularity of the focus spot, a parameter that is indispensable for assessing the roundness of the focal spot. The spot circularity value C evaluating the FID profile was computed as

$$C = \frac{4A\pi}{P^2} \tag{5.25}$$

where A is the spot area and P is the perimeter of the target spot. Circularity values of 1 indicate a perfect circle, with deviations from 1 reflecting a poor FID profile. The optimal coefficient of each mode, determined by a coarse coefficient scan with the low spatial frequency algorithm, were further evaluated by comparing the circularity value C difference from 1. This difference served as the mode selection criterion. To streamline the final correction, among modes meeting this criterion, the one with the lowest index was selected to simplify the outcome.

After identifying the optimal mode for aberration correction during preliminary scanning, a detailed rescan was conducted over the same range (0 to 1) with finer 0.05 increments. FID profile images were captured and analysed using a low spatial frequency algorithm and spot circularity value to pinpoint the coefficient that produces a focus spot closest to the ideal Airy disk. Achieving this spot indicated optimal system performance with minimal aberrations and improved image clarity. The corresponding pattern was then generated and loaded onto the SLM.

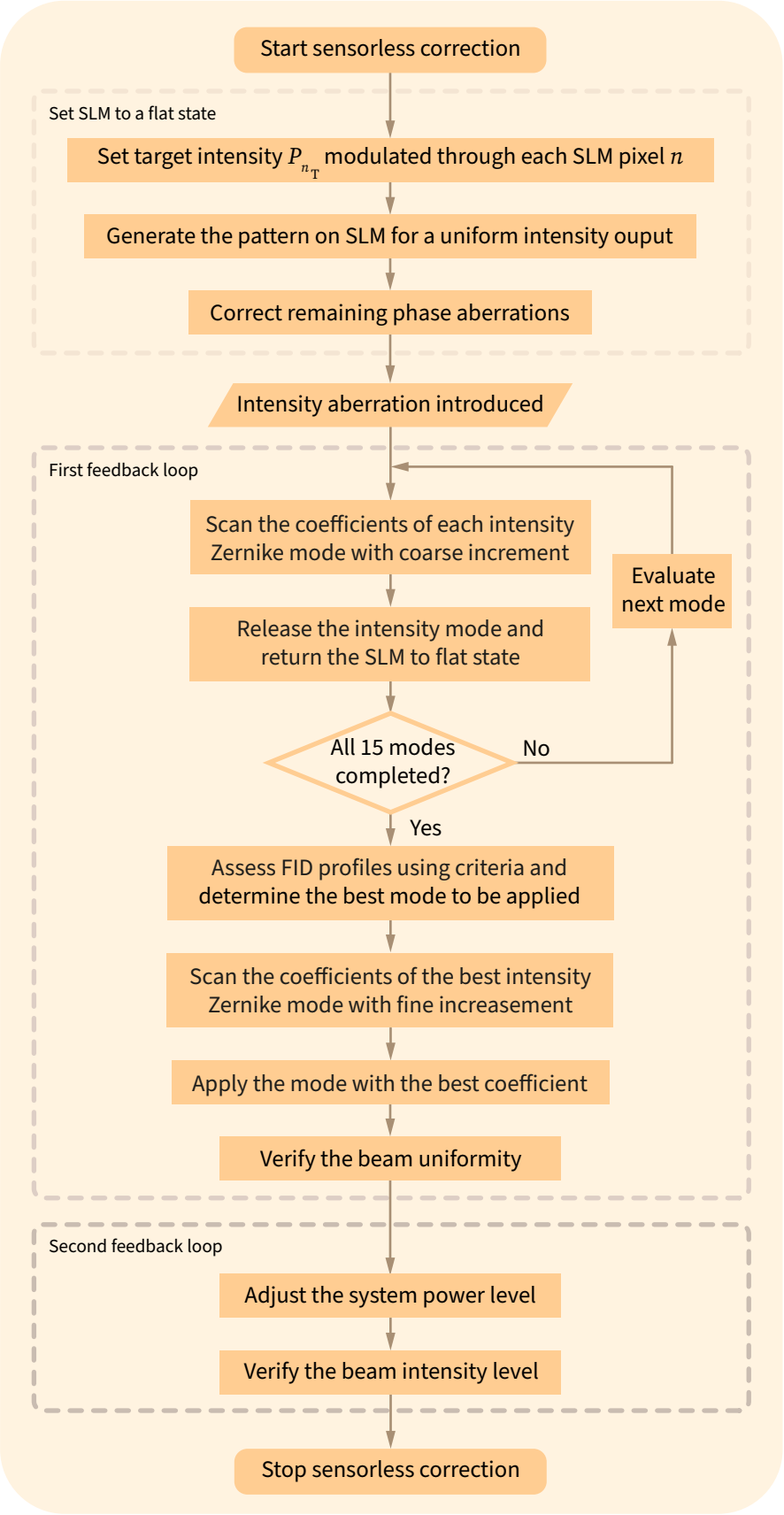

Figure 5.15: Flowchart outlining the sensorless correction methodology. A comprehensive visualisation of the sensorless correction workflow is presented. Steps from the initial calibration of the SLM using a calibrated LUT, through the iterative application and evaluation of intensity Zernike modes, to the final adjustments for both intensity profile uniformity and beam intensity level restoration are summarised.

Subsequent assessment of the captured focal plane image typically revealed a significant enhancement in image quality, though some residual discrepancies between the actual and the theoretically ideal focal spots may persist. These discrepancies were generally attributed to phase aberrations that occurred during the modulation of the correction pattern on the SLM. To address these residual phase aberrations, a conventional phase AO correction algorithm was introduced using the DM.

Following the initial correction loop that restored the intensity profile uniformity using the selected mode and coefficient, a second correction loop was initiated to reinstate the intensity level of the beam. This adjustment was accomplished by modifying the ND filter of the laser source to return the beam intensity to its original level. The entire sensorless correction workflow is depicted in the flowchart provided in **Figure 5.15**.

5.4 Experiment Results

Contrary to conventional AO techniques that assess phase and/or polarisation aberrations on the pupil plane, I-AO demands a comprehensive evaluation of intensity variation across the pupil plane, achievable through either direct measurement or indirect estimation (e.g., model-based optimisation of focal quality). Therefore, we propose two distinct I-AO methods for different imaging applications in previous Section 5.3. The first approach involves direct sensing using an aberration sensor, referred to as sensor-based AO. The second approach relies on indirect optimisation, known as sensorless AO[12,97,227]. Further elaboration and validation of both approaches are discussed in subsequent sections. For both I-AO methods, two important points are emphasised. First, the methods integrate the correction of both phase and intensity aberrations, addressing any additional phase errors induced by the AO device itself (geometrical effects) during the correction process. Second, it advances beyond the single closed-loop

feedback mechanism of conventional AO to incorporate a dual-loop feedback correction. The additional loop adds total intensity recovery to the restoration of phase and intensity uniformity. Further details will be elaborated in the following sections.

5.4.1 Sensor-Based Intensity Aberration Correction

The sensor-based I-AO approach goes through the following pipeline: 1) An intensity sensor, such as a monochrome camera, first acquires a reference frame by capturing the full intensity profile of the SLM in its flat state with no intensity aberration. This intensity profile was taken at a plane corresponding to the conjugate pupil plane of the objective lens in the aberrated imaging system. Details of how to calibrate the flat state of the SLM-based corrector, the relationship between SLM retardance and I-AO corrector intensity values, as well as the intensity compensation algorithm have already been elaborated in Section 5.2.3; 2) The distorted intensity profile in the presence of intensity aberrations was then measured to serve as feedback data; 3) The retardance values required for intensity pre-compensation was then calculated at the conjugate plane of the I-AO corrector to facilitate the first feedback correction loop (S1 in Figure 5.12); 4) These retardance values were applied to the I-AO corrector to achieve uniform intensity across the pupil. 5) The DM was further used to perform sensorless AO and compensate for both the geometrical phase aberrations induced by the SLM itself, and the systematic phase errors throughout the system. 6) With a uniform intensity profile obtained at the focal plane, the attenuator after the light source was finally adjusted based on the reference data to enhance the total intensity value, marking the end of the second feedback loop (S2 in Figure 5.12). Details of the sensor-based dual closed-loop feedback correction algorithm were described in Section 5.3.1. This methodology was validated through two experiments to showcase its viability.

The first experiment demonstrated the necessity of I-AO. Initially, an external spatially varying intensity aberration was introduced into an optical focusing system (see **Figure 5.16**,

I-AO off) and an attempt was made to carry out sensorless phase AO correction via the DM (see Figure 5.16, Phase AO on). The results show a persistent focus aberration, indicating that conventional phase AO correction cannot fully rectify the intensity aberrations due to their impact on interference in the focal plane, and results in an imperfect focal spot. After removing the intensity aberration, the original intensity distribution was restored across the pupil to achieve a diffraction-limited focal spot. From the above validation, it was confirmed that I-AO is essential for complete intensity aberration correction. The measurement of the intensity values across a cross-section of the focal spot for each step are presented in **Figure 5.17**.

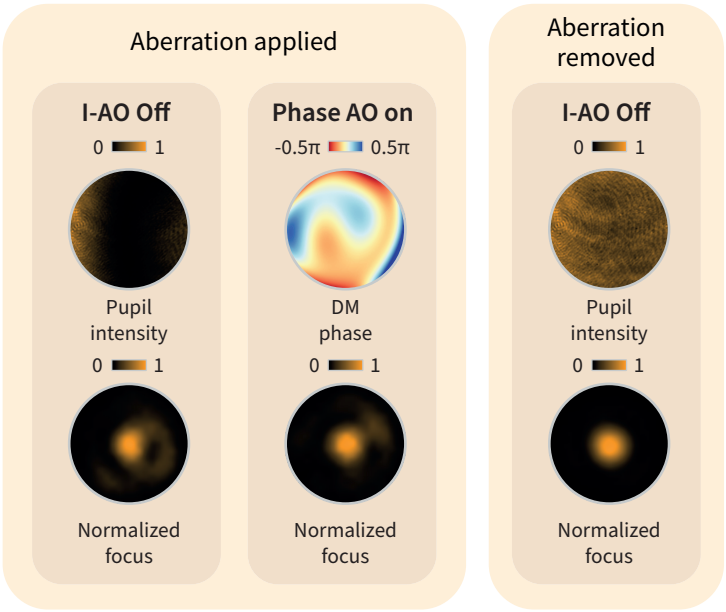

Figure 5.16: Experimental demonstration of the need for I-AO. Demonstration of the necessity of I-AO for intensity aberration correction by comparison with the results obtained using traditional phase-only AO correction. The intensity profile of the pupil, the phase applied to the DM and the profile of the focus are presented, for the conditions of I-AO off (with intensity aberration applied but no intensity aberration correction and no phase-only AO correction), phase-only AO on (intensity aberration applied, but no intensity aberration correction), I-AO off (without intensity aberration applied and no phase-only AO correction), separately.

The necessity of the I-AO corrector was then established by demonstrating that a single DM cannot adequately compensate for introduced intensity aberrations. Random intensity aberrations induce significant distortions in the FID , and cannot be corrected by conventional phase-only AO using a single DM, as observed from the results captured at the pupil and focal

planes. To demonstrate the consistency of system aberrations throughout the experiment and how the observed intensity aberrations were not attributed to these system aberrations, the external intensity aberration pattern was removed by restoring the SLM back to its flat state. In this condition, only inherent system aberrations were present. After the correction with conventional phase AO, the FID profile was restored to its original Airy disk shape, as observed at the pupil and focal planes. This outcome confirms that after the system aberrations have been corrected with phase AO, any distortion of the intensity profile in the system will be due to the intensity aberrations introduced throughout the experiment.

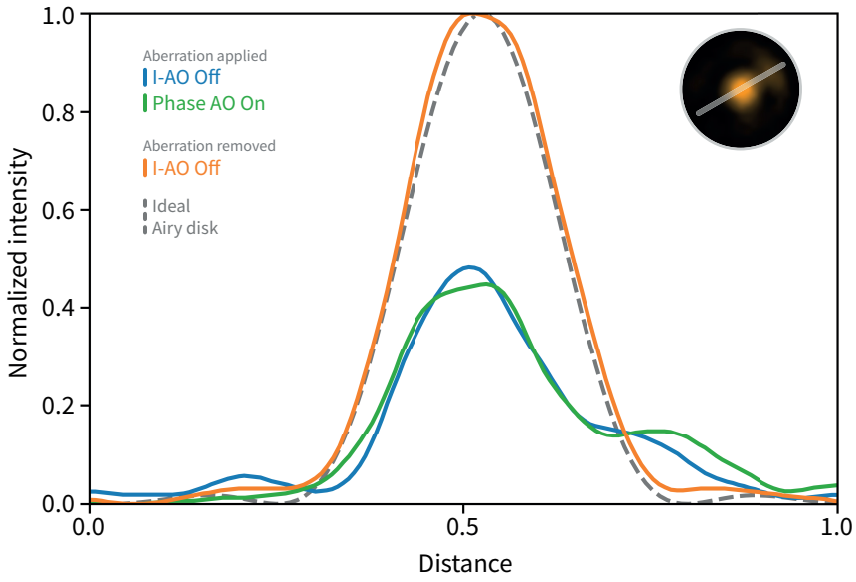

Figure 5.17: Cross-section of the FID in the experiment proof of the need for I-AO. Intensity profile plots along a sampled cross-section of the focus for each step in Figure 5.16. A plot of the ideal Airy disk is shown by the dashed line.

In the second experiment, a sensor-based I-AO correction was applied for the same intensity aberration as in the first experiment, with pupil and focal plane profiles depicted in **Figure 5.18** (I-AO off). Following the pipeline outlined earlier, the first feedback loop, S1, corrected the intensity profile based on the measured pupil image, resulting in a uniform intensity profile across the pupil as shown Figure 5.18 (I-AO S1).

Comparing the intensity profile along a cross-section of the focus before and after I-AO correction revealed marked improvements in both pupil intensity uniformity and the overall focal spot quality. Subsequently, sensorless phase adaptive optics (Phase AO on) addressed the remaining phase aberrations; and the final feedback loop S2 (I-AO S2), which actively corrected these intensity aberrations, demonstrated a clear improvement in the pupil intensity level. The figure highlights the gradual reduction in intensity irregularities as I-AO was progressively implemented, providing a clear comparison between the focal spot before and after intensity correction.

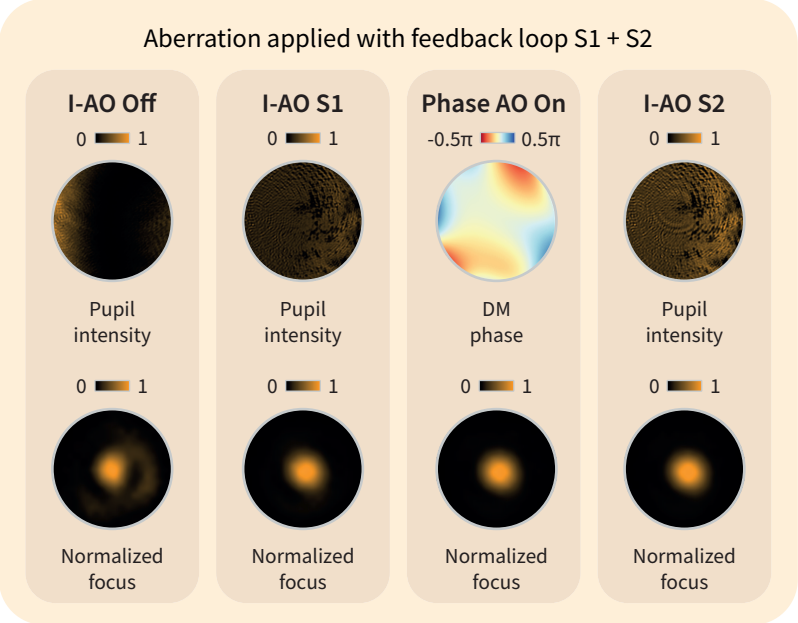

Figure 5.18: Experiment results for the sensor-based method. Sensor-based I-AO correction for the intensity aberration with a dual feedback loop. The intensity profile of the pupil, the phase applied to the DM, and the profile of the focus for each step are presented.

Figure 5.19 presents the cross-sectional views of the focal spot for each step of the correction process. Initially, without any correction, the cross-section exhibits significant distortions, with uneven intensity distribution that compromises focus quality. After applying phase AO, the central portion of the focus showed improvement, yet aberrations persisted, particularly in the outer regions of the beam. When feedback loop S1 was engaged, the intensity aberrations

were actively mitigated, resulting in a more uniform intensity profile. The cross-sections show how the aberration-induced intensity dips and peaks were progressively smoothed, leading to an almost ideal focal spot profile. The final correction loop S2 further corrects the profile closely in align with the theoretical Airy disk, which demonstrates the ability of the system to approach diffraction-limited performance when both phase and intensity corrections are applied.

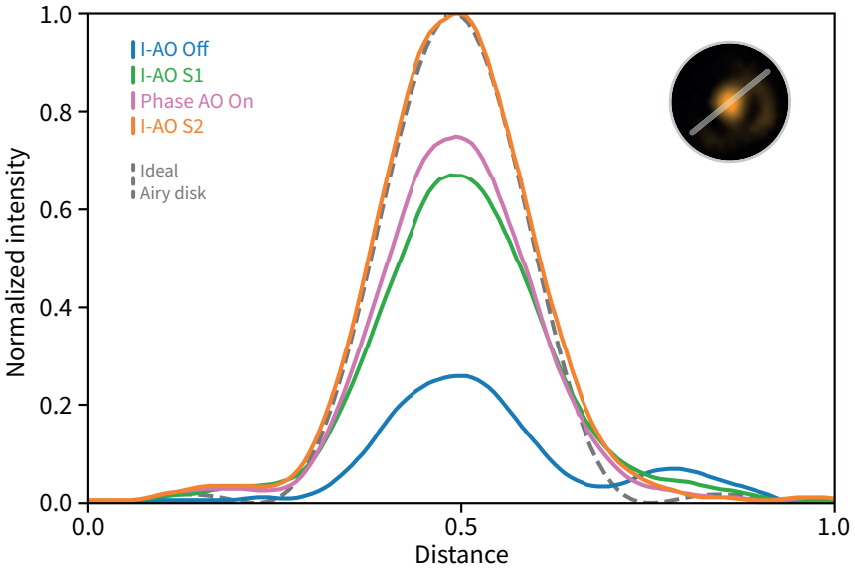

Figure 5.19: Cross-section of the FID for the sensor-based method. Intensity profile plots along a sampled cross-section of the focus for each step in Figure 5.18 with a dual feedback loop. A plot of the ideal Airy disk is shown by the dashed line.

The analysis of these results confirms that while phase AO alone improves focus quality by correcting phase distortions, it is insufficient for achieving optimal results in systems where intensity aberrations are significant. The implementation of I-AO not only compensates for phase issues but also corrects intensity distribution, yielding a more uniform and concentrated focal spot. The dual-feedback mechanism thus plays a critical role in refining both the intensity uniformity and the overall level, as demonstrated by the nearly ideal focus obtained after the correction process.

5.4.2 Sensorless Intensity Aberration Correction

Here, the feasibility of the sensorless I-AO approach is demonstrated, eliminating the need for direct sensor-based measurement of the intensity variation at the pupil plane, which is usually a challenging task in compact optical systems. Instead, this approach indirectly infers intensity aberrations by analysing the image of the focal spot as feedback. Mimicking conventional phase AO, and as discussed in Section 5.1.2, this method applies a series of pre-designed aberration correction patterns sequentially to the AO device, with the optimal correction determined by assessing the image quality metric of the low spatial frequency[283] and the focus spot circularity. It is crucial to note that: 1) The non-periodic and power-related nature of intensity variations complicates the use of orthogonal superposition of Zernike-like modes for correction, as mentioned in Section 5.1.2; 2) Similar to the sensorless technique in modern V-AO correction methods[227], the I-AO approach has to deal with the complex interplay between intensity and phase through geometrical links when modulating the SLM, suggesting the need for simultaneous correction of any additional phase errors introduced by the SLM during the intensity aberration correction.

During the correction process, 15 intensity Zernike modes, including piston, tip, and tilt – commonly omitted in conventional phase AO – are scanned and analysed. For each mode, images of the focal spot are captured at varying amplitudes. The optimal correction is determined by evaluating two key image metrics mentioned in Section 5.3.2: low spatial frequency and spot circularity, which are used to identify the best-performing intensity Zernike mode and its corresponding coefficient. Experiments were conducted to validate the sensorless approach for I-AO correction, employing the same external intensity aberration as that used during sensor-based I-AO validation. Recall Figure 5.14 which outlined the sensorless I-AO procedure. As discussed, it is similar to the sensor-based method, which also utilised a dual

closed-loop feedback loop, but in this case it relies on the image of the focal spot to infer the aberration indirectly. **Figure 5.20** shows the results for each correction step.

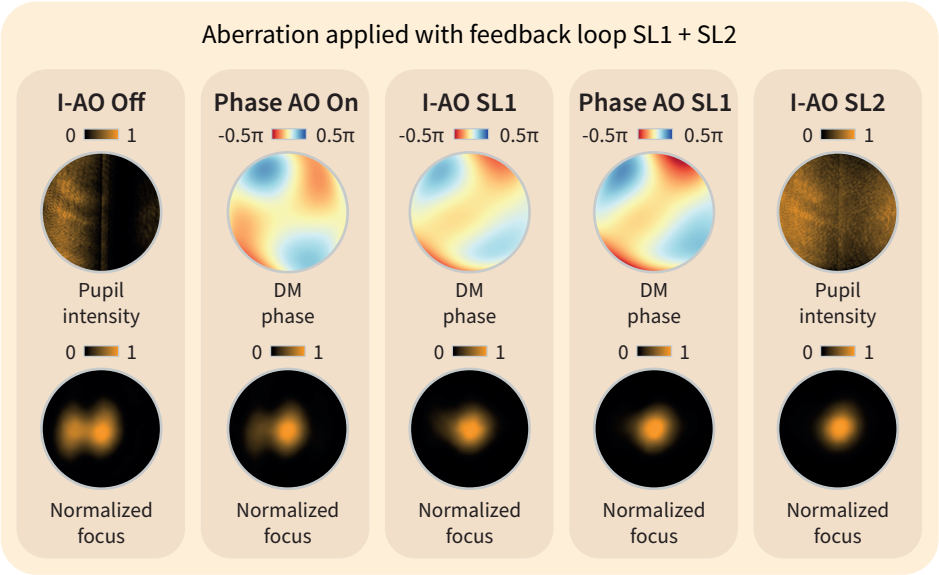

Figure 5.20: Experiment results for the sensorless method. Sensorless I-AO correction procedure for intensity aberration with dual closed-loop feedback correction. The intensity profile of the pupil, the phase applied to the DM and the intensity profile of the focus are presented, for the conditions of I-AO off, phase-only AO on, I-AO SL1, and I-AO SL2, separately.

Initially, the intensity aberration created an irregular focal spot (see Figure 5.20, I-AO off). Conventional sensorless phase-only AO was then applied to address the phase errors in the system introduced by the optical components, with the applied correction phase pattern and post-correction focal image shown in Figure 5.20 (Phase AO on). Following this, sensorless I-AO scans through a pre-determined set of intensity Zernike modes, identified the optimal SLM phase pattern composed of the best intensity Zernike mode and corresponding coefficient that yielded the highest image metric. The shape of the restored focal spot is demonstrated in Figure 5.20 (I-AO SL1). Conventional sensorless phase-only AO further corrects for residual phase errors and enhances intensity uniformity. The final DM phase pattern and resulting focal spot image are shown in Figure 5.20 (Phase AO on). Finally, feedback loop SL2 compensates for any intensity loss (see Figure 5.20, I-AO SL2), with the intensity profile plots along a cross-

section of each focal spot displayed in **Figure 5.21**. Comparing the beam intensity level and profile between the ideal and corrected focus spots reveals a clear improvement in the intensity profile quality during the sensorless correction step.

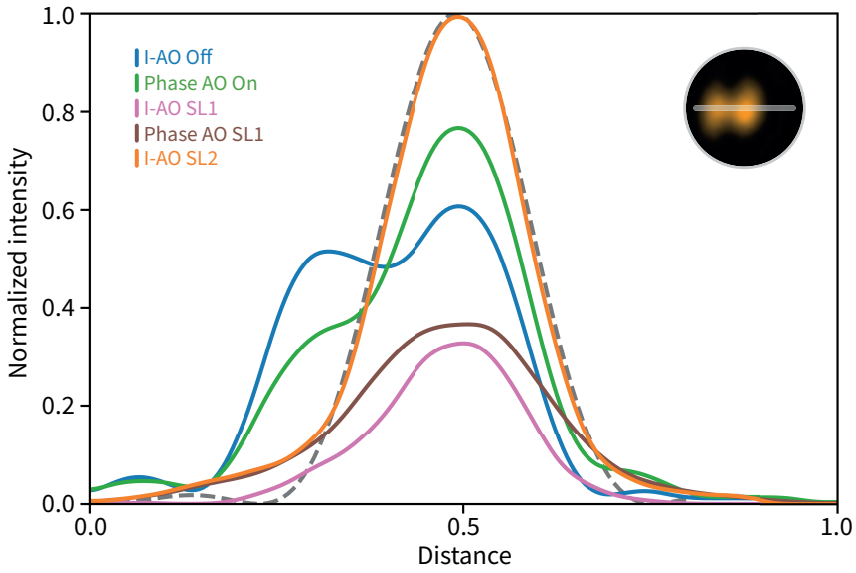

Figure 5.21: Cross-section of the FID for the sensorless method. Plots of the intensity profiles along a sampled cross-section of the focus for each step during the sensorless I-AO correction. A plot of the ideal Airy disk is shown by the dashed line.

The measurement results confirm the potential of sensorless I-AO for future applications requiring both intensity and phase correction, particularly in scenarios where adding extra hardware to measure the intensity aberration directly is constrained, highlighting its significance for indirect optimisation in compact optical imaging systems.

5.4.3 Discussion

In contrast to conventional AO, where the aberration profile on the pupil plane is not the compulsory information for conducting aberration correction, I-AO requires a method to determine the full intensity variation on the pupil plane, either directly from intensity sensor measurement, or indirectly from intensity aberration estimation (e.g., model-based optimisation of focal quality) through the adjustment of the intensity profile in the pupil domain. Based

on these principles, an I-AO technique has been introduced in this chapter in two different formats that can be applied in different scenarios. The first is the direct sensing via an intensity-aberration sensor, which is usually referred to as sensor-based AO. The second approach relates to the indirect optimisation methods, which are usually named as sensorless AO.

For the I-AO technique proposed, the following unique points are highlighted. First, it is a joint correction system encompassing both phase and intensity, which takes extra phase errors introduced by the AO device itself into consideration during the correction process. Second, the traditional single feedback closed-loop correction process for conventional AO has been extended to dual-loop correction, including restoration of the phase and intensity uniformity via a cascade of AO devices as well as recovery of the total intensity values via a direct modulation of the light source.

5.5 Summary

In summary, in this chapter, the concept of conventional phase AO has been extended to the intensity domain by jointly correcting intensity and phase aberration. I-AO can either be implemented using dual-loop feedback in a sensor-based approach using a camera, or through implementations of sensorless I-AO based on the focus spot measurement only, which harnesses novel intensity modes as well as advanced sensorless processes.

These two approaches provide a versatile toolkit for the compensation of intensity aberrations in a wide range of optical systems, which can be chosen to fit real-world applications. The sensor-based I-AO provides a full understanding of the intensity profile, hence enabling the I-AO corrector to do the pre-compensation directly. It should be noted that for I-AO, it should focus on intensity correction specifically. Considering that certain AO devices themselves (e.g., SLMs) would introduce extra unexpected phase aberration, and the possibility that the system

can exhibit residual phase aberration, a phase AO device (e.g., DM) was also included in the I-AO system as a key part to conduct phase compensation during the correction process.

The sensorless I-AO is a first attempt for using non-orthogonal modes to give a proof-of-concept demonstration for the use of aberration correction, which unlocks new areas to be explored. Along these lines, the modes used in this chapter are Zernike shape, which may or may not be the best mode to be applied for non-orthogonal modes, other modes such as Zonal[284] or newly designed modes may be more optimal. Also, considering the intensity modes for the sensorless optimisation process, new image metrics as well as different sensorless I-AO processes are areas that warrant further investigation. Moreover, I-AO can be used further in conjunction with vectorial adaptive optics to form a full-field advanced AO approach.

Overall, this chapter proposes novel I-AO techniques for the correction of intensity and phase aberrations. With these intensity dual-loop feedback control methods, this novel AO technique would benefit various research areas, ranging from astronomical telescopes to microscopes, with potential application in galaxy characterisation to clinical diagnosis.

If, in a century or a millennium, our descendants walk among the stars, the masses will sing her praises.

— An epithet to Kristen Wright

CHAPTER 6

Optical Quasiparticle Generation using Liquid Crystals

6.1 Topology of Quasiparticles

6.1.1 Introductions

Optical quasiparticles, which leverage complex optical properties to create structured light fields with unique and robust topological features, have gained increasing attention due to their potential in advanced applications such as structured light generation and control[285–289]. Structured light, which involves manipulating light fields to have specific spatial distributions, polarisations, or phase patterns, plays a crucial role in the formation and control of these quasiparticles[13,290–292]. This chapter demonstrates optical skyrmionic and meronic beams which are complex photonic quasiparticles generated and manipulated with structured light. Methods to generate these beams using liquid crystal (LC)-based spatial light modulators (SLMs) are proposed. The proposed optical skyrmions and optical merons introduce new dimensions for processing, transferring, and storing information in a condensed light field, with the potential to extend communication channel bandwidth and pave the way for next-generation high-volume on-chip optical computing.

The topology of electromagnetic waves with complex and structured spin textures, initially discovered in particle physics and condensed matter physics, has become a focal point in re-

search for next-generation information technology[293,294]. Optical quasiparticles that emulate spin topology by utilising the physical properties of the optical field are attracting growing attention, promising a new era in structured light control and generation[285,287]. Among these, skyrmions, originating from structured electric fields in evanescent waves and magnetic materials, have become prominent research topologies[295]. Skyrmions were first proposed by British physicist Tony Skyrme in 1961 to describe the general structure of nucleons and have since been widely considered in various research contexts, including magnetic materials, LC, and Bose-Einstein condensates[296–300]. Skyrmions offer topological robustness against external perturbations and their versatile textures provide new degrees of freedom for information encoding, leading to innovative outcomes ranging from chiral magnets to surface plasmons[301,302].

Following initial discoveries in magnetic systems, topology-protected quasiparticles have been successfully realised across a range of classical platforms. In magnetic systems, these quasiparticles store data through their unique spin configurations, ensuring data integrity even under fluctuating conditions[303]. Unlike traditional magnetic storage methods, skyrmions can be densely packed without interference, offering significantly higher data densities[304]. This advantage makes skyrmion-based memory devices highly attractive for computing technologies focused on efficiency and reliability[305,306].

Building on these advancements in magnetic systems, new applications for quasiparticles are now being explored in optical systems[285,287,289]. Due to their topological protection, optical skyrmions exhibit remarkable stability and resistance to external disturbances, positioning them as a breakthrough in data storage and information processing[286,307]. This robustness reduces the risk of data corruption and loss, highlighting skyrmion-based storage as a promising future technology for computing[308].

By leveraging the topological properties of optical skyrmions, researchers are developing

advanced photonic devices that can manipulate light with unprecedented precision[289,293,309]. These devices can control the angular momentum and polarisation of light, which are critical for high-resolution imaging and optical communication systems[22,291,310]. Optical skyrmions can be utilised to achieve precise and stable manipulation of light fields, providing significant advantages in applications such as information processing and photonic circuitry[23,311]. Furthermore, the study of optical skyrmions is driving innovation in the design of new materials and photonic structures[312]. Towards this end, researchers are developing novel metamaterials that exhibit unique optical properties not found in natural materials[313]. These innovations are paving the way for breakthroughs in various fields such as optical computing, optical sensing, and laser technologies.

In photonic systems, the optical quasiparticles can be described by 3D Stokes vectors, representing vectors on the surface of the Poincaré sphere[314,315]. This topological structure can be excited from optical devices with spatially varying optical properties. Among various quasiparticles, merons, which share similarities with skyrmions, have gained special attention in recent research[316]. Meron topology originates from Yang-Mills theory and, due to its similarity to skyrmions, is also known as a half skyrmion or baby skyrmion[317]. The existence of meron topology has been reported in photonic crystals, liquid crystal-filled microcavities, and surface-plasmon polarisation[318,319]. Unlike skyrmions with complete circular symmetry, meron structures possess half of the skyrmion topology, leading to non-integer skyrmion numbers. Meron topology can also possess higher orders by increasing its vorticity while maintaining topological protection.

In this chapter, a novel technique to generate optical skyrmionic and meronic beams of multiple orders in optics is proposed through the modulation of the polarisation field of the incident beam. This approach is evaluated both theoretically and experimentally, demonstrating

the versatility and effectiveness of the method. The creation of these quasiparticle structures is achieved using a cascaded array of SLMs. Using these cascaded universal optical modulators, it is shown that the structured light can be modulated with a spatially varying vectorial field, allowing for the generation of optical skyrmionic and meronic beams in any higher order with significant flexibility. This controllable optical quasiparticle generator has the potential to support the next-generation information technology. The experimental verification of the topological protection for both skyrmionic and meronic beams are presented, highlighting their robustness and stability. The ability to engineer and control these complex topological structures in light could lead to significant advancements in a range of fields including advanced microscopy and enhanced communication systems.

6.1.2 State of Polarisation

The polarisation of light is a fundamental element to construct optical beams and generate complex vector fields. In the study of light polarisation, Jones calculus and Stokes parameters are two fundamental frameworks for describing the state of polarisation (SoP).

Considering transverse light propagating in the z direction, the plane-wave component of the optical field in terms of complex quantities can be expressed as:

$$E_x(z,t) = E_{0x}\, e^{i(\omega t - kz + \delta_x)} \tag{6.1}$$

$$E_y(z,t) = E_{0y}\, e^{i(\omega t - kz + \delta_y)} \tag{6.2}$$

where z is the distance along the propagation direction, t is the time, ω is the angular frequency, k is the wave factor and δ_i is the initial phase for each axis. For polarisation transformation in an optical system, only the phase difference between the two components is of interest. Therefore, by suppressing the propagator $\tau = \omega t - kz$ and extracting the common phase δ_x and scalar

intensity $\sqrt{E_{0x}^2 + E_{0y}^2}$, Equation 6.1 and Equation 6.2 can be simplify into a 2×1 vector **E** as

$$\mathbf{E} = \sqrt{E_{0x}^2 + E_{0y}^2}\, e^{i\delta_x} \begin{bmatrix} \cos\alpha \\ \sin\alpha\, e^{i\delta} \end{bmatrix} \tag{6.3}$$

where $\cos\alpha = E_{0x}/\sqrt{E_{0x}^2 + E_{0y}^2}$, $\sin\alpha = E_{0y}/\sqrt{E_{0x}^2 + E_{0y}^2}$ and $\delta = \delta_y - \delta_x$. Since phase has the period of 2π, the phase difference δ has the range from $-\pi$ to π. Therefore, the normalised Jones vector **j** can be represented as

$$\mathbf{j} = \begin{bmatrix} \cos\alpha \\ \sin\alpha\, e^{i\delta} \end{bmatrix}. \tag{6.4}$$

By restoring the propagator $\tau = \omega t - kz$ and taking the real parts, Equation 6.1 and Equation 6.2 can be rewritten as

$$\frac{E_x}{E_{0x}} = \cos(\tau + \delta_x) = \cos\tau\cos\delta_x - \sin\tau\sin\delta_x \tag{6.5}$$

$$\frac{E_y}{E_{0y}} = \cos(\tau + \delta_y) = \cos\tau\cos\delta_y - \sin\tau\sin\delta_y. \tag{6.6}$$

Eliminating τ in Equation 6.5 and Equation 6.6 gives

$$\frac{E_x^2}{E_{0x}^2} + \frac{E_y^2}{E_{0y}^2} - 2\frac{E_x}{E_{0x}}\frac{E_y}{E_{0y}}\cos\delta = \sin^2\delta \tag{6.7}$$

where $\delta = \delta_y - \delta_x$.

Equation 6.7 is recognised as the equation of a rotated ellipse, indicating that the trace of the vector of the electromagnetic field of light follows an ellipse, known as optical polarisation. **Figure 6.1** shows the defined polarisation ellipse. The ellipse is inscribed within a rectangle whose edges are parallel to the coordinate axes x and y. The length of the rectangle edges can be determined by calculating the tangent points of the ellipse on the rectangle. Thus, the outer

boundary of the ellipse extends to $E_x = \pm E_{0x}$ and $E_y = \pm E_{0y}$.

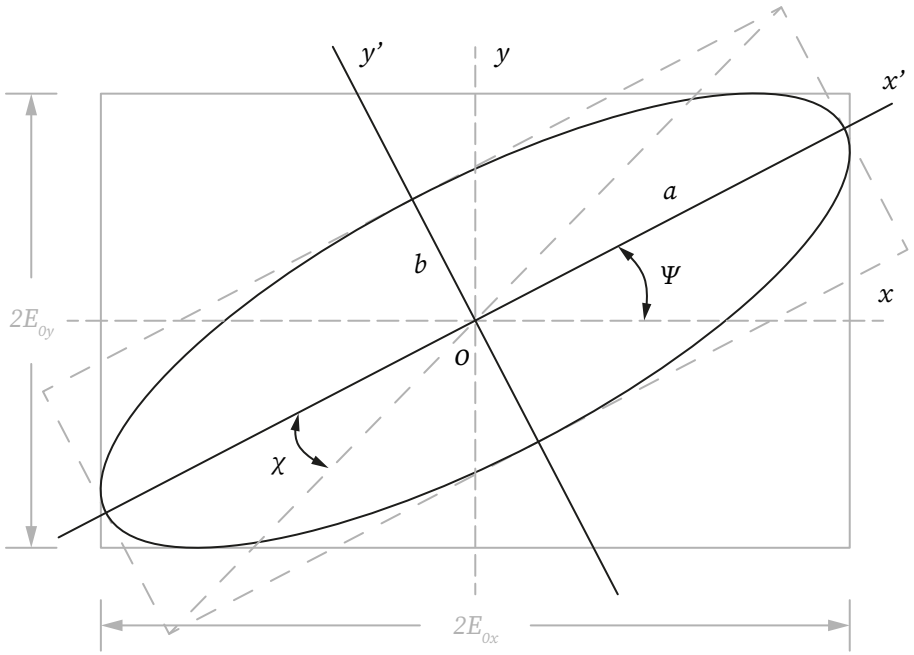

Figure 6.1: Illustration of the polarisation ellipse. The diagram depicts the geometric representation of the polarisation state of light, showing the orientation and ellipticity of the polarisation ellipse. The original axes are marked as x and y, while the rotated axes x' and y' align with the major and minor axes of the ellipse, whose lengths are a and b respectively. The ellipse is bounded in the rectangular box corresponding to electric field amplitudes $2E_{0x}$ and $2E_{0y}$ in the original axes. The rotation angle Ψ and the ellipticity χ are labelled as well. The rotation angle Ψ represents the angle between two sets of the axes and the ellipticity χ is formed by the major and minor axes of the ellipse.

Since it is a rotated ellipse, it is important to know its angle of rotation Ψ and the ellipticity angle χ, in connection with E_{0x}, E_{0y} and δ, which are the crucial parameters to describe the ellipse. For the rotated ellipse illustrated in Figure 6.1, the rotation angle Ψ is defined as the rotation from the original axis x towards the new axis x', ranging from 0 to π, and it can be represented as[278]

$$\tan 2\Psi = \frac{2E_{0x}E_{0y}\cos\delta}{E_{0x}^2 - E_{0y}^2} = \tan 2\alpha \cos\delta. \tag{6.8}$$

From the geometry of the rotated ellipse, the angle of ellipticity χ is defined by

$$\sin 2\chi = \frac{2E_{0x}E_{0y}\sin\delta}{E_{0x}^2 + E_{0y}^2} = \sin 2\alpha \sin\delta \tag{6.9}$$

where the range of angle χ falls in $[-\pi/4, \pi/4]$. Therefore, for an arbitrary polarisation state represented by normalised Jones vector **j** characterised by auxiliary angle α and phase difference δ, it has corresponding ellipses characterised with rotation angle Ψ and ellipticity χ, as expressed in Equation 6.8 and Equation 6.9.

The above analysis of the polarisation ellipse provides a useful representation of polarised light. By using the Jones vector, it provides a concise mathematical description of polarised light with time factors. In practical applications, it is often required to represent the polarisation state in a more concise way without time factors. This is achieved through the Stokes parameters, which offer a description of the SoP of polarised light by averaging the value of optical field over time. Unless specified otherwise, the light discussed in this chapter is fully polarised light. By expressing the optical amplitudes in terms of complex quantities as given in equations Equation 6.1 and Equation 6.2, the time-averaging process can be achieved by representing the real optical amplitudes in terms of the complex amplitudes. Thus the Stokes parameters for a plane wave are now obtained from the formula

$$S_0 = E_x E_x^* + E_y E_y^* \tag{6.10}$$

$$S_1 = E_x E_x^* - E_y E_y^* \tag{6.11}$$

$$S_2 = E_x E_y^* + E_y E_x^* \tag{6.12}$$

$$S_3 = i(E_x E_y^* - E_y E_x^*). \tag{6.13}$$

Substituting Equation 6.1 and Equation 6.2 into the above equations gives

$$S_0 = E_{0x}^2 + E_{0y}^2 \tag{6.14}$$

$$S_1 = E_{0x}^2 - E_{0y}^2 \tag{6.15}$$

$$S_2 = 2E_{0x}E_{0y}\cos\delta \tag{6.16}$$

$$S_3 = 2E_{0x}E_{0y}\sin\delta. \tag{6.17}$$

Recalling Equation 6.8 and Equation 6.9, the rotation angle Ψ and the ellipticity χ of the polarisation ellipse can be represented with Stokes parameters as

$$\tan 2\Psi = \frac{2E_{0x}E_{0y}\cos\delta}{E_{0x}^2 - E_{0y}^2} = \frac{S_2}{S_1} \tag{6.18}$$

$$\sin 2\chi = \frac{2E_{0x}E_{0y}\sin\delta}{E_{0x}^2 + E_{0y}^2} = \frac{S_3}{S_0}. \tag{6.19}$$

By putting the four Stokes parameters into a column form, the Stokes vector can be formed as

$$\mathbf{S} = \begin{bmatrix} S_0 \\ S_1 \\ S_2 \\ S_3 \end{bmatrix} = \begin{bmatrix} E_{0x}^2 + E_{0y}^2 \\ E_{0x}^2 - E_{0y}^2 \\ 2E_{0x}E_{0y}\cos\delta \\ 2E_{0x}E_{0y}\sin\delta \end{bmatrix}. \tag{6.20}$$

For fully polarised light, the total intensity I_0 can be represented as

$$I_0 = E_0 \cdot E_0^\dagger = E_{0x}^2 + E_{0y}^2 = S_0. \tag{6.21}$$

Recalling that $\cos\alpha = E_{0x}/\sqrt{E_{0x}^2 + E_{0y}^2}$ and $\sin\alpha = E_{0y}/\sqrt{E_{0x}^2 + E_{0y}^2}$, therefore, the normalised Stokes vector can be reformed as

$$\mathbf{S} = \begin{bmatrix} S_0 \\ S_1 \\ S_2 \\ S_3 \end{bmatrix} = \begin{bmatrix} 1 \\ \cos 2\alpha \\ \sin 2\alpha\cos\delta \\ \sin 2\alpha\sin\delta \end{bmatrix}. \tag{6.22}$$

Apart from using the auxiliary angle α and phase difference δ, the normalised Stokes vector can also be expressed in terms of the rotation angle Ψ and the ellipticity χ of the polarisation

ellipse using the following relationships rewritten from Equation 6.18 and Equation 6.19

$$S_2 = S_1 \tan 2\Psi \tag{6.23}$$

$$S_3 = S_0 \sin 2\chi \tag{6.24}$$

$$S_0^2 = S_1^2 + S_2^2 + S_3^2. \tag{6.25}$$

Thus the normalised Stokes vector can also be represented as

$$\mathbf{S} = \begin{bmatrix} S_0 \\ S_1 \\ S_2 \\ S_3 \end{bmatrix} = \begin{bmatrix} 1 \\ \cos 2\chi \cos 2\Psi \\ \cos 2\chi \sin 2\Psi \\ \sin 2\chi \end{bmatrix}. \tag{6.26}$$

The Stokes parameters in Equation 6.26 are analogous to geographic coordinates, enabling a comprehensive description of the polarisation state of an optical beam. By expressing polarisation in terms of the angles χ and Ψ, we can effectively represent its ellipticity and orientation on a unit sphere. This spherical representation, introduced by Henri Poincaré in 1892, is termed the Poincaré sphere. Poincaré's method involved initially representing the polarisation equations within a complex plane and subsequently projecting this plane onto a sphere via stereographic projection. This approach provides a powerful visual tool for analysing polarisation states, facilitating the understanding of phenomena such as phase shifts and elliptical polarisation. Additionally, the Poincaré sphere aids in visualising the transformation of polarisation states under various optical operations. **Figure 6.2** illustrates the Poincaré sphere, depicting an arbitrary polarisation state P on its surface, thus demonstrating the utility of this model in visualising and interpreting the intricate characteristics of polarised light.

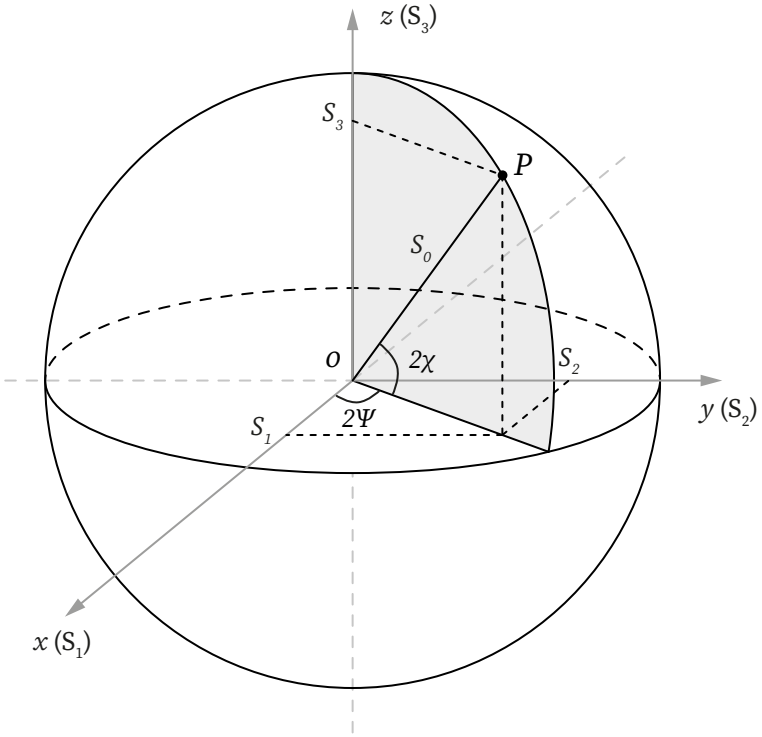

Figure 6.2: Illustration of the Poincaré sphere. The diagram represents the SoP of light, with points on the sphere surface corresponding to different polarisation states of fully polarised light. The axes S_1, S_2 and S_3 denote the Stokes parameters, which describe the polarisation state. The angle 2χ represents the ellipticity angle, while 2Ψ indicates the rotation angle of the polarisation ellipse. The radius S_0 represents the total intensity of the light. For fully polarised light, the Stokes parameters satisfy $S_0^2 = S_1^2 + S_2^2 + S_3^2$.

In favour of the following illustration of the SoP in the upcoming figure, the universal 2D colour bar for the figures is demonstrated. The coordinate chosen to represent the points in the RGB colour model is HSL, where each colour has three values (H, S, L) standing for hue, lightness and saturation. Saturation is fixed at its maximum value $S = 1$ for this colour bar, lightness L is related to the ellipticity χ in the the polarisation ellipse and hue H is to represent the rotation angle Ψ. The colour bar is presented in **Figure 6.3** with 2 labels on each axes, representing the hue H and lightness L in HSL colour coordinate as well as the polarisation ellipse parameters rotation angle Ψ and ellipticity χ they represent.

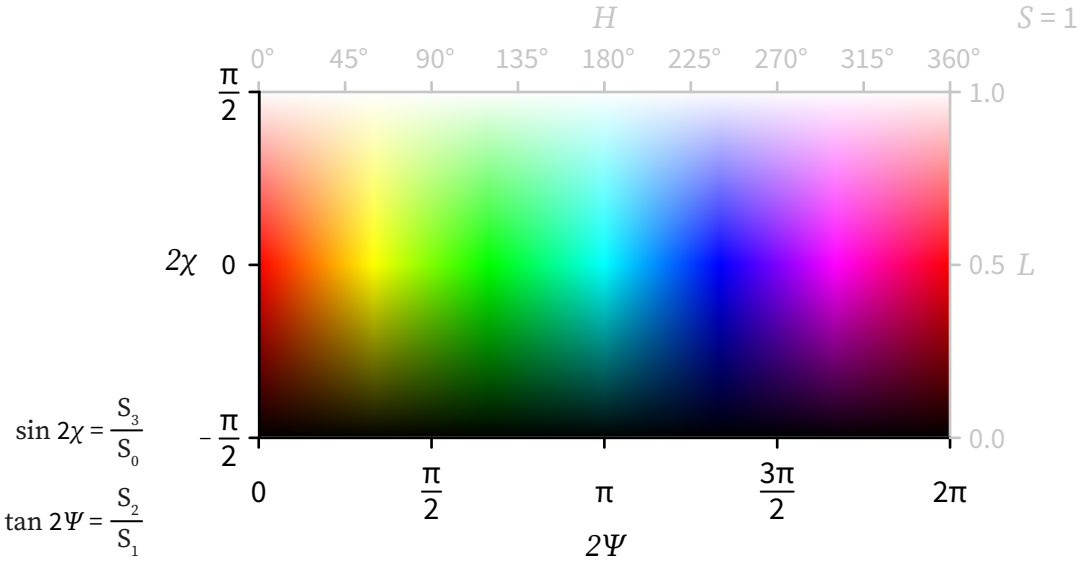

Figure 6.3: Illustration of the colour map for the SoP. This figure presents a universal 2D colour bar using the HSL (Hue, Saturation, Lightness) model to represent the states of polarisation. Saturation (S) is fixed at its maximum value ($S = 1$), while lightness (L) correlates with the ellipticity (χ) of the polarisation ellipse, and hue (H) represents the rotation angle (Ψ). The top axis indicates the hue H in degrees, corresponding to the rotation angle Ψ, and the right axis indicates the lightness L, corresponding to the ellipticity χ. This colour bar serves as a visual tool for interpreting and analysing the polarisation states depicted in subsequent figures.

Lightness (L) in the HSL model corresponds directly to the ellipticity (χ) of the polarisation ellipse, providing a visual indication of how stretched the ellipse is. Higher lightness values indicate greater ellipticity, making it closer to pure white and easy to discern different polarisation states at a glance. Hue (H), on the other hand, is used to represent the rotation angle (Ψ) of the polarisation ellipse, allowing for a straightforward depiction of the ellipse orientation for the colour.

The colour bar, shown in Figure 6.3, includes labels on each axis that not only indicate the HSL values (hue H and lightness L) but also correspond to the polarisation ellipse parameters they represent (rotation angle Ψ and ellipticity χ). This dual labelling provides a comprehensive tool for visualising and interpreting the characteristics of polarised light in a clear and intuitive manner.

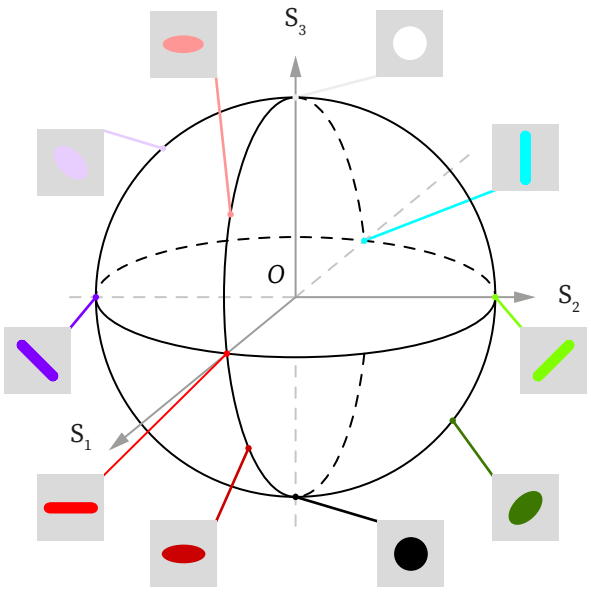

Figure 6.4: Visualisation of common polarisation states on the Poincaré sphere. This figure illustrates various common states of polarisation represented on a Poincaré sphere. Each point on the sphere corresponds to a distinct polarisation state, depicted through different colours and orientations. The axes S_1, S_2 and S_3 represent the Stokes parameters, which describe the polarisation state in 3D space. The insets show the corresponding polarisation ellipses for each state, demonstrating their respective orientations and ellipticities, with colourful polarisation ellipses. This visualisation aids in understanding how different polarisation states can be mapped onto the Poincaré sphere and analysed effectively.

Additionally, examples of common states of polarisation are provided in **Figure 6.4** for quick reference. These examples illustrate how different polarisation states appear within the HSL colour model, demonstrating the practical application of this visualisation technique in representing various polarisation states. The figures effectively demonstrate how different states of polarisation can be visually represented and analysed using the HSL colour model.

6.1.3 Optical Skyrmions and Optical Merons

Topological characteristics inherent in an optical vector field configuration in a 2D system can be formulated as follows[305]

$$S = \frac{1}{4\pi} \iint_{\sigma} \mathbf{n} \cdot \left(\frac{\partial \mathbf{n}}{\partial x} \times \frac{\partial \mathbf{n}}{\partial y} \right) dxdy \tag{6.27}$$

where S represents the skyrmion number (or the topology charge in general); $\mathbf{n}(x, y)$ denotes the vector field responsible for constructing the optical skyrmions and optical merons and σ serves as the spatial boundary confining the field. The confinement can extend to infinity, marking the disposition of an isolated optical skyrmion or meron, or it can encapsulate a cell within a periodic distribution. The skyrmion number, which is an integer in the skyrmionic beams or a fractional value in the meronic beams, quantifies the rotational occurrences of the vector $\mathbf{n}(x, y) = \mathbf{n}(r\cos\varphi, r\sin\varphi)$ on the unit sphere. Thus, when mapping back onto the unit sphere, the vector $\mathbf{n}(x, y)$ can be expressed as $\mathbf{n} = \mathbf{n}(\cos\alpha(\varphi)\sin\beta(r), \sin\alpha(\varphi)\sin\beta(r), \cos\beta(r))$, where $\alpha(\varphi)$ and $\sin\beta(r)$ are the mapping function for the 2D system.

In paraxial beams, the spatially varying normalised Stokes vector $\mathbf{S}(x, y)$ of the transverse electric field, as a map onto the Poincaré sphere, can form these topologically protected 2D optical quasiparticles[226,320]. By using different SoP $\mathbf{S}(x, y)$, which has the necessary form required for $\mathbf{n}$, various fields can be generated. Certain technical considerations arise regarding the continuity of optical field structures, but these can be sidestepped by focusing on optical skyrmions, whose field distributions exhibit well-defined topological properties and approach stable configurations at their boundaries[321]. The topological protection of the field arises from two key principles: the fact that the degree of a continuous function is always an integer and that it remains unchanged under continuous deformations. The main idea here is then to harness the axis shapes and orientations of a cascade of arbitrary retarder arrays (e.g. LC devices) to form complex optical skyrmions, which will be expanded in the next section.

Additionally, the skyrmion number can be dissected into two topology parameters:

$$\begin{aligned} S &= \frac{1}{4\pi}\int_0^{r_\sigma} \sin\beta(r)\,\frac{d\beta(r)}{dr}\,dr \int_0^{2\pi}\frac{d\alpha(\varphi)}{d\varphi}\,d\varphi \\ &= \frac{1}{2}\int_{\beta(0)}^{\beta(r_\sigma)} \sin\beta\,d\beta \cdot \frac{1}{2\pi}\int_{\alpha(0)}^{\alpha(2\pi)} d\alpha \\ &= \frac{1}{2}[\cos\beta]_{\beta(0)}^{\beta(r_\sigma)} \cdot \frac{1}{2\pi}[\alpha]_{\alpha(0)}^{\alpha(2\pi)} \\ &= p \cdot v \end{aligned} \quad . \tag{6.28}$$

The polarity p, which is denoted as $\frac{1}{2}[\cos\beta]_{\beta(0)}^{\beta(r_\sigma)}$, represents how the vector varies along the radial direction of the 2D system. The vorticity v, which is denoted as $\frac{1}{2\pi}[\alpha]_{\alpha(0)}^{\alpha(2\pi)}$, plays a pivotal role in governing the distribution of transverse field components[289].

For the simplest skyrmion configuration, the topology spans the entire unit sphere. As a result, the unit polarity and vorticity are each equal to $p = \pm 1$ and $v = \pm 1$, respectively. When dealing with vector field that encompass multiple skyrmion topologies, the polarity and vorticity values are scaled accordingly. This leads to higher-order meron configurations, each with distinct skyrmion numbers. **Figure 6.5** illustrates typical examples of both simple low-order and complex high-order skyrmion configurations. Figure 6.5(a) links planar vector fields to fields on sphere surfaces, showing how states of polarisation are utilised to construct skyrmions. It features arrows that represent the normalised Stokes vector and ellipses that denote the polarisation ellipse at each position. Figure 6.5(b) presents the fundamental unit sphere of skyrmions where the skyrmion number S is 1. The vector field, Stokes vector field, and skyrmionic field are displayed correspondingly. Figure 6.5(c) and Figure 6.5(d) depict high-order skyrmions with elevated levels of polarity (p) and vorticity (v), respectively, accompanied by their associated Stokes vector fields and skyrmionic fields.

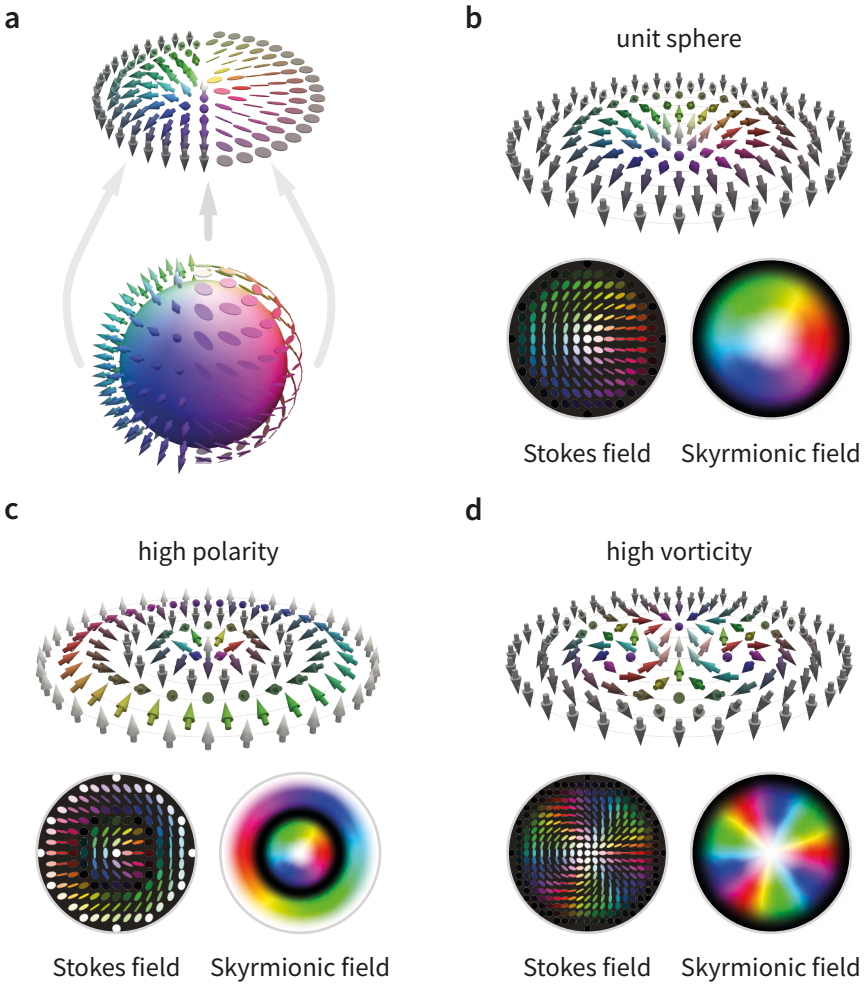

Figure 6.5: Topological configurations of skyrmions. The figure illustrates various skyrmions, emphasizing the diverse configurations of the vector field in different skyrmion structures. (a) shows the link between the planar vector fields and the field on sphere surface and how the states of polarisation are used to construct skyrmionic fields. The arrows represent the normalised Stokes vector and the ellipses are the polarisation ellipse for each position. (b) It shows the fundamental unit sphere of the skyrmionic field with the skyrmion number S being $S = 1$. The vector field is demonstrated with corresponding Stokes vector field and skyrmionic field. (c) A high-order skyrmion with high polarity p is illustrated with corresponding Stokes vector field and skyrmionic field. (d) A high-order skyrmion with high vorticity v is illustrated with corresponding Stokes vector field and skyrmionic field. The colour bar in this figure follows the definition in Figure 6.3.

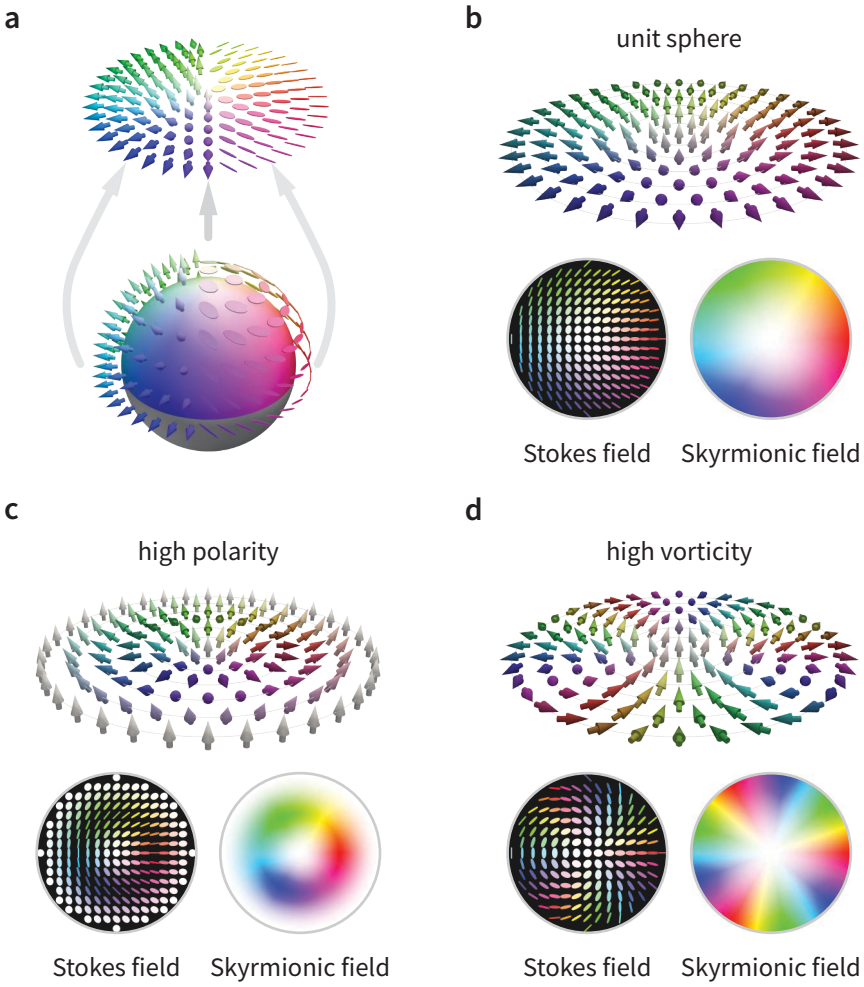

Figure 6.6: Topological configurations of merons. The figure illustrates various merons, emphasizing the diverse configurations of the vector field in different meron structures. (a) shows the link between the planar vector fields and field on sphere surface and how the states of polarisation are used to construct meronic fields. The arrows represent the normalised Stokes vector and the ellipses are the polarisation ellipse for each position. (b) shows the fundamental unit sphere of the skyrmionic field with the skyrmion number S being $S = 0.5$. The vector field is demonstrated with corresponding Stokes vector field and skyrmionic field. (c) A high-order meron with high polarity p is illustrated with corresponding Stokes vector field and skyrmionic field. (d) A high-order meron with high vorticity v is illustrated with corresponding Stokes vector field and skyrmionic field. The colour bar in this figure follows the definition in Figure 6.3.

In contrast, the simplest meron configuration only covers half of the unit sphere. Therefore, the unit polarity is $p = \pm 1/2$ and the unit vorticity remains $v = \pm 1$. For vector field exhibiting multiple meron topologies, their polarity and vorticity values will be multiples of these unit values, resulting in higher-order meron configurations with various skyrmion numbers. **Figure 6.6** showcase representative configurations of both simple low-order and complex high-order meron

configurations. In Figure 6.6(a), the vector field represents a simple meron mapping covering half the sphere, while Figure 6.6(b) shows the corresponding Stokes field and skyrmionic field for a unit sphere. Figure 6.6(c) and Figure 6.6(d) depict high-order meron with elevated levels of polarity (p) and vorticity (v), respectively, accompanied by their associated Stokes vector fields and meronic fields.

These visualisations highlight the distinct topological features of skyrmions and merons, demonstrating how the complexity of their configurations can be represented in an optical system by constructing the vector field with the SoP. These techniques allow researchers to observe the detailed structure and behaviour of these vector fields, providing insights into the stability and dynamics of optical skyrmions and optical merons.

6.2 Cascaded Liquid Crystal Devices for Beam Generation

6.2.1 Concept of Cascaded SLMs Configuration

Quasiparticles, emergent phenomena in condensed matter physics, can be constructed by structured light[321]. Structured light refers to light with tailored phase and polarisation properties, which can be precisely engineered using LC SLMs. These modulators offer the ability to finely control the polarisation states of light, providing a versatile tool for manipulating optical beams in novel ways.

In the context of complex light field generation with designed features, precise control over polarisation states is paramount. This control is achieved through a cascaded configuration where multiple reflective SLMs are placed sequentially along the light propagation path, positioned at normal incidence with minimal distance between them to avoid diffraction effects. Each SLM functions like an array of waveplates with adjustable retardance, enabling precise manipulation of the vectorial state of the beam profile. The modulation axis and retardance of

each SLM can be independently fine-tuned, allowing for the generation of complex structured light patterns. These patterns can facilitate advanced photonic applications, such as enhancing the capabilities of optical tweezers[322], improving imaging systems, and enabling sophisticated control in optical computing systems[323]. The concept illustration of cascaded SLMs structure is demonstrated in **Figure 6.7**.

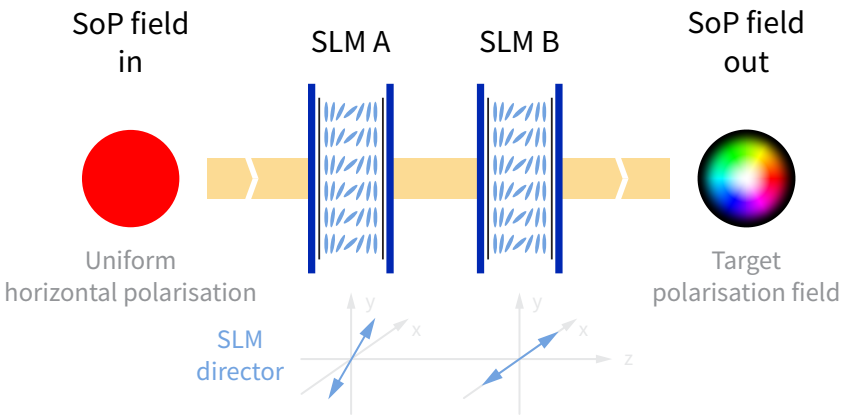

Figure 6.7: Conceptual illustration of the cascaded SLMs for structured light generation. The incoming beam with uniform horizontal polarisation passes through two cascaded SLMs. The first SLM is oriented at 45° to the input polarisation, followed by a second SLM which is also oriented at 45° to the first SLM. Each SLM acts as an adjustable waveplate, independently modulating the SoP of light. This configuration allows for precise control over the vectorial state of the beam profile, facilitating the creation of structured light patterns, such as skyrmionic beam demonstrated here as the output beam.

The core idea of using cascaded SLMs structure is to provide pixel-controlled, low functionality tunable devices to fully control the SoP of a light beam to generate arbitrary output polarisation field. SLMs offer both high spatial resolution and dynamic modulation capabilities, enabling the creation of intricate topological features and provide more precise manipulation of the retardance value and axis of the output Stokes field[139,324]. Leveraging the stacked configuration of SLMs, we attain novel topological control of light, enabling the generation of meronic beams in the polarisation field and theoretically realise any order of the optical skyrmionic and meronic beams. This active generation method employs cascaded SLMs as an array of arbitrary SoP modulators to transform a uniform polarisation field into a desired spatially varied

elliptical axes field distribution[274]. The simplicity of the method makes it ideal for exploring skyrmionic and meronic beams with higher orders and complexities, expanding its applicability across various fields.

For the generation of arbitrary polarisation states, a minimum of two SLM modulations is required, as the transition in polarisation state requires two free variables. The modulation axis of each SLM can be set at specific angles to achieve the desired polarisation state transitions, introducing phase shifts along the ordinary and extraordinary axes of the SLMs. Furthermore, in practical implementations, a waveplates assembly can be used between the SLMs to transform polarisation states without requiring mechanical rotation of the SLMs. Each SLM operates as a linear retarder with a fixed axis but variable retardance within a range of $\pm\pi$ radians. The change in polarisation state induced by each SLM pixel can be modelled as a transition on the Poincaré sphere, where cascaded SLMs produce sequences of rotations about different axes, enabling full control over the polarisation and phase of the light beam. This capability is critical for applications requiring high precision and adaptability, such as adaptive optics and complex beam shaping in advanced optical systems.

The process of the arbitrary polarisation state generation is illustrated in detail in **Figure 6.8**. The change in polarisation state induced by each SLM can be modelled as a transition on the Poincaré sphere, representing the SoP. The system performs a series of rotations on the Poincaré sphere, with each SLM contributing to the overall rotation path. The first SLM is oriented at 45° to the input light's polarisation, which moves the polarisation state along a circle on the Poincaré sphere. This initial rotation changes the linear polarisation state A to an intermediate state B. The second SLM, oriented at 45° relative to the first SLM, further rotates the polarisation state along another circle on the Poincaré sphere in a plane perpendicular to the first. This configuration allows the polarisation state to reach any point on the Poincaré sphere

by combining the effects of these two orthogonal rotations. The precision of the SLMs' control over retardance using the applied phase patterns enables fine adjustments to the polarisation state, ensuring that the desired state is accurately achieved.

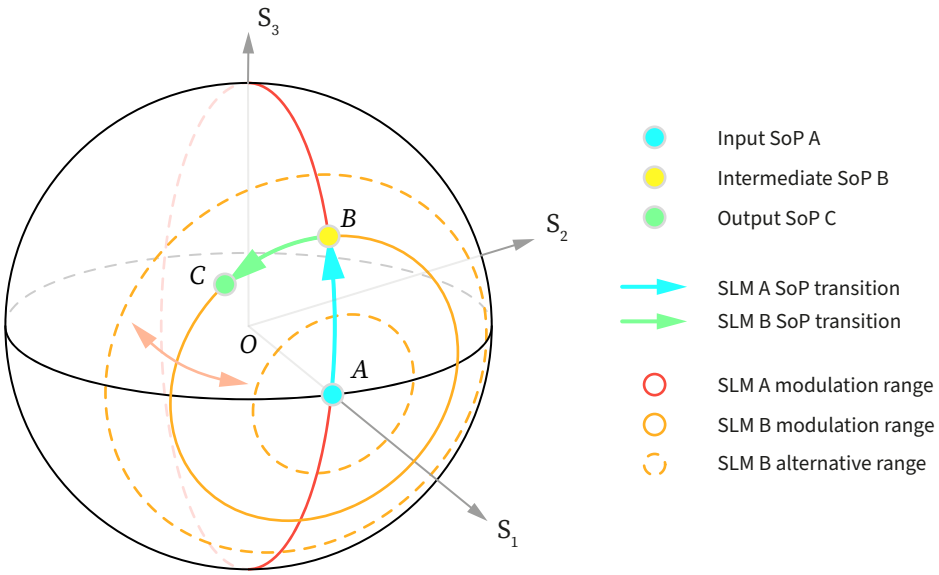

Figure 6.8: Transitions of the SoP on the Poincaré sphere for the two-SLM system. The axes S_1, S_2, and S_3 represent the Stokes vector components. Point A indicates a horizontally polarised input state; point B marks the SoP after modulation by the first SLM; point C shows the output state after modulation by the second SLM. Adjusting the retardance provided by the phase patterns on the two SLMs allows the translation of point C to any position on the surface of the Poincaré sphere from point A.

6.2.2 Mathematical Derivation

Starting with the Jones matrix, an arbitrary retarder can be characterised by its eigenvectors and eigenvalues, which represent two unique orthogonal axes and the corresponding phase shift between them. In general, by using the Jones vector of a beam from Equation 6.4 to represent the eigenvectors, the Jones matrix of an arbitrary retarder can be represented as:

$$\begin{aligned} J_{AR} &= \begin{bmatrix} \cos\alpha & -\sin\alpha e^{-i\delta} \\ \sin\alpha e^{i\delta} & \cos\alpha \end{bmatrix} \begin{bmatrix} e^{i\psi+i\phi/2} & 0 \\ 0 & e^{i\psi-i\phi/2} \end{bmatrix} \begin{bmatrix} \cos\alpha & \sin\alpha e^{-i\delta} \\ -\sin\alpha e^{i\delta} & \cos\alpha \end{bmatrix} \\ &= e^{i\psi} \begin{bmatrix} e^{i\phi/2}\cos^2\alpha + e^{-i\phi/2}\sin^2\alpha & (e^{i\phi/2} - e^{-i\phi/2})\sin\alpha\cos\alpha e^{-i\delta} \\ (e^{i\phi/2} - e^{-i\phi/2})\sin\alpha\cos\alpha e^{i\delta} & e^{i\phi/2}\sin^2\alpha + e^{-i\phi/2}\cos^2\alpha \end{bmatrix} \end{aligned} \tag{6.29}$$

where $e^{i\psi}$ in J_{AR} represents the absolute phase introduced by the medium, α represents auxiliary angle and δ represents phase difference mentioned in Section 6.1.2. And recall that, from that section, the incident beam in Equation 6.4 can be represented as Equation 6.22 in Mueller-Stokes formalism. Since our focus is on SoP rather than phase profile, this uniform phase shift factor will be omitted in the following discussion. Note that from the expression of the skyrmion number, it is clear that the absolute phase does not change the topology of the optical field.

By replacing the eigenvector terms in J_{AR} with Stokes vector notations, we can get the Jones matrix of an arbitrary retarder expressed in terms of the Stokes parameters:

$$J_{AR} = \begin{bmatrix} \cos(\phi/2) + i\sin(\phi/2)S_1 & \sin(\phi/2)(iS_2 + S_3) \\ \sin(\phi/2)(iS_2 - S_3) & \cos(\phi/2) - i\sin(\phi/2)S_1 \end{bmatrix}. \tag{6.30}$$

Furthermore, we can obtain the Mueller matrix of an arbitrary retarder from the Jones matrix[325]

$$\begin{aligned} M_{AR} &= A(J_{AR} \otimes J_{AR}^*)A^{-1} \\ &= \begin{bmatrix} 1 & 0 & 0 & 0 \\ 0 & S_1^2(1-\cos\phi) + \cos\phi & S_1S_2(1-\cos\phi) + S_3\sin\phi & S_1S_3(1-\cos\phi) - S_2\sin\phi \\ 0 & S_1S_2(1-\cos\phi) - S_3\sin\phi & S_2^2(1-\cos\phi) + \cos\phi & S_2S_3(1-\cos\phi) + S_1\sin\phi \\ 0 & S_1S_3(1-\cos\phi) + S_2\sin\phi & S_2S_3(1-\cos\phi) - S_1\sin\phi & S_3^2(1-\cos\phi) + \cos\phi \end{bmatrix} \\ &= \begin{bmatrix} 1 & \mathbf{0} \\ \mathbf{0}^T & \mathbf{m}_R \end{bmatrix} \end{aligned} \tag{6.31}$$

where $\otimes$ represents the Kronecker product, J_{AR}^* represents the complex conjugate of the above Jones matrix and A is in the form of:

$$A = \begin{bmatrix} 1 & 0 & 0 & 1 \\ 1 & 0 & 0 & -1 \\ 0 & 1 & 1 & 0 \\ 0 & i & -i & 0 \end{bmatrix}. \tag{6.32}$$

Note that the sub-matrix $\mathbf{m}_R$ of M_{AR} is actually a special orthogonal matrix, which can also be derived from Rodrigues rotation formula[326]. The physical meaning of the sub-matrix $\mathbf{m}_R$ suggests that for any given Stokes vector represented on the Poincaré sphere, the sub-matrix $\mathbf{m}_R$ corresponds to a rotation along the axis given by $S = [S_1, S_2, S_3]^T$ with angle ϕ on the sphere. Therefore, for pixels of the two SLMs, SLM A and SLM B, in Figure 6.8, their rotation axes are $S_A = [0, 1, 0]^T$ and $S_B = [1, 0, 0]^T$, and the corresponding Mueller matrices are

$$M_A = \begin{bmatrix} 1 & 0 & 0 & 0 \\ 0 & \cos\varphi_A & 0 & -\sin\varphi_A \\ 0 & 0 & 1 & 0 \\ 0 & \sin\varphi_A & 0 & \cos\varphi_A \end{bmatrix} \tag{6.33}$$

$$M_B = \begin{bmatrix} 1 & 0 & 0 & 0 \\ 0 & 1 & 0 & 0 \\ 0 & 0 & \cos\varphi_B & \sin\varphi_B \\ 0 & 0 & -\sin\varphi_B & \cos\varphi_B \end{bmatrix} \tag{6.34}$$

where φ_A and φ_B are the retardance to be applied on pixels of SLM A and SLM B, respectively.

Considering horizontal polarised incident light $S_{\text{in}} = [1, 1, 0, 0]$, the SoP of the output beam S_{out} can be represented as

$$\begin{aligned} S_{\text{out}} &= M_B \cdot M_A \cdot S_{\text{in}} \\ &= \begin{bmatrix} 1 & 0 & 0 & 0 \\ 0 & 1 & 0 & 0 \\ 0 & 0 & \cos\varphi_B & \sin\varphi_B \\ 0 & 0 & -\sin\varphi_B & \cos\varphi_B \end{bmatrix} \begin{bmatrix} 1 & 0 & 0 & 0 \\ 0 & \cos\varphi_A & 0 & -\sin\varphi_A \\ 0 & 0 & 1 & 0 \\ 0 & \sin\varphi_A & 0 & \cos\varphi_A \end{bmatrix} \begin{bmatrix} 1 \\ 1 \\ 0 \\ 0 \end{bmatrix}. \\ &= \begin{bmatrix} 1 \\ \cos\varphi_A \\ \sin\varphi_B \sin\varphi_A \\ \cos\varphi_B \sin\varphi_A \end{bmatrix} \end{aligned} \tag{6.35}$$

Therefore, for arbitrary target output SoP, $S_{\text{out}} = [1, S_1, S_2, S_3]$, the required retardance for

the SLMs can be derived as

$$\varphi_A = \arccos S_1 \tag{6.36}$$

$$\varphi_B = \arctan \frac{S_2}{S_3}. \tag{6.37}$$

6.3 Optical Skyrmionic and Meronic Beam Generation

6.3.1 Experiment Setup

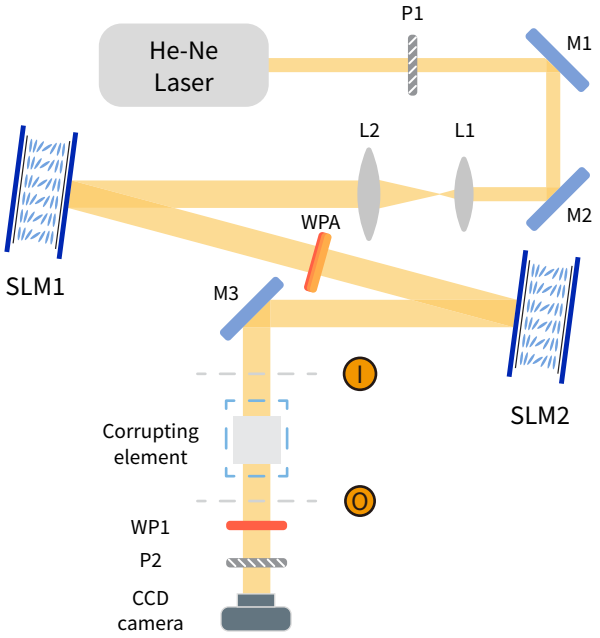

Figure 6.9: The experimental setup for Skyrmion and Meronic beam generation. A He-Ne laser with a wavelength of 633 nm is expanded, collimated, and polarised (P1) before passing through a pair of SLMs (Hamamatsu LCOS-SLM X15213-01) with a waveplate assembly (WPA) to shape the polarisation field into skyrmion and meronic beams. The generated beam is analysed with a polarimeter comprising a quarter-wave plate (WP1), a polariser (P2), and a CCD camera. The optical path also allows for the insertion of corrupting elements to test the topological protection properties of these generated beams.

The experiment in **Figure 6.9** employs a sophisticated optical configuration designed to generate and analyse the formation of skyrmion and meron optical beams. A Helium-Neon (He-Ne) laser operating at a wavelength of 633 nm serves as a stable and coherent light source. To

ensure the uniformity of the beam polarisation state, the beam is first controlled by a polariser (P1). Then, the He-Ne laser beam with a uniform horizontal polarisation field is expanded and collimated. The polarised beam then passes through a pair of SLMs (Hamamatsu LCOS-SLM X15213-01), with a waveplate assembly (WPA) to control the rotation of the light. The cascaded structure of the two SLMs shapes the polarisation field of the laser beam, allowing for the creation of complex light field patterns as discussed. By modulating the polarisation field of the incoming light, as described in Section 6.2, the SLMs can generate arbitrary polarisation fields with skyrmion and meronic beams. These beams are characterised by their unique and stable configurations, which are of significant interest in the study of topological properties of light. The precision in the modulation provided by the SLMs is critical for achieving the desired field configurations conducive to the generation of these beams.

Following their generation, the skyrmionic and meronic beams are analysed using a polarimeter. The polarimeter comprises a quarter-wave plate (WP2), a second polariser (P2), and a CCD camera. This assembly allows for a detailed examination of the polarisation states and the topological structures of the beam, facilitating a comprehensive analysis of the generated beams. Furthermore, to validate the topological protection of these skyrmion and meronic beams against external perturbations, a part of the optical path was reserved for the insertion of various corrupting elements to test their effects on the topological fields. By introducing controlled perturbations and observing the resulting changes in the topological structures, the experiment aims to demonstrate the robustness and stability of these optical beams. Additionally, to ensure that the beam propagation direction does not introduce significant errors in the cascaded configuration, the reflection angle of the beam is maintained within $\pm 3^{\circ}$, thereby preventing any appreciable impact on the resulting beam generation.

6.3.2 Generation of Skyrmionic Beam

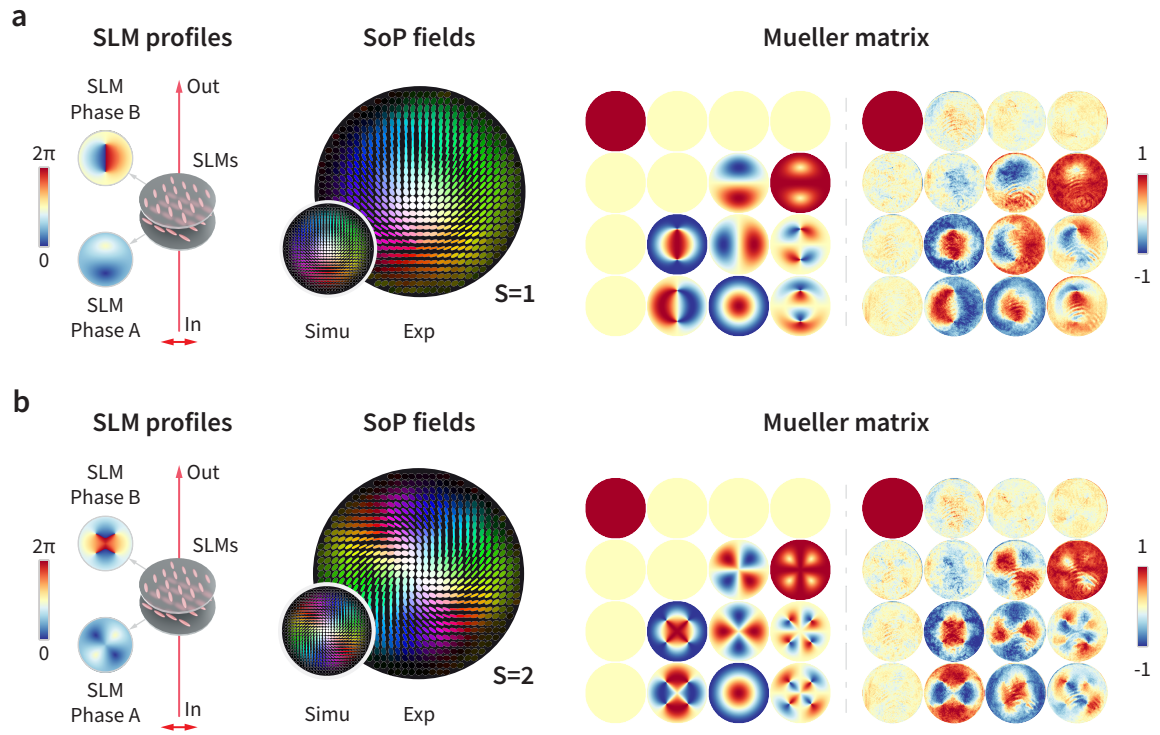

Figure 6.10: Results demonstrating the generation of low-order skyrmionic beams. The comparison between the simulated (Simu) and experimental (Exp) SoP fields for low-order skyrmionic beams demonstrates the consistency between the simulations (Simu) and experiment (Exp) data. The Mueller matrices corresponding to different phase configurations, where phase patterns A and B are independently loaded onto the two SLMs for beam modulation, are presented to validate the consistency of the modulation achieved by the cascaded SLMs. The skyrmionic beams generated in each subfigure exhibit the following configurations: (a) Skyrmionic beam with skyrmion number $S = 1$, polarity $p = 1$, and vorticity $v = 1$; (b) Skyrmionic beam with skyrmion number $S = 2$, polarity $p = 1$, and vorticity $v = 2$. The phase range of the pattern loaded onto the SLMs is represented by a scale bar from 0 to π , while the scale from -1 to 1 indicates the corresponding results for the Mueller matrices.

Utilising the proposed novel approach employing cascaded SLMs to generate optical skyrmions, we can achieve the generation of target complex topologies with high precision. The generated skyrmionic beam are demonstrated in **Figure 6.10**. Initially, a beam with a uniform horizontal linear polarisation field is introduced into the system. This initial condition sets the stage for controlled manipulation of the polarisation field throughout the process. Subsequently, we select an expected topological outcome of the polarisation field, which varies across the entire space. For simplicity, we continue the explanation using the topology depicted in Figure 6.10(a),

which represents the topology of a unit skyrmion sphere. In this figure, the expected outcome is a unit skyrmionic beam characterised by a polarity $p = +1$ and a vorticity $v = +1$. The choice of this specific polarity and vorticity allows for a clear demonstration of the capability of the system to generate and manipulate complex structures.

Based on the target outcome SoP field and the properties of the incident light, the corresponding retardance distributions are derived and corresponding phase patterns on each of the cascaded SLMs are calculated using Equation 6.36 and Equation 6.37. These calculations are critical, as they determine the exact phase modulations required to shape the incident light into the desired topological configuration. Once the retarder distributions are determined, they are encoded onto the SLMs to achieve the desired modulation. Each SLM in the cascade sequence transforms the polarisation field according to the calculation from Equation 6.36 and Equation 6.37, ensuring that the cumulative effect results in the target polarisation state. This encoding process involves precise alignment and calibration of the SLMs to ensure that the target distributions are accurately represented in the physical cascaded optical assembly.

Finally, further analysis of the outcome beam polarisation profiles and the optical properties of the cascaded SLMs are conducted based on data obtained using the polarimeter integrated into the system. The polarimeter measures the resulting polarisation states, allowing for detailed characterisation of the generated topological structures. The Stokes vector field of the output beam was measured and compared with target skyrmionic beam to verify the consistency with simulations. In addition, the Mueller matrices of the cascaded SLMs are also compared with the results from simulations to ensure that the designed patterns were properly loaded onto the SLMs. These simulations, derived from computational models taking into account the entire light-matter interaction process within the SLM system using Equation 6.33 and Equation 6.34, predict the final polarisation distribution and topological features based on Equation 6.35 with

a given S_{in}. In order to show that the proposed structure provides a high-quality generated field despite the complexity of the field, a skyrmionic beam with a higher vorticity order (polarity $p = +1$ and vorticity $v = +2$) was also generated and is presented in Figure 6.10(b), which agrees well with simulations.

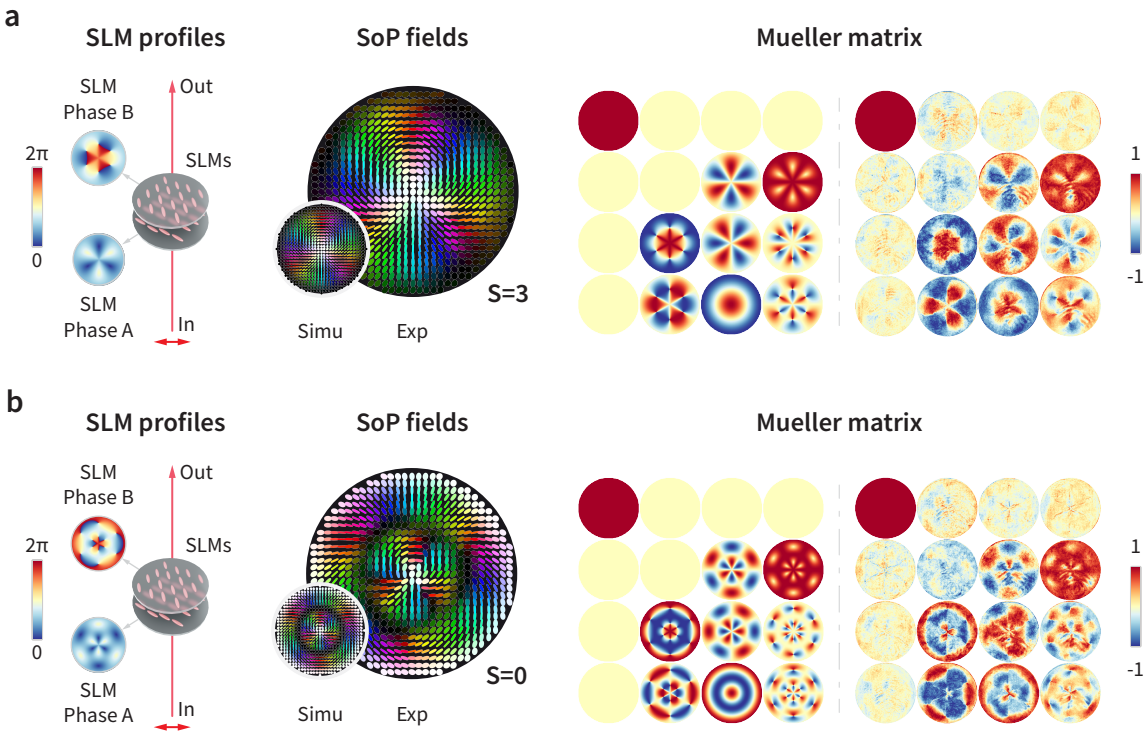

Figure 6.11: Results demonstrating the generation of high-order skyrmionic beams. The comparison between the simulated (Simu) and experimental (Exp) SoP fields for high-order skyrmionic beams demonstrates the consistency between the simulations (Simu) and experiment (Exp) data. The Mueller matrices corresponding to different phase configurations, where phase patterns A and B are independently loaded onto the two SLMs for beam modulation, are presented to validate the consistency of the modulation achieved by the cascaded SLMs. The skyrmionic beams generated in each subfigure exhibit the following configurations: (a) Skyrmionic beam with skyrmion number $S = 3$, polarity $p = 1$, and vorticity $v = 3$; (b) Skyrmionic beam with skyrmion number $S = 0$, polarity $p = 2$, and vorticity $v = 3$. The phase range of the pattern loaded onto the SLMs is represented by a scale bar from 0 to π , while the scale from -1 to 1 indicates the corresponding results for the Mueller matrices.

To demonstrate the versatility of the cascaded SLMs in generating the complex topological structures, skyrmionic beams with the same vorticity order $v = +3$ but with different polarity orders (polarity $p = +1$ and polarity $p = +2$) are illustrated in **Figure 6.11**(a) and Figure 6.11(b). Note that the higher orders of polarity here indicates the number of times the

topology field wraps around the sphere. Therefore, a polarity of $p = +2$ results in the skyrmion number S being zero as it wraps back and forth around the Poincaré sphere. The consistency between the simulation and experiment proves that complex skyrmionic beams can be realised using the cascaded SLM configuration using the same procedure as described above.

The proposed approach effectively utilises cascaded SLMs to modulate the polarisation field of the incident beam, achieving complex structures such as optical skyrmions. The process involves precise calculation and encoding of retarder distributions, followed by the analysis of the resulting polarisation profiles. The alignment between theoretical simulations and experimental observations confirms the validity and efficiency of this method. The ability to generate and control optical skyrmions with different vorticity orders, as shown in the figures, underscores the versatility and potential applications of this technique in advanced optical and material science research.

6.3.3 Generation of Meronic Beam

Utilising the same novel approach, a generated meronic beam is demonstrated in **Figure 6.12**. The same procedure was undertaken as described for the skyrmionic beam generation. The difference is that the target outcome field was different for the meronic beam (e.g., as the half unit sphere demonstrated in Figure 6.6(a)). Therefore, different retardance distributions on each of the cascaded SLMs had to be calculated and corresponding phase patterns are applied. In Figure 6.12(a), the expected outcome is a unit meronic beam characterised by a polarity $p = +0.5$ and a vorticity $v = +1$. In order to show the feasibility of the proposed structure, a meronic beam with a higher vorticity order (polarity $p = +0.5$ and vorticity $v = +2$) was also generated and is presented in Figure 6.12(b), which shows good agreement with the target outcome and the results from simulations.

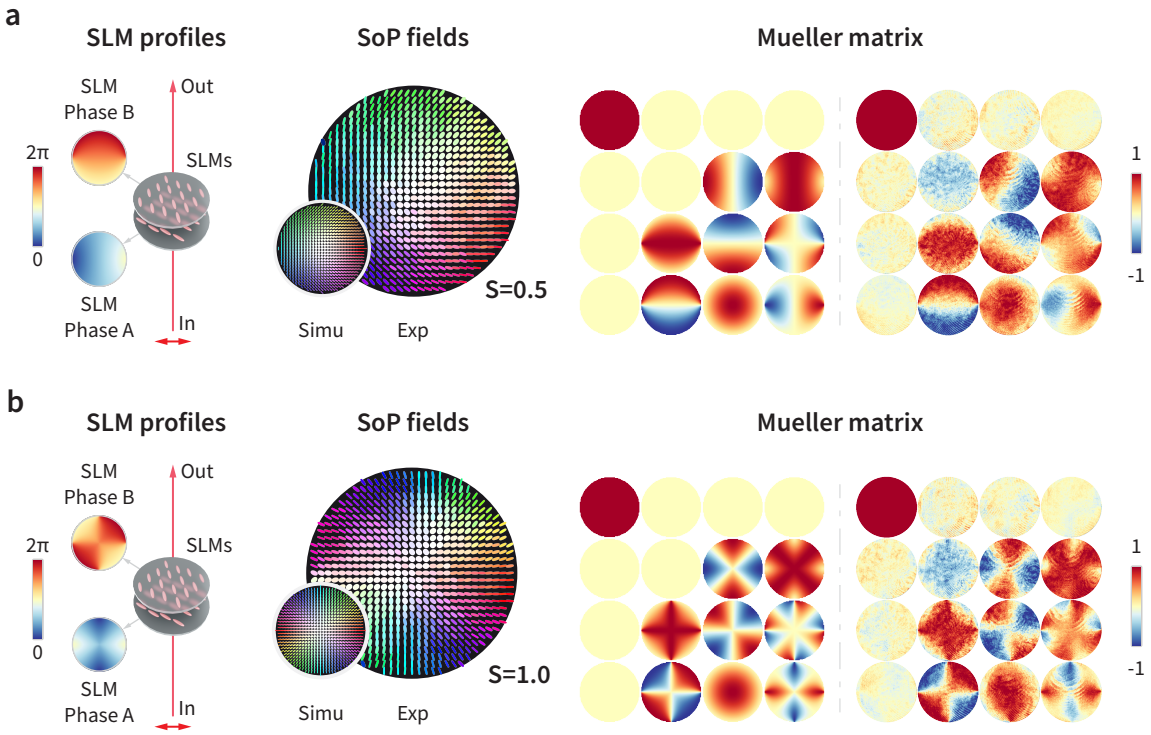

Figure 6.12: Results demonstrating the generation of low-order meronic beams. A comparison of the simulated and experimental SoP fields of low-order meronic beams demonstrates the consistency between the simulations (Simu) and experiment (Exp) data. Mueller Matrices for different configurations, where phase pattern A and B are loaded separately onto the two SLMs to modulate the beam, are presented to demonstrate the consistency and effectiveness of the modulation that the cascaded SLMs provide. The meronic beam generated in each subfigure has the configurations: (a) Meronic beam with skyrmion number $S = +1/2$, polarity $p = +1/2$ and vorticity $v = +1$. (b) Meronic beam with skyrmion number $S = +1$, polarity $p = +1/2$ and vorticity $v = +2$. The scale bar from 0 to π indicates the phase range of the pattern loaded onto the SLMs and the one from -1 to 1 relates to the results for the Mueller matrices.

Finally, further analysis of the outcome beam polarisation profiles and the optical properties of the cascaded SLMs are conducted based on data obtained using the polarimeter integrated into the system. The measured Stokes vector field of the output beam as well as the Mueller matrix of the cascaded SLMs are consistent with expectations. Furthermore, to demonstrate the versatility of the cascaded SLMs in generating complex optical vector field, optical meronic beams with the same high vorticity order $v = +3$ but with different polarity orders (polarity $p = +0.5$ and polarity $p = +1$) were generated and the results presented in **Figure 6.13**(a) and Figure 6.13(b). The consistency between the simulation and experiment results proves that complex meronic beams can be realised using the arrangement involving two cascaded SLMs.

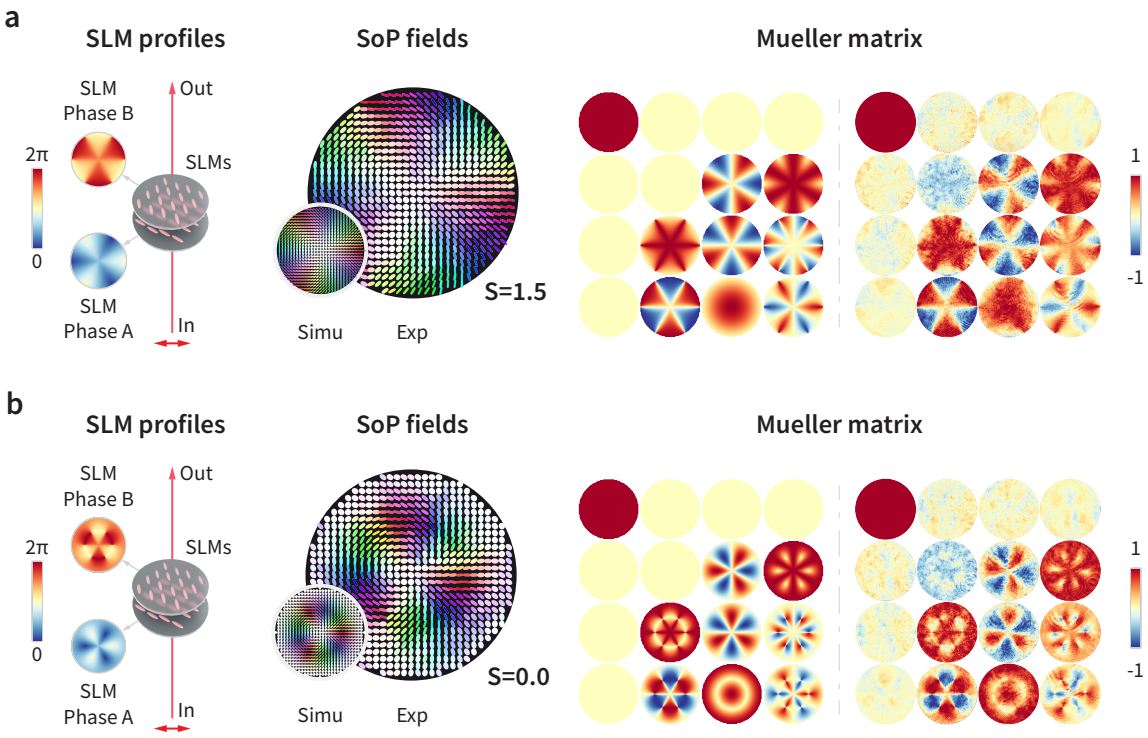

Figure 6.13: Results demonstrating the generation of high-order meronic beams. A comparison of the simulated and experimental SoP fields of high-order meronic beams demonstrates the consistency between the simulations (Simu) and experiment (Exp) data. Mueller Matrices for different configurations, where phase pattern A and B are loaded separately onto the two SLMs to modulate the beam, are presented to demonstrate the consistency and effectiveness of the modulation that the cascaded SLMs provided. The meronic beam generated in each subfigure has the configurations: (a) Meronic beam with skyrmion number $S = +1.5$, polarity $p = +1/2$ and vorticity $v = +3$. (b) Meronic beam with skyrmion number $S = 0$, polarity $p = 1$ and vorticity $v = +3$. The scale bar from 0 to π indicates the phase range of the pattern loaded on the SLMs and the one from -1 to 1 relates to the results for the Mueller matrices.

The proposed methodology leverages cascaded SLMs to modulate the polarisation field of an incident beam, facilitating the generation of complex topological structures, including skyrmion and meronic beams. This process entails the precise calculation and encoding of retarder distributions, followed by a comprehensive analysis of the resultant polarisation profiles. The congruence between theoretical simulations and experimental observations substantiates the validity and efficacy of this approach. Furthermore, the demonstrated capability to generate and manipulate skyrmion and meronic beams with varying vorticity orders, as illustrated in the figures, underscores the versatility and potential applications of this technique in advanced optical and material science research.

6.4 Evaluation of Topological Protection

6.4.1 Theoretical Background

In this section, we give a mathematical derivation of the topological protection properties of skyrmionic and meronic beams when passing through complex media. Heuristically, this protection comes from the homotopy invariance of the degree of a continuous function but can also be explicitly computed in certain cases. We show the result in the general anisotropic case. The isotropic case, as a special subset of anisotropic media, then follows immediately. To show the topological protection property of these beams, we derive below that the skyrmion number does not change after passing through multiple corruption elements.

In this framework, we consider the optical system exhibiting aberration with varying intensity, retardance, and depolarisation and one or multiple of them exist as corruptions to the topology of optical vector fields during propagation. For this experiment, a neutral density (ND) filter (acting as an attenuator), an SLM (behaving as our arbitrary retarder) and a liquid crystal (LC) glass cell (acting as an arbitrary depolariser) were utilised to simulate the occurrence of these corruptions in a real-world scenario.

The Mueller matrices for the ND filter, arbitrary retarder and arbitrary depolariser can be represented, respectively, as[278]

$$\mathbf{M}_{\text{ND}} = \begin{bmatrix} 1 & 0 & 0 & 0 \\ 0 & 1 & 0 & 0 \\ 0 & 0 & 1 & 0 \\ 0 & 0 & 0 & 1 \end{bmatrix} = \begin{bmatrix} 1 & 0 \\ 0 & \mathbf{I} \end{bmatrix} \tag{6.38}$$

$$\mathbf{M}_{\text{AR}} = \begin{bmatrix} 1 & 0 \\ 0 & \mathbf{m}_R \end{bmatrix} \tag{6.39}$$

$$\mathbf{M}_{\Delta d} = \begin{bmatrix} d_0 & 0 & 0 & 0 \\ 0 & d_1 & 0 & 0 \\ 0 & 0 & d_2 & 0 \\ 0 & 0 & 0 & d_3 \end{bmatrix} = \begin{bmatrix} 1 & 0 \\ 0 & \mathbf{m}_{\Delta d} \end{bmatrix} \tag{6.40}$$

where I is the identity matrix as the ND filter does not change the polarisation state of the beam; $\mathbf{m}_R$ is the rotation sub-matrix from Equation 6.31 in the arbitrary retarder; $\mathbf{m}_{\Delta d}$ is the sub-matrix of the arbitrary depolariser where d_1, d_2 and d_3 satisfy $0 \leqslant d_1, d_2, d_3 \leqslant d_0$.

For this topological protection study, we refer to the skyrmion number S' of an optical skyrmionic or skyrmionic field, which is restated here for convenience as

$$S' = \frac{1}{4\pi} \iint_{\sigma} \mathbf{n}' \cdot \left(\frac{\partial \mathbf{n}'}{\partial x} \times \frac{\partial \mathbf{n}'}{\partial y} \right) dxdy \tag{6.41}$$

where $\mathbf{n}' = [S_1', S_2', S_3']$ denotes the Stokes vector corresponding to $\mathbf{n} = [S_1, S_2, S_3]$ after passing through the corruption medium

For the ND filter, since it does not change the polarisation state of the beam, $\mathbf{n}' = \mathbf{n} = [S_1, S_2, S_3]$. Therefore, the optical vector field does not change, and neither does the skyrmion number. For the remaining two forms of corruption, the disturbed vector field $\mathbf{n}'$ can be represented as $\mathbf{n}' = \mathbf{mn}$ and the skyrmion number S' is then calculated as

$$S' = \frac{1}{4\pi} \iint_{\sigma} \mathbf{mn} \cdot \left(\frac{\partial \mathbf{mn}}{\partial x} \times \frac{\partial \mathbf{mn}}{\partial y} \right) dxdy \tag{6.42}$$

where $\mathbf{m}$ is the sub-matrix for either the arbitrary retarder ($\mathbf{m}_R$) or the arbitrary depolariser ($\mathbf{m}_{\Delta d}$). Then, considering that $\mathbf{m}$ is independent of x and y, we have:

$$\frac{\partial \mathbf{mn}}{\partial x} = \mathbf{m} \frac{\partial \mathbf{n}}{\partial x} \tag{6.43}$$

$$\frac{\partial \mathbf{mn}}{\partial y} = \mathbf{m}\frac{\partial \mathbf{n}}{\partial y} \tag{6.44}$$

As a result, the skyrmion density s can be represented as

$$\begin{aligned} s &= \mathbf{mn} \cdot \left(\frac{\partial \mathbf{mn}}{\partial x} \times \frac{\partial \mathbf{mn}}{\partial y} \right) \\ &= \mathbf{mn} \cdot \left(\mathbf{m}\frac{\partial \mathbf{n}}{\partial x} \times \mathbf{m}\frac{\partial \mathbf{n}}{\partial y} \right) \end{aligned} . \tag{6.45}$$

For the arbitrary retarder, since $\mathbf{m}_R$ is a rotation matrix with $\det(\mathbf{m}_R) = 1$, the skyrmion density can be simplified to:

$$\begin{aligned} s &= (\mathbf{m}_R\mathbf{n}) \cdot \mathbf{m}_R \left(\frac{\partial \mathbf{n}}{\partial x} \times \frac{\partial \mathbf{n}}{\partial y} \right) \\ &= \left(\mathbf{n}^T \mathbf{m}_R^T \mathbf{m}_R \right) \left(\frac{\partial \mathbf{n}}{\partial x} \times \frac{\partial \mathbf{n}}{\partial y} \right) \\ &= \mathbf{n}^T \left(\frac{\partial \mathbf{n}}{\partial x} \times \frac{\partial \mathbf{n}}{\partial y} \right) \\ &= \mathbf{n} \cdot \left(\frac{\partial \mathbf{n}}{\partial x} \times \frac{\partial \mathbf{n}}{\partial y} \right) \end{aligned} . \tag{6.46}$$

By substituting Equation 6.46 back into Equation 6.41, we obtain

$$\begin{aligned} S' &= \frac{1}{4\pi} \iint_\sigma \mathbf{n}' \cdot \left(\frac{\partial \mathbf{n}'}{\partial x} \times \frac{\partial \mathbf{n}'}{\partial y} \right) dxdy \\ &= \frac{1}{4\pi} \iint_\sigma \mathbf{m}_R\mathbf{n} \cdot \left(\frac{\partial \mathbf{m}_R\mathbf{n}}{\partial x} \times \frac{\partial \mathbf{m}_R\mathbf{n}}{\partial y} \right) dxdy \\ &= \frac{1}{4\pi} \iint_\sigma \mathbf{n} \cdot \left(\frac{\partial \mathbf{n}}{\partial x} \times \frac{\partial \mathbf{n}}{\partial y} \right) dxdy \\ &= S \end{aligned} . \tag{6.47}$$

Meanwhile, for the arbitrary depolariser, since $\mathbf{m}_{\Delta d}$ is an arbitrary matrix whose $\det(\mathbf{m}_{\Delta d}) \neq$

1, the skyrmion density can be simplified to

$$s = (\mathbf{m}_{\Delta d}\mathbf{n}) \cdot \operatorname{cof}\mathbf{m}_{\Delta d}\left(\frac{\partial \mathbf{n}}{\partial x} \times \frac{\partial \mathbf{n}}{\partial y}\right) \tag{6.48}$$

where $\operatorname{cof}\mathbf{m}_{\Delta d}$ is the cofactor matrix of $\mathbf{m}_{\Delta d}$ which is calculated as

$$\mathbf{m}_{\Delta d} = \begin{bmatrix} d_2 d_3 & 0 & 0 \\ 0 & d_1 d_3 & 0 \\ 0 & 0 & d_1 d_2 \end{bmatrix}. \tag{6.49}$$

Therefore, the skyrmion density can be further simplified to

$$\begin{aligned} s &= \left(\mathbf{n}^T \mathbf{m}_{\Delta d}^T \operatorname{cof}\mathbf{m}_{\Delta d}\right)\left(\frac{\partial \mathbf{n}}{\partial x} \times \frac{\partial \mathbf{n}}{\partial y}\right) \\ &= \left(\mathbf{n}^T \begin{bmatrix} d_1 & 0 & 0 \\ 0 & d_2 & 0 \\ 0 & 0 & d_3 \end{bmatrix}\begin{bmatrix} d_2 d_3 & 0 & 0 \\ 0 & d_1 d_3 & 0 \\ 0 & 0 & d_1 d_2 \end{bmatrix}\right)\left(\frac{\partial \mathbf{n}}{\partial x} \times \frac{\partial \mathbf{n}}{\partial y}\right). \\ &= d_1 d_2 d_3 \cdot \mathbf{n} \cdot \left(\frac{\partial \mathbf{n}}{\partial x} \times \frac{\partial \mathbf{n}}{\partial y}\right) \end{aligned} \tag{6.50}$$

It can be noticed that $d_1 d_2 d_3$ functions as the constant coefficients and does not effect the polarisation state of each point. Therefore, the vector field can be normalised throughout the whole beam and the skyrmion number is then derived as

$$\begin{aligned} S' &= \frac{1}{4\pi}\iint_{\sigma} \mathbf{n}' \cdot \left(\frac{\partial \mathbf{n}'}{\partial x} \times \frac{\partial \mathbf{n}'}{\partial y}\right) dxdy \\ &= \frac{1}{4\pi}\iint_{\sigma} (\mathbf{m}_{\Delta d}\mathbf{n}) \cdot \operatorname{cof}\mathbf{m}_{\Delta d}\left(\frac{\partial \mathbf{n}}{\partial x} \times \frac{\partial \mathbf{n}}{\partial y}\right) \\ &= \frac{1}{4\pi}\iint_{\sigma} \mathbf{n} \cdot \left(\frac{\partial \mathbf{n}}{\partial x} \times \frac{\partial \mathbf{n}}{\partial y}\right) dxdy \\ &= S \end{aligned}. \tag{6.51}$$

The aforementioned derivation rigorously demonstrates that the skyrmion number remains invariant despite the beam's traversal through multiple corruption elements. This invariance

highlights the robustness and stability of the skyrmionic beam under perturbative influences, thereby confirming the theoretical predictions and reinforcing the potential for practical applications in topological optical systems and materials science.

6.4.2 Topological Protection of Optical Skyrmions

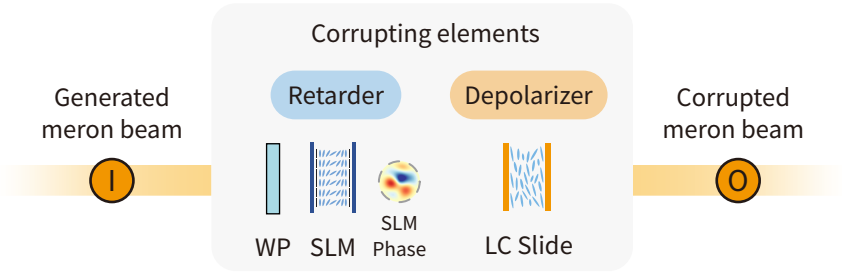

Figure 6.14: Inclusion of corrupting elements to test the robustness of Skyrmionic beams. To prove that skyrmionic beams are stable against external disturbances such as arbitrary retarders and arbitrary depolarisers, extra optical components are inserted into the system in Figure 6.9. Variable quarter waveplates (WPs) cascaded with an SLM that displays an arbitrary phase pattern was utilised to act as spatially varying retarders and a thin layer of nematic liquid crystal (LC), E7, filled between glass substrates served as both a retarder and weak light scatterer.

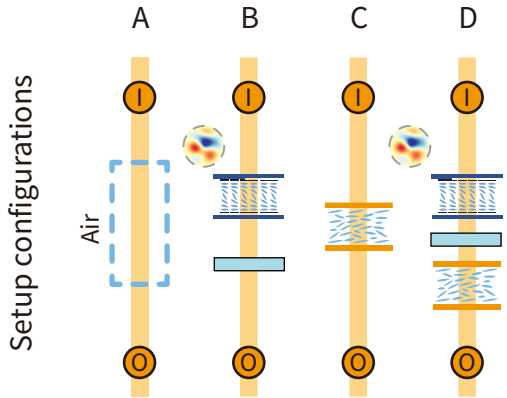

Figure 6.15: Combinations of corrupting elements for skyrmionic beams. Setup A is the reference configuration with no extra elements inserted into the system to disturb the skyrmionic beam. Setup B has the arbitrary retarder inserted with the displayed phase pattern demonstrated on the side. Setup C has the weak depolariser inserted. Finally, setup D is the combinations of corrupting elements to test the stability of the skyrmionic beams.

The experimental system configuration for testing the skyrmionic beam comprises various corrupting elements, including variable quarter waveplates (WPs) cascaded with an SLM that dis-

played an arbitrary phase pattern to act as a spatially varying retarder and a thin layer of nematic liquid crystal (LC) E7 filled between glass substrates that served as both a retarder and a weak light scatterer. These elements replicate common aberrations and corruptions found in optical systems. **Figure 6.14** illustrates the corrupting elements and **Figure 6.15** demonstrates different combinations along with their relative placements when inserted into the optical path in the experiment.

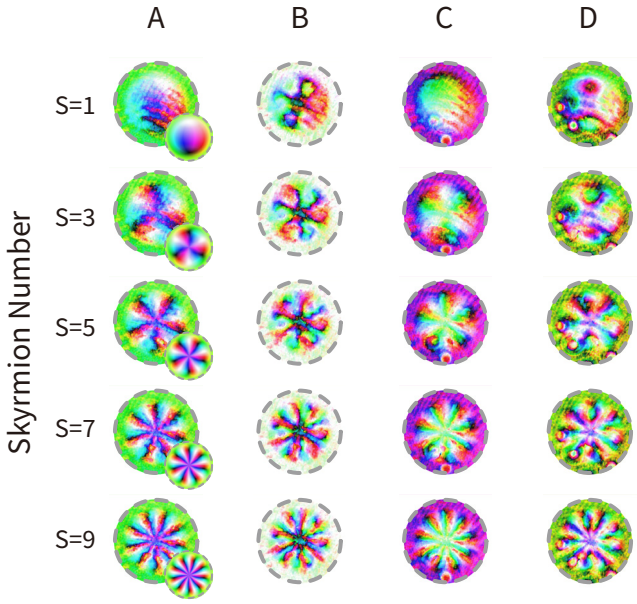

Figure 6.16: Experiment results of the skyrmionic beams through different corrupting elements. Skyrmionic beams with orders from 1 to 9 (in increments of 2) through configurations A to D (as demonstrated in Figure 6.15) are demonstrated. The effects of different corrupting elements on each skyrmionic beam are clearly illustrated. For the distribution with no disturbances in setup A, the output beam is compared with the ideal SoP fields, which are shown in the inset images. The colour bar for these images follows the definition in Figure 6.3. Note that the results presented in this figure were obtained in collaboration with our colleague Mr. An Aloysius Wang and are presented in our work[327].

The corresponding observed Stokes fields measured in the experiments are shown in **Figure 6.16**. During the experiment, specific techniques were employed to accurately determine the skyrmion numbers for the generated meronic beam. Firstly, only a small portion of the SLM area was utilised to create the spatially varying pattern for the target meronic beam, with the majority of the SLM pixels being filled based on the boundary conditions of the design.

Despite the imperfections observed in the SLM phase patterns, as shown in Figure 6.16 for setup configuration A, the resulting skyrmionic field closely aligns with the target skyrmionic field.

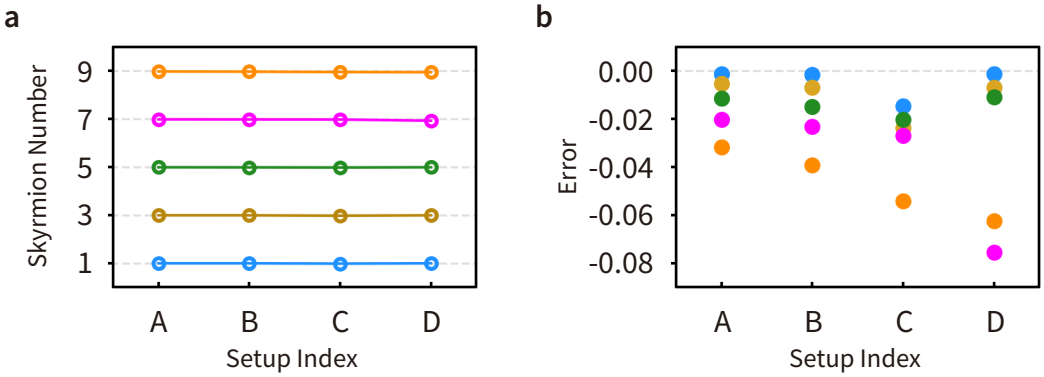

Figure 6.17: Analysis of skyrmion numbers and corresponding errors through different experimental configurations. (a) The calculated skyrmion numbers for various skyrmionic beams ($S = 1, 3, 5, 7, 9$) are shown for each setup (A to D, Figure 6.15) to demonstrate consistency across different experimental conditions. Each coloured dot represents the skyrmion number for a specific configuration. (b) The corresponding errors in the skyrmion number measurements for each setup index are displayed, with different colours indicating the different skyrmion numbers. The error values reflect the variation in skyrmion number measurements, highlighting the precision and reliability of the experimental configurations. Note that the results presented in this figure were obtained in collaboration with our colleague Mr. An Aloysius Wang and are presented in our work[327].

Secondly, a Gaussian filter was applied to all measurement results before numerically evaluating the skyrmion number for each configuration. This filtering mitigates the effects of measurement noise on the computation of partial derivatives for the skyrmion density and smooths the boundaries to reduce calculation perturbations. The calculated skyrmion numbers are shown in **Figure 6.17**(a), demonstrating good consistency between measurement and design for configurations A to D in Figure 6.15. Lastly, the error in the skyrmion number was defined as the difference between the computed and designed skyrmion numbers across all configurations, with the results depicted in Figure 6.17(b). The computed errors for configurations A to D exhibit relatively minor divergence, with a general trend of increasing as the target skyrmion number increases. Note that the results presented in this section (Section 6.4.2) were obtained

in collaboration with our colleague Mr. An Aloysius Wang and are presented in our work[327].

6.4.3 Topological Protection of Optical Merons

A similar experimental system configuration for testing the meronic beam comprises various corrupting elements, including a ND filter with ND = 0.2 serving as the attenuator, variable quarter WPs cascaded with an SLM that displays an arbitrary phase pattern to act as spatially varying retarders and a thin layer of nematic LC (E7) filled between glass substrates serving as both a retarder and weak light scatterer. **Figure 6.18** shows each corrupting element and **Figure 6.19** demonstrates different combinations along with the relative placement of the corrupting elements that were inserted into the optical path in the experiment.

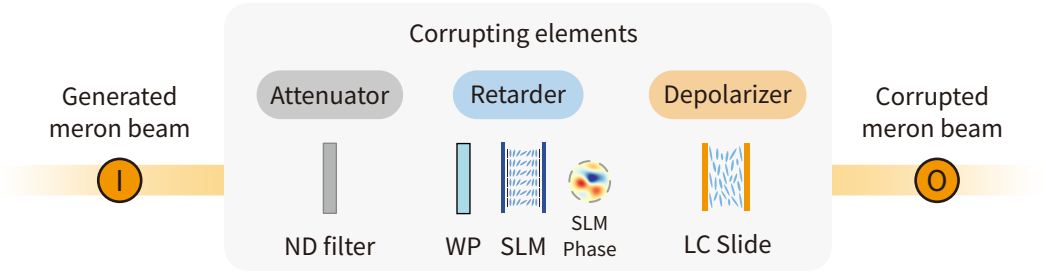

Figure 6.18: Corrupting elements to test the robustness of meronic beams. To prove that optical meronic beams are stable against external disturbances such as the propagation through arbitrary retarders and arbitrary depolarisers, extra optical components were inserted into the system in Figure 6.9. Neutral density (ND) filters with ND = 0.2 serve as the attenuator. Variable quarter waveplates (WPs) combined with an SLM that displayed an arbitrary phase pattern was used to act as spatially varying retarders and a thin layer of nematic liquid crystal (LC) E7 filled between glass substrates served as both a retarder and weak light scatterer.

The corresponding observed Stokes fields measured in the experiments are shown in **Figure 6.20**. The same method with a special design of the pattern at the edge and the Gaussian filter was applied to derive the desired Stokes fields measurement. Despite imperfections in the SLM phase patterns, as seen in Figure 6.20, the resulting skyrmion numbers closely match the target skyrmion numbers in configurations A to F.

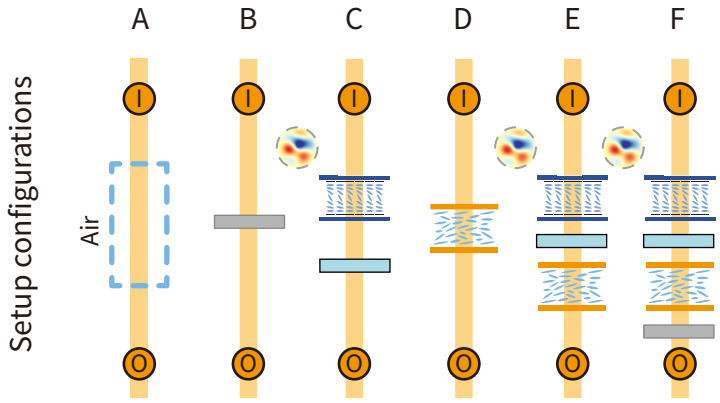

Figure 6.19: Combinations of corrupting elements for meronic beams. Setup A is the reference configuration with no extra elements inserted into the system to disturb the meronic beam. Setup B has the intensity attenuator inserted. Setup C has the arbitrary retarder inserted with the displayed phase pattern demonstrated on the side. Setup D has the weak depolariser inserted. Finally, setup D to E are the combinations of corrupting elements to test the stability of the meronic beams.

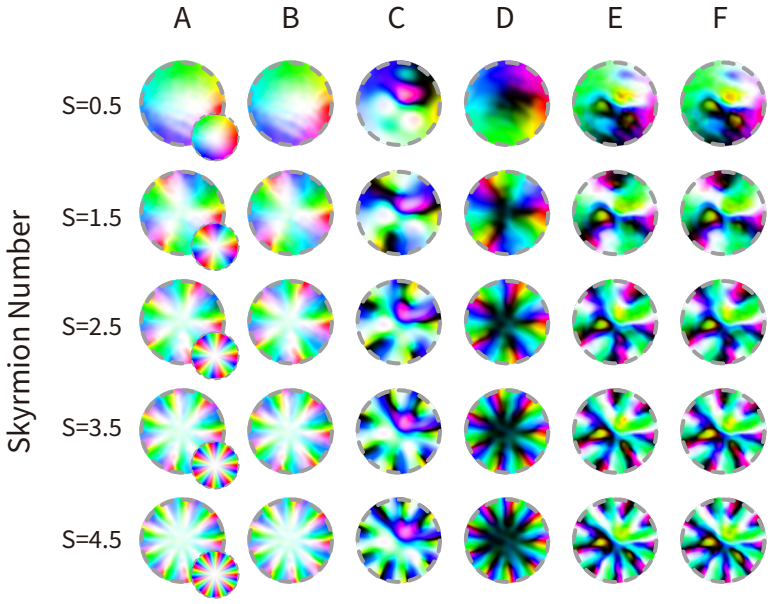

Figure 6.20: Experiment results of meronic beams propagating through different corrupting optical elements. Meronic beams with orders from 1 to 9 (in increments of 2) propagating through each one of setups A to F are demonstrated. The effects of different corrupting elements on each meronic beam are clearly illustrated. For the distribution with no disturbances in setup A, the output beam was compared with the ideal SoP fields, which are shown in the inset images. The colour bar for these images follows the definition in Figure 6.3.

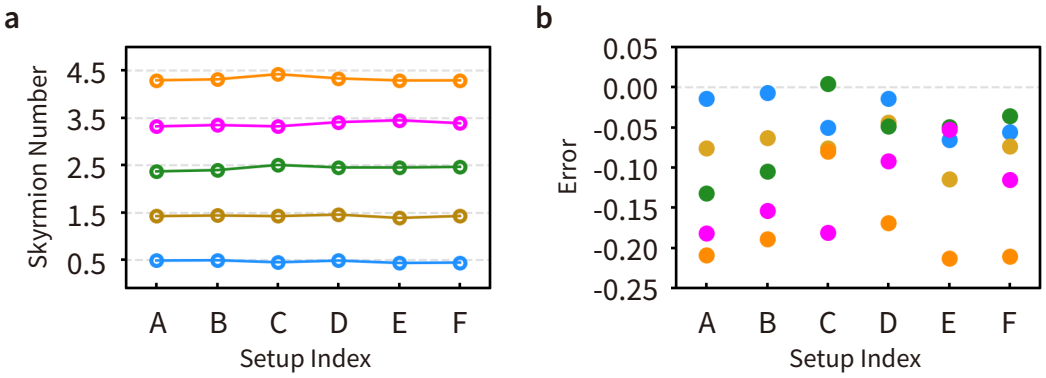

Figure 6.21: Analysis of skyrmion numbers and corresponding errors through different experimental configurations. (a) The calculated skyrmion numbers for various optical merons ($S = 0.5, 1.5, 2.5, 3.5, 4.5$) are shown for each configuration (A to F) to demonstrate consistency across different experimental conditions. Each coloured dot represents the skyrmion number for a specific setup. (b) The corresponding errors in skyrmion number measurements for each setup index are displayed, with different colours indicating different skyrmion numbers. The error values reflect the variation in skyrmion number measurements, highlighting the precision and reliability of the experimental setups.

The calculated skyrmion numbers are shown in **Figure 6.21**(a), demonstrating good consistency between measurement and design for configurations A to F. Lastly, the error of the skyrmion number was defined as the difference between the computed and designed skyrmion numbers across all configurations, with the results depicted in Figure 6.21(b). The computed errors for configurations A to F exhibit relatively minor divergence, with a general trend of increasing as the target skyrmion number increases.

6.4.4 Discussion of Results

One of the key properties of optical skyrmions and optical merons is their topological protection under external disturbances, making them ideal for next-generation information and communication technologies. The topological stability of these optical skyrmionic and meronic beams during transmission under commonly encountered perturbations are assessed. Signal intensity distortion caused by energy loss at the transition surface between different media was simulated using an ND filter. Signal phase distortion, caused by non-uniform refractive index profiles

in the transmission medium, was simulated using a variable quarter-wave plate cascaded with a SLM, which applied an arbitrary phase pattern constrained only by boundary conditions of optical skyrmions and optical merons. Signal polarisation distortion due to reflection and interference of optical components was simulated by introducing a nematic LC glass cell. Following experimental procedures, we illuminated these perturbations sequentially with skyrmionic and meronic beams configured with different skyrmion numbers. The resulting beam profiles were recorded using a Stokes polarimeter, and the beam profiles at the focus were captured by a CCD camera.

The experimental results demonstrate the robustness of the topology of these complex optical beams. By evaluating the skyrmion number of the topological fields, we observed consistent skyrmion numbers before and after introducing external perturbations. The consistent performance of these complex topologies, generated with cascaded SLMs, indicates their potential for robust optical communication approaches. To note here that the topological protection of the optical meronic beams is ensured due to its boundary conditions being maintained under the disturbances. Therefore, we predict that this protection may not hold under the influence of a uniform diattenuator (e.g., polarisers) which could potentially break the boundary conditions, leading to a loss of stability. This discrepancy presents an interesting challenge and opens up a pathway for further investigation in future research to explore how different diattenuation profiles might impact the stability and behaviour of optical merons.

This study provides compelling evidence of the robust topological protection offered by complex skyrmionic and meronic beams. Through evaluation of the skyrmion numbers, we confirmed their consistency before and after perturbations, highlighting the resilience of these structures under different conditions. Our findings validate the effectiveness of skyrmion and meron topologies generated with two cascaded SLMs, underscoring their potential in future

optical communication paradigms. In these studies, topological protection emerges through the interplay between global symmetries and long-range entanglement. These topologically protected states are immune to local defects and disorders, making them crucial for applications in optical computing and condensed matter physics. By demonstrating consistent performance despite perturbations, these study lay the foundation for developing robust and reliable optical communication systems to meet the demands of next-generation technologies.

6.5 Summary

In this work, the definition of complex optical skyrmions and merons is proposed in the realm of optics by modulating the polarisation field of structured light. The corresponding generation mechanisms utilised to realise these skyrmions and merons in optical systems are explained in detail. A critical advantage of these optical skyrmions and merons is their topological protection, inherited from their origins in physics, which we evaluate for performance in hypothetical real-world environments.

To define optical skyrmions and merons, a unified definition based on the physical origins of the skyrmion and meron was proposed, adapting them into optic field using structured light as the configuration medium. Extending the concept of skyrmion and meron from physics to optics and emerging field of vectorial optics opens a new chapter in nanophotonics, providing a novel perspective for controlling structured light. Additionally, an innovative approach to construct these optical skyrmions and merons actively using cascaded spatial light modulators (SLMs) is introduced. Utilising these cascaded universal optical modulators, structured light is pixelated and modulated in the active region to realise a spatially varying vectorial field, offering the flexibility to generate skyrmion and meron patterns of any order. Both low-order and high-order skyrmion and meron patterns are generated with high qualities and their field topo-

logical configurations verified. This controllable structured light generator unlocks potential for next-generation information technology. Experimental verification of topological protection in optical skyrmionic and meronic beams demonstrates consistent skyrmion number results, proving that optical skyrmions and optical merons are robust against common information perturbations in communication.

In summary, the proposed generation and analysis of optical skyrmionic and meronic beams unlocks new dimensions in processing, transferring, and storing information within a condensed light field, significantly extending the bandwidth of communication channels. This light-matter interaction in synthesising optical vector fields paves the way for applications spanning microscopy, high-volume on-chip optical computing, and beyond.

And one more thing ...

— Steve Jobs

CHAPTER 7

Conclusions and Future Work

This thesis focuses on the development and application of liquid crystal (LC) devices for optical beam control across four key systems: liquid crystal Dammann gratings, liquid crystal computer-generated holograms (LC CGHs), intensity adaptive optics (I-AO), and optical skyrmion and optical meron generation. Each research area harnesses the unique electro-optical properties of LCs to achieve advanced beam shaping and control.

The research on Dammann gratings highlights high-precision, laser-fabricated LC structures, achieving excellent structural accuracy and high diffraction efficiency. Both the switchable single-layer and interchangeable dual-layer gratings produced equal-intensity beam arrays with high-quality performance, making them ideal for advanced beam shaping applications. Using the same fabrication technology, switchable and interchangeable holographic structures were also created in LC devices. These holograms delivered high-quality results in displaying complex patterns, offering flexible and efficient control over complex designed light fields. LCs were also employed in spatial light modulators (SLMs) for real-time intensity aberration correction, utilising a novel dual feedback loop corrector. The sensor-based and sensorless correction methods, along with the designed correction patterns, highlighted the advantage of the proposed system in improving optical system performance. Furthermore, the generation of robust optical skyrmions and optical merons was achieved using cascaded LC devices as core optical

components. These beams, encoded with light polarisation, exhibited topological stability and accuracy.

Together, these systems are interconnected by the shared objective of enhancing precision, efficiency, and adaptability in optical beam shaping and control. This research not only highlights the current capabilities of LC devices in beam modulation but also lays the groundwork for future innovations, demonstrating how these diverse applications collectively drive the continuous evolution of LC technologies.

7.1 Diffractive Optical Elements

7.1.1 Conclusion

The first part of the thesis has focused on the development of new laser written LC diffractive optical elements, specifically switchable Dammann gratings and computer-generated holograms (CGHs). Chapter 3 presents results that demonstrate the successful design and fabrication of both single and bilayer LC Dammann gratings, showcasing their ability to switch between different gratings and produce distinct patterns in the replay field upon the application of a voltage. The validation of these designs through both simulations and experimental results confirms the high quality and good performance of the fabricated gratings. Furthermore, in Chapter 4, the development of advanced laser-written LC CGHs has exhibited high efficiency and adaptability in creating dynamic holographic images, with excellent performance in applications such as optical tweezers and dynamic displays.

In Chapter 3, the focus is on the design, fabrication, and performance evaluation of LC Dammann gratings, produced using the two-photon polymerisation direct laser writing (TPP-DLW) process. The fabrication achieved high structural precision, with up to 98% accuracy. Quantitative analysis showed diffraction efficiencies of up to 60% for the single-layer switchable

grating and 40% for the dual-layer interchangeable gratings, demonstrating strong performance in generating equal-intensity beam arrays. The gratings exhibited excellent intensity uniformity across the array, with minimal variation, making them well-suited for beam shaping and distribution applications. Response times were measured in the millisecond range, supporting their potential for dynamic beam modulation.

High fabrication accuracy with minimal defects was confirmed through simulations and SLM-based experiments, ensuring precise far-field diffraction predictions and optimised fabrication parameters. The gratings maintained stable diffraction efficiency from 25°C to 60°C and consistent multiwavelength performance by adjusting the voltage to maintain a π phase difference. Both single-layer switchable and bilayer interchangeable gratings demonstrated versatility for optical communications, computing, and laser beam shaping.

In Chapter 4, the focus is on the design and performance of laser-written LC computer-generated holograms (CGHs), a more advanced class of diffractive optical elements compared to Dammann gratings. CGH designs were first validated using a SLM, and both single-layer and bilayer switchable CGHs were fabricated using a polymerisable nematic LC mixture. Single-layer CGHs demonstrated the ability to switch on and off by adjusting the voltage, with response times varying based on LC thickness. For a 5 μm device, the rise time was 20 ms, and the fall time was 120 ms, while the thicker 20 μm device showed a rise time of 70 ms and a fall time of 430 ms.

Bilayer CGHs, designed to switch between two distinct images, such as the University of Oxford and Somerville College crests, exhibited faster transitions than single-layer devices, with a 50 ms rise time and 220 ms fall time. The improved performance of bilayer CGHs, with high contrast and fast switching, makes them ideal for dynamic optical systems. These CGHs showed excellent diffraction efficiency and fabrication feasibility, demonstrating their potential

for applications in adaptive optics, holographic displays, and reconfigurable optical systems.

7.1.2 Future Work

While Chapter 3 and Chapter 4 of this thesis have made significant strides in developing and characterising diffractive optical elements fabricated in LC devices for optical beam control, several avenues for future research remain. These include enhancing device fabrication techniques, exploring new algorithms to improve CGH performance and efficiency, and integrating LC-based devices into broader optical systems. Each of these directions offers the potential to advance LC technology and expand its applicability in cutting-edge optical applications.

(i) Improvements in Device Fabrication

Future research could improve the accuracy and efficiency of LC device fabrication by adopting a photo-initiator-free approach in the two-photon polymerisation direct laser writing (TPP-DLW) process. This method eliminates the need for traditional photo-initiators, resulting in higher structural purity and enhanced optical properties. Without photo-initiators, LC devices can operate across a broader wavelength spectrum, making them particularly well-suited for applications in the visible range, such as adaptive optics and dynamic holography. Early studies have demonstrated the potential of this approach for generating high-performance polymer networks, paving the way for more precise LC devices[328].

Another promising area is the exploration of alternative LC mixtures with higher birefringence or lower viscosity to increase modulation depths and switching speeds. Investigating polymerisable LC mixtures that offer better temperature stability and multi-wavelength compatibility could further expand the versatility of these devices. Additionally, advancements in multi-layer fabrication techniques may enable the development of complex bilayer or multilayer structures, allowing simultaneous control of multiple holographic images or beam patterns

within a single device. These improvements would enhance the utility of LC devices in applications such as augmented reality (AR) and virtual reality (VR), where rapid switching and high image fidelity are critical[329].

(ii) Algorithm Development for LC CGHs

Expanding the algorithms used to generate holographic patterns is another critical area for future research. Iterative algorithms, such as variants of the Gerchberg-Saxton (GS) algorithm — like the Yang-Gu Algorithm[330] or weighted GS algorithms[331] — and others like the holographic stereogram algorithm[332] or wavefront recording plane method[333], could improve the quality and efficiency of holographic reconstructions in LC CGHs. These algorithms could be optimised to handle complex 3D holographic patterns, enabling real-time hologram generation for more interactive displays.

Furthermore, adaptive algorithms could dynamically adjust CGH patterns based on real-time optical feedback, compensating for aberrations and misalignments to enhance hologram quality. This is particularly beneficial in biological imaging and free-space optical communication, where changing conditions impact system performance[334]. Machine learning algorithms could further refine CGH optimisation, improving precision, speed, and interactivity in holographic displays[335].

(iii) Integration into Optical Systems

The integration of LC devices into complete optical systems is a logical next step. For instance, switchable LC Dammann gratings and CGHs could be incorporated into optical communication systems, where they adjust beam shapes and transmission patterns based on transmission conditions[189]. The ability to switch between different holographic patterns on demand could also enable data multiplexing, improving bandwidth and overall efficiency in communications.

Additionally, future research could explore the integration of LC CGHs into 3D holographic displays[336]. The capacity to generate high-quality 3D images with switchable holograms positions LC CGHs as ideal candidates for AR and VR applications. Further exploration of this area could lead to the development of compact, low-cost 3D displays capable of switching between multiple images or viewpoints in real-time, offering a more immersive experience.

7.2 Intensity Adaptive Optics

7.2.1 Conclusion

In Chapter 5, the focus is on developing and applying LC devices for intensity aberration correction in optical systems. The chapter first explains optical aberrations, with particular emphasis on intensity aberrations, which significantly impair image resolution and contrast. These aberrations are especially problematic in astronomy, where precise imaging of faint celestial objects is essential, and in biomedical imaging, where high contrast is critical for accurate diagnoses. The chapter introduces novel intensity aberration correction modes, drawing on Zernike polynomials traditionally employed in phase adaptive optics (AO) and leveraging the architecture of the intensity adaptive optics (I-AO) corrector. Two correction methods are also proposed for the aberration compensation: the sensor-based and sensorless approaches. The sensor-based method directly measures intensity variations and applies compensation patterns to the corrector, while the sensorless approach uses feedback algorithms with intensity Zernike patterns to estimate and apply the optimal correction, effectively eliminating aberrations.

The development of a dual-loop feedback correction system is another key innovation discussed in this chapter. This system facilitates real-time correction of intensity aberrations by employing two feedback loops: one aimed at restoring intensity uniformity at the pupil plane and another for compensating energy loss and recovering total beam intensity. In the first

loop in the sensor-based method, the intensity profile is measured directly at the pupil plane and corrected by comparing the actual captured intensity at each pixel with the desired target intensity. Corrections are applied to adjust the intensity to match the target profile, using SLMs to generate the necessary patterns. The second loop in the sensor-based method then adjusts the overall system energy by regulating the illumination source to maintain the original beam intensity. The same dual-loop feedback correction procedures is performed for the sensorless method except for that the intensity aberration is estimated using designed patterns rather than the direct measurement. This dual-loop system, therefore, ensures both uniformity and total intensity restoration, significantly improving image quality in applications that require high precision, such as optical microscopy and astronomical imaging.

Experimental results demonstrate that traditional phase aberration corrections, which rely on adjusting the phase of the wavefront, are insufficient to correct intensity aberrations. These intensity aberrations lead to uneven energy distribution, which cannot be addressed by phase correction alone. Through the dual-loop system, both phase and intensity aberrations are corrected, leading to an almost ideal focal spot and a diffraction-limited performance. The experiments compared sensor-based and sensorless methods, highlighting that while the sensor-based approach offers direct measurements of intensity aberrations, the sensorless method, which infers aberrations through analysis of focal spot images, provides a more compact and hardware-efficient alternative. Each method has its strengths, with sensor-based systems offering more precise intensity measurements and sensorless systems excelling in scenarios where additional hardware cannot be integrated.

7.2.2 Future Work

Future work should prioritise the optimisation of intensity-adaptive optics (I-AO) techniques, with a focus on enhancing both correction accuracy and response times to meet the stringent

demands of high-resolution dynamic real-world applications, such as advanced microscopy and astronomical imaging. These improvements will be critical in addressing the growing need for more accurate, real-time adaptive corrections in systems where even minor aberrations can significantly affect image quality and overall system performance. By refining existing methodologies and exploring innovative approaches, the following future research topics will unlock the potential of I-AO in delivering sharper, more reliable imaging across a broader range of optical applications.

(i) Optimising Control Algorithm of I-AO Corrector

Optimising the I-AO control algorithm involves refining the dual-loop feedback mechanism with more advanced algorithms that dynamically adjust correction patterns in real time, using continuously updated intensity data. Machine learning models trained on extensive aberration datasets can also potentially been utilised to predict and implement more accurate correction patterns, accounting for complex, non-linear aberrations. This reduces computational load by bypassing traditional iterative methods, thus enhancing both the speed and responsiveness of the system[337]. Such advancements hold significant promise for improving the efficiency, accuracy, and robustness of real-time aberration correction in high-resolution imaging applications.

(ii) New Correction Modes and Image Metrics

Another avenue for improvement lies in investigating new intensity correction modes that expand beyond conventional Zernike polynomials. Exploring more complex basis functions or data-driven modes, tailored to specific aberration profiles in different imaging contexts, could improve the sensorless I-AO approach[338]. New image metrics, such as intensity variance minimisation or contrast enhancement, could be incorporated into the feedback algorithms to better estimate and correct intensity aberrations without relying on direct measurement[339,340].

(iii) Integration with Other Adaptive Optics Techniques

Integrating I-AO systems with vectorial adaptive optics (V-AO) could lead to comprehensive correction systems that simultaneously address both phase, polarisation, and intensity aberrations. V-AO corrector, capable of compensating for phase and polarisation related aberrations, could work in tandem with I-AO modules to manage phase, intensity, and polarisation effects within a single system. This would be particularly useful for high-contrast applications where all three factors influence image quality. For instance, combining I-AO and V-AO would enable systems to achieve higher Strehl ratios and more uniform intensity distributions, allowing for sharper and more accurate imaging of faint or complex objects.

(iv) Advancing Hardware Integration

To further advance the scope and impact of adaptive optics technologies, future efforts could also focus on improving hardware integration. Reducing the size and complexity of I-AO and V-AO systems through miniaturisation designs and integration with current imaging platforms would increase their practical applications, especially in areas such as endoscopy or space-based telescopes, where space and weight are limited[341]. Additionally, the development of faster and more energy-efficient SLMs or DMs could significantly improve system performance, enabling real-time correction even in dynamic or low-light environments.

7.3 Structured Light

7.3.1 Conclusion

In Chapter 6, the generation of optical skyrmions and optical merons through cascaded LC devices is thoroughly investigated, focusing on the creation and manipulation of skyrmions and merons. The chapter details the mechanisms of beam generation, their topological characteristics, and their robustness against external disturbances, while exploring their potential

applications in advanced optical systems such as optical computing and data transmission.

Using a setup of cascaded nematic LC SLMs, skyrmionic and meronic beams of varying orders were successfully generated. The experiments demonstrated topological protection of these structures, as they maintained their topological charge under manipulation. Specifically, skyrmion numbers were varied across a range, from low-order $S = 1$ to high-order $S = 9$ configurations for skyrmions and low-order $S = 0.5$ configurations to high-order $S = 4.5$ for merons, with precise control over the polarisation field achieved through cascaded SLM manipulation. Quantitatively, the control over the topological charge was fine-tuned with an accuracy of more than 95% for skyrmionic beams and 80% for meronic beams when adjusting the skyrmion number.

The robustness of these topological structures was confirmed through a series of tests involving external corruptions, including phase distortions, optical noise, and misalignment of optical elements. The experiments showed that the skyrmionic beams exhibited a deviation of less than 10% in skyrmion number when propagated through various corrupting optical elements. And both skyrmionic and meronic beams can recover their original skyrmion number after rounded the calculation results to their closest skyrmion numbers. This confirms the theoretical predictions of their topological protection. This level of resilience is crucial for their potential application in systems requiring high fidelity and stable data transfer.

This chapter concludes by highlighting the future potential of skyrmionic and meronic beams from cascaded LC-SLMs. Their stability against phase aberrations, with minimal beam profile changes, underscores their suitability for robust topological applications.

7.3.2 Future Work

The results presented in Chapter 6 lay the foundation for several promising avenues of future research in the field of optical skyrmions and optical merons. The ability to control skyrmion and meron structures with high precision opens up new possibilities in the field of topological photonics. To further advance the understanding and practical applications of optical skyrmions and optical merons, future work should focus on several key areas, including the generation of higher-order patterns, the development of new LC devices for structured illumination, and the integration of these technologies into the fundamental research in light and matter and emerging fields in future communications.

(i) High-Order Skyrmions and Merons

One direction for future research is to explore higher-order optical skyrmions and merons in more complex environments. This thesis successfully generated and tested optical skyrmions with topological charges up to $S = 9$ and optical merons up to $S = 4.5$ for robustness. However, investigating even higher-order configurations could provide deeper insights into beam interactions and stability under more extreme conditions, such as increased wavefront distortion or physical obstacles along the propagation path. Advancing the generation of optical skyrmions and merons will help identify the limitations of topological protection and expand the range of available generated beams. This helps the development of fundamental research in light-matter interaction and benefits future applications related to the duality symmetry, offering new opportunities to probe and manipulate complex topological states.

(ii) Advanced Structured Light Generators

A major technical advancement would involve the development of structured light generators beyond the use of cascaded SLMs. The current reliance on SLMs provides a high degree of con-

trol over polarisation fields, enabling the generation of skyrmions and merons. However, future research could explore using laser writing techniques to fabricate new types of liquid crystal devices specifically designed for structured illumination. These devices could offer similar control over the polarisation fields but with a simplified architecture that does not rely on the dynamic modulation of SLM technology. This shift would enable the generation of more complex fields with minimised device sizes, including higher-order skyrmions and merons, while potentially reducing the system complexity, cost, and power consumption. Laser-written LC devices and methods explored in Chapter 3 and Chapter 4 could be further optimised here for applications including high-volume data transmission systems or compact optical communication setups, where physical space and power efficiency are paramount. And also, the development of SLMs capable of continuous linear or elliptical polarisation tuning would significantly enhance our research capabilities, enabling more precise control over beam characteristics for a better structure light generation.

(iii) Towards Future Applications

A promising area for future research is optical computing, where skyrmions and merons, with their robust topological features, could be leveraged for encoding and transmitting high-density optical information. The stability and resilience of skyrmions and merons also make them excellent candidates for data encoding in next-generation optical communications. Encoding information within their topological properties - beyond just intensity or phase — would increase bandwidth and system robustness, making them less susceptible to signal degradation from field distortions or noise. Future work could explore their integration into fibre-optic communications, where they could serve as robust data carriers over long distances, even in challenging environments.

Additionally, combining insights from structured light generation with advanced liquid

crystal devices could enable highly efficient and compact communication systems. Custom LC-based structured light generators tailored for optical communications could significantly enhance data transmission fidelity and resilience compared to conventional methods.

7.4 Final Remarks

This thesis has showcased the transformative potential of LC devices in advanced optical systems, with applications spanning diffractive optical elements, adaptive optics, and structured light generation. The research combines experimental innovation with theoretical analysis, offering new insights into the future of optical technologies.

Chapter 3 introduced LC-based Dammann gratings, achieving efficient multi-wavelength beam generation with high diffraction efficiency and temperature stability. These capabilities were further expanded in Chapter 4, which explored laser-written LC CGHs, demonstrating adaptability, fast response times, and the potential to replace SLMs in compact optical systems. Chapter 5 investigated LC devices for real-time intensity aberration correction in adaptive optics, resulting in significant improvements in image quality, particularly for high-resolution microscopy. In Chapter 6, we generated and controlled optical fields — skyrmionic and meronic beams — investigating their robustness and potential use in next-generation high-density data transmission.

In conclusion, this work establishes LC devices as versatile tools for enhancing optical system performance, from structured light generation to the development of robust topological features for data encoding. These findings provide a strong foundation for future advancements in topological photonics, optical communication, optical computing and beyond.

Bibliography

1. Chandrasekhar, S. *Liquid Crystals* (Cambridge University Press, Cambridge, 2004).
2. Gennes, P.-G. and Prost, J. *The Physics of Liquid Crystals* (Clarendon Press, Oxford, 2013).
3. Yeh, P. and Gu, C. *Optics of Liquid Crystal Displays* (Wiley, Hoboken, NJ, 2010).
4. Yang, D.-K. and Wu, S.-T. *Fundamentals of Liquid Crystal Devices* (Wiley, Chichester, 2015).
5. Deubel, M. *et al.* Direct laser writing of three-dimensional photonic-crystal templates for telecommunications. *Nat. Mater.* **3,** 444 (2004).
6. Wright, A. J. and Poland, S. P. *Adaptive Optics for Aberration Correction in Optical Microscopy* in *Handbook of Photonics for Biomedical Engineering* (Springer, 2017).
7. He, C. and Booth, M. J. *Improvement of Resolution and Polarisation Measurement Precision in Biomedical Imaging Through Adaptive Optics* in *Polarized Light in Biomedical Imaging and Sensing* (Springer, 2022).
8. Davis, J. A., Guertin, J. and Cottrell, D. M. Diffraction-free beams generated with programmable spatial light modulators. *Appl. Optics* **32,** 6368 (1993).
9. Zhao, C. *et al.* Diffractive optical elements based on rewritable photoalignment for transparent display and smart windows. *Dig. Tech. Pap.* **49,** 1718 (2018).
10. García-Martínez, P. *et al.* Generation of Bessel beam arrays through Dammann gratings. *Appl. Optics* **51,** 1375 (2012).
11. He, Z. *et al.* Enlarging the eyebox of maxwellian displays with a customized liquid crystal Dammann grating. *Crystals* **11,** 195 (2021).
12. Booth, M. J. Wavefront sensorless adaptive optics for large aberrations. *Opt. Lett.* **32,** 5 (2006).
13. Hu, Q., He, C. and Booth, M. J. Arbitrary complex retarders using a sequence of spatial light modulators as the basis for adaptive polarisation compensation. *J. Opt.* **23,** 065602 (2021).
14. Lagerwall, J. P. F. and Scalia, G. A new era for liquid crystal research: applications of liquid crystals in soft matter nano-, bio- and microtechnology. *Curr. Appl. Phys.* **12,** 1387 (2012).
15. Tartan, C. C. *et al.* Read on demand images in laser-written polymerizable liquid crystal devices. *Adv. Opt. Mater.* **6,** 1800515 (2018).
16. Zhang, Z., You, Z. and Chu, D. Fundamentals of phase-only liquid crystal on silicon (LCOS) devices. *Light: Sci. Appl.* **3,** e213 (2014).
17. Thalhammer, G. *et al.* Speeding up liquid crystal SLMs using overdrive with phase change reduction. *Opt. Express* **21,** 1779 (2013).
18. Xue, L. *et al.* Fast analogue 2π phase modulation using a liquid crystal Pi-Cell. *Opt. Laser Technol.* **167,** 109773 (2023).
19. Davies, R. and Kasper, M. Adaptive optics for astronomy. *Annu. Rev. Astron. Astr.* **50,** 305 (2012).
20. Kubby, J. *Adaptive Optics for Biological Imaging* (CRC Press, Boca Raton, FL, 2013).
21. Yang, Y., Forbes, A. and Cao, L. A review of liquid crystal spatial light modulators: devices and applications. *Opto-Electron. Sci.* **2,** 230026 (2023).
22. Willner, A. E. *et al.* Optical communications using orbital angular momentum beams. *Adv. Opt. Photonics* **7,** 66 (2015).
23. Shen, Y. *et al.* Creation and control of high-dimensional multi-partite classically entangled light. *Light: Sci. Appl.* **10,** 50 (2021).
24. Forbes, A., de Oliveira, M. and Dennis, M. R. Structured light. *Nat. Photonics* **15,** 253 (2021).
25. Yoshida, H. *et al.* Optical tuning and switching of photonic defect modes in cholestericliquid crystals. *Appl. Phys. Lett.* **90,** 071107 (2007).
26. Maruo, S., Nakamura, O. and Kawata, S. Three-dimensional microfabrication with two-photon-absorbed photopolymerization. *Opt. Lett.* **22,** 132 (1997).
27. Tartan, C. C. *et al. Fabrication of micro- and nanometre-scale polymer structures in liquid crystal devices for next generation photonics applications* in *Liquid Crystals XX* (SPIE, 2016).
28. Schmidt, J. D. *et al. High-Resolution Liquid Crystal Spatial Light Modulators for Adaptive Optics* in *2006 IEEE Aerospace Conference* (IEEE, 2006).

29. Collings, P. J. and Hird, M. *Introduction to Liquid Crystals Chemistry and Physics* (Taylor & Francis Group, London, 2017).
30. Li, Q. *Liquid Crystals Beyond Displays: Chemistry, Physics, and Applications* (J. Wiley & Sons, Hoboken, NJ, 2012).
31. Friedel, G. Les états mésomorphes de la matière. *Ann. Phys.* **9,** 273 (1922).
32. Oseen, C. W. The theory of liquid crystals. *Trans. Faraday Soc.* **29,** 883 (1933).
33. O'Mara, W. C. *Liquid Crystal Flat Panel Displays* (Springer, New York, NY, 1993).
34. Frank, F. C. I. Liquid crystals. On the theory of liquid crystals. *Discuss. Faraday Soc.* **25,** 19 (1958).
35. Zocher, H. The effect of a magnetic field on the nematic state. *Trans. Faraday Soc.* **29,** 945 (1933).
36. Kumar, S. *Liquid Crystals* (Cambridge University Press, Cambridge, 2011).
37. Jerome, B. Surface effects and anchoring in liquid crystals. *Rep. Progr. Phys.* **54,** 391 (1991).
38. Malinauskas, M. *et al.* Ultrafast laser nanostructuring of photopolymers: a decade of advances. *Phys. Rep.* **533,** 1 (2013).
39. Raimondi, M. T. *et al.* Two-photon laser polymerization: from fundamentals to biomedical application in tissue engineering and regenerative medicine. *J. Appl. Biomater. Funct. Mater.* **10,** 56 (2012).
40. Kawata, S. *et al.* Finer features for functional microdevices. *Nature* **412,** 697 (2001).
41. Zhou, X., Hou, Y. and Lin, J. A review on the processing accuracy of two-photon polymerization. *AIP Advances* **5,** 030701 (2015).
42. Bogaerts, W. *et al.* Fabrication of photonic crystals in silicon-on-insulator using 248-nm deep UV lithography. *IEEE J. Sel. Top. Quantum Electron.* **8,** 928 (2002).
43. Vieu, C. *et al.* Electron beam lithography: resolution limits and applications. *Appl. Surf. Sci.* **164,** 111 (2000).
44. Watt, F. *et al.* Ion beam lithography and nanofabrication: a review. *Int. J. Nanosci.* **04,** 269 (2005).
45. Chou, S. Y. Nanoimprint lithography. *J. Vac. Sci. Technol.* **14,** 4129 (1996).
46. Bertsch, A., Jiguet, S. and Renaud, P. Microfabrication of ceramic components by microstereolithography. *J. Micromech. Microeng.* **14,** 197 (2003).
47. Walther, M. *et al.* Terahertz metamaterials fabricated by inkjet printing. *Appl. Phys. Lett.* **95,** 251107 (2009).
48. Pacholski, C., Kornowski, A. and Weller, H. Self-assembly of ZnO: from nanodots to nanorods. *Angew. Chem. - Int. Ed.* **41,** 1188 (2002).
49. Hollister, S. J. Porous scaffold design for tissue engineering. *Nat. Mater.* **4,** 518 (2005).
50. Selimis, A., Mironov, V. and Farsari, M. Direct laser writing: principles and materials for scaffold 3D printing. *Microelectron. Eng.* **132,** 83 (2015).
51. Cooke, M. N. *et al.* Use of stereolithography to manufacture critical-sized 3D biodegradable scaffolds for bone ingrowth. *J. Biomed. Mater. Res.* **64B,** 65 (2002).
52. Dhariwala, B., Hunt, E. and Boland, T. Rapid prototyping of tissue-engineering constructs, using photopolymerizable hydrogels and stereolithography. *Tissue Eng.* **10,** 1316 (2004).
53. Fisher, J. P. *et al.* Soft and hard tissue response to photocrosslinked poly(propylene fumarate) scaffolds in a rabbit model. *J. Biomed. Mater. Res.* **59,** 547 (2001).
54. Tan, K. H. *et al.* Scaffold development using selective laser sintering of polyetheretherketone hydroxyapatite biocomposite blends. *Biomaterials* **24,** 3115 (2003).
55. Chua, C. K. *et al.* Development of tissue scaffolds using selective laser sintering of polyvinyl alcohol/hydroxyapatite biocomposite for craniofacial and joint defects. *J. Mater. Sci.: Mater. Med.* **15,** 1113 (2004).
56. Gale, M. T. Fabrication of continuous-relief micro-optical elements by direct laser writing in photoresists. *Opt. Eng.* **33,** 3556 (1994).
57. Pelli, S. *et al.* Direct laser writing of ridge optical waveguides in silica-titania glass sol-gel films. *Opt. Mater.* **5,** 119 (1996).
58. Juodkazis, S., Mizeikis, V. and Misawa, H. Three-dimensional microfabrication of materials by femtosecond lasers for photonics applications. *J. Appl. Phys.* **106,** 051101 (2009).
59. Brasselet, E. *et al.* Photopolymerized microscopic vortex beam generators: precise delivery of optical orbital angular momentum. *Appl. Phys. Lett.* **97,** 211108 (2010).
60. Malinauskas, M. *et al.* Femtosecond laser polymerization of hybrid/integrated micro-optical elements and their characterization. *J. Opt.* **12,** 124010 (2010).
61. Amato, L. *et al.* Integrated three-dimensional filter separates nanoscale from microscale elements in a microfluidic chip. *Lab Chip* **12,** 1135 (2012).

62. Schizas, C. *et al.* On the design and fabrication by two-photon polymerization of a readily assembled micro-valve. *Int. J. Adv. Manuf. Technol.* **48,** 435 (2009).
63. Galanopoulos, S. *et al.* Design, fabrication and computational characterization of a 3D micro-valve built by multi-photon polymerization. *Micromachines* **5,** 505 (2014).
64. Torgersen, J. *et al.* Photo-sensitive hydrogels for three-dimensional laser microfabrication in the presence of whole organisms. *J. Biomed. Opt.* **17,** 1 (2012).
65. Torgersen, J. *et al.* Hydrogels for two-photon polymerization: a toolbox for mimicking the extracellular matrix. *Adv. Funct. Mater.* **23,** 4542 (2013).
66. Soukoulis, C. M. and Wegener, M. Past achievements and future challenges in the development of three-dimensional photonic metamaterials. *Nat. Photonics* **5,** 523 (2011).
67. Vaezi, M., Seitz, H. and Yang, S. A review on 3D micro-additive manufacturing technologies. *Int. J. Adv. Manuf. Technol.* **67,** 1721 (2012).
68. Gan, Z. *et al.* Three-dimensional deep sub-diffraction optical beam lithography with 9 nm feature size. *Nat. Commun.* **4,** 2061 (2013).
69. Fischer, J. and Wegener, M. Three-dimensional optical laser lithography beyond the diffraction limit. *Laser Photonics Rev.* **7,** 22 (2012).
70. Göppert-Mayer, M. Über Elementarakte mit zwei Quantensprüngen. *Ann. Phys. (Berl.)* **401,** 273 (1931).
71. Kaiser, W. and Garrett, C. G. B. Two-Photon Excitation in CaF_2:Eu^{2+}. *Phys. Rev. Lett.* **7,** 229 (1961).
72. Serbin, J. *et al.* Femtosecond laser-induced two-photon polymerization of inorganic–organic hybrid materials for applications in photonics. *Opt. Lett.* **28,** 301 (2003).
73. Kaneko, K. *et al.* Submicron diamond-lattice photonic crystals produced by two-photon laser nanofabrication. *Appl. Phys. Lett.* **83,** 2091 (2003).
74. Serbin, J., Ovsianikov, A. and Chichkov, B. Fabrication of woodpile structures by two-photon polymerization and investigation of their optical properties. *Opt. Express* **12,** 5221 (2004).
75. Maruo, S., Takaura, A. and Saito, Y. Optically driven micropump with a twin spiral microrotor. *Opt. Express* **17,** 18525 (2009).
76. Ovsianikov, A. *et al.* Two photon polymerization of polymer–ceramic hybrid materials for transdermal drug delivery. *Int. J. Appl. Ceram. Tec.* **4,** 22 (2007).
77. Ovsianikov, A. *et al.* Two-photon polymerization technique for microfabrication of CAD-designed 3D scaffolds from commercially available photosensitive materials. *J. Tissue Eng. Regen. M.* **1,** 443 (2007).
78. Klein, F. *et al.* Two-component polymer scaffolds for controlled three-dimensional cell culture. *Adv. Mater.* **23,** 1341 (2011).
79. Guo, R. *et al.* Micro lens fabrication by means of femtosecond two photon photopolymerization. *Opt. Express* **14,** 810 (2006).
80. Malinauskas, M. *et al.* A femtosecond laser-induced two-photon photopolymerization technique for structuring microlenses. *J. Opt.* **12,** 035204 (2010).
81. Wu, D. *et al.* High numerical aperture microlens arrays of close packing. *Appl. Phys. Lett.* **97,** 031109 (2010).
82. Kondo, T. *et al.* Three-dimensional microfabrication by femtosecond pulses in dielectrics. *Thin Solid Films* **453,** 550 (2004).
83. Boltasseva, A. and Shalaev, V. M. Fabrication of optical negative-index metamaterials: recent advances and outlook. *Metamaterials* **2,** 1 (2008).
84. Lim, T. W., Park, S. H. and Yang, D.-Y. Contour offset algorithm for precise patterning in two-photon polymerization. *Microelectron. Eng.* **77,** 382 (2005).
85. Takatoh, K. *Alignment Technologies and Applications of Liquid Crystal Devices* (Taylor & Francis, London, 2005).
86. Kawata, Y. *et al.* The alignment of nematic liquid crystals on photolithographic micro-groove patterns. *P. Soc. Photo-opt. Ins.* **16,** 1027 (1994).
87. Xie, A., Ito, T. and Higgins, D. A. Fabrication and characterization of polymer/liquid crystal composite diffractive optics by multiphoton methods. *Adv. Funct. Mater.* **17,** 1515 (2007).
88. Lee, C. H. *et al.* Local liquid crystal alignment on patterned micrograting structures photofabricated by two photon excitation direct laser writing. *Appl. Phys. Lett.* **93,** 173509 (2008).
89. Ji, Z. *et al.* Compartmentalized liquid crystal alignment induced by sparse polymer ribbons with surface relief gratings. *Opt. Lett.* **41,** 336 (2016).

90. Serra, F. *et al.* Nematic liquid crystals embedded in cubic microlattices: memory effects and bistable pixels. *Adv. Funct. Mater.* **23,** 3990 (2013).
91. Ho, C.-H. *et al.* Controllable light diffraction in woodpile photonic crystals filled with liquid crystal. *Appl. Phys. Lett.* **106,** 021113 (2015).
92. He, Z. *et al.* Polarization independent phase modulators enabled by two-photon polymerization. *Opt. Express* **25,** 33688 (2017).
93. Yoshida, H. *et al.* Bottom-up fabrication of photonic defect structures in cholesteric liquid crystals based on laser-assisted modification of the helix. *Adv. Mater.* **19,** 1187 (2007).
94. Ito, K. and Kimura, M. Optically induced rotation of microcylinders made of photopolymerizable nematic liquid crystal. *Jpn. J. Appl. Phys.* **49,** 040208 (2010).
95. Tartan, C. C. *et al.* Generation of 3-dimensional polymer structures in liquid crystalline devices using direct laser writing. *RSC Advances* **7,** 507 (2017).
96. Beckers, J. M. Adaptive optics for astronomy: principles, performance, and applications. *Annu. Rev. Astron. Astr.* **31,** 13 (1993).
97. Booth, M. J. Adaptive optical microscopy: the ongoing quest for a perfect image. *Light: Sci. Appl.* **3,** e165 (2014).
98. Ji, N. Adaptive optical fluorescence microscopy. *Nat. Methods* **14,** 374 (2017).
99. Porter, J. *Adaptive Optics for Vision Science* (Wiley, Hoboken, NJ, 2006).
100. Roddier, F. *Adaptive Optics in Astronomy* (Cambridge University Press, Cambridge, 1999).
101. Hampson, K. M. *et al.* Adaptive optics for high-resolution imaging. *Nat. Rev. Methods Primers* **1,** 68 (2021).
102. Tyson, R. *Principles of Adaptive Optics* (CRC Press, Boca Raton, FL, 2010).
103. Kolmogorov, A. N. The local structure of turbulence in incompressible viscous fluid for very large Reynolds numbers. *Proc. R. Soc. Lond. A* **434,** 9 (1991).
104. Hardy, J. W. *Adaptive Optics for Astronomical Telescopes* (Oxford University Press, Oxford, 1998).
105. Thibos, L. N. *et al.* Standards for reporting the optical aberrations of eyes. *J. Refract. Surg.* **18,** S652 (2002).
106. Thibos, L. N. *et al.* Statistical variation of aberration structure and image quality in a normal population of healthy eyes. *J. Opt. Soc. Amer. A* **19,** 2329 (2002).
107. Males, J. R. and Guyon, O. Ground-based adaptive optics coronagraphic performance under closed-loop predictive control. *J. Astron. Telesc. Instrum. Syst.* **4,** 1 (2018).
108. Diaz-Santana, L. *et al.* Benefit of higher closed-loop bandwidths in ocular adaptive optics. *Opt. Express* **11,** 2597 (2003).
109. Babcock, H. W. The possibility of compensating astronomical seeing. *PASP* **65,** 229 (1953).
110. Plöschner, M. *et al.* Spatial tomography of light resolved in time, spectrum, and polarisation. *Nat. Commun.* **13,** 4294 (2022).
111. Zhu, Z. *et al.* Compensation-free high-dimensional free-space optical communication using turbulence-resilient vector beams. *Nat. Commun.* **12,** 1666 (2021).
112. Ji, N., Milkie, D. E. and Betzig, E. Adaptive optics via pupil segmentation for high-resolution imaging in biological tissues. *Nat. Methods* **7,** 141 (2009).
113. Mrňa, L. *et al.* Adaptive optics for control of the laser welding process. *EPJ Web Conf.* **48** (eds Šulc, M. *et al.*) 00017 (2013).
114. Rigaut, F. and Neichel, B. Multiconjugate adaptive optics for astronomy. *Annu. Rev. Astron. Astr.* **56,** 277 (2018).
115. Rao, C. *et al.* Astronomical adaptive optics: a review. *PhotoniX* **5,** 16 (2024).
116. Le Louarn, M. *et al. Adaptive optics simulations for the European Extremely Large Telescope* in *Advances in Adaptive Optics II* (SPIE, 2006).
117. Booth, M. J. Adaptive optics in microscopy. *Philos. Trans. R. Soc. Math. Phys. Eng. Sci.* **365,** 2829 (2007).
118. Do, T. *et al.* Relativistic redshift of the star S0-2 orbiting the Galactic Center supermassive black hole. *Science* **365,** 664 (2019).
119. Vorontsov, M. *et al. Adaptive Optics for Free Space Laser Communications* in *Lasers, Sources and Related Photonic Devices* (OSA, 2010).
120. Zocchi, F. E. A simple analytical model of adaptive optics for direct detection free-space optical communication. *Opt. Commun.* **248,** 359 (2005).

121. Su, X. *et al.* Adaptive-optics-based turbulence mitigation in a 400 Gbit/s free-space optical link by multiplexing Laguerre–Gaussian modes varying both radial and azimuthal spatial indices. *Opt. Lett.* **48,** 6452 (2023).
122. Martínez Rey, N. *et al. Enabling efficient quantum communications with adaptive optics* in *Free-Space Laser Communications XXXIV* (SPIE, 2022).
123. Zhang, J. *et al.* Flexible and adaptive coherent PON for next-generation optical access network. *Opt. Fiber Technol.* **75,** 103190 (2023).
124. Chang, H. *et al.* Adaptive optics compensation for orbital angular momentum optical wireless communications. *IEEE Trans. Wireless Commun.* **21,** 11151 (2022).
125. Rodríguez, C. *et al.* An adaptive optics module for deep tissue multiphoton imaging in vivo. *Nat. Methods* **18,** 1259 (2021).
126. Gould, T. J. *et al.* Adaptive optics enables 3D STED microscopy in aberrating specimens. *Opt. Express* **20,** 20998 (2012).
127. Salter, P. S. and Booth, M. J. Adaptive optics in laser processing. *Light: Sci. Appl.* **8,** 110 (2019).
128. Kato, J.-i. *et al.* Multiple-spot parallel processing for laser micronanofabrication. *Appl. Phys. Lett.* **86,** 044102 (2005).
129. Kelemen, L., Valkai, S. and Ormos, P. Parallel photopolymerisation with complex light patterns generated by diffractive optical elements. *Opt. Express* **15,** 14488 (2007).
130. Jenness, N. J. *et al.* Three-dimensional parallel holographic micropatterning using a spatial light modulator. *Opt. Express* **16,** 15942 (2008).
131. Kuang, Z. *et al.* High throughput diffractive multi-beam femtosecond laser processing using a spatial light modulator. *Appl. Surf. Sci.* **255,** 2284 (2008).
132. He, C. *et al.* A reconfigurable arbitrary retarder array as complex structured matter. *Nat. Commun.* Accepted (2024).
133. Ma, Y. *et al. Polarization adaptive optics for enhanced Stokes vector measurements* in *Polarized Light and Optical Angular Momentum for Biomedical Diagnostics 2024* (SPIE, 2024).
134. Dai, Y. *et al.* Active compensation of extrinsic polarization errors using adaptive optics. *Opt. Express* **27,** 35797 (2019).
135. Tyson, R. and Lakshminarayanan, V. Adaptive optics. *J. Mod. Optic.* **59,** 1032 (2012).
136. Rukosuev, A. L. *et al.* Adaptive optics system for real-time wavefront correction. *Atmos. Oceanic Opt.* **28,** 381 (2015).
137. Vishniakou, I. and Seelig, J. D. Wavefront correction for adaptive optics with reflected light and deep neural networks. *Opt. Express* **28,** 15459 (2020).
138. Shannon, R. R. *The Art and Science of Optical Design* (Cambridge University Press, Cambridge, 1997).
139. Hu, Q. *et al.* A universal framework for microscope sensorless adaptive optics: generalized aberration representations. *APL Photonics* **5,** 100801 (2020).
140. Wang, J. and Zhang, Y. Adaptive optics in super-resolution microscopy. *Biophys. Rep.* **7,** 267 (2021).
141. Hu, Q. *et al.* Universal adaptive optics for microscopy through embedded neural network control. *Light: Sci. Appl.* **12,** 270 (2023).
142. Hu, Q., Hailstone, M. and Booth, M. J. *Efficient and versatile aberration correction through sensorless adaptive optics* in *Three-Dimensional and Multidimensional Microscopy: Image Acquisition and Processing XXIX* (SPIE, 2022).
143. Ares, J., Mancebo, T. and Bará, S. Position and displacement sensing with Shack–Hartmann wave-front sensors. *Appl. Optics* **39,** 1511 (2000).
144. Platt, B. C. and Shack, R. History and principles of Shack-Hartmann wavefront sensing. *J. Refract. Surg.* **17,** S573 (2001).
145. Vérinaud, C. On the nature of the measurements provided by a pyramid wave-front sensor. *Opt. Commun.* **233,** 27 (2004).
146. Shatokhina, I., Hutterer, V. and Ramlau, R. Review on methods for wavefront reconstruction from pyramid wavefront sensor data. *J. Astron. Telesc. Instrum. Syst.* **6,** 1 (2020).
147. Bifano, T. G. Adaptive optic correction using microelectromechanical deformable mirrors. *Opt. Eng.* **41,** 561 (2002).
148. Zou, W., Qi, X. and Burns, S. A. Wavefront-aberration sorting and correction for a dual-deformable-mirror adaptive-optics system. *Opt. Lett.* **33,** 2602 (2008).

149. Sun, H., Kasdin, N. J. and Vanderbei, R. Efficient wavefront sensing for space-based adaptive optics. *J. Astron. Telesc. Instrum. Syst.* **6,** 1 (2020).
150. Biasi, R. *et al. High density, low power, contactless VCM-based adaptive mirror prototype* in *Adaptive Optics Systems VIII* (SPIE, 2022).
151. Roorda, A. and Duncan, J. L. Adaptive optics ophthalmoscopy. *Annu. Rev. Vis. Sci.* **1,** 19 (2015).
152. Talone, B. *et al.* Experimental determination of shift-less aberration bases for sensorless adaptive optics in nonlinear microscopy. *Opt. Express* **29,** 37617 (2021).
153. Jian, Y. *et al.* Lens-based wavefront sensorless adaptive optics swept source OCT. *Sci. Rep.* **6,** 27620 (2016).
154. Zernike, F. Beugungstheorie des Schneidenver fahrens und seiner verbesserten Form, der Phasenkontrast-methode. *Physica* **1,** 689 (1934).
155. Noll, R. J. Zernike polynomials and atmospheric turbulence. *J. Opt. Soc. Am.* **66,** 207 (1976).
156. Lakshminarayanan, V. and Fleck, A. Zernike polynomials: a guide. *J. Mod. Optic.* **58,** 545 (2011).
157. Jian, Y. *et al.* Wavefront sensorless adaptive optics optical coherence tomography for in vivo retinal imaging in mice. *Biomed. Opt. Express* **5,** 547 (2014).
158. Nousiainen, J. *et al.* Adaptive optics control using model-based reinforcement learning. *Opt. Express* **29,** 15327 (2021).
159. Guo, Y. *et al.* Adaptive optics based on machine learning: a review. *Opto-Electron. Adv.* **5,** 200082 (2022).
160. Zhang, P. *et al.* Deep learning-driven adaptive optics for single-molecule localization microscopy. *Nat. Methods* **20,** 1748 (2023).
161. Zhang, Q. *et al.* Adaptive optics for optical microscopy. *Biomed. Opt. Express* **14,** 1732 (2023).
162. Hua, H., Liu, Y. and Yong, K. The effect of pretilt and twisted angle on twisted nematic liquid crystal filter. *Opt. Spectrosc.* **125,** 275 (2018).
163. Meng, X. *et al.* Study of optical rotation generated by the twisted nematic liquid crystal film: based on circular birefringence effect. *Appl. Optics* **58,** 5301 (2019).
164. Rosen, J. *Holography* (IntechOpen, London, 2023).
165. Grunwald, R. *et al. Structuring light by combining spatial modulation and fast angular shaping* in *Complex Light and Optical Forces XVII* (SPIE, 2023).
166. Singh, S. *Advanced Applications of Liquid Crystals* in *Handbook of Liquid Crystals—Volume II* (Springer, 2024).
167. Dammann, H. and Görtler, K. High-efficiency in-line multiple imaging by means of multiple phase holograms. *Opt. Commun.* **3,** 312 (1971).
168. Dammann, H. and Klotz, E. Coherent optical generation and inspection of two-dimensional periodic structures. *Opt. Acta Int. J. Opt.* **24,** 505 (1977).
169. Killat, U., Rabe, G. and Rave, W. Binary phase gratings for star couplers with high splitting ratio. *Fiber Integrated Opt.* **4,** 159 (1982).
170. Jahns, J. *et al.* Dammann gratings for laser beam shaping. *Opt. Eng.* **28,** 281267 (1989).
171. Mait, J. N. Design of Dammann gratings for two-dimensional, nonseparable, noncentrosymmetric responses. *Opt. Lett.* **14,** 196 (1989).
172. Krackhardt, U. and Streibl, N. Design of Dammann-gratings for array generation. *Opt. Commun.* **74,** 31 (1989).
173. Franssila, S. *Introduction to Microfabrication* (John Wiley & Sons, Chichester, 2010).
174. Anscombe, N. Direct laser writing. *Nat. Photonics* **4,** 22 (2010).
175. Gissibl, T. *et al.* Two-photon direct laser writing of ultracompact multi-lens objectives. *Nat. Photonics* **10,** 554 (2016).
176. Moreno, I. *et al.* Encoding generalized phase functions on Dammann gratings. *Opt. Lett.* **35,** 1536 (2010).
177. Ye, Z. *et al.* Equilateral triangle hexagonal array by crossing two one-dimensional Dammann gratings with 60°. *Microw. Opt. Techn. Let.* **63,** 2297 (2021).
178. Yuan, Z.-N. *et al.* Fast LiDAR systems based on ferroelectric liquid crystal Dammann grating. *P. Soc. Photo-opt. Ins.* **48,** 1402 (2021).
179. Morrison, R. L. Symmetries that simplify the design of spot array phase gratings. *J. Opt. Soc. Amer. A* **9,** 464 (1992).
180. Vasara, A. *et al.* Binary surface-relief gratings for array illumination in digital optics. *Appl. Optics* **31,** 3320 (1992).
181. Zhou, C. and Liu, L. Numerical study of Dammann array illuminators. *Appl. Optics* **34,** 5961 (1995).

182. Zhou, C., Jia, J. and Liu, L. Circular Dammann grating. *Opt. Lett.* **28,** 2174 (2003).
183. Yu, J. *et al.* Three-dimensional Dammann array. *Appl. Optics* **51,** 1619 (2012).
184. Dickinson, A. and Prise, M. E. Free-space optical interconnection scheme. *Appl. Optics* **29,** 2001 (1990).
185. Xiang, C. *et al. Direct laser writing lithography technology based on rotating two-dimensional Dammann grating* in *Holography, Diffractive Optics, and Applications VIII* (SPIE, 2018).
186. Pang, H. *et al.* Alternative design of Dammann grating for beam splitting with adjustable zero-order light intensity. *IEEE Photonics J.* **11,** 1 (2019).
187. Liu, K. *et al. Binocular three-dimensional measurement system using a Dammann grating* in *Holography, Diffractive Optics, and Applications VI* (SPIE, 2014).
188. Ge, S.-J. *et al.* Optical array generator based on blue phase liquid crystal Dammann grating. *Opt. Mater. Express* **6,** 1087 (2016).
189. Fan, F. *et al.* Ferroelectric liquid crystal Dammann grating by patterned photoalignment. *Crystals* **7,** 79 (2017).
190. Wang, X.-Q. *et al.* Electrically/optically tunable photo-aligned hybrid nematic liquid crystal Dammann grating. *Opt. Lett.* **41,** 5668 (2016).
191. Yuan, Z.-N. *et al.* Fast-response cloud-point ferroelectric liquid crystal Dammann grating for lidar applications based on double-cell setup. *Dig. Tech. Pap.* **51,** 769 (2020).
192. Chigrinov, V. *et al.* Anchoring properties of photoaligned azo-dye materials. *Phys. Rev. E* **68,** 061702 (2003).
193. Shi, Y. *et al.* Two-photon laser-written photoalignment layers for patterning liquid crystalline conjugated polymer orientation. *Adv. Funct. Mater.* **31,** 2007493 (2020).
194. Sandford O'Neill, J. J. *et al.* Electrically-tunable positioning of topological defects in liquid crystals. *Nat. Commun.* **11,** 2203 (2020).
195. Sandford O'Neill, J. *et al.* 3D switchable diffractive optical elements fabricated with two-photon polymerization. *Adv. Opt. Mater.* **10,** 2102446 (2022).
196. Bueno-Ibarra, M. A. *et al.* Fast autofocus algorithm for automated microscopes. *Opt. Eng.* **44,** 063601 (2005).
197. Stewart, I. W. *The Static and Dynamic Continuum Theory of Liquid Crystals* (CRC Press, Boca Raton, FL, 2019).
198. Vardanyan, K. K. *et al.* Polymer scaffolding model for holographic polymer-dispersed liquid crystals. *Appl. Phys. Lett.* **81,** 4736 (2002).
199. Shim, H. *et al.* Enhancement of frequency modulation response time for polymer-dispersed liquid crystal. *P. Soc. Photo-opt. Ins.* **43,** 1390 (2016).
200. Stoykova, E. *et al. 3D Capture and 3D Contents Generation for Holographic Imaging* in *Holographic Materials and Optical Systems* (InTech, 2017).
201. Shi, L. *et al.* Towards real-time photorealistic 3D holography with deep neural networks. *Nature* **591,** 234 (2021).
202. Cheremkhin, P. A. *et al. Demonstration of digital hologram recording and 3D-scenes reconstruction in real-time* in *Optical Modelling and Design IV* (SPIE, 2016).
203. Liu, S. and Takaki, Y. Optimization of phase-only computer-generated holograms based on the gradient descent method. *Appl. Sci.* **10,** 4283 (2020).
204. Matsushima, K. *Fabrication of High-Definition CGH* in *Introduction to Computer Holography* (Springer, 2020).
205. Fratz, M., Fischer, P. and Giel, D. M. Full phase and amplitude control in computer-generated holography. *Opt. Lett.* **34,** 3659 (2009).
206. Mann, C. J. *et al.* High-resolution quantitative phase-contrast microscopy by digital holography. *Opt. Express* **13,** 8693 (2005).
207. Chang, C. *et al.* Speckle-suppressed phase-only holographic three-dimensional display based on double-constraint Gerchberg–Saxton algorithm. *Appl. Optics* **54,** 6994 (2015).
208. Zhou, P. *et al.* Dynamic compensatory Gerchberg–Saxton algorithm for multiple-plane reconstruction in holographic displays. *Opt. Express* **27,** 8958 (2019).
209. Zuo, J., Leng, J. and Fu, Y. Optimized phase-only hologram generation for high-quality holographic display. *Appl. Optics* **61,** 10519 (2022).
210. Chen, L. *et al.* Phase hologram optimization with bandwidth constraint strategy for speckle-free optical reconstruction. *Opt. Express* **29,** 11645 (2021).

211. Alonzo, C. A., Rodrigo, P. J. and Glückstad, J. Photon-efficient grey-level image projection by the generalized phase contrast method. *New J. Phys.* **9,** 132 (2007).
212. Chen, H.-C. and Cheng, C.-J. Holographic optical tweezers: techniques and biomedical applications. *Appl. Sci.* **12,** 10244 (2022).
213. Aharoni, T. and Shoham, S. Phase-controlled, speckle-free holographic projection with applications in precision optogenetics. *Neurophotonics* **5,** 1 (2018).
214. Freese, W. *et al.* Optimized electron beam writing strategy for fabricating computer-generated holograms based on an effective medium approach. *Opt. Express* **19,** 8684 (2011).
215. Călin, B.-Ş. *et al.* Laser fabrication of diffractive optical elements based on detour-phase computer-generated holograms for two-dimensional Airy beams. *Appl. Optics* **57,** 1367 (2018).
216. Li, Y. and Hong, M. Parallel laser micro/nano-processing for functional device fabrication. *Laser Photonics Rev.* **14,** 1900062 (2020).
217. Poleshchuk, A. G. and Korolkov, V. P. *Laser writing systems and technologies for fabrication of binary and continuous relief diffractive optical elements* in *International Conference on Lasers, Applications, and Technologies 2007: Laser-assisted Micro- and Nanotechnologies* (SPIE, 2007).
218. Sun, H.-B. and Kawata, S. Two-photon laser precision microfabrication and its applications to micro-nano devices and systems. *J. Lightwave Technol.* **21,** 624 (2003).
219. Fleisch, M. *et al.* Laser-written polymeric scaffolds for micro-patterned liquid crystal alignment. *P. Soc. Photo-opt. Ins.* **46,** 2075 (2019).
220. Saha, S. K. *et al.* Radiopaque resists for two-photon lithography to enable submicron 3d imaging of polymer parts via x-ray computed tomography. *ACS Appl. Mater. Interfaces* **10,** 1164 (2017).
221. Seldowitz, M. A., Allebach, J. P. and Sweeney, D. W. Synthesis of digital holograms by direct binary search. *Appl. Optics* **26,** 2788 (1987).
222. Guo, C., Liu, S. and Sheridan, J. T. Iterative phase retrieval algorithms I: optimization. *Appl. Optics* **54,** 4698 (2015).
223. Gerchberg, R. W. and Saxton, W. O. A practical algorithm for the determination of phase from image and diffraction plane pictures. *Optik* **35,** 237 (1972).
224. Fienup, J. R. Phase retrieval algorithms: a comparison. *Appl. Optics* **21,** 2758 (1982).
225. Salgado-Remacha, F. J. Reducing the variability in random-phase initialized Gerchberg-Saxton algorithm. *Opt. Laser Technol.* **85,** 30 (2016).
226. Shen, Y. *et al.* Polarization aberrations in high-numerical-aperture lens systems and their effects on vectorial-information sensing. *Remote Sens.* **14,** 1932 (2022).
227. He, C., Antonello, J. and Booth, M. J. Vectorial adaptive optics. *eLight* **3,** 23 (2023).
228. Schmidt, D. *et al. A review of solar adaptive optics* in *Adaptive Optics Systems V* (SPIE, 2016).
229. Jian, H. *et al.* Effectiveness of adaptive optics system in satellite-to-ground coherent optical communication. *Opt. Express* **22,** 16000 (2014).
230. Liu, C. *et al.* Adaptive optics for the free-space coherent optical communications. *Opt. Commun.* **361,** 21 (2016).
231. Girkin, J. M., Poland, S. and Wright, A. J. Adaptive optics for deeper imaging of biological samples. *Curr. Opin. Biotech.* **20,** 106 (2009).
232. Vangindertael, J. *et al.* An introduction to optical super-resolution microscopy for the adventurous biologist. *Methods Appl. Fluoresc.* **6,** 022003 (2018).
233. Ji, N., Sato, T. R. and Betzig, E. Characterization and adaptive optical correction of aberrations during in vivo imaging in the mouse cortex. *Proc. Natl. Acad. Sci.* **109,** 22 (2011).
234. Thompson, L. A. Adaptive optics in astronomy. *Phys. Today* **47,** 24 (1994).
235. Martinez, N. Atmospheric pre-compensation of ground-to-space communications with adaptive optics: past, present and future—a field review. *Photonics* **10,** 858 (2023).
236. Zhang, S. *et al.* Extending the detection and correction abilities of an adaptive optics system for free-space optical communication. *Opt. Commun.* **482,** 126571 (2021).
237. Liu, R. *et al.* Direct wavefront sensing enables functional imaging of infragranular axons and spines. *Nat. Methods* **16,** 615 (2019).
238. Miller, D. T. and Kurokawa, K. Cellular-scale imaging of transparent retinal structures and processes using adaptive optics optical coherence tomography. *Annu. Rev. Vis. Sci.* **6,** 115 (2020).
239. He, C. *et al.* Polarisation optics for biomedical and clinical applications: a review. *Light: Sci. Appl.* **10,** 194 (2021).

240. He, C. and Booth, M. J. *Vectorial adaptive optics: correction of polarization and phase* in *Imaging and Applied Optics Congress 2022 (3D, AOA, COSI, ISA, pcAOP)* (Optica Publishing Group, 2022).
241. Ma, Y. *et al.* Vectorial adaptive optics for advanced imaging systems. *J. Opt.* **26,** 065402 (2024).
242. Zhang, Q. and Gu, M. Vectorial adaptive optics: expanding the frontiers of optical correction. *Light: Sci. Appl.* **13,** 32 (2024).
243. Walther, P. *et al.* Experimental one-way quantum computing. *Nature* **434,** 169 (2005).
244. Tuchin, V. V., Wang, L. V. and Zimnyakov, D. A. *Optical Polarization in Biomedical Applications* (Springer, Berlin, 2006).
245. Ramella-Roman, J. C., Saytashev, I. and Piccini, M. A review of polarization-based imaging technologies for clinical and preclinical applications. *J. Opt.* **22,** 123001 (2020).
246. Dai, Y. *Adaptive optics for phase and polarization control* PhD thesis (University of Oxford, 2019).
247. Tao, X. *et al. A three-photon microscope with adaptive optics for deep-tissue in vivo structural and functional brain imaging* in *Neural Imaging and Sensing* (SPIE, 2017).
248. Morizet, J. *et al.* High-speed polarization-resolved third-harmonic microscopy. *Optica* **6,** 385 (2019).
249. Chen, L. *et al.* Advances of super-resolution fluorescence polarization microscopy and its applications in life sciences. *Comput. Struct. Biotechnol. J.* **18,** 2209 (2020).
250. Žurauskas, M. *et al.* IsoSense: frequency enhanced sensorless adaptive optics through structured illumination. *Optica* **6,** 370 (2019).
251. Gwosch, K. C. *et al.* MINFLUX nanoscopy delivers 3D multicolor nanometer resolution in cells. *Nat. Methods* **17,** 217 (2020).
252. Wang, J. *et al.* Implementation of a 4Pi-SMS super-resolution microscope. *Nat. Protoc.* **16,** 677 (2020).
253. Hao, X. *et al.* Three-dimensional adaptive optical nanoscopy for thick specimen imaging at sub-50-nm resolution. *Nat. Methods* **18,** 688 (2021).
254. Booth, M. *et al.* Aberrations and adaptive optics in super-resolution microscopy. *Microscopy* **64,** 251 (2015).
255. Lukin, V. P. Adaptive optics in the formation of optical beams and images. *Phys.-Uspekhi* **57,** 556 (2014).
256. Anche, R. M. *et al.* Polarization aberrations in next-generation giant segmented mirror telescopes (GSMTs): I. Effect on the coronagraphic performance. *Astron. Astrophys.* **672,** A121 (2023).
257. Wang, C. *et al.* Multiplexed aberration measurement for deep tissue imaging in vivo. *Nat. Methods* **11,** 1037 (2014).
258. Wang, K. *et al.* Direct wavefront sensing for high-resolution in vivo imaging in scattering tissue. *Nat. Commun.* **6,** 7276 (2015).
259. Bisch, N. *et al.* Adaptive optics aberration correction for deep direct laser written waveguides in the heating regime. *Appl. Phys. A* **125,** 364 (2019).
260. Lin, R. *et al.* Subcellular three-dimensional imaging deep through multicellular thick samples by structured illumination microscopy and adaptive optics. *Nat. Commun.* **12,** 3148 (2021).
261. Giallorenzi, T. G. Optical communications research and technology: fiber optics. *Proc. IEEE* **66,** 744 (1978).
262. Gu, M., Li, X. and Cao, Y. Optical storage arrays: a perspective for future big data storage. *Light: Sci. Appl.* **3,** e177 (2014).
263. Pfrommer, T. and Hickson, P. High resolution mesospheric sodium properties for adaptive optics applications. *Astron. Astrophys.* **565,** A102 (2014).
264. Schwertner, M., Booth, M. J. and Wilson, T. Characterizing specimen induced aberrations for high NA adaptive optical microscopy. *Opt. Express* **12,** 6540 (2004).
265. Edrei, E. and Scarcelli, G. Memory-effect based deconvolution microscopy for super-resolution imaging through scattering media. *Sci. Rep.* **6,** 33558 (2016).
266. Sirico, D. G. *et al.* Compensation of aberrations in holographic microscopes: main strategies and applications. *Appl. Phys. B* **128,** 78 (2022).
267. Zhao, M. *et al.* Phase characterisation of metalenses. *Light: Sci. Appl.* **10,** 52 (2021).
268. Marcos, S. *et al.* Impact of astigmatism and high-order aberrations on subjective best focus. *J. Vision* **15,** 4 (2015).
269. Bertolotti, J. and Katz, O. Imaging in complex media. *Nat. Phys.* **18,** 1008 (2022).
270. Welford, W. T. *Aberrations of Optical Systems* (CRC Press, New York, NY, 2017).
271. Marcos, S. *et al.* Vision science and adaptive optics, the state of the field. *Vision Res.* **132,** 3 (2017).
272. Vacalebre, M. *et al.* Advanced optical wavefront technologies to improve patient quality of vision and meet clinical requests. *Polymers* **14,** 5321 (2022).

273. Antonello, J. and Verhaegen, M. Modal-based phase retrieval for adaptive optics. *J. Opt. Soc. Amer. A* **32,** 1160 (2015).
274. Hu, Q. *et al.* Arbitrary vectorial state conversion using liquid crystal spatial light modulators. *Opt. Commun.* **459,** 125028 (2020).
275. Steane, A. M. An introduction to spinors. *arXiv* (2013).
276. Theocaris, P. S. and Gdoutos, E. E. *Matrix Theory of Photoelasticity* (Springer, Berlin, 1979).
277. Gutiérrez-Vega, J. C. Pancharatnam–Berry phase of optical systems. *Opt. Lett.* **36,** 1143 (2011).
278. Goldstein, D. H. *Polarized Light* (CRC Press, Boca Raton, FL, 2017).
279. Carl, M. Influence of polarization aberrations on point images. *J. Opt. Soc. Amer. A* **34,** 967 (2017).
280. Chipman, R. A., Lam, W.-S. T. and Young, G. *Polarized Light and Optical Systems* (CRC Press, Boca Raton, FL, 2018).
281. Pancharatnam, S. Generalized theory of interference, and its applications: Part 1. Coherent pencils. *Proc. Indian Acad. Sci. - Sect. A* **44,** 247 (1956).
282. He, C. *et al.* Full Poincaré polarimetry enabled through physical inference. *Optica* **9,** 1109 (2022).
283. Debarre, D., Booth, M. J. and Wilson, T. Image based adaptive optics through optimisation of low spatial frequencies. *Opt. Express* **15,** 8176 (2007).
284. Zhang, B. *et al.* Deep learning assisted zonal adaptive aberration correction. *Front. Phys.* **8,** 621966 (2021).
285. Litchinitser, N. M. *et al. Structured light-matter interactions in engineered optical media* in *High Contrast Metastructures VI* (SPIE, 2017).
286. Tsesses, S. *et al.* Optical skyrmion lattice in evanescent electromagnetic fields. *Science* **361,** 993 (2018).
287. Dai, Y. *et al.* Plasmonic topological quasiparticle on the nanometre and femtosecond scales. *Nature* **588,** 616 (2020).
288. Sugic, D. *et al.* Particle-like topologies in light. *Nat. Commun.* **12,** 6785 (2021).
289. Shen, Y., Martínez, E. C. and Rosales-Guzmán, C. Generation of optical skyrmions with tunable topological textures. *ACS Photonics* **9,** 296 (2022).
290. Rubinsztein-Dunlop, H. *et al.* Roadmap on structured light. *J. Opt.* **19,** 013001 (2016).
291. Forbes, A. Structured light from lasers. *Laser Photonics Rev.* **13,** 1900140 (2019).
292. Lazarev, G. *et al.* Beyond the display: phase-only liquid crystal on silicon devices and their applications in photonics. *Opt. Express* **27,** 16206 (2019).
293. Chen, C. *et al.* Topological spin texture of chiral edge states in photonic two-dimensional quantum walks. *Phys. Rev. Lett.* **129,** 046401 (2022).
294. Li, Z. *et al.* Discovery of topological magnetic textures near room temperature in quantum magnet $TbMn_6Sn_6$. *Adv. Mater.* **35,** 2211164 (2023).
295. Wu, J.-S. and Smalyukh, I. I. Hopfions, heliknotons, skyrmions, torons and both abelian and nonabelian vortices in chiral liquid crystals. *Liq. Cryst. Rev.* **10,** 34 (2022).
296. Skyrme, T. H. R. A non-linear field theory. *Proc. R. Soc., Lond., Ser. A* **260,** 127 (1961).
297. Skyrme, T. H. R. A unified field theory of mesons and baryons. *Nucl. Phys.* **31,** 556 (1962).
298. Al Khawaja, U. and Stoof, H. Skyrmions in a ferromagnetic Bose–Einstein condensate. *Nature* **411,** 918 (2001).
299. Battye, R. A., Cooper, N. R. and Sutcliffe, P. M. Stable skyrmions in two-component Bose-Einstein condensates. *Phys. Rev. Lett.* **88,** 080401 (2002).
300. Fukuda, J.-i. and Žumer, S. Quasi-two-dimensional skyrmion lattices in a chiral nematic liquid crystal. *Nat. Commun.* **2,** 246 (2011).
301. Fert, A., Reyren, N. and Cros, V. Magnetic skyrmions: advances in physics and potential applications. *Nat. Rev. Mater.* **2,** 17031 (2017).
302. Liao, Z. *et al.* Plasmonic skyrmions with bound states in the continuum. *APL Photonics* **8,** 096103 (2023).
303. Wiesendanger, R. Nanoscale magnetic skyrmions in metallic films and multilayers: a new twist for spintronics. *Nat. Rev. Mater.* **1,** 16044 (2016).
304. Luo, Y. *et al.* Skyrmion lattice creep at ultra-low current densities. *Commun. Mater.* **1,** 83 (2020).
305. Nagaosa, N. and Tokura, Y. Topological properties and dynamics of magnetic skyrmions. *Nat. Nanotechnol.* **8,** 899 (2013).
306. Gilbert, D. A. *et al.* Realization of ground-state artificial skyrmion lattices at room temperature. *Nat. Commun.* **6,** 8462 (2015).

307. Liu, C. *et al.* Disorder-induced topological state transition in the optical skyrmion family. *Phys. Rev. Lett.* **129,** 267401 (2022).
308. Tamura, R. *et al. Generation of optical skyrmion by using a spatial light modulator with a self-interferometer configuration* in *Optical Manipulation and Structured Materials Conference* (SPIE, 2023).
309. Bai, C. *et al.* Dynamic tailoring of an optical skyrmion lattice in surface plasmon polaritons. *Opt. Express* **28,** 10320 (2020).
310. Willner, A. E. *et al.* Orbital angular momentum of light for communications. *Appl. Phys. Rev.* **8,** 041312 (2021).
311. Malik, M. *et al.* Multi-photon entanglement in high dimensions. *Nat. Photonics* **10,** 248 (2016).
312. Kildishev, A. V., Boltasseva, A. and Shalaev, V. M. Planar photonics with metasurfaces. *Science* **339,** 1232009 (2013).
313. Menzel, C. *et al.* Asymmetric transmission of linearly polarized light at optical metamaterials. *Phys. Rev. Lett.* **104,** 253902 (2010).
314. Liu, Y. *et al.* Realization of polarization evolution on higher-order Poincaré sphere with metasurface. *Appl. Phys. Lett.* **104,** 191110 (2014).
315. Colas, D. *et al.* Polarization shaping of Poincaré beams by polariton oscillations. *Light: Sci. Appl.* **4,** e350 (2015).
316. Lei, X. *et al.* Metastability of photonic spin meron lattices in the presence of perturbed spin-orbit coupling. *Opt. Express* **31,** 2225 (2023).
317. Chernodub, M. N. Yang–Mills theory in Landau gauge as a liquid crystal. *Phys. Lett. B* **637,** 128 (2006).
318. Wu, X. *et al.* Direct observation of valley-polarized topological edge states in designer surface plasmon crystals. *Nat. Commun.* **8,** 1304 (2017).
319. Lu, C. *et al.* Nanoparticle deep-subwavelength dynamics empowered by optical meron–antimeron topology. *Nano Lett.* **24,** 104 (2023).
320. Gao, S. *et al.* Paraxial skyrmionic beams. *Phys. Rev. A* **102,** 053513 (2020).
321. Shen, Y. *et al.* Optical skyrmions and other topological quasiparticles of light. *Nat. Photonics* **18,** 15 (2023).
322. Wang, X.-G. *et al.* The optical tweezer of skyrmions. *npj Comput. Mater.* **6,** 140 (2020).
323. Psaroudaki, C., Peraticos, E. and Panagopoulos, C. Skyrmion qubits: challenges for future quantum computing applications. *Appl. Phys. Lett.* **123,** 260501 (2023).
324. Sarkar, S., Samanta, K. and Joseph, J. Study of polarization effects in phase-controlled multi-beam interference lithography towards the realization of sub-micron photonic structures. *J. Opt.* **22,** 085105 (2020).
325. Fujiwara, H. *Spectroscopic Ellipsometry: Principles and Applications* (Wiley, Chichester, 2007).
326. Rodrigues, O. Des lois géométriques qui régissent les déplacements d'un système solide dans l'espace, et de la variation des coordonnées provenant de ces déplacements considérés indépendamment des causes qui peuvent les produire. fre. *J. Math. Pures Appl.* **9,** 380 (1840).
327. Wang, A. A. *et al.* Topological protection of optical skyrmions through complex media. *Light: Sci. Appl.* **13,** 314 (2024).
328. Nakayama, A. *et al.* Photoinitiator-free two-photon polymerization of biocompatible materials for 3D micro/nanofabrication. *Adv. Opt. Mater.* **10,** 2200474 (2022).
329. Huang, Y., He, Z. and Wu, S.-T. Fast-response liquid crystal phase modulators for augmented reality displays. *Opt. Express* **25,** 32757 (2017).
330. Yang, G.-z. *et al.* Gerchberg–Saxton and Yang–Gu algorithms for phase retrieval in a nonunitary transform system: a comparison. *Appl. Optics* **33,** 209 (1994).
331. Poland, S. P. *et al.* Development of a doubly weighted Gerchberg–Saxton algorithm for use in multibeam imaging applications. *Opt. Lett.* **39,** 2431 (2014).
332. Zhang, H. *et al.* Fully computed holographic stereogram based algorithm for computer-generated holograms with accurate depth cues. *Opt. Express* **23,** 3901 (2015).
333. Arai, D. *et al.* Acceleration of computer-generated holograms using tilted wavefront recording plane method. *Opt. Express* **23,** 1740 (2015).
334. Jin, C. *et al.* Precise 3D computer-generated holography based on non-convex optimization with spherical aberration compensation (SAC-NOVO) for two-photon optogenetics. *Opt. Express* **29,** 20795 (2021).
335. Hossein Eybposh, M. *et al.* DeepCGH: 3D computer-generated holography using deep learning. *Opt. Express* **28,** 26636 (2020).
336. Zheng, Y.-W. *et al.* Holographic near-eye display system with large viewing area based on liquid crystal axicon. *Opt. Express* **30,** 34106 (2022).

337. Tian, Q. *et al.* DNN-based aberration correction in a wavefront sensorless adaptive optics system. *Opt. Express* **27,** 10765 (2019).
338. Prengère, L., Kulcsár, C. and Raynaud, H.-F. Zonal-based high-performance control in adaptive optics systems with application to astronomy and satellite tracking. *J. Opt. Soc. Amer. A* **37,** 1083 (2020).
339. Lee, S. and Kim, C. Ramp distribution-based contrast enhancement techniques and over-contrast measure. *IEEE Access* **7,** 73004 (2019).
340. Kong, X.-Y., Liu, L. and Qian, Y.-S. Low-light image enhancement via poisson noise aware retinex model. *IEEE Signal Process. Lett.* **28,** 1540 (2021).
341. Wang, C. and Ji, N. Pupil-segmentation-based adaptive optical correction of a high-numerical-aperture gradient refractive index lens for two-photon fluorescence endoscopy. *Opt. Lett.* **37,** 2001 (2012).

$$\mathtt{life} = \left(\int_{\mathtt{birth}}^{\mathtt{death}} \mathtt{learn}\, \mathtt{dt} + \sum_{\mathtt{acquaintance}}^{\mathtt{confidant}} \mathtt{friend} + \bigcup_{\mathtt{storgic}}^{\mathtt{conjugal}} \mathtt{love} + \lim_{\mathtt{aim} \to \infty} \mathtt{aspiration} \right) \times (1 + \varepsilon_{\mathtt{luck}})$$